VILNIUS UNIVERSITY

VYTAUTAS BUTKUS

Decoherence and Dephasing of Vibronic Excitons

Doctoral dissertation

Physical sciences, Physics (02P)

Vilnius, 2015

Dissertation was prepared at Vilnius university in 2011–2015.

Scientific supervisor –

prof. Leonas Valkūnas (Vilnius university, Physical sciences, Physics – 02P).

VILNIAUS UNIVERSITETAS

VYTAUTAS BUTKUS

Vibroninių eksitonų išsifazavimas ir dekoherencija

Daktaro disertacija

Fiziniai mokslai, Fizika (02P)

Vilnius, 2015

Disertacija rengta 2011–2015 metais Vilniaus universitete.

Mokslinis vadovas –

prof. Leonas Valkūnas (Vilniaus universitetas, fiziniai mokslai, fizika – 02P).

Contents

List of abbreviations

2D two-dimensional

BChl bacteriochlorophyll

BRC bacterial reaction center

Chl chlorophyll

DO displaced oscillator

DoF degrees of freedom

DQC double quantum coherence

ED electronic dimer

EET electronic energy transfer

ENAQT environment-assisted quantum transport

ES electronic spectroscopy

ESA excited state absorption

FC Franck–Condon

FCP fucoxanthin–chlorophyll protein

FMO Fenna–Matthews–Olson

FWHM full width at half maximum

FWM four wave mixing

GSB ground state bleaching

IR infrared

LO local oscillator

NMR nuclear magnetic resonance

PE photon echo

P–P pigment–protein

RWA rotating-wave approximation

SB system–bath

SC semi-classical

SF system–field

SE stimulated emission

TDDFT time-dependent density functional theory

TPA two-particle approximation

UV ultraviolet

VA vibrational aggregate

VD vibrational dimer

Introduction

The concept of exciton defines a collective and delocalized electronic excitation in the solid state or molecular systems. Such excitations are *coherent*, that is, the phase relationship of the quantum wavepackets, established on two or more spatially separated atoms or molecules, is maintained to some extent both in space and time. However, the quantum superposition state is not immune from the *dephasing*, that might be caused by many different factors, usually related to the interaction with the surroundings.

Many spectroscopic phenomena of electronic nature in organic molecular assemblies, for example, the motional narrowing in J-aggregates[1,2] or band formation of the absorption spectrum,[3] have been understood by employing the Frenkel exciton concept.[4] In the Frenkel exciton, an electron–hole pair is localized over a single constituent of the molecular crystal.[5] It is different from the large-radius Wannier–Mott excitons that are created in the solid state upon electronic excitation.[6]

In contrast to static and ordered solid state systems, molecular complexes are prone to static or/and dynamic disorder, and nuclear (intermolecular and intramolecular) rearrangements, which accompany the exciton dynamics, such as the photo-induced energy transfer.[6–8] Coupling to vibrational degrees introduces a distinct complexity into the (vibronic) exciton theory;[9] such electronic–vibrational interaction is often a dominating factor, shaping the molecular spectrum. The effects of vibrational borrowing, which allows forbidden electronic transitions through simultaneous excitation of certain asymmetric vibrations,[10] or the Jahn–Teller effect, regarding nuclear instability of degenerate electronic states,[11] are just a few physical situations, where the electronic–vibrational interaction beyond the adiabatic approximation becomes very important.

Recent advances of the ultrashort laser spectroscopy, allowing preparation of picosecond or femtosecond laser pulse sequences, have opened a wide window for studying coherent properties of molecular systems on ultrafast time scales. Together with the available high-resolution information of the structure of these complexes, direct evaluation of coherent exciton dynamics became possible. For example, using femtosecond pulses, one can generate a superposition of molecular

eigenstates and directly observe it as quantum beats (also referred to as coherences) in the transient absorption[12–14] or the two-dimensional spectrum.[15,16] Due to the interaction of the wavepacket with the surroundings (for pigment molecules of biological origin it is usually the protein scaffold), quantum superposition has to be considered within the theoretical framework of open quantum systems.[6,8,17,18] At the heart of this theory it is shown, that the superposition state is entangled with the surroundings and is very fragile due to energy fluctuations of the thermal energy reservoir. The resulting decay of the established superposition state is governed by the phenomenon of *decoherence*,[18] which is taken as a more specific term than *dephasing*, referring to a general loss of the phase relationship due to decoherence, exciton relaxation or ensemble averaging. In this thesis, both terms of *decoherence* and *dephasing* will be used in description of coherent dynamics of vibronic excitons and its signatures in spectra. Decoherence is more pronounced in weakly disordered systems at low temperatures. All these mechanisms are simultaneously active and shape the spectra of molecular systems, therefore the coherent exciton dynamics become extremely complicated.

The topic of dephasing and decoherence in open quantum systems recently received a significant boost when the coherent beatings persisting beyond the characteristic decoherence time scale of quantum electronic state were reported for the monumental Fenna–Matthews–Olson (FMO) complex.[15,19] The FMO complex is a photosynthetic antenna, involved in excitation transfer to the reaction center of membranic photosynthetic apparatus of the green sulfur bacteria.[20] The nature (whether electronic[19] or vibrational[21–25]) and role (in energy[26–29] and charge[30,31] transfer) of the long-lived dynamic coherences are still being debated along with the suggestion, that electronic–vibrational mixing[29,32–35] could maintain it for as long as a few picoseconds. Therefore, the question, regarding the role of dephasing of coherence and its interplay with the nuclear degrees of freedom in molecular systems, remains open.

The **main goal** of this thesis is to determine the significance of dephasing and decoherence of vibronic excitons in molecular systems and define the signatures of electronic–vibrational interaction in the two-dimensional electronic spectra regarding the evolution of molecular excitation and quantum coherences. To achieve this goal, the following tasks were formulated:

- Establish and develop a theoretical framework, based on the perturbative response function formalism, for theoretical simulations of linear and nonlinear spectra of systems consisting of an arbitrary number of molecules and different levels of abstraction of the description of the bath.

- Extend the developed formalism to describe the vibronic coupling in molec-

ular aggregates and assess its signatures in the two-dimensional electronic spectroscopy.

- Develop methods or find signatures, how to identify and distinguish between spectral properties that are of electronic, vibrational or quantum mechanically mixed nature.

- Apply the obtained knowledge to the analysis of the experimental results of the molecular six-porphyrin nanoring.

Novelty and relevance of the results

In an adiabatic framework (i. e., assuming the Born–Oppenheimer approximation), the motion of electrons in molecules is decoupled from the slow intramolecular and intermolecular vibrations. Such a treatment gives us the picture of the potential energy surface of an electronic state; nonadiabatic changes occur only when the molecules approach the region on the potential surface where the adiabatic approximation breaks down, for example, at a conical intersection or in an avoided crossing region at the electronic–vibrational resonance of vibronic excitons. Such effects play an important role in photochemistry[36] and various theoretical methods have been developed to account it for.[35,37] However, the theory of vibronic coupling and its implications in the novel method of the two-dimensional electronic spectroscopy is still being developed. In this thesis, the perturbative response function theory of the two-dimensional spectroscopy for the Frenkel excitons is derived (chapters 1 and 2). In Chapter 3, it is extended to describe vibronic excitons with the two-particle description of vibrational states and the Redfield relaxation theory for a molecular aggregate consisting of an arbitrary number of chromophores.

Knowledge about the signatures of the static energy disorder in the two-dimensional spectra is limited. Signatures of the static energy disorder can be directly estimated from the spectrum, since the separation of the inhomogeneous and the homogeneous lineshapes is inherently given by the experimental technique itself. In this thesis we show, how the static energy disorder influences the coherences of molecular systems: the presence of decoherence and dephasing, controlled by the static energy disorder, can provide both short-lived and long-lived quantum coherences (Section 2.3.3), but the effect on electronic, vibrational and mixed coherences is essentially different[38] (Section 3.3.3). We are able to explain the lifetimes and origins of coherent beatings in a number of recently reported experiments.[30,39–42]

Regarding the discussion of a possible role of electronic versus vibrational coherences, it is crucial to find a strong criterion for identification of the nature of the experimentally observed coherences. It was proposed, that the distinction can be obtained by analyzing the so-called rephasing and nonrephasing two-dimensional spectra,[43] temperature dependence of the spectra,[44] or by applying the short-time Fourier transform of the time-resolved spectroscopic signals.[45] Here, in sections 3.1 and 3.2, we propose the method of distinction between electronic and vibrational coherences by means of the so-called coherence maps, which are constructed from a set of the time-dependent two-dimensional spectra.[34,46,47] Our method has already aided in the identification of experimentally observed vibrational and mixed coherences which were shown to be responsible for speeding up the charge transfer in photosynthesis.[30]

Vibronic exciton theory does not rule out the electronic and vibrational coherences to simultaneously co-exist in the same system. However, clear experimental characterization of coherences with different origin and their interconnection has been elusive. Experimental results, supported by our theoretical considerations of the molecular six-porphyrin nanoring presented in Chapter 4, demonstrate the co-existence of electronic, vibrational and mixed coherences for the first time.[48] Our elaborate considerations of the beatings in the two-dimensional spectra is also a novel principle, how the analysis of coherences can aid in determining the energy states of the system.[49]

Statements of the thesis

1. Quantum coherences of electronic, vibrational or mixed nature can be discriminated by analyzing coherent oscillations in the two-dimensional spectrum. For each type of coherence, these differences appear as typical amplitude and phase patterns in the constructed coherence maps.

2. The effect of static energy disorder on the coherences depends on the nature of the states involved in the quantum superposition. The amplitude and the lifetime of the coherences of purely electronic origin is dramatically reduced by the disorder; coherences of vibrational origin weakly depend on the disorder. However, the lifetime of the electronic coherences can be extremely enhanced if the conditions for the decoherence-limited quantum beats are fulfilled.

3. For vibronically coupled systems, the lifetime of excitonic coherences is determined by the coupling to discrete modes of intramolecular vibrations and by the proximity of the system parameters to the electronic–vibrational resonance, as it leads to the coherence lifetime borrowing phenomenon.

4. The electronic and vibronic energy level structure of the six-porphyrin nanoring is determined by the non-trivial combined effect of the static energy disorder, vibronic coupling and small geometric deformations of the nanoring. These properties can be directly assessed from the analysis of quantum coherences in the two-dimensional spectra.

List of publications

The results were published in a book chapter

1. D. Abramavicius, V. Butkus, L. Valkunas, *Interplay of Exciton Coherence and Dissipation in Molecular Aggregates. Semiconductors and Semimetals, Volume 85. Quantum Efficiency in Complex Systems, Part II: From Molecular Aggregates to Organic Solar Cells* (edited by Uli Würfel, Michael Thorwart, and Eicke R.Weber) San Diego: Academic Press, 2011, 3–46. ISBN: 978-0-12-391060-8.

and publications:

1. D. Abramavicius, V. Butkus, J. Bujokas, L. Valkunas. *Manipulation of two-dimensional spectra of excitonically coupled molecules by narrow-bandwidth laser pulses*, Chemical Physics **372**, 22–32 (2010).

2. V. Butkus, D. Abramavicius, A. Gelzinis, L. Valkunas. *Two-dimensional optical spectroscopy of molecular aggregates*, Lithuanian Journal of Physics **50**, 267–303 (2010).

3. V. Butkus, L. Valkunas, D. Abramavicius. *Molecular vibrations-induced quantum beats in two-dimensional electronic spectroscopy*, The Journal of Chemical Physics **137**, 044513 (2012).

4. V. Butkus, D. Zigmantas, L. Valkunas, D. Abramavicius. *Vibrational vs. electronic coherences in 2D spectrum of molecular systems*, Chemical Physics Letters **545**, 40-43 (2012).

5. V. Butkus, D. Zigmantas, L. Valkunas, D. Abramavicius. *Phase relationships of spectral oscillations in 2D molecular spectroscopy*, EPJ Web of Conferences **41**, 05021 (2013).

6. V. Butkus, D. Zigmantas, D. Abramavicius, L. Valkunas. *Distinctive character of electronic and vibrational coherences in disordered molecular aggregates*, Chemical Physics Letters **387**, 93–98 (2013).

7. V. Butkus, L. Valkunas, D. Abramavicius. *Vibronic phenomena and exciton-vibrational interference in two-dimensional spectra of molecular aggregates*, The Journal of Chemical Physics **140**, 034306 (2014).

8. E. Bašinskaitė, V. Butkus, D. Abramavicius, L. Valkunas. *Vibronic models for nonlinear spectroscopy simulations*, Photosynthesis Research **121**, 95–106 (2014).

9. V. Butkus, A. Gelzinis, R. Augulis, A. Gall, C. Büchel, B. Robert, D. Zigmantas, L. Valkunas, D. Abramavicius. *Coherence and population dynamics of chlorophyll excitations in FCP complex: Two-dimensional spectroscopy study*, The Journal of Chemical Physics **21**, 212414 (2015).

For all Publications, the author of this dissertation was involved in a substantial part of writing and a major part of theoretical simulations. For the book chapter, author wrote one section, containing introduction of theory of spectroscopy and simulation results. For publications 1–7, the author performed all simulations and derived the majority of analytical expressions. For Publication 8, the author carried out simulations of the 2D spectra and substantially contributed to developing of the theoretical expressions and writing. For Publication 9, the author performed analysis of experimental data and wrote most of the paper.

Scientific papers with results, not included in the thesis:

1. T. Vasiliauskas, V. Butkus, E. Šermukšnis, V. Palenskis, J. Vyšniauskas. *Computer simulation of transient processes in DFB semiconductor lasers*, Lithuanian Journal of Physics **47**, 397–402 (2007).

2. V. Butkus, T. Mančal. *Electron–phonon coupling in coherent two-dimensional electronic spectroscopy*. *WDS'10 Proceedings of Contributed Papers: Part III – Physics*, Prague: Matfyzpress, 2010, 7–12. ISBN 978-80-7378-141-5.

3. V. Butkus, A. Gelzinis, L. Valkunas. *Quantum coherence and disorder-specific effects in simulations of 2D optical spectra of one-dimensional J-aggregates*, The Journal of Physical Chemistry A **115**, 3876–3885 (2011).

4. E. Songaila, R. Augulis, A. Gelzinis, V. Butkus, A. Gall, C. Büchel, B. Robert, D. Zigmantas, D. Abramavicius, L. Valkunas. *Ultrafast energy transfer from chlorophyll c_2 to chlorophyll a in fucoxanthin–chlorophyll protein complex*, Journal of Physical Chemistry Letters **4**, 3590–3595 (2013).

5. F. D. Fuller, J. Pan, A. Gelzinis, V. Butkus, S. S. Senlik, D. E. Wilcox, C. F. Yocum, L. Valkunas, D. Abramavicius, J. P. Ogilvie. *Vibronic coherence in oxygenic photosynthesis*, Nature Chemistry **6**, 706–711 (2014).

6. A. Gelzinis, V. Butkus, E. Songaila, R. Augulis, A. Gall, C. Büchel, B. Robert, D. Zigmantas, D. Abramavicius, L. Valkunas. *Mapping energy transfer pathways in fucoxanthin–chlorophyll protein complex by two-color two-dimensional electronic spectroscopy*, Biochimica et Biophysica Acta **1847**, 241–247 (2015).

List of conferences

1. V. Butkus, T. Mančal. *Electron–phonon coupling in coherent two-dimensional electronic spectroscopy*, 19th Annual Conference of Doctoral Students – WDS 2010 (Prague, Czech Republic, 2010).

2. V. Butkus, A. Gelzinis, L. Valkunas. *Two-dimensional spectroscopy of excitonically coupled molecular aggregates,* 14th International Symposium on Ultrafast Phenomena in Semiconductors (Vilnius, Lithuania, 2010).

3. A. Gelzinis, V. Butkus, L. Valkunas. *Two-dimensional optical spectroscopy of linear J-aggregates of pseudoisocyanine*, 53rd Scientific Conference for Young Students of Physics and Natural Sciences Open Readings 2010 (Vilnius, Lithuania, 2010).

4. V. Butkus, D. Abramavicius, L. Valkunas. *Evidences of vibrational and electronic coherences in two-dimensional spectra of molecular complexes,* Frontiers in Optics 2011 / Laser Science XXVII (San Jose, USA, 2011).

5. V. Butkus, D. Abramavicius, L. Valkunas. *Evidences of vibrational and electronic coherences in two-dimensional spectra of molecular complexes,* Vilnius Workshop on Non-Linear Spectroscopy and Open Quantum Systems (Vilnius, Lithuania, 2011).

6. V. Butkus, D. Abramavicius, A. Gelzinis, L. Valkunas. *Quantum coherence in simulations of 2D optical spectra of excitonically-coupled molecular aggregates*, 54th Scientific Conference for Young Students of Physics and Natural Sciences Open Readings 2011 (Vilnius, Lithuania, 2011).

7. V. Butkus, D. Abramavicius, D. Zigmantas, R. Augulis, L. Valkunas. *Intramolecular vibrations and quantum coherence dynamics in 2D spectra simulations of porphyrin hexamer*, 12th International Conference Electronic and Related Properties of Organic Systems (Vilnius, Lithuania, 2011).

8. V. Butkus, D. Zigmantas, D. Abramavicius, L. Valkunas. *Vibracinės ir elektroninės prigimties koherentiniai reiškiniai molekulinių agregatų dvimačiuose spektruose*, LNFK39 programa ir pranešimų tezės (Vilnius, Lithuania, 2011).

9. V. Butkus, D. Zigmantas, D. Abramavicius, L. Valkunas. *Vibrational and electronic coherences in 2D spectrum of molecular systems*, 10th Nordic Femtochemistry Conference (Hovs Hallar, Sweden, 2012).

10. V. Butkus, D. Zigmantas, L. Valkunas, D. Abramavicius. *Coherent electronic and vibronic processes in 2D molecular spectroscopy*, XVIII International Conference on Ultrafast Phenomena (Lausanne, Switzerland, 2012).

11. V. Butkus, D. Zigmantas, D. Abramavicius, L. Valkunas. *Signatures of molecular vibrations in two-dimensional electronic spectroscopy*, The Sixth International Conference on Coherent Multidimensional Spectroscopy (Berlin, Germany, 2012).

12. V. Butkus, D. Abramavicius, L. Valkunas. *Coherent electronic and vibrational dynamics in the electronic 2D spectra of molecular dimers*, 2013 Conference on Lasers and Electro-Optics Europe and International Quantum Electronics Conference (Munich, Germany, 2013).

13. V. Butkus, D. Zigmantas, D. Abramavicius, L. Valkunas. *Electronic, vibronic and mixed coherences observed in 2D spectroscopy of molecular systems*, Quantum Effects in Biological Systems Workshop (Vienna, Austria, 2013).

14. V. Butkus, D. Zigmantas, D. Abramavicius, L. Valkunas. *Elektroninės ir virpesinės prigimties koherentiniai reiškiniai dvimačiuose molekulinių kompleksų spektruose*, LNFK40 programa ir pranešimų tezės (Vilnius, Lithuania, 2013).

15. V. Butkus, L. Valkunas, D. Abramavicius. *Manifestation of vibronic coupling in two-dimensional spectroscopy of molecular aggregates*, The Seventh International Conference on Coherent Multidimensional Spectroscopy (Eugene, USA, 2014).

16. V. Butkus, A. Gelzinis, F. D. Fuller, J. P. Ogilvie, L. Valkunas, D. Abramavicius. *Vibronic coherence in photosynthetic molecular complexes*, Naujametė fizikos konferencija *LT*Φ 2015 (Vilnius, Lithuania, 2015).

17. V. Butkus, H. Dong, G. R. Fleming, D. Abramavicius, L. Valkunas. *Dephasing-limited and decoherence-limited quantum coherences in disordered molecular complexes,* LNFK41 programa ir pranešimų tezės (Vilnius, Lithuania, 2015).

18. V. Butkus. *Signatures of exciton–vibrational interference in 2D spectra of supermolecules*, Quantum Effects in Biological Systems Workshop (Florence, Italy, 2015).

Chapter 1

Two-dimensional electronic spectroscopy

The idea of the two-dimensional (2D) spectroscopy came from the nuclear magnetic resonance (NMR) studies of geometric information of molecular structure in solution and atomic arrangements in the solid state. Already in 1950s it was concluded, that it is impossible to spectrally distinguish between the independent resonances, caused by the spin–spin interactions, by measuring the linear response and nonlinear methods are required.[50] Experimental techniques, which employed pulse pair interactions with the systems, were suggested. The goal was to reproduce the correlation maps, or the "two-dimensional spectra", which would show the amplitude $S(\omega_1, \omega_2)$ of the response, depending on the frequencies of the applied "pumping" (ω_1) and the "probing" (ω_2) electromagnetic fields at radio frequencies. 2D NMR techniques, such as COSY (correlation spectroscopy) and NOESY (nuclear Overhauser enhancement spectroscopy) have been extensively used to study structural and dynamical properties of proteins in solutions.[51] The importance of the multidimensional NMR spectroscopy is reflected by the fact, that in 1991 the Nobel prize in chemistry was awarded to one of the founders of the 2D NMR spectroscopy Richard R. Ernst "for his contributions to the development of the methodology of high resolution nuclear magnetic resonance (NMR) spectroscopy".[52]

The multidimensional NMR techniques are the excellent tools to study the structural information of systems, which evolve slowly (millisecond time scale). If the time scales of the dynamical processes (such as fluctuations of solvent environment, excitation and charge transfer, etc.) in the systems are shorter, transient fluorescence or absorption spectroscopies are able to provide more insight, however, with a huge trade-off in the structural resolution. 2D infrared (IR) spectroscopy can then be used, since it provides chemical bond-specific structural resolution with the time resolution ranging from femtoseconds to milliseconds.[53]

Its structural sensitivity stems from the coupling between vibrational modes that give characteristic infrared bands in the 2D IR spectrum.[54–56]

2D electronic spectroscopy (ES)—an analogue of the 2D NMR or 2D IR techniques with electromagnetic fields in the visible region—was a logical further extension in order to probe the molecular dynamics triggered by the optical excitations.[57]

In 2D ES, an experimental four-wave mixing (FWM) scheme with the heterodyne detection is applied (Fig. 1.1). Three noncollinear, weak, ultrashort, phase-controlled laser pulses interact with the sample at times τ_1, τ_2 and τ_3. The induced third-order polarization within the sample is the source of the outgoing electric field, radiated in multiple directions $\pm\mathbf{k}_1 \pm \mathbf{k}_2 \pm \mathbf{k}_3$, where $\mathbf{k}_1$, $\mathbf{k}_2$ and $\mathbf{k}_3$ are the wavevectors of the three incoming pulses. Signal, exclusively generated in the $\mathbf{k}_{\mathrm{PE}} \equiv -\mathbf{k}_1 + \mathbf{k}_2 + \mathbf{k}_3$ direction, is denoted as the photon echo (PE) signal. Since the absolute interaction time is irrelevant due to the system being in the thermal equilibrium before the first interaction, the PE signal can be characterized as a three-variable function $W(\tau, T, t)$ of positive delay times between the successive laser pulses $\tau \equiv \tau_2 - \tau_1$ and $T \equiv \tau_3 - \tau_2$, and the detection time t. The time delays between the adjacent laser pulses (τ and T) are controlled with a high precision. Additional heterodyne pulse $\mathbf{k}_{\mathrm{h}}$ usually does not pass through the sample, but aids in the signal detection and noise reduction. A two-dimensional one-sided Fourier transform of the first delay time interval and the signal detection time, that is, $\tau \to \omega_\tau$ and $t \to \omega_t$, is applied to the signal.[58–62] Then, the transformed data can be plotted as the two-dimensional spectrum at the fixed *waiting time* T, which is the parameter of the exciton wavepacket time evolution.[15, 26, 43, 60, 62–67]

Schematic examples of the 2D spectrum at the initial ($T = 0$) and long ($T \gg 0$) waiting times are shown in Fig. 1.2. The diagonal peaks (positioned at $\omega_\tau = \omega_t$) reflect the energy eigenstates; the off-diagonal peaks (or the so-called cross-peaks) ($\omega_\tau \neq \omega_t$) show correlations and coherences within the system. Energy transfer between the eigenstates is manifested by the decrease of the diagonal peak and simultaneous increase of the corresponding cross-peak with the waiting time T. The inhomogeneous and the homogeneous broadenings (indicated as σ_{inh} and σ_{h}, respectively) can be separated in the 2D spectrum as the peak elongation along and across the diagonal, respectively. The nomenclature of the 2D spectrum representation, used in Fig. 1.2 (direction of axes, color scales and contour lines), will be further used throughout this thesis.

Since different delay times are independent parameters, the time resolution of the 2D spectrum (waiting time T) is in principle unrelated to the frequency resolution (ω_t and ω_τ), what is never available in a classical pump–probe signal. In experiments, however, the resolution is limited by the pulse lengths and higher-

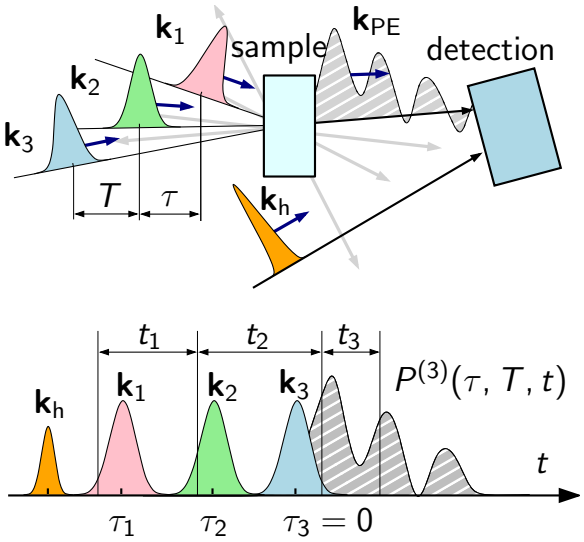

Fig. 1.1. Experimental scheme of the two-dimensional electronic spectroscopy and definitions of variables: τ_1, τ_2 and τ_3 are the times of three laser pulses exciting the sample, while t_1, t_2 and t_3 are the time variables for the system response function (see text for details). Non-PE directions of the outgoing electric field are indicated by the gray arrows.

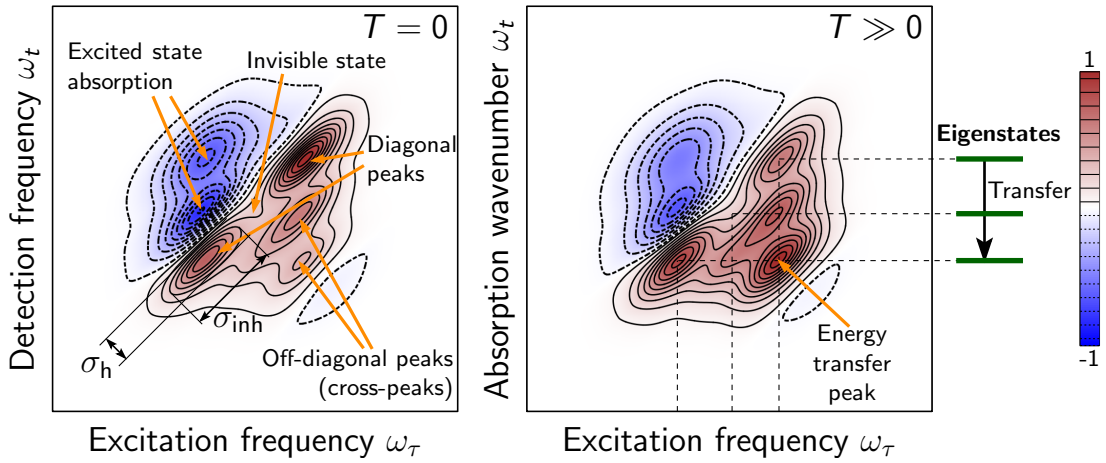

Fig. 1.2. Example of the absorptive 2D spectrum with inhomogeneous and homogeneous lineshape widths identified as σ_{inh} and σ_{h}, respectively, at the initial ($T = 0$) and long ($T \gg 0$) waiting times. Excitation relaxation through the eigenstates is indicated by the energy level diagram on the right. Spectra are drawn using the different color scales, normalized to the maximum of each spectrum. Contour lines are drawn at every 10% ($\pm 5\%$, $\pm 15\%$, ..., 95%) with respect the maximum value; contours for negative values are shown by dashed lines.

order effects. The pulse overlap regions induce variations in 2D spectra due to mixing with various interaction sequences;[68] higher order contributions induce intensity-dependence and exciton–exciton annihilation.[63]

Using the reduced system density operator ($\widehat{\sigma}$) formalism (detailed further in Section 1.3.1), the sequence of the three system–field interactions can be represented as follows. At the initial time the system is in the thermal equilibrium, population state $\widehat{\sigma} = |\text{g}\rangle\langle\text{g}|$. After the first interaction with a weak ultrashort pulse the coherence state $|\text{e}\rangle\langle\text{g}|$ is created. The second pulse after time τ creates a population in the ground state $|\text{g}\rangle\langle\text{g}|$ or in the excited state $|\text{e}\rangle\langle\text{e}|$, or a dynamic coherence in the excited state $|\text{e}\rangle\langle\text{e}'|$, which might be observed as beatings over

the waiting time T in the 2D spectrum. The third interaction creates a great variety of coherent states and the electromagnetic field is radiated by a stimulated emission, leaving the system in the population state $|\mathrm{e}\rangle\langle\mathrm{e}|$ or $|\mathrm{g}\rangle\langle\mathrm{g}|$. During the time between the interactions, various processes on different time scales can occur: dephasing and decoherence, excitation, coherence and charge transfer, chemical exchange, etc. As it will be shown later, the 2D ES signals can be directly linked to the dynamics of the reduced system density operator.

In the experiment, both positive and negative values of the delay time τ can be introduced. For a positive delay $\tau > 0$, the *rephasing* signal $W_{\mathbf{k}_\mathrm{I}}(\omega_\tau, T, \omega_t)$ is obtained in the PE direction $\mathbf{k}_\mathrm{I} \equiv \mathbf{k}_\mathrm{PE}$. It shows the opposite system density operator phase rotation (dephasing) at τ and t time intervals and so it "rephases" the system density operator and eliminates inhomogeneous broadening at $t = \tau$ (the photon echo[69]). The inhomogeneous broadening is observed as peak elongation along the diagonal, while the peak width in the anti-diagonal direction is purely due to the homogeneous broadening. Signal, denoted as the *nonrephasing*, is generated at the non-PE direction $\mathbf{k}_\mathrm{II} = +\mathbf{k}_1 - \mathbf{k}_2 + \mathbf{k}_3$. It does not have the inhomogeneous contribution eliminated and the peak lineshapes are oriented in the anti-diagonal direction. The same signal is measured in the $\mathbf{k}_\mathrm{PE}$ direction if the first and the second pulses are mutually interchanged (assuming $\tau < 0$). The sum of the rephasing and nonrephasing signals gives the pump–probe-like, or the *absorptive* 2D spectrum.[43,67,70] Usually the absorptive or rephasing spectrum is the most useful in the spectral analysis.

However, meeting the requirements for the phase stabilized laser excitation pulses was challenging[71] and the first experiments of the 2D ES were performed on the Fenna–Matthews–Olson (FMO) complex only in 2004 by Brixner et al.[62,72]

1.1 Objects

During the last decade, 2D ES has been applied to many different systems, ranging from nanostructures in the solid states to the whole photosynthetic bacteria. Let us review the key objects of the recent researches and highlight the outcomes of this technique.

Photosynthetic systems. The first results of 2D ES on the FMO complex proposed a very detailed scheme of the energy transfer between bacteriochlorophylls (BChls) and the subsequent theoretical considerations by Cho et al.[73] estimated the exciton delocalization and transfer rates of the complex. No beatings in the spectra were observed in this particular experiment due to poor temporal resolution. However, in 2007 oscillations in the 2D spectrum of the FMO complex were

extracted by Engel et al.[15]

At the time of the first experiments of the 2D ES performed on the photosynthetic FMO complex, knowledge about the features in the time-resolved 2D electronic spectra was plain (just as simplified, as introduced up to this point of the thesis; the whole truth is given below). The waiting time dependence of the diagonal peaks was thought to represent the dynamics of the eigenstate populations solely and dynamics of the off-diagonal peaks—only dynamics of the coherences, site couplings and energy transfer. In the context of this picture, the opposite phase oscillations of the diagonal and off-diagonal peaks observed in the first FMO experiments[15] have been suggested to witness the ultra-efficient excitation transfer in an oscillating, or the *wavelike*[13], manner. However, this idea and the fact, that the observed oscillations persisted for at least 660 fs at the temperature of 77 K (later, the coherence lifetime was found to be even longer, 1.5 ps[19]), was contradicting the fact that the electronic coherences at non-special conditions decay so rapidly that they are unable to affect the electronic energy transfer (EET).[74] Especially at physiological temperatures, electronic coherences should be very fragile due to energy fluctuations and inhomogeneities induced by the environment.

The observed long-lived quantum beatings in the photosynthetic complexes has gained much attention from the quantum information community, since one of the main obstacles of the quantum computing devices is the short-lived quantum superposition states,[75] that cannot be stored, transmitted or processed. At the same time biophysicists raised the idea that quantum effects are significant for biological purposes and are being favored by the natural selection.[76,77] Quantum coherence in photosynthesis, magnetoreception of the migrating birds, olfaction and other biological phenomena that are questioned to be substantially influenced by the quantum effects are now referred as the subjects of the new discipline of "Quantum biology".[78,79]

The long-lived electronic coherences have cause headaches for many theoretical chemists and physicists for years, since the standard Förster[80] and Redfield[81] relaxation theories did not provide coherence lifetimes anything close to a few hundreds of femtoseconds at the physiological conditions. Non-secular mechanism of quantum transfer, that enables the interaction between coherences and populations,[8,82] inherently neglected in the Redfield theory, was proposed to explain the phase shifts of oscillatory features in the spectra.[27] Spatially correlated environment motion was employed to explain the long lifetime of electronic coherences,[83] however this mechanism was later reported as being of a minor significance in the realistic pigment–protein complexes.[84] The concept of the proposed purely quantum coherence-induced energy transfer speed-up has been intensively criticized[85]

and other mechanisms of environment-assisted quantum transport (ENAQT),[32] which defines the optimal amount of environmental noise, leading to the enhancement of excitation transfer, or supertransfer,[86] which amounts to the enhancement of the long-range incoherent transport by the short-range coherence, were proposed.

Since the first results of 2D ES on the FMO complex, the method has been successfully applied for studies of a number of different photosynthetic systems; 2D ES essentially helped to establish or update existing kinetic schemes of light-harvesting antennae and reaction centers of plants[30,31,87,88] and bacteria.[64,89,90] 2D ES was also performed on the whole photosystem I complex demonstrating signatures of fast energy transfer[91] and on the whole intact green sulfur bacteria,[92] uncovering the connection between the chlorosome, the FMO complex and the reaction center.

Most of these findings were obtained from experiments and theoretical simulations performed using (or assuming) the knowledge of structural organization of the pigment molecules (often with resolution of a few angströms). Thus, these studies were valuable not only for widening a general understanding of the physical mechanisms within molecular systems, but also were convenient for testing and interpreting the outcomes of the new method of 2D ES. As the method itself has already been well approved and appreciated,[93] it only recently became useful to apply the developed tools of analysis of the 2D spectra for more obscure molecular systems. For instance, for the fucoxanthin–chlorophyll protein (FCP) complex, the information on the molecular structure of which is very limited.[94–97] The FCP complex is the intrinsic membrane light-harvesting protein in diatoms—unicellular chromophyte algae inhabiting marine environment and accounting for nearly a quarter of the global primary production.[98–100] In our studies of the two-dimensional spectroscopy,[49,101,102] many properties of this complex were resolved. From analysis of dynamics of the two-dimensional spectra of Chl *a* and Chl *c* Q_y absorption bands at room temperature we have reported ultrafast energy transfer between Chl *c* and Chl *a* with signatures of excitonic coupling.[101] Also, by applying the two-color two-dimensional spectroscopy[103–107], we have mapped the carotenoid–chlorophyll energy transfer pathways and resolved spectral heterogeneity of carotenoids in FCP.[102] It was found, that carotenoids fucoxanthins in FCP are spectrally distinguishable and yet transfer energy to chlorophylls (Chls) very efficiently. Additional analysis of the coherence dynamics in spectra measured at 77K temperature allowed us to identify chlorophyll *a* and fucoxanthin intramolecular vibrations dominating over the first few picoseconds and revealed previously not identified mutually non-interacting chlorophyll *c* states participating in femtosecond or picosecond energy transfer to the Chl *a* molecules.[49] Consideration of

separated coherent and incoherent dynamics allowed us to propose the vibrations-assisted coherent energy transfer between Chl *c* and Chl *a* and the overall spatial arrangement of chlorophyll molecules, as well.

Conjugated polymers. Conjugated polymers have their great potential in various organic photovoltaic devices. The basic principle of photovoltaic devices is that exciton, created by photoexcitation, at the interface of the conjugated polymer and electron acceptor dissociates into an electron and a hole. This charged potential can then be converted to electricity via electron transfer.[108] However, ultrafast processes of exciton delocalization and vibrational relaxation can occur on time scales preceding or accompanying the electron transfer.[109] Both processes are closely related to vibrational phenomena and influence the exciton dissociation. Therefore, the interest to understand the role of interaction of electronic and vibrational degrees of freedom on the excited state dynamics in conjugated polymers stays high.

The carbon–carbon (C−C and C=C) vibrational stretchings as well as the torsional modes are the most significant for vibrational relaxation in conjugated polymers.[110] Population relaxation of the torsional mode has a long relaxation time scale of 1-100 ps,[111] while relaxation time scale of C−C and C=C stretching modes were found to be shorter than 100 fs.[112,113] As the vibrational relaxation has a significant effect on exciton dynamics in conjugated systems, it was also suggested to be responsible for a "hot" electron transfer process, allowing to avoid the recombination of electrons and holes in organic polymers. There are also strong evidences that quantum coherences have a dominating role in the early stages of the charge transfer dynamics in optical photovoltaic materials.

One of the first experiments of the 2D electronic spectroscopy on conjugated polymers (MEH–PPV*) were performed by Milota et al.[114] The results suggested a perceptible role of energetic disorder in the optical response of MEH–PPV. Later, Collini et al. studied electronic energy transfer in MEH–PPV[115] and observed coherences, persisting over 250 fs at room temperature and concluded, that quantum transport effects could occur along conjugated polymer chains. 2D ES study of electron transfer dynamics in P3HT/PCBM† blends have proposed a significant role of vibrational coherence in the ultrafast charge transfer, as the vibrational coherence was observed to be directly transferred from the P3HT exciton to the P3HT hole polaron in the crystalline domain and exciton exceeded other photophysical dynamics including vibrational relaxation.[116]

*poly[2-methoxy,5-(2´-ethyl-hexoxy)-1,4-phenylenevinylene]

†poly(3-hexylthiophene)/[6,6]-phenyl-C61 butyric acid methyl ester

J-aggregates. Despite the obvious differences between linear J-aggregates of spatially coupled molecules and conjugated polymers—chains of chemically coupled molecules—the photophysical properties of both systems are similar.[117] J-aggregates were discovered in 1936 independently by Jelley[118] and Scheibe,[119] who observed concentration-dependent (i. e. aggregation-dependent) narrowing and red-shift of the main absorption peak (the so-called J-band) in spectrum of pseudoisocyanine dye. During the recent decades, J-aggregates have been extensively studied both experimentally and theoretically with the aim to disclose their potential as nonlinear optical materials and artificial light harvesters.[120]

2D ES was applied in studies of cylindrical (bi-tubular) J-aggregates.[26,121–123] Apart from clear identification of exciton transfer between tubes, quantum coherences and population oscillations were also observed. By analyzing only the J-band of one-dimensional J-aggregate it was demonstrated that 2D ES visualizes the intra-band, heterogeneous dephasing dynamics and the non-uniform broadening of the J-band with respect to the main diagonal is a signature of an interplay of population transfer and the spectral diffusion[124] and intra-band coherences.[26] Analysis of the 2D spectra of the J-aggregate provides the possibility to determine the exciton delocalization size due to the J-band.[125]

Based on the analysis of the coherence maps, constructed from time-resolved 2D spectra (will be introduced here in Section 2.3.2), vibrational coherence dynamics in the electronic ground and excited states were distinguished.[122] Polarization-controlled 2D electronic spectroscopy has recently yielded in uncovering the vibronic origin of long-lived coherences of the bi-tubular J-aggregate.[123]

Other systems. Two-dimensional spectroscopy was applied in studies of isolated molecules in solution with the aim to analyze their vibrational and solvent-dependent properties in both ground and excited states. From the 2D spectrum of the Q-band of chlorophyll *a*, which is dominated by the Q_y electronic transition and a few known discrete vibrational modes, the solvent-dependent inhomogeneous broadening was reported and the solvent response time scales were estimated.[126] In the 2D ES study of isolated porphyrin molecules in solution, phase of quantum beatings was exactly mapped by using the coherence maps. The results further questioned the reliability of assignments on coherence to an electronic or vibrational origin solely on the basis of phase shifts between peaks in the 2D spectrum.[127]

Semiconductors are an ideal system for studying excitonic many-body effects, which are essential for developing a general understanding of physics of optoelectronic devices such as laser diodes. The low-temperature spectrum of semiconductor quantum wells is dominated by excitons, the dynamics of which can be

probed by using various methods of coherent multi-dimensional spectroscopy.[128] In a 2D ES study of quantum wells in bulk GaAs by Cundiff et al,[129] different hole spin states, known as heavy holes and light holes due to their different effective masses, were probed in the IR region. It was show, that in most situations the many-body effects dominate the response, but they can be suppressed using the polarization-controlled experiment techniques.

Semiconductor quantum dots are also the subjects of the coherent multidimensional spectroscopy. Especially due to their potential as components of solar cells and quantum computing devices. 2D ES was recently used in a study of self-assembled InAs/GaAs quantum dots by Fingerhut et al.[130] By probing the cross-peaks in the 2D ES signals, coupling between various transitions was revealed. These findings were beyond what could be inferred from linear and nonlinear 1D techniques. The PbS quantum dot photocell was recently studied by the means of the coherent 2D photocurrent spectroscopy.[131] Theoretical studies regarding heterogeneity of the quantum dot sizes[132] and the vibronic content[133] have also been reported.

Recently, 2D ES experiments on the negatively charged nitrogen–vacancy centers in diamond were reported by Huxter et al.[134] The observed picosecond relaxation within the phonon sideband and beatings due to strongly coupled local vibrational modes provided new insights into the dephasing and relaxation processes in these systems, which are very attractive for various applications, ranging from quantum computing to biological sensing.[135]

1.2 Theory of signal detection

The whole multi-pulse experiment can be conceptually partitioned into two stages. In the first stage the system interacts with the classical incoming field, which modifies the optical properties—induces dynamic nonlinear polarization—of a material.[136] If the magnetic system properties are neglected, this interaction is described by the quantum mechanical polarization operator. In the second stage the expectation value of the induced polarization is treated as a source of the emission field. This stage is captured by classical electrodynamics and is described by the Maxwell equations.

The set of the Maxwell–Liouville equations describes both stages of system excitation and signal generation processes:

$$\nabla^2\mathbf{E}(\mathbf{r},t)+\frac{1}{c^2}\frac{\partial^2}{\partial t^2}\mathbf{E}(\mathbf{r},t)=-\frac{4\pi}{c^2}\frac{\partial^2}{\partial t^2}\mathbf{P}(\mathbf{r},t), \tag{1.1a}$$

$$\mathbf{P}(\mathbf{r},t)=\mathrm{Tr}\left[\widehat{\mathbf{P}}(\mathbf{r})\widehat{\rho}(t)\right], \tag{1.1b}$$

$$\frac{\partial\widehat{\rho}(t)}{\partial t} = -\frac{\mathrm{i}}{\hbar}\left[\widehat{H},\widehat{\rho}(t)\right]. \tag{1.1c}$$

They read as follows: the first equation (1.1a) is the relationship between the induced nonlinear polarization $\mathbf{P}(\mathbf{r},t)$ of the system and the outgoing electric field (signal $\mathbf{E}(\mathbf{r},t)$). It is derived from the Maxwell equations in the Gaussian units. Equation (1.1b) is the definition of the induced nonlinear polarization $\mathbf{P}(\mathbf{r},t)$ as the expectation value of the polarization operator $\widehat{\mathbf{P}}(\mathbf{r})$, represented by the trace of its product with the system density operator $\widehat{\rho}(t)$. The third expression (1.1c) is the equation of motion of the system density operator under the influence of the excitation field. Here $\widehat{H}$ is the semi-classical (SC) Hamiltonian, that describes the quantum system under the influence of the classical electric field as an external force.

It is obvious that having the density operator described properly, we would be able to obtain the nonlinear polarization and the outgoing electric field, which (or its intensity) is an actual measurable quantity. Thus, an adequate description of the system density operator $\widehat{\rho}(t)$ can be formulated as the main goal of the theory of nonlinear spectroscopy.

Equations (1.1a)–(1.1c) describe an arbitrary spectroscopy experiment and are fundamental for the microscopic theory of spectroscopy. In the following sections of this chapter, the first two Maxwell–Liouville equations will be separately described. Special requirements for the two-dimensional electronic spectroscopy will allow us to simplify Eq. (1.1a) for the nonlinear polarization considerably (Sec. 1.2). The general formulas for the 2D ES signals in the framework of the perturbative third-order response function theory will be derived in Sec. 1.3.

1.2.1 Nonlinear polarization

The incoming optical electric fields induce the dynamic nonlinear polarization in the medium. We can expand the polarization in the time domain in terms of the different orders of nonlinearity:

$$\mathbf{P}(\mathbf{r},t) = \mathbf{P}^{(1)}(\mathbf{r},t) + \mathbf{P}^{(2)}(\mathbf{r},t) + \ldots = \mathbf{P}^{(1)}(\mathbf{r},t) + \mathbf{P}_{\mathrm{NL}}(\mathbf{r},t). \tag{1.2}$$

Here $\mathbf{P}_{\mathrm{NL}}$ denotes all nonlinear contributions. Similar expansion can be made in the frequency domain in terms of harmonic components of the incoming field:

$$\begin{aligned}\mathbf{P}(\mathbf{r},\omega) = \widehat{\chi}^{(1)}(\omega)\mathbf{E}(\mathbf{r},\omega) + \widehat{\chi}^{(2)}(\omega;\omega_1,\omega_2)\mathbf{E}(\mathbf{r},\omega_1)\mathbf{E}(\mathbf{r},\omega_2) \\ + \widehat{\chi}^{(3)}(\omega;\omega_1,\omega_2,\omega_3)\mathbf{E}(\mathbf{r},\omega_1)\mathbf{E}(\mathbf{r},\omega_2)\mathbf{E}(\mathbf{r},\omega_3) + \ldots\end{aligned} \tag{1.3}$$

Here $\widehat{\chi}^{(1)}$, $\widehat{\chi}^{(2)}$, and $\widehat{\chi}^{(3)}$ are the linear, the second-order and the third-order susceptibility tensors, respectively. We will drop the vector notations of polarization and electric fields assuming, that

- the medium is isotropic and nondispersive (this allows us to replace the susceptibility tensors by constants), and
- the polarizations of the incident excitation pulses are equal (we will come back to this question in Sec. 2.2.1).

The optical field in principle may be given as a superposition of harmonic components. Then Eq. (1.3) will involve summations (integrals) over the incoming field frequencies.

For example, let us consider the second-order contribution

$$P^{(2)}(\mathbf{r},\omega) = \chi^{(2)}(\omega;\omega_1,\omega_2)E(\mathbf{r},\omega_1)E(\mathbf{r},\omega_2) \tag{1.4}$$

and the incoming field

$$E(\mathbf{r},t) = \mathcal{E}(t)\exp(\mathrm{i}\mathbf{k}_0\mathbf{r} - \mathrm{i}\omega_0 t) + \mathcal{E}(t)\exp(-\mathrm{i}\mathbf{k}_0\mathbf{r} + \mathrm{i}\omega_0 t), \tag{1.5}$$

which represents a single linearly polarized pulse with wavevector $\mathbf{k}_0$ and frequency ω_0. $\mathcal{E}(t)$ is the slowly-varying amplitude of the pulse. The Fourier transform of the field gives

$$E(\mathbf{r},\omega) = \mathcal{E}(\omega-\omega_0)\exp(\mathrm{i}\mathbf{k}_0\mathbf{r}) + \mathcal{E}(\omega+\omega_0)\exp(-\mathrm{i}\mathbf{k}_0\mathbf{r}). \tag{1.6}$$

In the case of the ultrashort pulse we may substitute the Fourier frequency ω (it can be both positive and negative) by $\pm\omega_0$. By neglecting the dispersion in the material and by inserting Eq. (1.6) into Eq. (1.4), we obtain

$$\begin{aligned} P^{(2)}(\mathbf{r},\omega) \propto\ & \exp\left(\mathrm{i}(\mathbf{k}_0+\mathbf{k}_0)\mathbf{r}\right)\chi^{(2)}(\omega;\omega_0,\omega_0) \\ & + \exp\left(\mathrm{i}(\mathbf{k}_0-\mathbf{k}_0)\mathbf{r}\right)\chi^{(2)}(\omega;\omega_0,-\omega_0) \\ & + \exp\left(\mathrm{i}(-\mathbf{k}_0+\mathbf{k}_0)\mathbf{r}\right)\chi^{(2)}(\omega;-\omega_0,\omega_0) \\ & + \exp\left(\mathrm{i}(-\mathbf{k}_0-\mathbf{k}_0)\mathbf{r}\right)\chi^{(2)}(\omega;-\omega_0,-\omega_0). \end{aligned} \tag{1.7}$$

The obtained expression shows, that the incoming fields are mixed together and the induced polarization may involve various combinations of their wavevectors. Additionally, we can associate these polarization configurations with various nonlinear processes. For instance,

$$\chi^{(2)}(\omega;\omega_0,\omega_0) = \delta(\omega-2\omega_0)\chi^{(2)}(2\omega_0;\omega_0,\omega_0) \tag{1.8}$$

is the second harmonic generation and

$$\chi^{(2)}(\omega;\omega_0,-\omega_0)=\delta(\omega)\chi^{(2)}(0;\omega_0,-\omega_0) \tag{1.9}$$

represents the creation of the constant optical polarization of the sample, known as the optical rectification.[136] For the higher orders of polarization, we would get a similar mixing of the incoming fields (multiwave mixing) and would obtain different sets of the signal wavevectors.

1.2.2 Phase-matching

We would like to rewrite the Maxwell–Liouville equation (1.1a) in a simpler form. To do that, a few assumptions have to be made. First, the polarization term in Eq. (1.1a) contains all terms of the nonlinear polarization, given by Eq. (1.2), but the second-order polarization is zero due to the isotropy of the sample,[69] that is,

$$P(\mathbf{r},t)=\chi^{(1)}E(\mathbf{r},t)+P_{\mathrm{NL}}(\mathbf{r},t). \tag{1.10}$$

Second, we neglect the linear absorption losses of the sample by postulating that the first-order susceptibility $\chi^{(1)}(\omega)$ is a real quantity. Third, we assume that the linear response is local in space for all relevant frequencies and the dielectric function is expressed as the refraction index,

$$n^2(\omega)=\varepsilon(\omega)=1+4\pi\chi^{(1)}(\omega). \tag{1.11}$$

Then Eq. (1.1a) can be rewritten for all higher-order polarizations $P_{\mathrm{NL}}(\mathbf{r},t)$:

$$\nabla^2E(\mathbf{r},t)+\frac{n^2}{c^2}\frac{\partial^2}{\partial t^2}E(\mathbf{r},t)=-\frac{4\pi}{c^2}\frac{\partial^2}{\partial t^2}P_{\mathrm{NL}}(\mathbf{r},t). \tag{1.12}$$

Second-order polarization in the case of interaction of the material and a single laser pulse with wavevector $\mathbf{k}_0$ was described previously and resulted in four terms with frequencies $\omega=\pm\omega_0\pm\omega_0$ (Eq. (1.7)). The wavevector $\mathbf{k}_s=\pm\mathbf{k}_0\pm\mathbf{k}_0$ in these terms also defines the direction of the outgoing signal due to the phase-matching condition.

In the case of the interaction with three pulses with different wavevectors $\mathbf{k}_1$, $\mathbf{k}_2$ and $\mathbf{k}_3$ (and the corresponding angular frequencies ω_1, ω_2 and ω_3), the third-order polarization and the signal would be relevant only for the frequency and wavevector combinations $\omega_s=\pm\omega_1\pm\omega_2\pm\omega_3$ and $\mathbf{k}_s=\pm\mathbf{k}_1\pm\mathbf{k}_2\pm\mathbf{k}_3$, and the two-photon interactions such as $\pm2\mathbf{k}_1\pm\mathbf{k}_2$, $\pm2\mathbf{k}_1\pm\mathbf{k}_3$, etc.

The third-order polarization, relevant for the four-wave mixing signal of the 2D

ES, can be expanded as a series of components according to their propagation direction $\{\mathbf{k}_s\}$ and frequency $\{\omega_s\}$, summed over the index s in the following way:

$$P^{(3)}(\mathbf{r}, t) = \sum_s P_s^{(3)}(t) \exp\left(\mathrm{i}\mathbf{k}_s\mathbf{r} - \mathrm{i}\omega_s t\right), \tag{1.13}$$

Since the electric field is linear in polarization, each nonlinear component of the polarization is defined by Eq. (1.12). For a single term in the third-order polarization expansion,

$$P_{\mathrm{NL}}(\mathbf{r}, t) \equiv P_s(t) \exp\left(\mathrm{i}k_s z - \mathrm{i}\omega_s t\right), \tag{1.14}$$

which propagates along the z axis parallel to $\mathbf{k}_s$, we look for a solution of the electric field (Eq. (1.1a)) in one dimension in the form of

$$E(\mathbf{r}, t) = E_s(\mathbf{r}, t) \exp(\mathrm{i}k_s' z - \mathrm{i}\omega_s t) + \mathrm{c.c.}, \tag{1.15}$$

where $k_s' = \frac{\omega_s}{c} n(\omega_s)$ is the wavevector of the emitted field, expressed via the refractive index of the medium $n(\omega_s)$ for frequency ω_s and the speed of light c.

The rapidly oscillating part of the third-order polarization is extracted making $P_s(t)$ in Eq. (1.14) a slowly-varying envelope of the temporal third-order polarization dynamics. For the slowly-varying envelope function, the relation

$$\left|\frac{\partial}{\partial t} P_s(t)\right| \ll |\omega_s P_s(t)| \tag{1.16}$$

holds. The same approximation is valid for the electric field envelope $E_s(z, t)$. Similarly, the slowly-varying spatial amplitude of the electric field makes its second derivative negligible. Insertion eqs. (1.14) and (1.15) into Eq. (1.12), and application the approximations gives us

$$\mathrm{i}k_s' \frac{\partial}{\partial z} E_s(z, t) = -2\pi \frac{\omega_s^2}{c^2} P_s(t) \exp(\mathrm{i}\Delta k_s z), \tag{1.17}$$

where $\Delta k_s \equiv k_s - k_s'$. By integrating this over the sample length from $z = 0$ to $z = L$ we get

$$E_s(L, t) = \mathrm{i} \frac{2\pi\omega_s}{n(\omega_s)c} L P_s(t) \mathrm{sinc}\left(\frac{\Delta k_s L}{2}\right) \exp\left(\mathrm{i}\frac{\Delta k_s L}{2}\right). \tag{1.18}$$

The $\mathrm{sinc}(x) \equiv \sin(x)/x$ function is related to the phase-matching condition. If the sample size is smaller than the wavelength (i. e. $L \ll \lambda$), the signal field is radiated with an arbitrary wavevector since $\Delta k_s L \ll 1$ and the sinc function is equal to 1.

For macroscopic samples ($L \gg \lambda$), the sinc function can be approximated as the Dirac δ function with respect to Δk_s. In that case, the signal is generated only in the $k_s' = k_s$ direction.[69, 137]

We have treated the experimental setup as one-dimensional, but at this point we can make generalizations for signals in three dimensions. For microscopic samples, smaller than the wavelength of the incident field, the signal is not direction-selective. This has implications, for instance, in the nonlinear single-molecule spectroscopy, where the selectivity of the signals cannot be achieved by the phase-matching of the optical signal.[138] Thus, collinear excitation geometry and the phase-cycling technique,[139] fluorescence detection (photon counting) and photocurrent detection (electron counting) can be employed to perform nonlinear spectroscopy on single molecules.[140, 141] For macroscopic samples (much larger than the field wavelength) the direction-selective signal contains a multiple interference, stemming from each point in the sample. The interference is positive only at the signal wavevector equal to the wavevector of the polarization. Collinear excitation pulse geometry is also used in experimental realizations with the pulse shapers and the phase-matching contributions are obtained via the phase-cycling.[107, 142]

1.2.3 Homodyne and heterodyne detection

Phase-matching provides a powerful utility in the multiwave mixing experiment: while the total polarization may cause electric field radiation in many spatial directions, the detector can be in a position, where only one specific component of the total signal field is captured. Equation (1.18) reflects, that the electric field $E_s(L, t)$ detected along the direction of wavevector $\mathbf{k}_s$ will be linearly proportional to the corresponding component of the induced polarization due to the phase-matching. The detected intensity of the electric field $I_s(t)$ is then proportional to the amplitude of the polarization squared:

$$I_s \propto |E_s(L, t)|^2 \propto L^2 |P_s(t)|^2 . \tag{1.19}$$

This is a very convenient result since it shows that any spectroscopic measurement can be simulated just by knowing the time dependence of the nonlinear polarization of the system. This relationship holds for the *homodyne detection* regime where the intensity of the polarization-induced electric field is measured.

In the *heterodyne detection* scheme the detector measures a superposition of the electric field, emitted from the sample, and the external local oscillator (LO)

pulse, applied in the signal direction $\mathbf{k}_s$. Then the detected intensity is

$$I_s \propto |E_{\mathrm{LO}}(t) + LP_s(t)|^2 = |E_{\mathrm{LO}}(t)|^2 + L^2 |P_s(t)|^2 + 2L\mathrm{Re}\left[E^*_{\mathrm{LO}}(t)P_s(t)\right]. \tag{1.20}$$

The first two terms of this expression can be neglected since the polarization is very weak and the LO pulse is well known, and can be subtracted. The measured quantity is then defined by the integral

$$W(t) \equiv \mathrm{Re}\int_{-\infty}^{\infty} \mathrm{d}\tau \left[E^*_{\mathrm{LO}}(\tau)P_s(\tau)\right]. \tag{1.21}$$

If we treat the LO as a δ-shaped, the measurement will give

$$W(t) = \mathrm{Re}P_s(t). \tag{1.22}$$

This result also involves the phase difference between the polarization and the LO pulse ϕ. If the phase difference is fixed, we can also probe the imaginary part of the induced polarization by taking $\phi = \pi/2$. From Eq. (1.21) it is then possible to extract both real and imaginary parts of the induced polarization. In that case we define the heterodyne signal as the complex signal, equivalent to the induced polarization.

The above given relationships and considerations might not work in some certain cases. The generated signal must be very weak, compared the incoming laser radiation, so that the incoming field is not affected by the multiwave mixing. Electric field and the induced polarization dependence (Eq. (1.19)) is incorrect for the optically dense samples since the reabsorption effects are significant: then the polarization induction is not separable from the field propagation.

1.3 Response function theory

1.3.1 Reduced density operator

When the components of a molecular system are smaller than the optical wavelength of the incident electric field, the interaction of a molecule and a the field can approximately described as the interaction of an electric dipole and electromagnetic field. This is known as the dipole approximation. The total semi-classical Hamiltonian can then be written as follows:

$$\widehat{H} = \widehat{H}_{\mathrm{S}} + \widehat{H}_{\mathrm{B}} + \widehat{H}_{\mathrm{SB}} + \widehat{H}_{\mathrm{int}} = \widehat{H}_{\mathrm{mat}} - \widehat{\mu}E(t). \tag{1.23}$$

Here $\widehat{H}_{\mathrm{S}}$ is the system's Hamiltonian, containing all degrees of freedom (DoF), which have to be included explicitly. The second term, $\widehat{H}_{\mathrm{B}}$ represents the reservoir (bath). The bath has infinite number of degrees of freedom, they are not directly observable and, thus, must be treated approximately. $\widehat{H}_{\mathrm{SB}}$ is the interaction between the system and the reservoir. These terms of the Hamiltonian constitute the material part of the system $\widehat{H}_{\mathrm{mat}}$, which does not include the optical field. The last term, $\widehat{H}_{\mathrm{int}} = -\widehat{\mu}E(t)$, is the dipolar system–field (SF) interaction.

The dynamics of the system governed by the Hamiltonian is more conveniently described using superoperators.[6,69] Superoperators perform certain operation on "traditional" operators. For example, a commutator with the semi-classical Hamiltonian can be written as a superoperator in the following way:

$$\mathcal{L}\widehat{A} \equiv \left[\widehat{H}, \widehat{A}\right] = \widehat{H}\widehat{A} - \widehat{A}\widehat{H}. \tag{1.24}$$

This particular superoperator $\mathcal{L}$ is denoted as the *Liouville superoperator (Liouvillian).* We will need a few more superoperators, which can be introduced in a similar way:

$$\mathcal{L}_{\mathrm{mat}}\widehat{A} \equiv \left[\widehat{H}_{\mathrm{mat}}, \widehat{A}\right], \tag{1.25}$$

$$\mathcal{L}_{\mathrm{int}}\widehat{A} \equiv \left[\widehat{\mu}, \widehat{A}\right] E(t) = \mathcal{V}\widehat{A}E(t). \tag{1.26}$$

The equation of motion for the density operator $\widehat{\rho}(t)$, which represents the system and the bath, is the Liouville–von Neumann equation:

$$\frac{\partial}{\partial t}\widehat{\rho}(t) = -\frac{\mathrm{i}}{\hbar}\left[\widehat{H}_{\mathrm{mat}} - \widehat{\mu}E(t), \widehat{\rho}(t)\right] = -\frac{\mathrm{i}}{\hbar}\mathcal{L}_{\mathrm{mat}}\widehat{\rho}(t) + \frac{\mathrm{i}}{\hbar}\mathcal{L}_{\mathrm{int}}\widehat{\rho}(t). \tag{1.27}$$

This equation is equivalent to the Schrödinger equation except that the wavefunction and the Hamiltonian is replaced by the density operator and the Liouville superoperator, respectively. Thus, all the formalism of quantum mechanics can be directly applied in the Liouville space, which is a direct product space of two Hilbert spaces. A regular operator, that can be represented as the $N \times N$ matrix in the Hilbert space, is replaced by a N^2 length vector in the Liouville space. An arbitrary superoperator can then be written as a $N^2 \times N^2$ size matrix. The operation of a superoperator on an operator then amounts to the matrix and vector multiplication.

However, this equation cannot be solved exactly since the number of DoF of the bath is infinite. Instead, the reduced density operator $\widehat{\sigma}(t)$ is introduced, which is defined only within the system's DoF. This is accomplished by averaging

over the reservoir DoF:

$$\widehat{\sigma}(t) = \mathrm{Tr}_{\mathrm{B}} \left\{ \widehat{\rho}(t) \right\}. \tag{1.28}$$

Assuming that the bath is in the thermodynamical equilibrium at all times we can write the bath density operator as

$$\widehat{\rho}_{\mathrm{B}} = \mathcal{Z}_B^{-1} \exp(-\beta \widehat{H}_{\mathrm{B}}), \tag{1.29}$$

where

$$\mathcal{Z}_{\mathrm{B}} = \sum_{\nu} \exp(-\beta E_{\nu}^{(\mathrm{B})}) \tag{1.30}$$

is the bath partition function in terms of its eigenstates with energies $E_{\nu}^{(B)}$; $\beta = (k_{\mathrm{B}} T)^{-1}$ is the inverse thermal energy. The density matrix of the whole system is now a direct product of the system and the bath density matrices: $\widehat{\rho} = \widehat{\sigma} \otimes \widehat{\rho}_B$. This level of description is known as the Born approximation.[8]

We will be interested in the dynamics of the reduced density operator. It is possible to derive the equation of motion for the system density operator using an approximate perturbation theory method with respect to the system–bath (SB) interaction. The time-local equation of motion is obtained in the Markov approximation, where the system correlation time is accepted to be much smaller than the time scale of the relevant system dynamics.

1.3.2 Series expansion of density operator

In this section, we will perform a perturbative expansion of the reduced density operator. We will account for the system–field interaction perturbatively while keeping the material part as the reference. Also, we will temporally neglect the bath and assume, that the material Hamiltonian describes the system only. The reduced density operator is then equal to the full density operator, $\widehat{\sigma}(t) = \widehat{\rho}(t)$.

The following steps of the time-dependent perturbation theory application is typical for the most spectroscopic calculations. For this type of description, the interaction picture in the Liouville space is more useful than the Schrödinger or the Heisenberg picture in the Hilbert space. Essentially it represents the description of the problem in a rotating frame and the evolution of the whole system can then be described as of the reference. As the reference Hamiltonian is time-independent, the evolution operator in the Liouville space can be defined as[69]

$$\mathcal{U}_{\mathrm{mat}}(t) \equiv \exp\left\{ -\frac{\mathrm{i}}{\hbar} \mathcal{L}_{\mathrm{mat}} t \right\} \tag{1.31}$$

and any time-dependent quantity (e. g. a system density operator) can be trans-

formed into the interaction picture like

$$\widehat{\rho}^{\mathsf{I}}(t) = \mathcal{U}^{\dagger}_{\mathsf{mat}}(t)\widehat{\rho}(t). \tag{1.32}$$

Here $\mathcal{U}^{\dagger}_{\mathsf{mat}}(t)$ denotes a Hermitian conjugate operator. The transition between the Liouville and the Hilbert space is accomplished by

$$\mathcal{U}^{\dagger}_{\mathsf{mat}}(t)\widehat{\rho}(t) \Leftrightarrow \widehat{U}^{\dagger}(t)\widehat{\rho}(t)\widehat{U}(t). \tag{1.33}$$

Here the evolution operator

$$\widehat{U}^{\dagger} = \exp\left\{\frac{\mathsf{i}}{\hbar}\widehat{H}_{\mathsf{mat}}t\right\} \tag{1.34}$$

acts on density operator's *bra* from the left and $\widehat{U}$ – on *ket* from the right. Having defined the material evolution operator, we are able to move to the interaction picture and write down the Liouville–von Neumann equation for the full density operator with respect to the perturbative interaction Liouvillian:

$$\frac{\partial}{\partial t}\widehat{\rho}^{\mathsf{I}}(t) = \frac{\mathsf{i}}{\hbar}\mathcal{L}^{\mathsf{I}}_{\mathsf{int}}(t)\widehat{\rho}^{\mathsf{I}}(t) = \frac{\mathsf{i}}{\hbar}\mathcal{V}(t)\widehat{\rho}^{\mathsf{I}}(t)E(t). \tag{1.35}$$

Here $\mathcal{V}(t) = \mathcal{U}^{\dagger}_{\mathsf{mat}}(t)\mathcal{V}\mathcal{U}_{\mathsf{mat}}(t)$. The system part ($\mathcal{L}_{\mathsf{mat}}$) is included into the evolution operator and the interactional term is left in the equation of motion. This expression can be formally integrated:

$$\widehat{\rho}^{\mathsf{I}}(t) = \widehat{\rho}^{\mathsf{I}}(t_0) + \frac{\mathsf{i}}{\hbar}\int\limits_{t_0}^{t} \mathsf{d}\tau\mathcal{V}(\tau)\widehat{\rho}^{\mathsf{I}}(\tau)E(\tau). \tag{1.36}$$

Now we can move back to the Schrödinger picture. Since we treat the system density operator as describing an equilibrium system state at the initial time t_0, the molecular evolution operator does not affect it. Thus, by repeatedly inserting the right hand side portion of Eq. (1.36) into the $\widehat{\rho}^{\mathsf{I}}(t)$ term within the integral, one would obtain an infinite series, which in the Schrödinger picture is

$$\begin{aligned}\widehat{\rho}(t) = \widehat{\rho}_{\mathsf{eq}} &+ \frac{\mathsf{i}}{\hbar}\int\limits_{t_0}^{t} \mathsf{d}\tau\mathcal{U}_{\mathsf{mat}}(t)\mathcal{V}(\tau)\widehat{\rho}_{\mathsf{eq}}E(\tau) \\ &+ \left(\frac{\mathsf{i}}{\hbar}\right)^2\int\limits_{t_0}^{t}\mathsf{d}\tau\int\limits_{t_0}^{\tau}\mathsf{d}\tau'\mathcal{U}_{\mathsf{mat}}(t)\mathcal{V}(\tau)\mathcal{V}(\tau')\widehat{\rho}_{\mathsf{eq}}E(\tau)E(\tau')\end{aligned} \tag{1.37}$$

$$+\left(\frac{\mathrm{i}}{\hbar}\right)^3\int_{t_0}^{t}\mathrm{d}\tau\int_{t_0}^{\tau}\mathrm{d}\tau'\int_{t_0}^{\tau'}\mathrm{d}\tau''\mathcal{U}_{\mathrm{mat}}(t)\mathcal{V}(\tau)\mathcal{V}(\tau')\mathcal{V}(\tau'')\widehat{\rho}_{\mathrm{eq}}E(\tau)E(\tau')E(\tau'')+\ldots$$

This expression is the series expansion of the system density operator. Further we will consider the first few terms of the expansion separately.

1.3.3 Linear and third-order response functions

The second term of Eq. (1.37) is the first-order density operator expansion term. Linear polarization can be expressed, using Eq. (1.1b):

$$P^{(1)}(t)=\mathrm{Tr}\left\{\widehat{\mu}\cdot\frac{\mathrm{i}}{\hbar}\int_{t_0}^{t}\mathrm{d}\tau\mathcal{U}_{\mathrm{mat}}(t)\mathcal{V}(\tau)\widehat{\rho}_{\mathrm{eq}}E(\tau)\right\}=\int_{t_0}^{t}\mathrm{d}\tau S^{(1)}(t,\tau)E(\tau),\quad(1.38)$$

where we have changed the polarization operator $\widehat{\mathbf{P}}(\mathbf{r})$ to $\widehat{\mu}$ and defined the linear response function $S^{(1)}(t,\tau)$ as

$$S^{(1)}(t,\tau)=\frac{\mathrm{i}}{\hbar}\mathrm{Tr}\left\{\widehat{\mu}\mathcal{U}_{\mathrm{mat}}(t)\mathcal{V}(\tau)\widehat{\rho}_{\mathrm{eq}}\right\}=\frac{\mathrm{i}}{\hbar}\mathrm{Tr}\left\{\widehat{\mu}\mathcal{U}_{\mathrm{mat}}(t-\tau)\mathcal{V}\widehat{\rho}_{\mathrm{eq}}\right\}.\quad(1.39)$$

By defining the variable change $t_1\equiv t-\tau$ and sending the initial time (system is in unaffected by the interactions then) to $t_0\to-\infty$, one would obtain

$$P^{(1)}(t)=\int_{0}^{\infty}\mathrm{d}t_1S^{(1)}(t_1)E(t-t_1).\quad(1.40)$$

In the expression of the system response function (Eq. (1.39)) the superoperators are replaced by commutators of the Hilbert space:

$$S^{(1)}(t_1)=\frac{\mathrm{i}}{\hbar}\mathrm{Tr}\{\widehat{\mu}\mathcal{U}_{\mathrm{mat}}(t_1)\mathcal{V}\widehat{\rho}_{\mathrm{eq}}\}\Longleftrightarrow\frac{\mathrm{i}}{\hbar}\mathrm{Tr}\left\{\widehat{\mu}U(t_1)[\widehat{\mu},\widehat{\rho}_{\mathrm{eq}}]U^{\dagger}(t_1)\right\}\quad(1.41)$$

or

$$S^{(1)}(t)=\frac{\mathrm{i}}{\hbar}\theta(t)\left\{J(t)-J^{*}(t)\right\}\quad(1.42)$$

with

$$J(t)\equiv\mathrm{Tr}\left\{\widehat{\mu}(t)\widehat{\mu}(0)\widehat{\rho}_{\mathrm{eq}}\right\}.\quad(1.43)$$

For the third-order polarization we get

$$P^{(3)}(t)=\int_{t_0}^{t}\mathrm{d}\tau\int_{t_0}^{\tau}\mathrm{d}\tau'\int_{t_0}^{\tau'}\mathrm{d}\tau''S^{(3)}(t,\tau,\tau',\tau'')E(\tau)E(\tau')E(\tau'').\quad(1.44)$$

Here we have defined the third-order system response function $S^{(3)}(t,\tau,\tau',\tau'')$. In the Liouville space it is given by

$$S^{(3)}(t,\tau,\tau',\tau'') = \left(\frac{\mathrm{i}}{\hbar}\right)^3 \mathrm{Tr}\left[\widehat{\mu}\mathcal{U}_{\mathrm{mol}}(t)\mathcal{V}(\tau)\mathcal{V}(\tau')\mathcal{V}(\tau'')\widehat{\rho}_{\mathrm{eq}}\right]. \tag{1.45}$$

By changing the time variables to $t_3 \equiv t-\tau$, $t_2 \equiv \tau-\tau'$, $t_1 \equiv \tau'-\tau''$ (the Jakobian is equal to -1) and $t_0 \to -\infty$, we obtain

$$P^{(3)}(t) = \int_0^\infty \mathrm{d}t_3 \int_0^\infty \mathrm{d}t_2 \int_0^\infty \mathrm{d}t_1 S^{(3)}(t_3,t_2,t_1)E(t-t_3)E(t-t_3-t_2)E(t-t_3-t_2-t_1). \tag{1.46}$$

This formula is the most useful expression of the third-order polarization. It was obtained by applying a perturbative scheme upon the equation of motion of the system density operator. It is a convolution of the third-order response function and a product of the electric field functions. In Eq. (1.46) the third order polarization is a function of t, but it is also dependent on T and τ via the electric field components, representing the laser pulse configuration (see Fig. 1.1). Now we must find an efficient way to calculate the system response function and express the multiplication of electric fields in a convenient form.

In the expression of the third-order system response function (Eq. (1.45)) the superoperators are replaced by commutators of the Hilbert space:

$$\begin{aligned} S^{(3)}(t_3,t_2,t_1) &= \left(\frac{\mathrm{i}}{\hbar}\right)^3 \mathrm{Tr}\left[\widehat{\mu}\mathcal{U}_{\mathrm{mol}}(t_3)\mathcal{V}\mathcal{U}_{\mathrm{mol}}(t_2)\mathcal{V}\mathcal{U}_{\mathrm{mol}}(t_1)\mathcal{V}\widehat{\rho}_{\mathrm{eq}}\right] \qquad (1.47)\\ &= \left(\frac{\mathrm{i}}{\hbar}\right)^3 \mathrm{Tr}\left\{\widehat{\mu}U(t_3)\left[\widehat{\mu},U(t_2)\left[\widehat{\mu},U(t_1)\left[\widehat{\mu},\widehat{\rho}_{\mathrm{eq}}\right]U^\dagger(t_1)\right]U^\dagger(t_2)\right]U^\dagger(t_3)\right\}. \end{aligned}$$

By expanding the commutators we get

$$S^{(3)}(t_3,t_2,t_1) = \left(\frac{\mathrm{i}}{\hbar}\right)^3 \theta(t_1)\theta(t_2)\theta(t_3)\sum_{\alpha=1}^{4}\left[R_\alpha(t_3,t_2,t_1) - R_\alpha^*(t_3,t_2,t_1)\right], \tag{1.48}$$

where

$$R_1(t_3,t_2,t_1) = \mathrm{Tr}\left[\widehat{\mu}(t_1)\widehat{\mu}(t_1+t_2)\widehat{\mu}(t_1+t_2+t_3)\widehat{\mu}(0)\widehat{\rho}_{\mathrm{eq}}\right], \tag{1.49a}$$

$$R_2(t_3,t_2,t_1) = \mathrm{Tr}\left[\widehat{\mu}(0)\widehat{\mu}(t_1+t_2)\widehat{\mu}(t_1+t_2+t_3)\widehat{\mu}(t_1)\widehat{\rho}_{\mathrm{eq}}\right], \tag{1.49b}$$

$$R_3(t_3,t_2,t_1) = \mathrm{Tr}\left[\widehat{\mu}(0)\widehat{\mu}(t_1)\widehat{\mu}(t_1+t_2+t_3)\widehat{\mu}(t_1+t_2)\widehat{\rho}_{\mathrm{eq}}\right], \tag{1.49c}$$

$$R_4(t_3,t_2,t_1) = \mathrm{Tr}\left[\widehat{\mu}(t_1+t_2+t_3)\widehat{\mu}(t_1+t_2)\widehat{\mu}(t_1)\widehat{\mu}(0)\widehat{\rho}_{\mathrm{eq}}\right]. \tag{1.49d}$$

Heaviside functions in Eq. (1.48) emphasize the principle of causality: as it is

seen in Eq. (1.46), the third-order polarization on time t depends on the electric field at earlier times. In other words, the electric field in the past determines the polarization in the future, so if any of system response function arguments is negative, the function must be zero. Also one can notice that the system response function is always real. It is clear from the experiment, since the polarization is a measurable quantity and has a corresponding Hermitian quantum mechanical operator, the average of which is always real.

However, the whole system response depends on electric field (i. e. the direction and time of incident pulses). So it is possible to express all permutations of interaction orders and directions in the selected base by the so-called double-sided Feynman diagrams. It will be shown in Sec. 2.2.

1.3.4 Overlapping electric fields in perturbative expansion

Let us consider the product of the total incoming field (from Eq. (1.46))

$$E(\mathbf{r}, t-t_3-t_2-t_1)E(\mathbf{r}, t-t_3-t_2)E(\mathbf{r}, t-t_3). \tag{1.50}$$

For convenience we can separate a spatial phase $\Phi_j = \mathbf{k}_j\mathbf{r}$ from the time-dependent factors and identify the interaction sequence:[68]

$$E_j(\mathbf{r}, t-t_3-t_2-t_1) \equiv E_j^{[1]}\mathrm{e}^{\mathrm{i}\Phi_j} + \overline{E}_j^{[1]}\mathrm{e}^{-\mathrm{i}\Phi_j}, \tag{1.51a}$$

$$E_j(\mathbf{r}, t-t_3-t_2) \equiv E_j^{[2]}\mathrm{e}^{\mathrm{i}\Phi_j} + \overline{E}_j^{[2]}\mathrm{e}^{-\mathrm{i}\Phi_j}, \tag{1.51b}$$

$$E_j(\mathbf{r}, t-t_3) \equiv E_j^{[3]}\mathrm{e}^{\mathrm{i}\Phi_j} + \overline{E}_j^{[3]}\mathrm{e}^{-\mathrm{i}\Phi_j}, \tag{1.51c}$$

where $E_j^{[1]}$ denotes a forward-propagating pulse, which interacts first with the system; $E_j^{[2]}$ stands for the second-interacting pulse and $E_j^{[3]}$ – for the third. $\overline{E}_j^{[m]} = E_j^{[m]*}$ indicates the backward propagation (conjugate part); here both $j,\ m = 1, 2, 3$. The expressions for $E_j^{[m]}$ are as follows:

$$E_j^{[1]} \equiv \mathcal{E}_j(t-t_3-t_2-t_1-\tau_j)\mathrm{e}^{-\mathrm{i}\omega_j(t-t_3-t_2-t_1-\tau_j)}\mathrm{e}^{\mathrm{i}\phi_j}, \tag{1.52a}$$

$$E_j^{[2]} \equiv \mathcal{E}_j(t-t_3-t_2-\tau_j)\mathrm{e}^{-\mathrm{i}\omega_j(t-t_3-t_2-\tau_j)}\mathrm{e}^{\mathrm{i}\phi_j}, \tag{1.52b}$$

$$E_j^{[3]} \equiv \mathcal{E}_j(t-t_3-\tau_j)\mathrm{e}^{-\mathrm{i}\omega_j(t-t_3-\tau_j)}\mathrm{e}^{\mathrm{i}\phi_j}. \tag{1.52c}$$

Here τ_j indicates the absolute times of the system–field interactions, i. e. $\tau_1 \equiv \tau+T+t$, $\tau_2 \equiv T+t$ and $\tau_3 \equiv t$ (see Fig. 1.1). Since we are considering a response in the PE direction $-\mathbf{k}_1+\mathbf{k}_2+\mathbf{k}_3$, we can neglect terms which have different from $-\Phi_1+\Phi_2+\Phi_3$ spatial phase factors after substituting eqs. (1.51a)–(1.51c) into Eq (1.46). Assuming that all electric field pulses being the same frequency

($\omega_0 \equiv \omega_1 = \omega_2 = \omega_3$) and phases are not tuned ($\phi_1 = \phi_2 = \phi_3 = 0$), the product of the total incoming field (Eq. (1.50)) is

$$\begin{aligned}
&\Big\{ \left(\overline{E}_1^{[1]} E_2^{[2]} E_3^{[3]} + \overline{E}_1^{[1]} E_3^{[2]} E_2^{[3]} \right) \mathrm{e}^{\mathrm{i}\omega_0(t_3 - t_1)} \\
&\times \left(E_2^{[1]} \overline{E}_1^{[2]} E_3^{[3]} + E_3^{[1]} \overline{E}_1^{[2]} E_2^{[3]} \right) \mathrm{e}^{\mathrm{i}\omega_0(t_3 + t_1)} \\
&\times \left(E_2^{[1]} E_3^{[2]} \overline{E}_1^{[3]} + E_3^{[1]} E_2^{[2]} \overline{E}_1^{[3]} \right) \mathrm{e}^{\mathrm{i}\omega_0(t_3 + 2t_2 + t_1)} \Big\} \mathrm{e}^{\mathrm{i}\omega_0(t - \tau)}.
\end{aligned} \tag{1.53}$$

Terms in this product lie in three groups according to their phase factors. They are $\mathrm{e}^{\mathrm{i}\omega_0(t_3 - t_1)}$, $\mathrm{e}^{\mathrm{i}\omega_0(t_3 + t_1)}$ and $\mathrm{e}^{\mathrm{i}\omega_0(t_3 + 2t_2 + t_1)}$. As it will be shown later in Sec. 2.2.4, the system response function can be decomposed into components having opposite phase factors. In a multiplication of the system response function and the electric field product, some of these phase factors will cancel making that term slowly-varying, while the others will be modulated by the sum frequencies. Integration over time (Eq. (1.46)) makes the latter ones negligible compared to the integrals of the slowly-varying terms. This elimination is known as the rotating-wave approximation (RWA).

1.3.5 Two-dimensional photon echo signal at impulsive limit

The two-dimensional photon echo spectrum is obtained by performing the 2D Fourier transform of polarization $P^{(3)}(\tau, T, t)$, detected in the $\mathbf{k}_\mathrm{I} = -\mathbf{k}_1 + \mathbf{k}_2 + \mathbf{k}_3$ direction, over the time variables τ and t. As it was mentioned in the introduction, separation of the rephasing ($\mathbf{k}_\mathrm{I}$) and nonrephasing ($\mathbf{k}_\mathrm{II}$) signals is possible according to the range of the waiting time τ. For the rephasing signal ($\tau > 0$),

$$W_{\mathbf{k}_\mathrm{I}}(\omega_\tau, T, \omega_t) = \int_0^\infty \mathrm{d}\tau \mathrm{e}^{\mathrm{i}\omega_\tau \tau} \int_{-\infty}^\infty \mathrm{d}t \mathrm{e}^{\mathrm{i}\omega_t t} P^{(3)}_{\mathbf{k}_\mathrm{I}}(\tau, T, t). \tag{1.54}$$

In the scheme of the nonrephasing signal generation, the first two pulses are interchanged, but the detection still takes place in the $\mathbf{k}_\mathrm{I}$ direction:

$$W_{\mathbf{k}_\mathrm{II}}(\omega_\tau, T, \omega_t) = \int_0^\infty \mathrm{d}\tau \mathrm{e}^{\mathrm{i}\omega_\tau \tau} \int_{-\infty}^\infty \mathrm{d}t \mathrm{e}^{\mathrm{i}\omega_t t} P^{(3)}_{\mathbf{k}_\mathrm{II}}(\tau, T, t). \tag{1.55}$$

The integration over t is carried out only along the positive axis since the third-order response is not created before the third laser pulse.

For ultrashort excitation pulses, the electric field can be approximated as the δ functions, which allows us to get rid of the integration in the third-order polar-

ization expression (Eq. (1.46)). Then the third-order polarization is equal to the system response function itself and variables of the time delays in the experiment (τ, T and t) are equivalent to those of the system response function (t_1, t_2 and t_3). Then the rephasing and nonrephasing spectra can calculated as

$$W_{\mathbf{k}_\mathrm{I}}(\omega_1, t_2, \omega_3) = \int_0^\infty \mathrm{d}t_1 \mathrm{e}^{\mathrm{i}\omega_1 t_1} \int_{-\infty}^\infty \mathrm{d}t_3 \mathrm{e}^{\mathrm{i}\omega_3 t_3} S^{(3)}_{\mathbf{k}_\mathrm{I}}(t_1, t_2, t_3) \tag{1.56}$$

and

$$W_{\mathbf{k}_\mathrm{II}}(\omega_1, t_2, \omega_3) = \int_0^\infty \mathrm{d}t_1 \mathrm{e}^{\mathrm{i}\omega_1 t_1} \int_{-\infty}^\infty \mathrm{d}t_3 \mathrm{e}^{\mathrm{i}\omega_3 t_3} S^{(3)}_{\mathbf{k}_\mathrm{II}}(t_1, t_2, t_3) \tag{1.57}$$

respectively. This approximation is denoted as the *impulsive limit* and is very useful for simulations of the 2D spectra if the pulse overlap effects[72] are negligible. Implications of the finite laser pulses to the 2D spectra of molecular systems were broadly discussed by us elsewhere.[68] In the following considerations we will always assume the impulsive limit conditions for simulations and use the new time variables $t_1 \equiv \tau$, $t_2 \equiv T$ and $t_3 \equiv t$, and frequency variables $\omega_1 \equiv \omega_\tau$ and $\omega_3 \equiv \omega_t$.

Chapter 2

Spectroscopic signals of basic electronic systems

In this chapter, we will apply the third-order system response function formalism for a few model systems. We will account for the system–bath coupling in different ways, but will not pass over the Born–Oppenheimer approximation which prevents the electronic–vibrational mixing and all the consequent non-adiabatic phenomena (let us leave that for Chapter 3).

For a general electronic two-level system (Section 2.1), we will describe the bath only phenomenologically—i. e. assume that coupling to the nuclear degrees of freedom induces simple dephasing of the system response, represented by the Kubo lineshape model. That will allow us to obtain elegant analytical expressions for spectroscopic signals of the linear absorption and the 2D spectroscopy in some cases.

In Section 2.2, the general multi-level system in contact with a harmonic bath is considered. We will assume the bilinear coupling of system's electronic degrees of freedom to the nuclear coordinates of the bath, defined as the infinite set of harmonic oscillators. Spectral density will be introduced and its properties will be described. In Section 2.2.4, we will apply the developed formalism for the 2D ES of general molecular (Frenkel) excitonic systems.

The simplest excitonically coupled system—an electronic dimer—will be thoroughly analyzed in Section 2.3. Apart from its two-dimensional spectrum (Section 2.3.1), the coherent beatings (Section 2.3.2) and the dephasing under the influence of the static energy disorder (Section 2.3.3) will be considered.

2.1 Two-level system

A molecule in solution can be represented as a simple quantum system of two energy states. Let us define its ground state as $|\mathrm{g}\rangle$ and electronically excited state

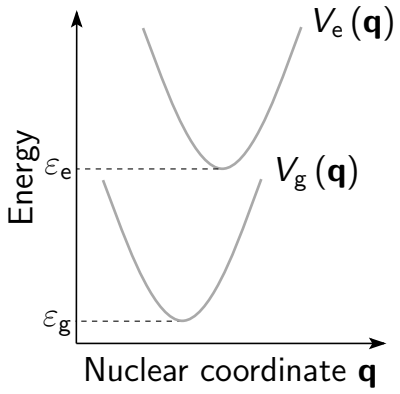

Fig. 2.1. Potentials of the two-level system under consideration.

as $|e\rangle$. We will express the nuclear DoF through the vector $\mathbf{q}$ of some generalized bath coordinates. These coordinates could represent the bath, lattice structure kinetics, etc. In the adiabatic regime the material Hamiltonian is

$$\widehat{H}_{\mathrm{mat}} = H_g(\mathbf{q})|g\rangle\langle g| + H_e(\mathbf{q})|e\rangle\langle e|. \tag{2.1}$$

The electronic ground and excited states are not coupled, since the rates of phenomena related to such coupling (for example, excited state relaxation to $|g\rangle$) are usually by a few orders longer compared to the electronic phenomena in the excited state, we are interested in.

The full energy of the electronic ground and excited states is the sum of the excitation energies ε_g and ε_e at the potential minima, kinetic energy of nuclear vibrations $T(\mathbf{q})$ and the vibrational potential energy (adiabatic potential) $V_g(\mathbf{q})$ and $V_e(\mathbf{q})$ (Fig. 2.1).

The material Hamiltonian of the two-level system,

$$\widehat{H}_{\mathrm{mat}} = [\varepsilon_g + T(\mathbf{q}) + V_g(\mathbf{q})]\,|g\rangle\langle g| + [\varepsilon_e + T(\mathbf{q}) + V_e(\mathbf{q})]\,|e\rangle\langle e|, \tag{2.2}$$

can be split into parts representing the system, the bath and the system–bath interaction as it was defined in Eq. (1.23):

$$\widehat{H}_{\mathrm{mat}} = \widehat{H}_S + \widehat{H}_B + \widehat{H}_{SB}. \tag{2.3}$$

These parts of the Hamiltonian can be written as

$$\widehat{H}_B = [T(\mathbf{q}) + V_g(\mathbf{q})]\,(|g\rangle\langle g| + |e\rangle\langle e|)\,, \tag{2.4}$$

$$\widehat{H}_S = \varepsilon_g|g\rangle\langle g| + [\varepsilon_e + \langle V_e(\mathbf{q}) - V_g(\mathbf{q})\rangle_{\mathbf{q}}]\,|e\rangle\langle e|, \tag{2.5}$$

$$\widehat{H}_{SB} = [V_e(\mathbf{q}) - V_g(\mathbf{q}) - \langle V_e(\mathbf{q}) - V_g(\mathbf{q})\rangle_{\mathbf{q}}]\,|e\rangle\langle e|. \tag{2.6}$$

The average energy gap, defined as $\langle V_e(\mathbf{q}) - V_g(\mathbf{q})\rangle_{\mathbf{q}}$, was added to the system's part and subtracted from $\widehat{H}_{SB}$ (thus making a zero contribution in the material Hamiltonian). It ensures, that the interaction part is zero at the thermodynamical equilibrium. The system–bath coupling term is expressed via the energy gap fluctuation term

$$\Delta V_{eg}(\mathbf{q}) = V_e(\mathbf{q}) - V_g(\mathbf{q}) - \langle V_e(\mathbf{q}) - V_g(\mathbf{q})\rangle_{\mathbf{q}}. \tag{2.7}$$

We will treat the system–bath coupling as the perturbation later on. The molecular Hamiltonian in the matrix notation for the two-level system is very simple:

$$\widehat{H}_{mat} = H_B(\mathbf{q}) \begin{pmatrix} 1 & 0 \\ 0 & 1 \end{pmatrix} + \begin{pmatrix} \varepsilon_g & 0 \\ 0 & \overline{\varepsilon}_e \end{pmatrix} + \Delta V_{eg}(\mathbf{q}) \begin{pmatrix} 0 & 0 \\ 0 & 1 \end{pmatrix}. \tag{2.8}$$

Here $\overline{\varepsilon}_e \equiv \varepsilon_e + \langle V_e(\mathbf{q}) - V_g(\mathbf{q})\rangle_{\mathbf{q}}$.

The dipole moment operator of the two-level system is written assuming the Franck–Condon (FC) approximation. That is, the electronic transition occurs instantaneously, without any changes in nuclear DoF, and the polarization operator in the dipole approximation is equivalent to the dipole operator, which does not depend on the nuclear coordinates:

$$\widehat{\mu} = d_{eg}\left(|e\rangle\langle g| + |g\rangle\langle e|\right). \tag{2.9}$$

Here d_{eg} is the norm of the molecular dipole vector*.

The last ingredient for the Maxwell–Liouville equations (1.1a)–(1.1c) is the system density operator. Since the energy of the electronic transition usually is in the UV or visible region and the energy gap is greater than the thermal energy, we can assume that initially the system is in the equilibrium state, defined by the equilibrium ground state density operator,

$$\widehat{\rho}_{eq} = |g\rangle\langle g| \otimes \widehat{\rho}_B, \tag{2.10}$$

which, in turn, is defined as the tensor product of the ground state density operator $|g\rangle\langle g|$ and the density operator of the whole bath $\widehat{\rho}_B$.

*In general, the dipole moment operator should be a vector, as well as d_{eg}. However, in Section 1.2.1 we chose to neglect the polarization of the incoming electric field. Therefore, the scalar product in the system–field interaction term in Hamiltonian (1.23), turns into a simple product of an operator and the electric field function.

2.1.1 Linear response

The system linear response function is given by eqs. (1.42) and (1.43). Substituting our definitions of the Hamiltonian (eqs. (2.4)–(2.6)), the dipole moment operator (Eq. (2.9)) and system density operator (Eq. (2.10)) into Eq. (1.43) gives

$$\begin{aligned} J(t) &= \mathrm{Tr}\left[\widehat{\mu}(t)\widehat{\mu}(0)\widehat{\rho}_{\mathrm{eq}}\right] = d_{\mathrm{eg}}^2 \mathrm{Tr}\left[\mathrm{e}^{\frac{\mathrm{i}}{\hbar}H_{\mathrm{g}}(\mathbf{q})t}\mathrm{e}^{-\frac{\mathrm{i}}{\hbar}H_{\mathrm{e}}(\mathbf{q})t}\widehat{\rho}_{\mathrm{eq}}\right] \\ &= d_{\mathrm{eg}}^2 \mathrm{e}^{-\mathrm{i}\omega_{\mathrm{eg}}t}\mathrm{Tr}\left[\mathrm{e}^{-\frac{\mathrm{i}}{\hbar}\Delta V_{\mathrm{eg}}(\mathbf{q})t}\widehat{\rho}_{\mathrm{eq}}\right]. \end{aligned} \tag{2.11}$$

Here, we extracted the energy gap $\hbar\omega_{\mathrm{eg}} = \overline{\varepsilon}_{\mathrm{e}} - \varepsilon_{\mathrm{g}}$, and in the exponential of the evolution operators only the vibrational part was left.

Within the trace operation in Eq. (2.11), in the exponential we have a perturbative part (system–bath coupling) of the excited state Hamiltonian, therefore, it is the excited state evolution operator in the interaction picture. It is known from the time-dependent perturbation theory, that it can be written as a positive time ordered exponential of the perturbation term,[69]

$$U_{\mathrm{ge}}(t) = \mathrm{e}^{\frac{\mathrm{i}}{\hbar}H_{\mathrm{g}}t}\mathrm{e}^{-\frac{\mathrm{i}}{\hbar}H_{\mathrm{e}}t} = \mathrm{exp}_{+}\left\{-\frac{\mathrm{i}}{\hbar}\int_0^t \mathrm{d}\tau \Delta\widehat{V}_{\mathrm{eg}}(\tau)\right\}. \tag{2.12}$$

We have dropped the notation of the nuclear coordinate $\mathbf{q}$ here. Similarly,

$$U_{\mathrm{eg}}(t) = \mathrm{e}^{\frac{\mathrm{i}}{\hbar}H_{\mathrm{e}}t}\mathrm{e}^{-\frac{\mathrm{i}}{\hbar}H_{\mathrm{g}}t} = \mathrm{exp}_{-}\left\{\frac{\mathrm{i}}{\hbar}\int_0^t \mathrm{d}\tau \Delta\widehat{V}_{\mathrm{eg}}(\tau)\right\}. \tag{2.13}$$

By inserting this into $J(t)$ expression (Eq. (2.11)) and expanding it to the second order we obtain

$$\begin{aligned} J(t) = d_{\mathrm{eg}}^2 \mathrm{e}^{-\mathrm{i}\omega_{\mathrm{eg}}t}\Bigg\{1 &- \frac{\mathrm{i}}{\hbar}\int_0^t \mathrm{d}\tau \mathrm{Tr}\left[\Delta\widehat{V}_{\mathrm{eg}}(\tau)\widehat{\rho}_{\mathrm{eq}}\right] \\ &+ \left(\frac{\mathrm{i}}{\hbar}\right)^2 \int_0^t \mathrm{d}\tau \int_0^\tau \mathrm{d}\tau' \mathrm{Tr}\left[\Delta\widehat{V}_{\mathrm{eg}}(\tau)\Delta\widehat{V}_{\mathrm{eg}}(\tau')\widehat{\rho}_{\mathrm{eq}}\right]\Bigg\}. \end{aligned} \tag{2.14}$$

The second term in Eq. (2.14) is zero at the thermodynamical equilibrium.[69] After performing the second-order cumulant expansion[143] of this expression, we obtain

$$J(t) = d_{\mathrm{eg}}^2 \mathrm{e}^{-\mathrm{i}\omega_{\mathrm{eg}}t - g(t)}, \tag{2.15}$$

where

$$g(t) \equiv \left(\frac{1}{\hbar}\right)^2 \int_0^t \mathrm{d}\tau \int_0^\tau \mathrm{d}\tau' \mathrm{Tr}\left[\Delta\widehat{V}_{\mathrm{eg}}(\tau)\Delta\widehat{V}_{\mathrm{eg}}(\tau')\widehat{\rho}_{\mathrm{eq}}\right] \tag{2.16}$$

is the so-called lineshape function, defined as the double integral

$$g(t) = \int_0^t \mathrm{d}\tau \int_0^\tau \mathrm{d}\tau' C(\tau) \tag{2.17}$$

of the two-point energy gap correlation function

$$C(\tau) = \frac{1}{\hbar^2}\mathrm{Tr}\left[\Delta\widehat{V}_{\mathrm{eg}}(\tau)\Delta\widehat{V}_{\mathrm{eg}}(0)\widehat{\rho}_{\mathrm{eq}}\right]. \tag{2.18}$$

Having the linear response function derived, we are now able to obtain the full expression of our first observable—the absorption coefficient of the two-level system.

The absorption coefficient $\kappa_{\mathrm{a}}(\omega)$ determines the decrease of the intensity of monochromatic radiation of frequency ω when propagating through the sample according to the Beer–Lambert law,

$$I(\omega) = I_0(\omega)\mathrm{e}^{-\kappa_{\mathrm{a}}(\omega)L}. \tag{2.19}$$

Here $I_0(\omega)$ is the intensity of the light source and $I(\omega)$ is the intensity of light after the sample and L is the distance of light propagation in the sample. $\kappa_{\mathrm{a}}(\omega)$ is related to the imaginary part of the linear susceptibility.[6,69] Therefore, according to eqs. (1.3) and (1.40), the linear absorption coefficient is proportional to the imaginary part of the Fourier transform of the linear response function:

$$\begin{aligned}\kappa_{\mathrm{a}}(\omega) &= \frac{\omega}{n(\omega)c}\mathrm{Im}\chi^{(1)}(\omega) = \frac{\omega}{n(\omega)c}\mathrm{Im}\frac{P^{(1)}(\omega)}{E(\omega)} \\ &= \frac{\omega}{n(\omega)c}\mathrm{Im}\int_0^\infty \mathrm{e}^{\mathrm{i}\omega t}S^{(1)}(t)\mathrm{d}t.\end{aligned} \tag{2.20}$$

Refractive index $n(\omega)$ can be assumed to be constant in the narrow-bandwidth spectra.

We can derive analytical expressions for the absorption coefficient in a few asymptotic cases of the so-called *fast modulation (homogeneous) limit* and *slow modulation (inhomogeneous) limit*. Both of these limits can be demonstrated by the Kubo lineshape model,[55,144] which assumes exponential form of the energy

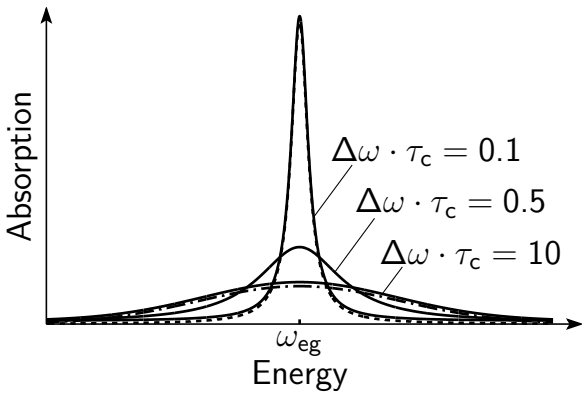

Fig. 2.2. Absorption spectrum of the two-level system, calculated using Kubo lineshape model with parameters $\Delta\omega \cdot \tau_c = 0.1$, 0.5 and 10, keeping $\Delta\omega$ constant. Dashed and dashed–dotted lines show absorption spectra calculated using analytical formulas at the homogeneous and inhomogeneous limits (equations (2.24) and (2.26), respectively).

gap correlation function,

$$C_{\text{Kubo}}(t) = \Delta\omega^2 \mathrm{e}^{-\frac{t}{\tau_c}}, \tag{2.21}$$

where $\Delta\omega$ is the amplitude of energy fluctuations and τ_c is the correlation time. The Kubo lineshape function is then

$$g_{\text{Kubo}}(t) = \Delta\omega^2 \tau_c^2 \left(\mathrm{e}^{-\frac{t}{\tau_c}} + \frac{t}{\tau_c} - 1 \right). \tag{2.22}$$

Homogeneous limit. Homogeneous limit accounts for the case when the frequency fluctuations are uncorrelated or very rapid with respect to the correlation time, i. e., $\tau_c \ll \Delta\omega^{-1}$. Then the energy gap correlation function narrows down to the δ function and the corresponding lineshape function simplifies to

$$g_{\text{fast}}(t) = \Delta\omega^2 \tau_c t \equiv \gamma t, \tag{2.23}$$

where γ is denoted as the pure dephasing rate. The absorption coefficient is then given by

$$\kappa_{\text{a-fast}}(\omega) = \frac{\omega d_{\text{eg}}^2}{n(\omega) c \hbar} \left(\frac{\gamma}{\gamma^2 + (\omega - \omega_{\text{eg}})^2} - \frac{\gamma}{\gamma^2 + (\omega + \omega_{\text{eg}})^2} \right). \tag{2.24}$$

Since $\gamma \ll \omega_{\text{eg}}$, the prefactor in this equation can be treated as a constant through the width of the peak. Thus, the resulting lineshape is the Lorentzian function (shown in Fig. 2.2 by the dashed line) centered at ω_{eg} with 2γ for the full width at half maximum (FWHM).

Inhomogeneous limit. In the inhomogeneous limit the opposite relationship between the system fluctuation amplitude and the correlation time is assumed, $\tau_c \gg \Delta\omega^{-1}$. Expanding the exponential in Eq. (2.22) to the second order of

small parameter t/τ_c gives the lineshape function

$$g_{\text{slow}}(t) = \frac{1}{2}\Delta\omega^2 t^2. \tag{2.25}$$

The corresponding energy gap correlation function is constant, $C_{\text{slow}}(t) = \Delta\omega^2$, and the absorption coefficient is

$$\kappa_{\text{a-slow}}(\omega) = \frac{\sqrt{\pi}\omega d_{\text{eg}}^2}{\sqrt{2}\Delta\omega n(\omega) c\hbar}\left(\mathrm{e}^{-\frac{(\omega-\omega_{\text{eg}})^2}{2\Delta\omega^2}} - \mathrm{e}^{-\frac{(\omega-\omega_{\text{eg}})^2}{2\Delta\omega^2}}\right). \tag{2.26}$$

The spectral lineshape of the absorption spectrum (show in Fig. 2.2 as dashed-dotted line) is Gaussian with the standard deviation $\Delta\omega$.

The absorption spectrum in the intermediate case ($\Delta\omega\tau_c = 0.5$, see Fig. 2.2) corresponds to neither ideal Gaussian nor the Lorentzian lineshapes.

2.1.2 Third-order response and 2D spectrum

To obtain the expression for the 2D spectrum we have to perform the same steps as for the absorption spectrum, just considering the third-order response function in Eq. (1.48). The expressions for auxiliary functions $R_\alpha(t_3, t_2, t_1)$ ($\alpha = 1 \ldots 4$) can be generalized by introducing the four-point correlation function

$$F(\tau_1, \tau_2, \tau_3, \tau_4) = \mathrm{Tr}\left[\widehat{\mu}(\tau_1)\widehat{\mu}(\tau_2)\widehat{\mu}(\tau_3)\widehat{\mu}(\tau_4)\widehat{\rho}_{\text{eq}}\right]. \tag{2.27}$$

By inserting the definitions of the dipole moment and the system density operator of the two-level system (equations (2.9) and (2.10), respectively), the four-point correlation function can be rewritten as

$$\begin{aligned} F(\tau_1, \tau_2, \tau_3, \tau_4) = {} & d_{\text{eg}}^4 \mathrm{e}^{-\mathrm{i}\omega_{\text{eg}}(\tau_1-\tau_2+\tau_3-\tau_4)} \\ & \times \mathrm{Tr}\left[U_{\text{ge}}(\tau_1)U_{\text{eg}}(\tau_2)U_{\text{ge}}(\tau_3)U_{\text{eg}}(\tau_4)\widehat{\rho}_{\text{eq}}\right]. \end{aligned} \tag{2.28}$$

Insertion of the evolution operators from eqs. (2.12) and (2.13) and the cumulant expansion gives

$$\begin{aligned} F(\tau_1, \tau_2, \tau_3, \tau_4) = {} & d_{\text{eg}}^4 \mathrm{e}^{-\mathrm{i}\omega_{\text{eg}}(\tau_1-\tau_2+\tau_3-\tau_4)} \\ & \times \mathrm{e}^{-g(\tau_{12})+g(\tau_{13})-g(\tau_{14})-g(\tau_{23})+g(\tau_{24})-g(\tau_{34})}, \end{aligned} \tag{2.29}$$

which is now suitable to calculate the full response function. The lineshape function is real and the response function simplifies to

$$S^{(3)}(t_3, t_2, t_1) = -4\hbar^{-3} d_{\text{eg}}^4 \theta(t_1)\theta(t_2)\theta(t_3)\mathrm{e}^{-g(t_3)-g(t_1)} \tag{2.30}$$

$$\times \left[\sin\omega_{eg}(t_3+t_1)e^{f(t_3,t_2,t_1)} + \sin\omega_{eg}(t_3-t_1)e^{-f(t_3,t_2,t_1)}\right],$$

where

$$f(t_3,t_2,t_1) = -g(t_2) + g(t_2+t_3) + g(t_1+t_2) - g(t_1+t_2+t_3). \tag{2.31}$$

In contrast to the calculation of the absorption coefficient, where we treated the sample exciting radiation as a continuous monochromatic wave of tunable frequency, here we have the impulsive excitation signal.

The components of the system response function, that survive RWA and contribute to the $\mathbf{k}_I = -\mathbf{k}_1 + \mathbf{k}_2 + \mathbf{k}_3$ pulse propagation direction are determined by Eq. (1.53). Thus, the first and the second term in brackets in Eq. (2.30) will contribute to the rephasing and nonrephasing spectrum, respectively:

$$S^{(3)}_{\mathbf{k}_I}(t_1,t_2,t_3) = -\frac{4d_{eg}^4}{\hbar^3}\sin\omega_{eg}(t_3-t_1)e^{-g(t_3)-g(t_1)-f(t_3,t_2,t_1)}, \tag{2.32}$$

$$S^{(3)}_{\mathbf{k}_{II}}(t_1,t_2,t_3) = -\frac{4d_{eg}^4}{\hbar^3}\sin\omega_{eg}(t_3+t_1)e^{-g(t_3)-g(t_1)+f(t_3,t_2,t_1)}. \tag{2.33}$$

The two-dimensional spectrum at the impulsive limit is calculated by performing the Fourier transform of the third-order system response function (eqs. (1.56) and (1.57)). In the homogeneous limit, the lineshape function is linear with respect to the time argument (Eq. (2.23)), thus, $f(t_3,t_2,t_1) = 0$ and the Fourier transforms yield

$$W_{\mathbf{k}_I}(\omega_1,t_2,\omega_3) = \frac{2id_{eg}^4}{\hbar^3}\left[\frac{1}{\gamma - i(\omega_1-\omega_{eg})}\cdot\frac{1}{\gamma - i(\omega_3+\omega_{eg})} - \frac{1}{\gamma - i(\omega_1+\omega_{eg})}\cdot\frac{1}{\gamma - i(\omega_3-\omega_{eg})}\right] \tag{2.34}$$

and

$$W_{\mathbf{k}_{II}}(\omega_1,t_2,\omega_3) = \frac{2id_{eg}^4}{\hbar^3}\left[\frac{1}{\gamma - i(\omega_1+\omega_{eg})}\cdot\frac{1}{\gamma - i(\omega_3+\omega_{eg})} - \frac{1}{\gamma - i(\omega_1-\omega_{eg})}\cdot\frac{1}{\gamma - i(\omega_3-\omega_{eg})}\right]. \tag{2.35}$$

As discussed above, in the experiment the relative phase of the local oscillator pulse with respect to the sample exciting pulses defines the measured real and imaginary parts of the signal (Eq. (1.21)). It is customary to define the real

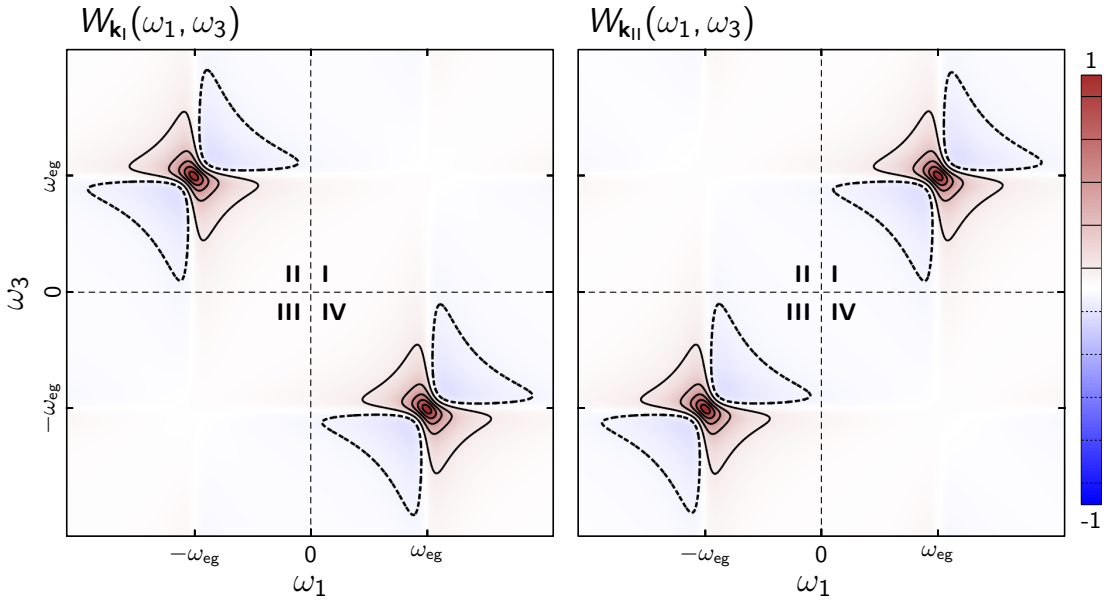

Fig. 2.3. Rephasing ($W_{\mathbf{k}_\mathrm{I}}$) and nonrephasing ($W_{\mathbf{k}_\mathrm{II}}$) spectra in the homogeneous limit (eqs. (2.34) and (2.35)) for both positive and negative excitation and emission frequencies. Quadrants of the (ω_1, ω_3) plane are enumerated as I through IV. Contours are plotted at $\pm 10\%$, $\pm 30\%$, $\pm 50\%$, ... of maximum value of spectrum; contours for negative values are shown by dashed lines.

part of the spectrum as the absorption-type signal, maintaining positive peaks in different parts of the (ω_1, ω_3) plane, and the imaginary part as the dispersive signal, representing changes of the refractive index for specified excitation and detection frequencies. Real parts of the rephasing and nonrephasing signals in the homogeneous limit are represented in Fig. 2.3 using the most common convention; this amounts to multiplying eqs. (2.34) and (2.35) by $(-\mathrm{i})$ and changing the sign of the signal at $\omega_3 < 0$. The rephasing and nonrephasing signals contribute to different quadrants of the (ω_1, ω_3) plane. The rephasing signal in the second quadrant is completely symmetric to the peak in the fourth quadrant with respect to $\omega_3 = \omega_1$ line; nonrephasing signal contributes to quadrants I and III with symmetry with respect to $\omega_3 = -\omega_1$ line. By convention, signals of the upper plane ($\omega_3 > 0$) are considered, and the rephasing spectrum is drawn with the excitation axis inverted ($\omega_1 \to -\omega_1$).

For the absorptive spectrum, summation of the rephasing (inverted with respect to the ω_1 axis) and the nonrephasing contributions:

$$W(|\omega_1|, t_2, \omega_3) = W_{\mathbf{k}_\mathrm{I}}(-\omega_1, t_2, \omega_3) + W_{\mathbf{k}_\mathrm{II}}(\omega_1, t_2, \omega_3). \tag{2.36}$$

Absorptive, rephasing and nonrephasing spectra calculated using Kubo model at the waiting time $t_2 = 0$ are shown in Fig. 2.4. Dependence of the spectrum on t_2 of a two-level system in the Kubo model is included in the auxiliary function

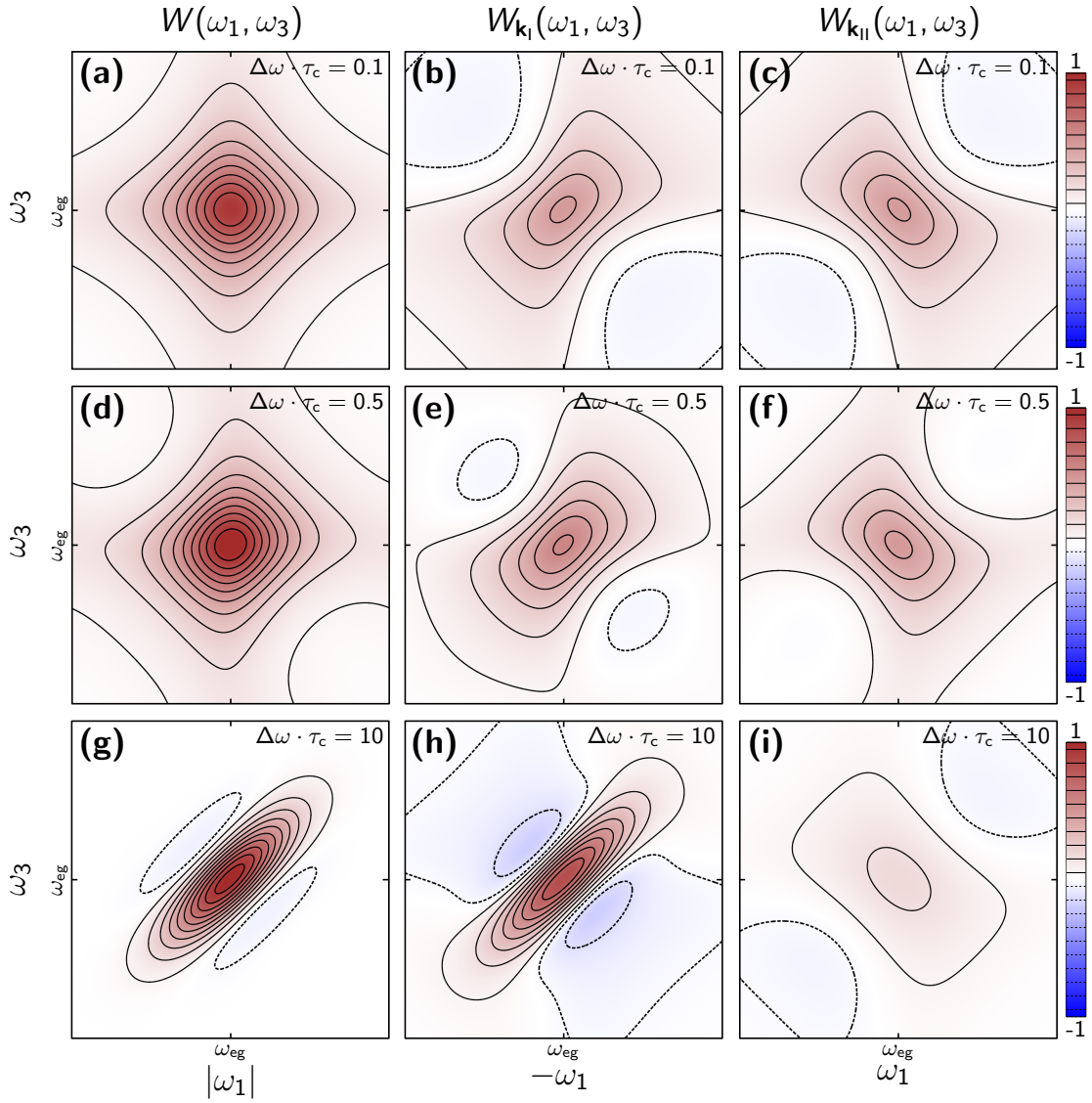

Fig. 2.4. Real parts of the absorptive **(a, d, g)**, the rephasing **(b, e, h)**, and the nonrephasing **(c, f, i)** two-dimensional spectra, calculated using Kubo model with $\Delta\omega\cdot\tau_c = 0.1$, 0.5 and 10. Spectra in each row are shown using the same color scale, normalized to the maximum of the corresponding absorptive spectrum.

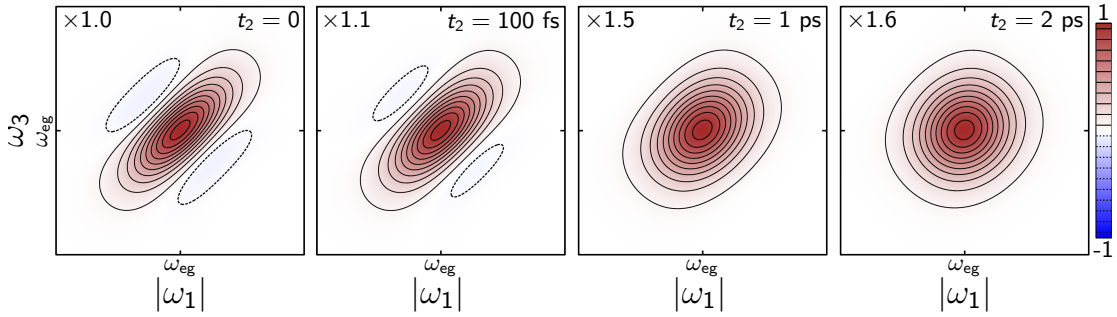

Fig. 2.5. Real parts of the absorptive two-dimensional spectra at waiting time $t_2 = 0$ fs, 100 fs, 1 ps and 2 ps, calculated using Kubo lineshape model with correlation time $\tau_c = 1$ ps and amplitude $\Delta\omega = 0.005\,\mathrm{ps}^{-1}$. Spectra are normalized to the maximum of spectrum at $t_2 = 0$; normalization factors are indicated at the upper left corner of each spectrum.

$f(t_1, t_2, t_3)$ only (Eq. (2.31)). It is easily shown, that in case of the homogeneous and the inhomogeneous limits, the function does not depend on the waiting time. Such picture shows how spectral diffusion is reflected in the absorptive 2D spectrum. In the homogeneous limit, no correlation of energy fluctuations exists and the peak in the spectrum (Fig. 2.4a) is "round" (its diagonal and anti-diagonal widths are equal). In the inhomogeneous limit, a complete correlation of the energy gap fluctuations is assumed; therefore, the diagonal (inhomogeneous) and anti-diagonal (homogeneous) widths of the diagonally elongated peak (Fig. 2.4g) is constant in the waiting time.

The intermediate case with correlation time $\tau_c = 1$ ps and amplitude $\Delta\omega = 0.005\,\mathrm{ps}^{-1}$ ($\Delta\omega \cdot \tau_c = 5$) is demonstrated in Fig. 2.5 at waiting times $t_2 = 0$, 100 fs, 1 ps and 2 ps. The absorptive spectrum being elongated along the diagonal becomes round at $t_2 \approx \tau_c$ indicating spectral diffusion and the loss of correlation of energy fluctuations.

A few important factors were not included into consideration of the two-level system. This does not allow us to establish a direct link between the calculated spectra using the Kubo lineshape model and the real experimental observables of a simple two-level molecule. These are the static energy disorder and the waiting time dynamics. Static energetic disorder is caused by molecules interacting with slightly different environment in the sample, thus, having different energies ω_{eg} and and results in inhomogeneous lineshape broadening. In calculations, this is taken into consideration by performing averaging of spectra with random energy gaps of the Gaussian distribution[34] or including an additional mode of slow bath fluctuations to the spectral density.[145] In spectra, the static energy disorder contributes to the diagonal peak elongation, but not the anti-diagonal. Therefore, inhomogeneously broadened peaks will not become round at long waiting times, as shown here. The waiting time dynamics amount to additional mechanisms apart from the spectral diffusion, responsible for the decay of the signal in the waiting time. Both of these components of the theoretical description of the 2D ES will be thoroughly discussed in the following chapters.

2.2 Multi-level system in contact with harmonic bath

Let us consider a general system, given by a set of the energy eigenstates $|m\rangle$, where $m = 1, \ldots, N$ and the ground state $|g\rangle$. The system Hamiltonian is:

$$\widehat{H}_S = \sum_m^N \varepsilon_m \widehat{B}_m^\dagger \widehat{B}_m. \tag{2.37}$$

Here $\widehat{B}_m^\dagger$ and $\widehat{B}_m$ are the electronic excitation at the m-th eigenstate creation and annihilation operators, respectively; ε_m is the energy of the m-th eigenstate. The ground state energy is zero. We choose to describe the bath as an infinite set $\{\alpha\}$ of harmonic oscillators with the unitary effective mass. The Hamiltonian of the bath is then:

$$\widehat{H}_{\mathrm{B}} = \sum_\alpha \frac{1}{2}\left(\widehat{p}_\alpha^2 + w_\alpha^2 \widehat{x}_\alpha^2\right). \tag{2.38}$$

Here $\widehat{p}_\alpha$ is the momentum and $\widehat{x}_\alpha$ is the coordinate operators and w_α is the frequency of the α-th bath oscillator. The Hamiltonian can be quantized using bosonic creation/annihilation operators of the bath oscillators

$$\widehat{a}_\alpha^\dagger \equiv \sqrt{\frac{w_\alpha}{2\hbar}}\widehat{x}_\alpha - \mathrm{i}\frac{1}{\sqrt{2\hbar w_\alpha}}\widehat{p}_\alpha \tag{2.39}$$

and

$$\widehat{a}_\alpha \equiv \sqrt{\frac{w_\alpha}{2\hbar}}\widehat{x}_\alpha + \mathrm{i}\frac{1}{\sqrt{2\hbar w_\alpha}}\widehat{p}_\alpha. \tag{2.40}$$

The system–bath interaction is given in the bilinear form

$$\widehat{H}_{\mathrm{SB}} = \sum_{m,n=0}^{N}\sum_\alpha \sqrt{2w_\alpha}\, d_{mn,\alpha}\widehat{x}_\alpha \widehat{B}_m^\dagger \widehat{B}_n. \tag{2.41}$$

It describes the coupling of electronic excitation to the bath coordinates via coupling constant $d_{mn,\alpha}$. The dipole moment operator is given in its general form

$$\widehat{\boldsymbol{\mu}} = \sum_m^N \boldsymbol{\mu}_m\left(\widehat{B}_m^\dagger + \widehat{B}_m\right). \tag{2.42}$$

Diagonal fluctuations. First we neglect the off-diagonal fluctuations by assuming that energy fluctuations of different sites are uncorrelated, i. e.,

$$d_{mm,\alpha} = \delta_{mn} d_{mn,\alpha}. \tag{2.43}$$

In that case the system dynamics is adiabatic, i. e., the system eigenstates are not affected by the fluctuations of the environment. Applying the four-point correlation function (Eq. (2.27)) to a general scheme of the system–dipole moment operator interactions (Fig. 2.6), one can obtain

$$F(\tau_1,\tau_2,\tau_3,\tau_4) = \sum_{cba}\left\langle \boldsymbol{\mu}_{\mathrm{g}c}\boldsymbol{\mu}_{cb}\boldsymbol{\mu}_{ba}\boldsymbol{\mu}_{\mathrm{a}g}\right\rangle \mathcal{F}_{cba}^{(\mathrm{C})}(\tau_1,\tau_2,\tau_3,\tau_4). \tag{2.44}$$

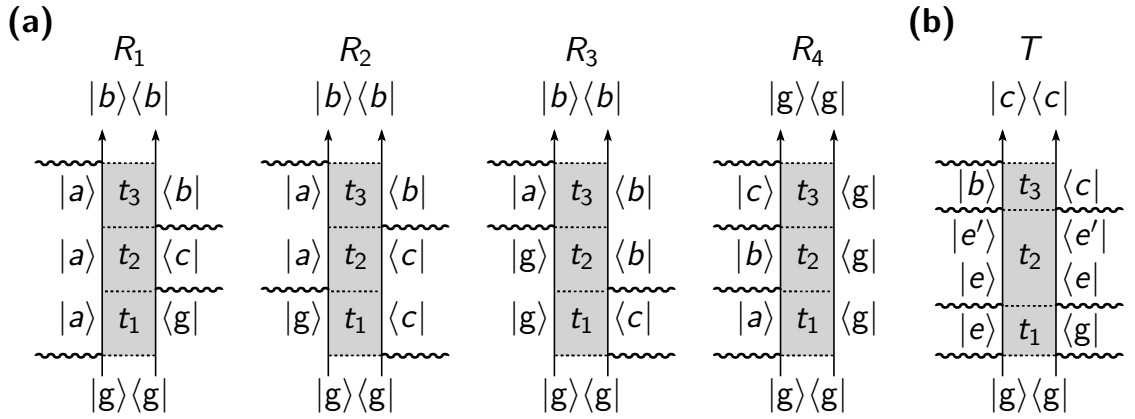

Fig. 2.6. Double-sided Feynman diagrams, corresponding to the components of the nonlinear response function in eqs. (1.49a)–(1.49d) for a general multilevel system **(a)** and a general Feynman diagram for a population transfer process **(b)**.

Here indices a, b, c and d enumerate the arbitrary system eigenstates; index "C" denotes the coherent limit with the population transfer not included. Angular brackets here indicate the orientationally averaged scalar product of the dipole vectors and the polarizations of the laser pulses. We will come back to the description of this product in Sec. (2.2.1).

The four-point correlation function is then

$$\mathcal{F}^{(\mathrm{C})}_{cba}(\tau_1,\tau_2,\tau_3,\tau_4) = \mathrm{e}^{-\frac{\mathrm{i}}{\hbar}(\varepsilon_c\tau_{43}+\varepsilon_b\tau_{32}+\varepsilon_a\tau_{21})} f^{(\mathrm{C})}_{cba}(\tau_1,\tau_2,\tau_3,\tau_4), \tag{2.45}$$

where

$$\begin{aligned} f^{(\mathrm{C})}_{cba}(\tau_1,\tau_2,\tau_3,\tau_4) = \mathrm{Tr}_{\mathrm{B}}\Big\{ & \mathrm{e}_+^{-\frac{\mathrm{i}}{\hbar}\int_0^{\tau_1}\mathrm{d}\tau \Delta V_{gc}(\tau)} \mathrm{e}_+^{-\frac{\mathrm{i}}{\hbar}\int_0^{\tau_2}\mathrm{d}\tau \Delta V_{cb}(\tau)} \\ & \times \mathrm{e}_+^{-\frac{\mathrm{i}}{\hbar}\int_0^{\tau_3}\mathrm{d}\tau \Delta V_{ba}(\tau)} \mathrm{e}_+^{-\frac{\mathrm{i}}{\hbar}\int_0^{\tau_4}\mathrm{d}\tau \Delta V_{ag}(\tau)} \Big\}. \end{aligned} \tag{2.46}$$

The second-order cumulant expansion of this expression results in[70]

$$\begin{aligned} f^{(\mathrm{C})}_{cba}(\tau_1,\tau_2,\tau_3,\tau_4) = \exp\Big[& -g_{cc}(\tau_{43}) - g_{bb}(\tau_{32}) - g_{aa}(\tau_{21}) - g_{cb}(\tau_{42}) \\ & + g_{cb}(\tau_{43}) + g_{cb}(\tau_{32}) - g_{ca}(\tau_{41}) + g_{ca}(\tau_{42}) + g_{ca}(\tau_{31}) \\ & - g_{ca}(\tau_{32}) - g_{ba}(\tau_{31}) + g_{ba}(\tau_{32}) + g_{ba}(\tau_{21}) \Big]. \end{aligned} \tag{2.47}$$

The lineshape function $g_{ab}(t)$ is given by the correlation function $C_{aa,bb}(t)$ integral:[69]

$$g_{ab}(t) = \int_0^t \mathrm{d}\tau \int_0^\tau \mathrm{d}\tau' C_{aa,bb}(\tau-\tau'), \tag{2.48}$$

where

$$C_{ab,cd}(\tau) = \frac{1}{\hbar^2}\mathrm{Tr}\left[\Delta\widehat{V}_{ab}(\tau)\Delta\widehat{V}_{cd}(0)\widehat{\rho}_{\mathrm{eq}}\right]. \tag{2.49}$$

Because of the trace operation being invariant under the cyclic permutations, chronologically with respect to their time arguments the ordered dipole moment operators can act upon the *bra* or *ket* of the density operator. These sequences for eqs. (1.49a)–(1.49d) are conveniently expressed schematically using the abstract double-sided Feynman diagrams[54, 59, 69, 146] (Fig. 2.6a). Vertical arrows denote the time direction; variables t_1, t_2 and t_3 are the time intervals between two successive interactions of the dipole operator and the system density operator; horizontal lines show the side of the dipole operator's action upon the density operator. A ket and a bra during the same time interval ($|m\rangle\langle n|$) denotes a state of coherence if $m \neq n$, or population if $m = n$, corresponding to an element of the system density matrix being affected.

Off-diagonal fluctuations. Let us consider now additional off-diagonal fluctuations. The system dynamics are now of two types: the coherence evolution and the population transport. During the coherence evolution, the diagonal fluctuations modulate the oscillation frequency and the off-diagonal fluctuations add the lifetime-induced dephasing. During the population evolution, the off-diagonal fluctuations induce the population transport and the effect of the diagonal fluctuations is included in the transport rate. Feynman diagrams with incoherent transport (indicated by superscript "I") are used[145] to describe the population transfer. The addition to the system response function (Eq. (1.48)) is obtained:

$$T(t_3, t_2, t_1) = -\left(\frac{\mathrm{i}}{\hbar}\right)^3 \theta(t_1)\theta(t_2)\theta(t_3) \sum_{cbe'e} \left\langle \boldsymbol{\mu}_{cb}\boldsymbol{\mu}_{\nu\nu'}\boldsymbol{\mu}_{\mathrm{eg}}^2 \right\rangle G_{e'e}(t_2)\mathcal{F}^{(\mathrm{I})}_{cbe'e}(t_3, t_2, t_1). \tag{2.50}$$

Here indices c and b denote states in the coherence $|b\rangle\langle c|$ during t_3 in population transfer diagrams; $\nu\nu'$ has to be changed to $e'b$ when the signal is generated on the left side of the diagram, and to ce', when it is generated on the right. $G_{e'e}(t_2)$ is the Green's function that is a probability of population state $|e\rangle\langle e|$ to be transferred to $|e'\rangle\langle e'|$ in time t_2 (or population survival probability when $e' = e$). The four-point correlation function, describing incoherent population dynamics during the waiting time, is

$$\mathcal{F}^{(\mathrm{I})}_{cbe'e}(t_3, t_2, t_1) = \mathrm{e}^{\mathrm{i}\omega_{cb}t_3 - \mathrm{i}\omega_{\mathrm{eg}}t_1 - (\gamma_c+\gamma_b)t_3 - \gamma_e t_1 + f^{(\mathrm{I})}_{cbe}(t_3,t_2,t_1)}, \tag{2.51}$$

where

$$\begin{aligned} f^{(\mathrm{I})}_{cbe}(t_3, t_2, t_1) = \exp\Big[&- g_{ee}(t_1) - g_{bb}(t_3) - g^*_{cc}(t_3) \\ &- g_{be}(t_1 + t_2 + t_3) + g_{be}(t_1 + t_2) + g_{be}(t_2 + t_3) \end{aligned} \tag{2.52}$$

$$+ g_{ce}(t_1 + t_2 + t_3) - g_{ce}(t_1 + t_2) - g_{ce}(t_2 + t_3)$$
$$+ g_{cb}(t_3) + g^*_{bc}(t_3) + g_{ce}(t_2) - g_{be}(t_2)\Big].$$

γ_ν is the dephasing constant, that is a sum of an inverse state lifetime and the pure dephasing[145]

$$\gamma_\nu = |K_{\nu\nu}|/2 + \widetilde{\gamma}_\nu. \tag{2.53}$$

2.2.1 Orientational averaging

So far we have neglected the polarizations of the incoming laser fields. Also, by assuming the scalar dipole moment operator (Eq. (2.9)), we were able to express the system–field interaction term in Eq. (1.23) as the product of the scalar dipole moment operator $\widehat{\mu}$ and the scalar electric field $E(t)$. However, for each double-sided Feynman diagram in Fig. (2.6), all interactions of the dipole moment operator and the density operator (eqs. (1.49a)-(1.49d)) carry the scalar products of the unitary vectors $\mathbf{e}_j$, representing the polarization of the j-th laser pulse $\mathbf{k}_j$[†], and the dipole moment vector $\boldsymbol{\mu}_j$, corresponding to the j-th transition.

Obviously, laser pulse polarizations are defined in the reference frame of the laboratory and are fixed, while the dipole moment vectors of each molecular complex in the sample can have an arbitrary random orientation with respect to them[‡]. It means, that we cannot neglect the orientations of the dipole moment vectors with respect to the laser pulse polarizations and have to perform the averaging over isotropic distribution of the former. In eqs. (2.44) and (2.50) such averaging was denoted as

$$\langle \boldsymbol{\mu}_1\boldsymbol{\mu}_2\boldsymbol{\mu}_3\boldsymbol{\mu}_4 \rangle \equiv \langle (\boldsymbol{\mu}_1 \cdot \mathbf{e}_1)(\boldsymbol{\mu}_2 \cdot \mathbf{e}_2)(\boldsymbol{\mu}_3 \cdot \mathbf{e}_3)(\boldsymbol{\mu}_4 \cdot \mathbf{e}_4) \rangle . \tag{2.54}$$

One obvious, but expensive, way to perform such averaging is to directly integrate this product of scalar products over all possible orientations of the molecular system, represented by the Euler angles. Alternatively, one can perform orientational averaging using an appropriate matrix transformation.[147]

In a traditional 2D ES, polarizations of each laser pulse are linear and identical and the detection takes place along the same direction ($\mathbf{e}_1 = \mathbf{e}_2 = \mathbf{e}_3 = \mathbf{e}_4$). Such a scheme is often denoted as the *XXXX* or "all-parallel" configuration of the laser

[†]Actually, $\mathbf{e}_1$, $\mathbf{e}_2$ and $\mathbf{e}_3$ are the linear polarization vectors of the first three laser pulses in the FWM experiment and $\mathbf{e}_4$ is the linear polarization of the detection.

[‡]Of course, it is not true if the molecules in the solution are aligned. For example, in the continuously flowing liquid sample;[123] however, such conditions are met exceptionally rarely.

pulses. In this case, the product in Eq. (2.54) reduces to a simple expression:[6,148]

$$\langle \boldsymbol{\mu}_1\boldsymbol{\mu}_2\boldsymbol{\mu}_3\boldsymbol{\mu}_4\rangle_{XXXX} = \frac{2}{15}\Big[(\boldsymbol{\mu}_1\cdot\boldsymbol{\mu}_2)(\boldsymbol{\mu}_3\cdot\boldsymbol{\mu}_4) + (\boldsymbol{\mu}_1\cdot\boldsymbol{\mu}_3)(\boldsymbol{\mu}_2\cdot\boldsymbol{\mu}_4) + (\boldsymbol{\mu}_1\cdot\boldsymbol{\mu}_4)(\boldsymbol{\mu}_2\cdot\boldsymbol{\mu}_3)\Big]. \tag{2.55}$$

Actually, the manipulation of the polarization of each individual pulse $\mathbf{e}_j$ in the 2D ES can be used to suppress or enhance some specific double-sided Feynman diagrams. For example, the so-called "cross-polarization" (CP) configuration, in which the relative polarization orientations of the laser pulses and the detector $\mathbf{e}_1$–$\mathbf{e}_4$ are $\pi/4$, $-\pi/4$, $\pi/2$ and 0, respectively, can be used to suppress these contributions, where the first two dipole moment vectors are parallel.[39,149] The expression for the corresponding product is:

$$\langle \boldsymbol{\mu}_1\boldsymbol{\mu}_2\boldsymbol{\mu}_3\boldsymbol{\mu}_4\rangle_{\mathrm{CP}} = \frac{1}{15}\left[(\boldsymbol{\mu}_1\cdot\boldsymbol{\mu}_3)(\boldsymbol{\mu}_2\cdot\boldsymbol{\mu}_4) - (\boldsymbol{\mu}_1\cdot\boldsymbol{\mu}_4)(\boldsymbol{\mu}_2\cdot\boldsymbol{\mu}_3)\right]. \tag{2.56}$$

Even more sophisticated polarization configurations can be used to promote or suppress the desired contributions in the spectrum.[150] In this thesis, only *XXXX* polarization configuration is considered.

2.2.2 Spectral density

The system–bath coupling represented by Eq. (2.41) introduces fluctuations into the energy of the electronic excited state due to low-frequency bath modes at the fixed temperature. The most convenient form to describe such fluctuations is the time correlation operator

$$C(t) = \mathrm{Tr}_{\mathrm{B}}\left\{\widehat{Q}_e(t)\widehat{Q}_e(0)\widehat{\rho}_{\mathrm{eq}}\right\}. \tag{2.57}$$

Here the normalized thermally equilibrated density operator of the bath is given by Eq. 1.29:

$$\widehat{\rho}_{\mathrm{eq}} = \mathcal{Z}^{-1}\exp\left(-\sum_\alpha \beta\hbar w_\alpha\left(\widehat{a}^\dagger_\alpha\widehat{a}_\alpha + \frac{1}{2}\right)\right) \tag{2.58}$$

and

$$\widehat{Q}_e(t) = \sum_\alpha \hbar w_\alpha\sqrt{s_\alpha}\left(\widehat{a}^\dagger_\alpha(t) + \widehat{a}_\alpha(t)\right) \tag{2.59}$$

is the fluctuating collective bath coordinate in the Heisenberg representation. Here, s_α is the so-called Huang–Rhys factor, which indicates the strength of the α-th vibrational mode. The exact form of the correlation function describes the high-frequency modes as well. Trace in Eq. (2.57) amounts to averaging over the infinite set $\{\alpha\}$ of harmonic oscillators. Inclusion of eqs. (2.58) and (2.59) into

the trace gives

$$C(t) = \sum_{\alpha} \hbar^2 w_\alpha^2 s_\alpha \left(\coth \frac{\beta\hbar w_\alpha}{2} \cos w_\alpha t - \mathrm{i} \sin w_\alpha t \right), \tag{2.60}$$

which is the well-known form of the two-point correlation function of generalized bath coordinates.[8] The Fourier transform of the equation is a real function

$$\mathcal{C}(\omega) = \int_{-\infty}^{\infty} \mathrm{d}t \mathrm{e}^{\mathrm{i}\omega t} C(t) \equiv \mathcal{C}'(\omega) + \mathcal{C}''(\omega), \tag{2.61}$$

where $\mathcal{C}'(\omega)$ and $\mathcal{C}''(\omega)$ are even and odd functions of ω. $\mathcal{C}''(\omega)$ is the temperature-independent function. We denote it as the spectral density:

$$\mathcal{C}''(\omega) = -2 \int_0^{\infty} \sin \omega t \mathrm{Im} C(t) \mathrm{d}t. \tag{2.62}$$

Note, that the different definition of the spectral density, namely $J(\omega) \equiv \omega^2 \mathcal{C}''(\omega)$, might also used.[8] $\mathcal{C}'(\omega)$ and $\mathcal{C}''(\omega)$ are related by the fluctuation–dissipation theorem[8]

$$\mathcal{C}'(\omega) = \coth\left(\beta\hbar\omega/2\right) \mathcal{C}''(\omega) \tag{2.63}$$

and the system reorganization energy is defined as

$$\lambda = \frac{1}{\pi} \int_0^{\infty} \frac{\mathcal{C}''(\omega)}{\omega} \mathrm{d}\omega. \tag{2.64}$$

The lineshape function $g(t)$ is an integral transformation of the correlation function $C(t)$ of system-bath fluctuations, or for its Fourier transform (Eq. (2.61)),

$$g(t) \equiv -\frac{1}{2\pi} \int_{-\infty}^{\infty} \mathrm{d}\omega \frac{\mathcal{C}(\omega)}{\omega^2} \left[\exp(-\mathrm{i}\omega t) + \mathrm{i}\omega t - 1 \right]. \tag{2.65}$$

Assuming that the system is coupled to a continuous spectrum of bath frequencies, the correlation function Eq. (2.60) can be calculated for a predefined distribution. We introduce the density of the Huang–Rhys parameter as a function of vibrational frequency, $\{s_\alpha\} \to s(\omega)\mathrm{d}\omega$, which may have a peak at some dominant normal-mode frequency ω_0. Then, from eqs. (2.60) and (2.62) the spectral density is obtained as

$$\mathcal{C}''(\omega) = \pi\hbar^2\omega^2 \left[s(\omega) - s(-\omega) \right]. \tag{2.66}$$

For instance, if we consider a vibrational damped mode it will be represented by a broad peak in the spectral density of the system–bath coupling. In case of the Gaussian-type coupling

$$s_{\mathrm{G}}(\omega) = \frac{1}{\sqrt{2\pi}\gamma} \mathrm{e}^{-\frac{(\omega-\omega_0)^2}{2\gamma^2}} \tag{2.67}$$

the spectral density function is

$$\mathcal{C}''_{\mathrm{G}}(\omega) = \lambda\mu \cdot \frac{\sqrt{\pi}}{\sqrt{2}\gamma} \left[\mathrm{e}^{-\frac{(\omega-\omega_0)^2}{2\gamma^2}} - \mathrm{e}^{-\frac{(\omega+\omega_0)^2}{2\gamma^2}} \right], \tag{2.68}$$

while the Lorentzian-type coupling

$$s_{\mathrm{L}}(\omega) = \frac{1}{\pi} \frac{1}{(\omega-\omega_0)^2 + \gamma^2} \tag{2.69}$$

leads to

$$\mathcal{C}''_{\mathrm{L}}(\omega) = \lambda\mu \cdot \frac{4\omega\omega_0\gamma}{\left(\omega^2 - \omega_0^2 - \gamma^2\right)^2 + 4\omega^2\gamma^2}. \tag{2.70}$$

μ is just a scaling constant inserted here for convenience: the expression of μ is later chosen in order for λ to be equal to the reorganization energy.

At this point, no approximations regarding the description of the bath were applied—equations (2.68) and (2.70) are consistent with the fluctuation–dissipation theorem. The inverse Fourier transform of them would give the time correlation functions, which in the case of Gaussian and Lorentzian couplings, decay as $\mathrm{e}^{-\gamma^2 t^2/2}$ and $\mathrm{e}^{-\gamma t}$, respectively. The spectral densities include the damping parameter γ and vibrational frequency ω_0. By taking various limits with respect to these parameters, different damping regimes can be achieved representing different conditions of the bath, and both spectral densities (eqs. (2.68) and (2.70)) can be used in numerical simulations.

We further analyze different regimes of *undamped*, *damped* and *overdamped* vibrational motion considering the Lorentzian-type coupling, since it is related to the exponentially-decaying time correlation function, which is a natural decay pattern in most physical situations. When a single bath mode is assumed, i. e., when the spectral density function is obtained as a Fourier transform of a single term of Eq. (2.60), the spectral density is given by

$$\mathcal{C}''_{\mathrm{u}}(\omega) = \pi s \omega_0^2 \left[\delta(\omega-\omega_0) - \delta(\omega+\omega_0)\right]. \tag{2.71}$$

The reorganization energy in this case is $s\omega_0$ and the lineshape function is

$$g_{\mathrm{u}}(t) = s \left[\coth\frac{\beta\hbar\omega_0}{2} \left(1 - \cos\omega_0 t\right) + \mathrm{i}\left(\sin\omega_0 t - \omega_0 t\right) \right]. \tag{2.72}$$

This vibrational mode leads to non-decaying, *undamped,* vibrational motion. Such spectral density, given by δ functions, is not realistic because the dissipation, which leads any vibrational motion due to the molecular interaction with its environment, is neglected. Damping induces the decay of the correlation function over time and the corresponding spectral density should have a finite-width smooth peak. Such *damped* regime is achieved by taking $\gamma < \omega_0$ in Eq. (2.70), leading to

$$\mathcal{C}''_{\mathrm{d}}(\omega) = \frac{2\sqrt{2}\lambda\omega\omega_0^2\gamma}{\left(\omega^2 - \omega_0^2\right)^2 + 2\gamma^2\omega^2}. \tag{2.73}$$

This spectral density function with reorganization energy λ has a peak at ω_0 and the peak width is defined by the damping strength γ, differently from Eq. (2.71), where the peak is the δ function (Fig. 2.7a).

The opposite, *overdamped*, regime is usually represented by the Brownian oscillator model. This regime can be postulated semi-classically, i. e., by using the exponentially decaying classical correlation function

$$\mathcal{C}_{\mathrm{cl}}(t) = 2\lambda k_{\mathrm{B}} T \exp(-\gamma|t|). \tag{2.74}$$

Its Fourier transform,

$$\mathcal{C}_{\mathrm{cl}}(\omega) = 4\gamma\lambda k_{\mathrm{B}} T(\omega^2 + \gamma^2)^{-1}, \tag{2.75}$$

now represents the even (classical) part $\mathcal{C}'(\omega)$ of the total quantum correlation function. Since the classical trajectory reflects the high temperature limit, we have $\mathcal{C}''(\omega) = \frac{1}{2}\beta\hbar\omega\mathcal{C}'(\omega)$ and obtain the Drude–Lorentz spectral density representing the classical Brownian particle[8]

$$\mathcal{C}''_{\mathrm{o-sc}}(\omega) = \frac{2\lambda\gamma\omega}{\omega^2 + \gamma^2} \tag{2.76}$$

with reorganization energy λ and the relaxation rate γ. The full quantum correlation function in the frequency domain can now be constructed by the direct application of the fluctuation–dissipation relation Eq. (2.63). Therefore, we denote the bath described by such spectral density as the *overdamped semi-classical bath*. At the high-temperature limit[69] the corresponding lineshape function is approximated as

$$g_{\mathrm{o-sc}}(t) = \frac{\lambda}{\gamma}\left(\frac{2}{\beta\gamma} - \mathrm{i}\right)(\mathrm{e}^{-\gamma t} + \gamma t - 1). \tag{2.77}$$

Evidently, the overdamped bath can also be obtained from Eq. (2.70). In the

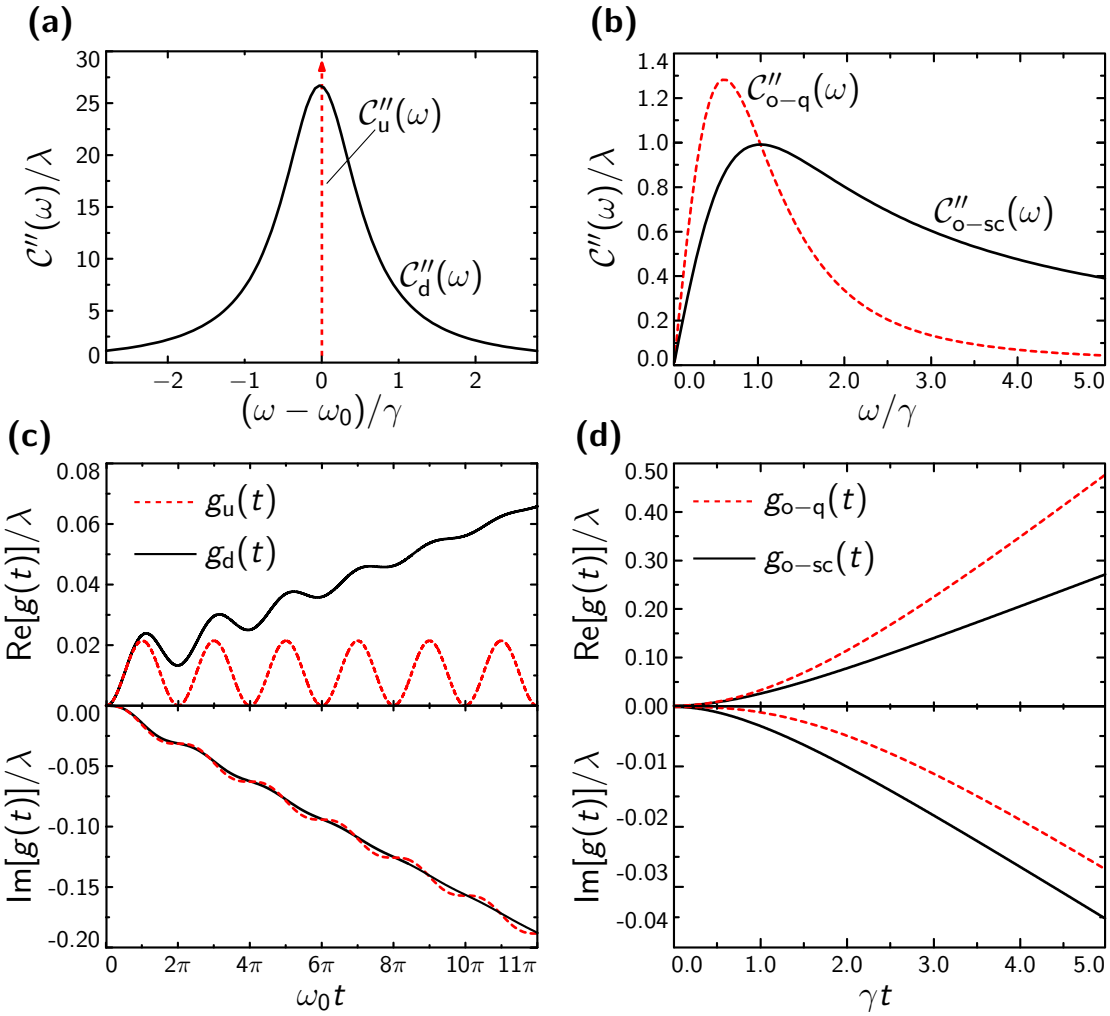

Fig. 2.7. **(a)** *Undamped* ($\mathcal{C}''_{\rm u}(\omega)$, red dashed line) and *damped* ($\mathcal{C}''_{\rm d}(\omega)$, black solid line) spectral density functions. **(b)** *Overdamped quantum* ($\mathcal{C}''_{\rm o-q}(\omega)$, red dashed line) and *overdamped semiclassical* ($\mathcal{C}''_{\rm o-sc}(\omega)$, black solid line) spectral density functions. The real and imaginary parts of the corresponding lineshape functions are shown in **(c)** and **(d)**, respectively. Notice the different scale for the imaginary parts.

limit of $\gamma \gg \omega_0$ it yields a rather different spectral density function

$$\mathcal{C}''_{\rm o-q}(\omega) = \frac{4\lambda\omega\gamma^3}{(\omega^2+\gamma^2)^2}. \tag{2.78}$$

We denote this regime as the *quantum overdamped*. The reorganization energies are equal to λ for both types of the overdamped spectral density. The semiclassical spectral density function is equal to λ at its maximum at $\omega = \gamma$, while the quantum function has its maximum value $\mathcal{C}''_{\rm o-q}(\omega_{\rm peak}) = \frac{3\sqrt{3}}{4}\lambda \approx 1.3\lambda$, where $\omega_{\rm peak} = \sqrt{3}/3\gamma \approx 0.58\gamma$ (see Fig. 2.7b). The quantum overdamped spectral density converges to zero faster at high frequency, therefore, it is more suitable for numerical applications. At the high-temperature limit the corresponding lineshape

function is given by

$$g_{\mathrm{o-q}}(t) = \frac{\lambda}{\gamma}\left(\frac{2}{\beta\gamma} - \mathrm{i}\right)\left(\mathrm{e}^{-\gamma t}\gamma t + 2\mathrm{e}^{-\gamma t} - 2 + \gamma t\right) + \frac{\lambda\beta}{2}\left(1 + \frac{4}{\beta^2\gamma^2}\right)\left(\mathrm{e}^{-\gamma t} + \gamma t - 1\right). \tag{2.79}$$

2.2.3 Relaxation in multi-level system

Let us describe the relaxation through the eigenstates of the multi-level system. The concept of the Green's function was introduced above, in the discussion about the off-diagonal energy fluctuations. The Green's function is a solution of the Pauli master equation

$$\frac{\mathrm{d}}{\mathrm{d}t}G_{e'e}(t) = \sum_{j\neq e'} K_{e'j}G_{je} - \left(\sum_{j\neq e'} K_{je'}\right)G_{e'e}, \tag{2.80}$$

where K_{ij} are the population transport rates, that can be calculated using different relaxation theories. This equation can be represented in the matrix form

$$\frac{\mathrm{d}}{\mathrm{d}t}\widehat{G}(t) = -\widehat{\widetilde{K}}\widehat{G}(t), \tag{2.81}$$

where the population transport rates matrix is constructed as: $\widetilde{K}_{ab} = -K_{ab} + \delta_{ab}\sum_j K_{jb}$. By applying an unitary transformation upon the explicit solution of Eq. (2.81), we obtain

$$\widehat{G}(t) = \widehat{Q}\exp(-\widehat{Q}^{-1}\widehat{\widetilde{K}}\widehat{Q}t)\widehat{Q}^{-1} \tag{2.82}$$

and

$$G_{e'e}(t) = \sum_j Q_{e'j}Q^{-1}_{je}\mathrm{e}^{-\lambda_j t}. \tag{2.83}$$

Here, $\widehat{Q}$ is the eigenvector matrix of $\widehat{\widetilde{K}}$, $\widehat{Q}^{-1}$ is its inverse and λ_j are the eigenvalues. Population transport rates can be calculated using traditional Redfield relaxation theory:[70,151]

$$K_{ab} = C''_{ab,ab}(\omega_{ab})[\coth(\beta\hbar\omega_{ab}/2) - 1], \tag{2.84}$$

where $\hbar\omega_{ab} = \varepsilon_a - \varepsilon_b$ and

$$C''_{ab,cd}(\omega) = \frac{1 - \exp(-\beta\hbar\omega)}{2}\int_{-\infty}^{\infty}\mathrm{d}t\mathrm{e}^{\mathrm{i}\omega t}C_{ab,cd}(t). \tag{2.85}$$

2.2.4 Molecular excitons

Let us consider a general multi-chromophore system consisting of N electronically interacting two-level systems. Nonlinear optical properties of such complexes of coupled chromophores (e. g., molecular aggregates, proteins, etc.) are described using a Frenkel exciton model,[5,152] which defines the following material Hamiltonian:

$$\widehat{H}_{\mathsf{mat}} = \sum_{m=1}^{N} \epsilon_m \widehat{B}_m^{\dagger} \widehat{B}_m + \sum_{m}^{N} \sum_{n \neq m}^{N} J_{nm} \widehat{B}_m^{\dagger} \widehat{B}_n + \widehat{H}_{\mathsf{int}}. \tag{2.86}$$

Here, ϵ_m and J_{mn} are the site energy of the m-th chromophore and the resonant coupling constant between n-th and m-th chromophores, respectively. If the intermolecular distances are much larger than intramolecular, the resonant interaction can be calculated as the Coulomb coupling between charge densities of the molecules, approximated as electric dipoles (the dipole–dipole approximation).[6,153] Then, the resonance coupling constant can be expressed by the molecular transition dipoles:

$$J_{mn} = \frac{(\boldsymbol{\mu}_m \cdot \boldsymbol{\mu}_n)}{|\mathbf{R}_{mn}|^3} - 3\frac{(\boldsymbol{\mu}_m \cdot \mathbf{R}_{mn})\,(\boldsymbol{\mu}_n \cdot \mathbf{R}_{mn})}{|\mathbf{R}_{mn}|^5}. \tag{2.87}$$

Here $\mathbf{R}_{mn}$ is a vector, drawn from the middle point of $\boldsymbol{\mu}_m$ to the middle point of vector $\boldsymbol{\mu}_n$. Extended dipole approximation,[154] transition density cube method[155] or the transition charge from electrostatic potential (TrEsp)[156,157] method can be used to calculate the excitonic coupling beyond the dipole–dipole approximation.

The theory used to describe the spectroscopic properties of such systems is essentially the same as for a general multi-level system described previously, only here we have to calculate the eigenstates and transform other quantities (transition dipole moments, correlation coefficients, etc.) to the eigenstate basis from the Frenkel excitonic Hamiltonian.

Thus, the system eigenstates will consist of the zero-vibrational ground state $|\mathsf{g}\rangle$ and the bands (manifolds) of the singly-excited and the doubly excited states. Each state of the singly-excited state manifold is denoted as $|\mathsf{e}_j\rangle$ ($j = 1 \ldots N$) with corresponding optical transition to the ground state $\omega_{\mathsf{e}_j\mathsf{g}}$. The number of the doubly-excited states is $N(N-1)/2$ and they are denoted as $|\mathsf{f}_k\rangle$ with optical transitions to the singly-excited states $\omega_{\mathsf{f}_k\mathsf{e}_j}$; the direct transition to the ground state is forbidden. The Hamiltonian matrix $\widehat{h}^{(1)}$ of the singly-excited states is simply the reference Hamiltonian of Eq. (2.86): $h_{jk}^{(1)} = \delta_{jk}\epsilon_j + \zeta_{jk}J_{jk}$, where $\zeta_{jk} = 1 - \delta_{jk}$. The matrix elements of the doubly-excited state Hamiltonian are $h_{(kl),(mn)}^{(2)} \equiv (\epsilon_k + \epsilon_l)\delta_{km}\delta_{ln} + J_{km}\delta_{ln}\zeta_{km} + J_{ln}\delta_{km}\zeta_{ln}$. Transition from the site basis to the exciton basis as well as eigenenergies are obtained by using the unitary

transformations,

$$\widehat{U}^{-1}\widehat{h}^{(1)}\widehat{U} = \widehat{\Omega}, \tag{2.88}$$

$$\widehat{V}^{-1}\widehat{h}^{(2)}\widehat{V} = \widehat{W}. \tag{2.89}$$

As previously, we assume that the system–bath interaction Hamiltonian $\widehat{H}_{\mathrm{SB}}$ describes the diagonal fluctuations of the molecular transition energies, each molecule has its own independent set of fluctuating coordinates uncorrelated to the other molecules, and fluctuations of different molecules are statistically independent. In the exciton basis, we obtain fluctuating transition energies and couplings between the eigenstates. These fluctuations are characterized by the spectral densities

$$C''_{\mathrm{e}_1\mathrm{e}_2,\mathrm{e}_3\mathrm{e}_4}(\omega) = \left[\sum_m U^{-1}_{m\mathrm{e}_1} U^{-1}_{m\mathrm{e}_2} U^{-1}_{m\mathrm{e}_3} U^{-1}_{m\mathrm{e}_4}\right] \mathcal{C}''(\omega), \tag{2.90a}$$

$$C''_{\mathrm{e}_1\mathrm{e}_2,\mathrm{f}_3\mathrm{f}_4}(\omega) = \left[\sum_m U^{-1}_{m\mathrm{e}_1} U^{-1}_{m\mathrm{e}_2} \sum_k^{k\neq m} \nu^{(\mathrm{f}_3)}_{mk}\nu^{(\mathrm{f}_4)}_{mk}\right] \mathcal{C}''(\omega), \tag{2.90b}$$

$$C''_{\mathrm{f}_1\mathrm{f}_2,\mathrm{e}_3\mathrm{e}_4}(\omega) = C''_{\mathrm{e}_3\mathrm{e}_4,\mathrm{f}_1\mathrm{f}_2}(\omega), \tag{2.90c}$$

$$C''_{\mathrm{f}_1\mathrm{f}_2,\mathrm{f}_3\mathrm{f}_4}(\omega) = \left[\sum_m \left(\sum_k^{k\neq m} \nu^{(\mathrm{f}_1)}_{mk}\nu^{(\mathrm{f}_2)}_{mk}\right)\left(\sum_l^{l\neq m} \nu^{(\mathrm{f}_3)}_{ml}\nu^{(\mathrm{f}_4)}_{ml}\right)\right] \mathcal{C}''(\omega). \tag{2.90d}$$

Here $\nu^{(k)}_{nm}$ denotes the element of $\widehat{V}^{-1}$ of the k-th row and and the column, corresponding to the diagonal element $\epsilon_n + \epsilon_m$ of the doubly-excited state Hamiltonian matrix. The explicit relation is $\nu^{(k)}_{mn} = V^{-1}_{k\gamma}$, where $\gamma = \frac{1}{2}(2N-m)(m-1)+n-m$, n, $m = 1, 2 \ldots N$. We have also extended the eigenvector matrix of the doubly-excited states by taking $\nu^{(f)}_{mn} \equiv \nu^{(f)}_{nm}$, which lets us simplify the expressions considerably.

The transition dipoles of the interband transitions (eigendipoles) are obtained, by applying the same unitary transformation:

$$\boldsymbol{\mu}_{\mathrm{ge}_j} = \sum_m U^{-1}_{jm}\boldsymbol{\mu}_m \tag{2.91}$$

$$\boldsymbol{\mu}_{\mathrm{e}_j\mathrm{f}_k} = \sum_{m=1}^{N-1}\sum_{n=m+1}^{N} \nu^{(k)}_{mn}(U^{-1}_{jn}\boldsymbol{\mu}_m + U^{-1}_{jm}\boldsymbol{\mu}_n). \tag{2.92}$$

We will only consider the electronic transitions between the excitonic bands and the ground state. Therefore, the response function components (eqs. (1.49a)-(1.49d)) will only contain oscillating terms of the evolution operator of frequencies, corresponding to these interband energy gaps (approximately the same frequency $\overline{\omega}$ for all interband transitions). One can see that in the expressions there are two

types of phase factors, $-\mathrm{i}\overline{\omega}(t_1+t_3)$ and $-\mathrm{i}\overline{\omega}(t_1-t_3)$. The opposite phase factors of electromagnetic field oscillations of frequency ω_0 are in the electromagnetic field expression Eq. (1.53). In the experiment, $\omega_0 \approx \overline{\omega}$ is satisfied. Multiplication of the system response function and electric field part under integration in Eq. (1.46) then results in terms of the sum\ phase factors. In the case of constructive (or destructive) interference of phase factors, rapidly (or slowly) oscillating terms are obtained. Integrals of rapidly-varying functions are much smaller and can be neglected (RWA). The third-order polarization then reads

$$
\begin{aligned}
P^{(3)}(\tau, T, t) = \mathrm{e}^{-\mathrm{i}\omega_0(t-\tau)} \int_0^\infty \int_0^\infty \int_0^\infty \mathrm{d}t_3 \mathrm{d}t_2 \mathrm{d}t_1 \qquad (2.93)\\
\times \Big\{ S^{(3)}_{\mathbf{k}_\mathrm{I}}(t_3, t_2, t_1) \times \left[\overline{E}_1^{[1]} E_2^{[2]} E_3^{[3]} + \overline{E}_1^{[1]} E_3^{[3]} E_2^{[2]} \right] \mathrm{e}^{\mathrm{i}\omega_0(t_3-t_1)}\\
+ S^{(3)}_{\mathbf{k}_\mathrm{II}}(t_3, t_2, t_1) \times \left[E_2^{[1]} \overline{E}_1^{[2]} E_3^{[3]} + E_3^{[1]} \overline{E}_1^{[2]} E_2^{[3]} \right] \mathrm{e}^{\mathrm{i}\omega_0(t_3+t_1)}\\
+ S^{(3)}_{\mathbf{k}_\mathrm{III}}(t_3, t_2, t_1) \times \left[E_2^{[1]} E_3^{[2]} \overline{E}_1^{[3]} + E_3^{[1]} E_2^{[2]} \overline{E}_1^{[3]} \right] \mathrm{e}^{\mathrm{i}\omega_0(t_3+2t_2+t_1)} \Big\},
\end{aligned}
$$

where $S^{(3)}_{\mathbf{k}_\mathrm{I}}(t_3, t_2, t_1) = -R_1^* + R_2 + R_3$, $S^{(3)}_{\mathbf{k}_\mathrm{II}}(t_3, t_2, t_1) = -R_2^* + R_1 + R_4$ and $S^{(3)}_{\mathbf{k}_\mathrm{III}}(t_3, t_2, t_1) = -R_3^* + R_4$ are the system response functions for the $\boldsymbol{k}_\mathrm{I}$, $\boldsymbol{k}_\mathrm{II}$ and $\boldsymbol{k}_\mathrm{III}$ interaction sequences, respectively. Auxiliary response functions R_α are related to the four-point correlation functions[158] (eqs. (2.44) and (2.50)). These interaction sequences of the evolution operator and the dipole moment operator can be expressed by the double-sided Feynman diagrams (Fig. 2.6). They correspond to different physical processes – excited state absorption (ESA, diagrams $-R_1^*$ and $-R_2^*$), stimulated emission (SE, diagrams R_2 and R_1), ground state bleaching (GSB, diagrams R_3 and R_4) or double quantum coherence pathways (DQC, diagrams $-R_3^*$ and R_4). Additionally, ESA′ and SE′ diagrams involving population transfer are indicated in Fig. 2.6. In the further discussion we will use the notations of the ESA, SE, GSB or DQC diagrams instead of auxiliary R_α functions, introduced in eqs. (1.49a)–(1.49d). Complete expressions for $S^{(3)}_{\mathbf{k}_\mathrm{I}}$–$S^{(3)}_{\mathbf{k}_\mathrm{III}}$ can be found elsewhere.[159]

2.3 Electronic dimer

We denote a pair of electrostatically-only interacting molecules an electronic dimer (ED). It is the simplest system for which excitonic effects can be demonstrated. We assume the dipole–dipole coupling between the molecules and that both dipole vectors lie in a single plane. Therefore the geometry of the dimer can fully be described by the dipole strengths $|\boldsymbol{\mu}_1|^2$ and $|\boldsymbol{\mu}_2|^2$, interdipole distance vector

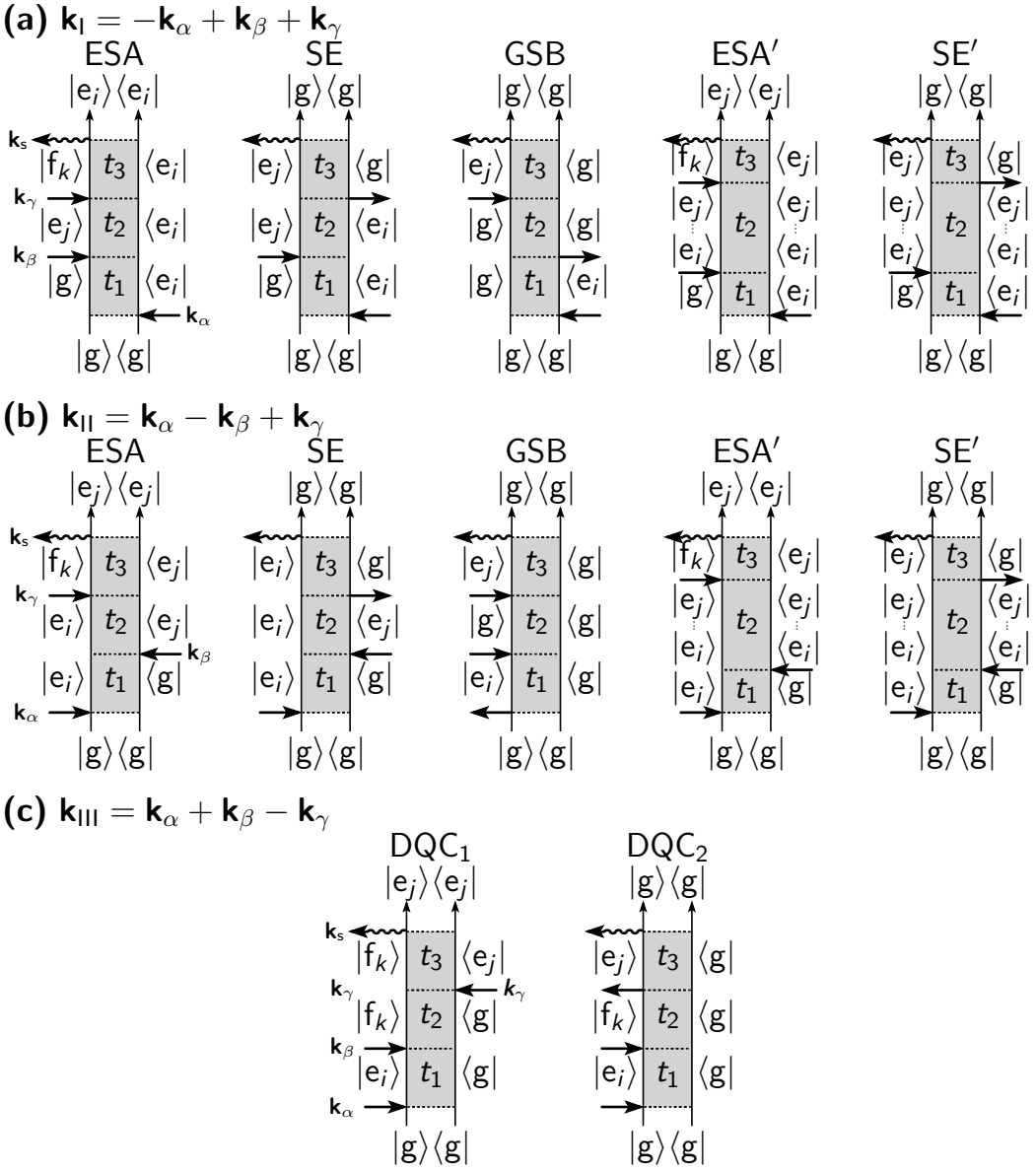

Fig. 2.8. Double-sided Feynman diagrams, illustrating a repetitive dipole moment interaction with the both sides of the system density operator. Contributions to the spatial $\mathbf{k}_{\mathrm{I}}$ **(a)**, $\mathbf{k}_{\mathrm{II}}$ **(b)** and $\mathbf{k}_{\mathrm{III}}$ **(c)** directions. Indices α, β, and γ denote different arbitrary numbers, representing all possible orderings of the system–field interactions.

$\mathbf{R}_{12}$, and the mutual angle ϕ (see Fig. 2.9a). In the Frenkel exciton Hamiltonian (Eq. (2.86)) the chromophore site energies are denoted as $\epsilon_1 = \epsilon + \delta_0$ and $\epsilon_2 = \epsilon$:

$$\widehat{H}_{\mathrm{mat}} = \begin{pmatrix} \epsilon + \delta_0 & J \\ J & \epsilon \end{pmatrix}. \tag{2.94}$$

The Hamiltonian is diagonalized and the eigenenergies for the singly- and doubly-excited states are

$$\varepsilon_{\mathrm{e}_2} = \frac{1}{2}(\epsilon_1 + \epsilon_2) + \frac{1}{2}\Delta^0_{\mathrm{e}}, \tag{2.95}$$

$$\varepsilon_{e_1} = \frac{1}{2}(\epsilon_1 + \epsilon_2) - \frac{1}{2}\Delta_e^0 \tag{2.96}$$

and

$$\varepsilon_f = \varepsilon_{e_1} + \varepsilon_{e_2} = \epsilon_1 + \epsilon_2. \tag{2.97}$$

Here

$$\Delta_e^0 \equiv \sqrt{\delta_0^2 + 4J^2} \tag{2.98}$$

is the excitonic energy gap, dependent on the site energy difference δ_0 and the resonance coupling constant J.

It is sometimes convenient to express the variables using the so-called *mixing angle*, defined as:[67, 160, 161]

$$\theta = \frac{1}{2}\arctan\left(\frac{2J}{\delta_0}\right). \tag{2.99}$$

Then the eigenstate transformation matrix is

$$\widehat{U}^{-1} = \begin{pmatrix} -\sin\theta & \cos\theta \\ \cos\theta & \sin\theta \end{pmatrix} \tag{2.100}$$

The singly-excited state energies can then be written as

$$\varepsilon_{e_1} = \epsilon_1 \sin^2\theta + \epsilon_2 \cos^2\theta - 2J\cos\theta\sin\theta \tag{2.101}$$

and

$$\varepsilon_{e_2} = \epsilon_1 \cos^2\theta + \epsilon_2 \sin^2\theta + 2J\cos\theta\sin\theta. \tag{2.102}$$

According to Eq. (2.92), the transition dipole moments between the eigenstates

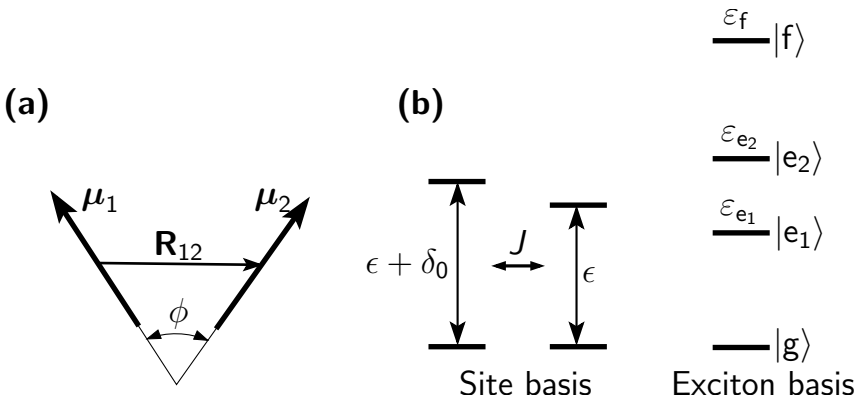

Fig. 2.9. Definitions of geometric **(a)** and energy **(b)** variables of the electronic dimer.

and transition dipole moments in the site basis are related as

$$\boldsymbol{\mu}_{\mathrm{ge}_1} = -\sin\theta\boldsymbol{\mu}_1 + \cos\theta\boldsymbol{\mu}_2, \tag{2.103}$$

$$\boldsymbol{\mu}_{\mathrm{ge}_2} = \cos\theta\boldsymbol{\mu}_2 + \sin\theta\boldsymbol{\mu}_2 \tag{2.104}$$

and

$$\boldsymbol{\mu}_{\mathrm{e}_1\mathrm{f}} = \cos\theta\boldsymbol{\mu}_1 - \sin\theta\boldsymbol{\mu}_2, \tag{2.105}$$

$$\boldsymbol{\mu}_{\mathrm{e}_2\mathrm{f}} = \sin\theta\boldsymbol{\mu}_1 + \cos\theta\boldsymbol{\mu}_2. \tag{2.106}$$

If the dipole moments are of the unit length, $|\boldsymbol{\mu}_1| = |\boldsymbol{\mu}_2| = 1$, the squares of the transition dipoles represent the oscillator strengths and read:

$$\left|\boldsymbol{\mu}_{\mathrm{e}_1\mathrm{g}}\right|^2 = \left|\boldsymbol{\mu}_{\mathrm{fe}_1}\right|^2 = 1 - \frac{2J}{\sqrt{\delta_0^2 + 4J^2}}\cos\phi, \tag{2.107}$$

$$\left|\boldsymbol{\mu}_{\mathrm{e}_2\mathrm{g}}\right|^2 = \left|\boldsymbol{\mu}_{\mathrm{fe}_2}\right|^2 = 1 + \frac{2J}{\sqrt{\delta_0^2 + 4J^2}}\cos\phi. \tag{2.108}$$

2.3.1 2D spectrum of electronic dimer

For demonstrative purposes, let us use the electronic dimer parameters similar to those in Ref.[159] Site energies $\epsilon_1 = 11800\,\mathrm{cm}^{-1}$ and $\epsilon_2 = 12200\,\mathrm{cm}^{-1}$, resonant coupling constant $J = 100\,\mathrm{cm}^{-1}$ and the angle between the molecular dipoles $\phi = \frac{\pi}{6}$. We use the semiclassical overdamped Brownian oscillator model (Eq. (2.76)) with the relaxation rate and the reorganization energy set to $\gamma = 50\,\mathrm{cm}^{-1}$ and $\lambda = 30\,\mathrm{cm}^{-1}$, respectively. The population transfer rates, calculated using the secular Redfield theory (Eq. (2.84)) for the eigenstates at $\varepsilon_{\mathrm{e}_1} = 11776\,\mathrm{cm}^{-1}$ and $\varepsilon_{\mathrm{e}_2} = 12224\,\mathrm{cm}^{-1}$ are: $K_{1\leftarrow 2} = 4$ ps (downward) and $K_{2\leftarrow 1} = 17$ ns (upward) at temperature $T = 77$ K.

The calculated rephasing 2D electronic spectra of the electronic dimer at waiting times $t_2 = 0$, 1 ps, 4 ps and 10 ps are shown in Fig. 2.10. The spectra contain both diagonal and off-diagonal elements. Since the angle between the transition dipoles is smaller than $\pi/2$ and the sign of the resonance coupling constant is positive, such a dimer is of the so-called "H" type with a typical signature of larger oscillator strength for the transition to the higher energy state. This is also related to the lower off-diagonal peak being negative at initial waiting times.

The most evident picosecond dynamics in the spectra are the redistribution of the peak intensities. It can be clearly seen in Fig. 2.10b–c, where the femtosecond and picosecond time-dependent traces of amplitudes of all four peaks

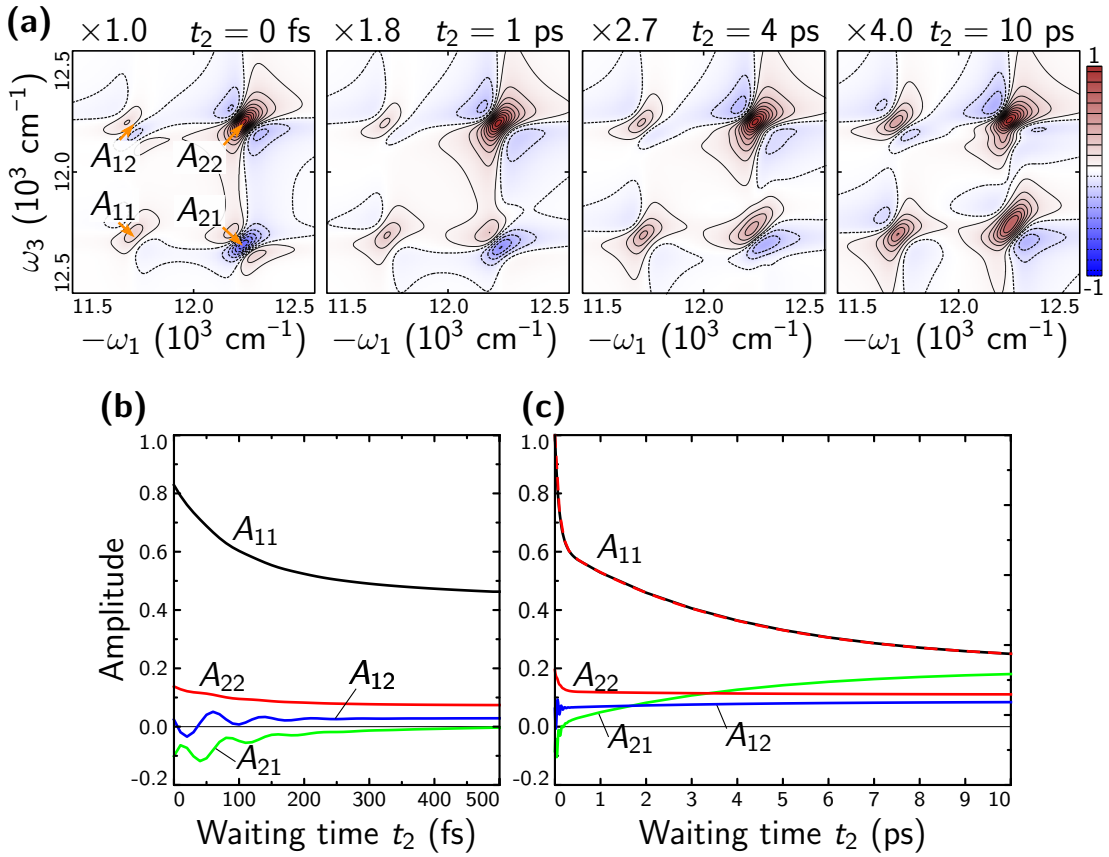

Fig. 2.10. **(a)** 2D electronic spectra of ED at waiting times $t_2 = 0$, 1 ps, 4 ps and 10 ps. Spectra are normalized to the maximum value of spectrum at $t_2 = 0$; normalization factors are indicated above each spectrum. **(b–c)** Intensities of diagonal (A_{11} and A_{22}) and off-diagonal (A_{21} and A_{22}) peaks in calculated 2D spectra of the electronic dimer: **(b)** waiting time range $t_2 = 0 - 500$ fs and **(c)** $t_2 = 0 - 10$ ps. Exponential fit of the upper diagonal peak dynamics is shown by the red dashed line (see text for details).

of the spectrum are shown separately. All peaks decay and broaden due to spectral diffusion, but for the coupled system the amplitude changes because of the population transfer, as well. Therefore, the two-exponential fit of the evolution of the upper diagonal peak gives two time scales of $\tau_1 = 92$ fs and $\tau_2 = 3.9$ fs. The time scale closely matches the bath relaxation time $\gamma^{-1} = 106$ fs and the downward population transfer rate $K_{1\leftarrow 2} = 4$ ps.

As can be seen from the dissection of the spectra into components corresponding to different Feynman diagrams (Fig. 2.11), most of the changes comes from the ESA and SE diagrams—that is, from those, which contain population evolution during the waiting time. Only the GSB contribution is not affected by the population transport and the peaks only broaden with the waiting time.

At the short waiting time ($t_2 = 0$), the population transport is negligible and the diagonal peaks consist solely of the SE and GSB contributions (Fig. 2.11e-f). These two diagonal peaks represent two singly-excited states and are created

when $e_j = e_i$, while the off-diagonal peaks correspond to $e_j \neq e_i$. The cross-peaks are created by the superposition of positive GSB and SE and negative ESA (Fig. 2.11d) contributions.

At the long waiting time ($t_2 = 10$ ps) we see signatures of the downhill population transfer. The ESA contribution refers to transition from the population of the lowest single-exciton state $|e_1\rangle\langle e_1|$ to the double-excited state $|f_1\rangle\langle e_1|$ solely. This is clearly indicated by an upper off-diagonal element in Fig. 2.11g, while the off-diagonal peak for $|e_2\rangle\langle e_2| \rightarrow |f_1\rangle\langle e_2|$ transition is dominant at the waiting time $t_2 = 0$ fs (Fig. 2.11a). The similar explanation holds for the population transfer-related lower off-diagonal peak that is seen in the SE diagram spectrum

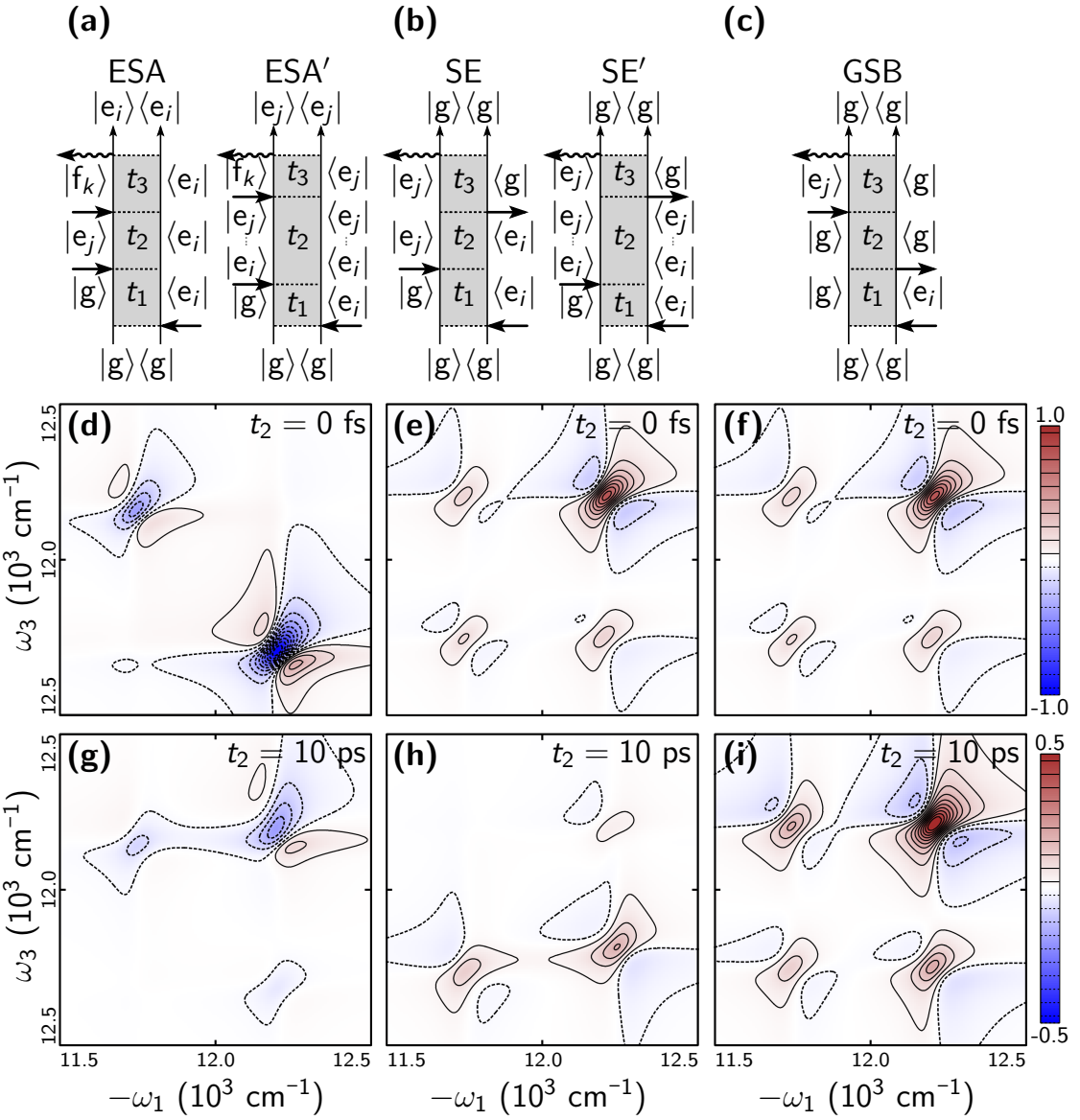

Fig. 2.11. Double-sided Feynman diagrams: **(a)** ESA, **(b)** SE and **(c)** GSB, and their contributions to the rephasing 2D spectrum at waiting time $t_2 = 0$ **(d–f)** and $t_2 = 10$ ps **(g–i)**. The spectra in rows are drawn using the same color scale.

at $t_2 = 10$ ps (Fig. 2.11h). The GSB contribution does not involve population transfer, thus, the waiting time dependence reflects the spectral diffusion only (compare Fig. 2.11f and i).

2.3.2 Phase of coherent beatings in 2D spectrum

In Fig. 2.10a it is clearly seen, that the coherent beatings of the cross-peaks have phase shift with respect to each other. Such phase difference was first experimentally observed in 2D spectra of marine algae by Collini et al.[162] and opposite phase beats in the spectral regions, symmetric with respect to the diagonal line, were claimed to be witnessing (or having a role in) the wavelike quantum transport and ultra-efficient excitation transfer. However, we have shown,[46] that the phase difference can be explained by the properties of coherences in the 2D spectrum without invoking any sophisticated quantum mechanisms.

If the environment-induced relaxation is neglected, the 2D signal (response function at the impulsive limit) can be written as a sum of resonant contributions of the type

$$W(\omega_3, t_2, \omega_1) = \int_0^\infty \mathrm{d}t_1 \mathrm{e}^{\mathrm{i}\omega_1 t_1} \int_{-\infty}^\infty \mathrm{d}t_3 \mathrm{e}^{\mathrm{i}\omega_3 t_3} G_3(t_3) G_2(t_2) G_1(\pm t_1). \tag{2.109}$$

The propagator (Green's function) of the density matrix $G_j(t_j)$ for the j-th ($j = 1, 2, 3$) time delay is of the one-sided exponential function type

$$G_j(t_j) = \theta(t_j) \exp(-\mathrm{i}\overline{\omega}_j t_j - \gamma_j t_j) \tag{2.110}$$

Here $\overline{\omega}_j$ coincides with the energy gap ω_{ab} between the *left* and *right* states ($|a\rangle\langle b|$) of the system density matrix relevant to the time interval t_j; γ_j is the dephasing constant added phenomenologically to the evolution. The Fourier transforms in Eq. (2.109) map the contributions to the frequency–frequency plot $(t_1, t_3) \to (\omega_1, \omega_3) \sim (\mp|\overline{\omega}_1|, \overline{\omega}_3)$ (the upper sign is for the rephasing, $\mathbf{k}_\mathrm{I}$, signal, the lower – for the nonrephasing, $\mathbf{k}_\mathrm{II}$, signal). Diagonal peaks at $\omega_1 = \mp\omega_3$ are usually distinguished, while the anti-diagonal line is defined as $\mp\omega_1 + \omega_3 = \text{const}$. The whole 2D signal is a function of the waiting time t_2: either oscillatory for coherences $|a\rangle\langle b|$ with characteristic oscillation energy $\overline{\omega}_2 = \omega_{ab} \neq 0$, or static for populations $|a\rangle\langle a|$ ($\overline{\omega}_2 = 0$).

Eq. (2.109) together with the Green's function definition in Eq. (2.110) can be analytically integrated. For a single contribution $W(\omega_3, t_2, \omega_1)$ giving rise to a peak at $(\omega_1, \omega_3) = (\mp\overline{\omega}_1, \overline{\omega}_3)$ we shift the origin of the (ω_1, ω_3) plot to the peak center by introducing the displacements ($\omega_1 + \overline{\omega}_1 = -s_1$, $\omega_3 - \overline{\omega}_3 = s_3$ for the

rephasing pathways, and $\omega_1 - \overline{\omega}_1 = s_1$, $\omega_3 - \overline{\omega}_3 = s_3$ for the nonrephasing). For $\gamma = \gamma_1 = \gamma_3$ we get the peak profile for the real part of the cross-peak:

$$W(s_3, t_2, s_1) = L(s_1, s_3)\mathrm{e}^{-\gamma_2 t_2} \cos\left[\overline{\omega}_2 t_2 + \phi(s_1, s_3)\right], \tag{2.111}$$

where the lineshape and phase for the $\mathbf{k}_\mathrm{I}$ signal are

$$L(s_1, s_3) = \frac{\sqrt{\left(\gamma^2 - s_1 s_3\right)^2 + \gamma^2 (s_3 + s_1)^2}}{\left(s_3^2 + \gamma^2\right)\left(s_1^2 + \gamma^2\right)} \tag{2.112}$$

and

$$\phi(s_1, s_3) = -\mathrm{sgn}\left(s_3 + s_1\right) \cdot \arccos\left(\frac{\gamma^2 - s_1 s_3}{\sqrt{\left(\gamma^2 - s_1 s_3\right)^2 + \gamma^2 (s_3 + s_1)^2}}\right), \tag{2.113}$$

respectively. Analogous expressions for the $\mathbf{k}_\mathrm{II}$ signal can be found elsewhere.[46]

The 2D spectra of a single oscillatory contribution, defined by eqs. (2.111)–(2.113) with $\varepsilon_2 \neq 0$ are shown in Fig. 2.12a at different delay times. It follows, that the oscillation of a single peak is not of the "breathing" type, where each point follows harmonic oscillations with the same phase, but rather a "wavelike" propagation along the axis perpendicular to the diagonal. Indeed, the phase $\phi(s_1, s_2)$ of the cosine in Eq. (2.111) changes from $-\pi$ to π when going across the diagonal, while the amplitude $L(s_1, s_2)$ is symmetric and positive (see Fig. 2.12b). At the center of the peak ($s_1 = s_3 = 0$), we have $\phi = 0$, leading to $W \propto \cos(\overline{\omega}_2 t_2)$. However, for $s_1 \neq 0$ and $s_3 \neq 0$ we find $W \propto \cos(|\overline{\omega}_2|\, t_2 + \phi(s_1, s_3))$ with $\phi(s_1, s_3) \neq 0$. Thus, *the displacement from the peak center determines the phase of the spectral oscillations*. Note that the sign of the phase ϕ is opposite for the peaks above ($\overline{\omega}_2 < 0$) and below ($\overline{\omega}_2 > 0$) the diagonal line, and this applies for all contributions.

A very convenient way to represent the overall complexity of oscillations in the 2D spectrum is by using the so-called coherence maps,[27,46,122,127,132,163–166] shown in Fig. 2.12c. With the 2D spectrum at some fixed delay time t_2 drawn as contours, the phase and amplitude of oscillations can be represented by color using the hue–saturation scale. Setting the hue value to the oscillation phase and the saturation to the oscillation amplitude, one obtains a colored map, which bleaches out in the regions where no oscillations are present (Fig. 2.12c, left). If the information of the phase is not needed, it is more representative to plot only the amplitude, as it is shown on the right panel of Fig. 2.12c. We will use both representations of the coherence map further in this thesis.

The link between the theoretical coherence map and the experimental observ-

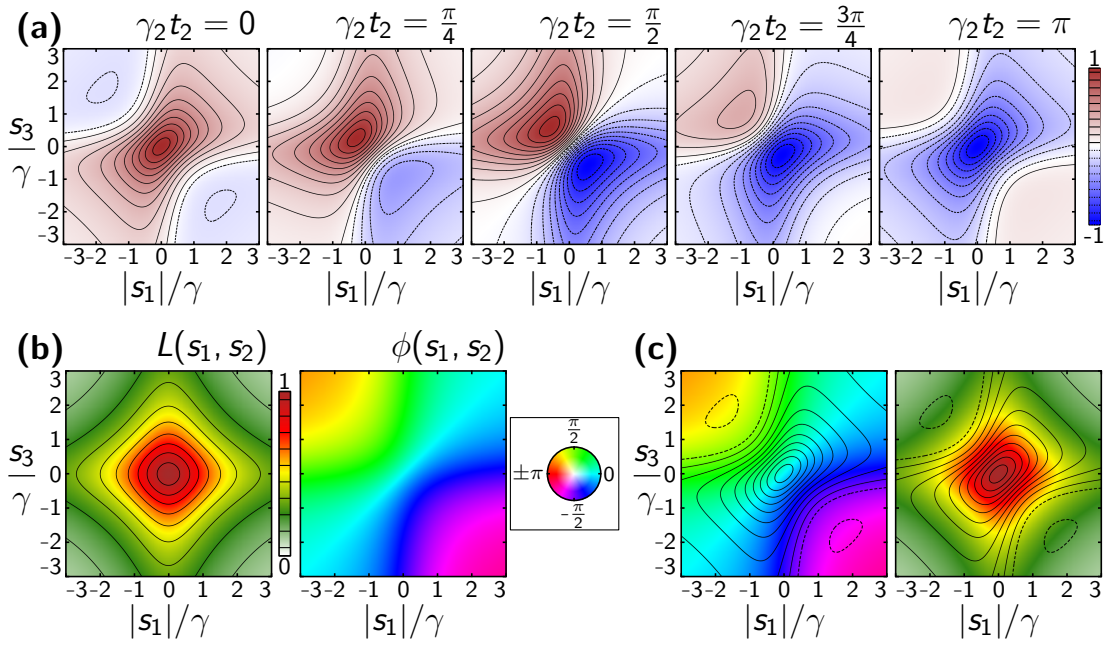

Fig. 2.12. Dynamics of a single oscillating peak in the 2D spectrum. **(a)** 2D spectra at delay times $t_2 = 0$, $t_2 = \frac{\pi}{4}\gamma_2^{-1}$, $t_2 = \frac{\pi}{2}\gamma_2^{-1}$, $t_2 = \frac{3\pi}{4}\gamma_2^{-1}$ and $t_2 = \pi\gamma_2^{-1}$; the color scale for each spectrum is normalized to the maxima of each spectra. **(b)** Functions $L(s_1, s_2)$ and $\phi(s_1, s_2)$, defined by eqs. (2.112) and (2.113). **(c)** Two different representations of coherence maps: with (left) or without (right) the phase information. 2D spectrum at $t_2 = 0$ is shown by contours.

ables is direct, since the experimental coherence maps can be constructed by performing the Fourier transform of each data point in the 2D spectrum over the waiting time t_2 after subtraction of the slow exponential decay contributions:

$$A(|\omega_1|, \omega_2, \omega_3) = \int_0^\infty \mathrm{e}^{-\mathrm{i}\omega_2 t_2} S_{\text{residuals}}(|\omega_1|, t_2, \omega_3)\mathrm{d}t_2. \qquad (2.114)$$

The amplitude and the phase which completely describes the oscillations of every point of the 2D spectrum are then extracted from the complex function $A(|\omega_1|, \omega_2, \omega_3)$. As the dependence of the amplitude on frequency ω_2 oscillation is available for every point of ω_1 and ω_3. The maximum of the coherence map as a function of ω_2 can be used as a representative variable that would characterize oscillation frequencies of the importance:

$$\mathcal{A}_{\max}(\omega_2) = \max\left[\text{Abs}\, A(|\omega_1|, \omega_2, \omega_3)\right]_{\omega_2 = \text{const.}}. \qquad (2.115)$$

Then, the oscillation map is a Fourier amplitude, plotted against the excitation and detection frequencies ω_1 and ω_3 for a fixed Fourier frequency ω_2 (in the case discussed here, $\omega_2 = \overline{\omega}_2$). Each coherence map can then be integrated over ω_1 and ω_3 and the integral value represented as a function of coherence frequency

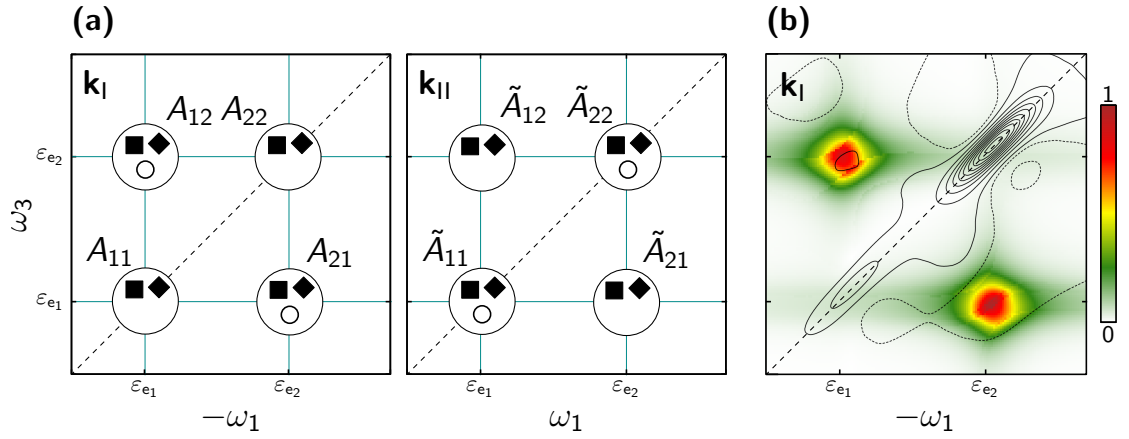

Fig. 2.13. **(a)** Arrangement of non-oscillatory (full symbols) and oscillatory (open symbols) contributions ($\diamond$ – GSB, $\square$ – SE and $\circ$ – ESA) in the rephasing ($\mathbf{k}_\mathrm{I}$) and nonrephasing ($\mathbf{k}_\mathrm{II}$) 2D spectrum of the electronic dimer**.** **(b)** The oscillation map ($\mathbf{k}_\mathrm{I}$ signal) at frequencies $\omega_2 = \omega_\mathrm{ED}$.

ω_2. Such a dependency would show the averaged distribution of various oscillation frequencies.

Alternatively, one can choose to represent the amplitude of the observed oscillations by the value of the coherence map norm (Frobenius norm), which is equal to the square root of the sum of squares of the data points of coherence maps at frequency ω_2:

$$\mathcal{A}_\mathrm{norm}(\omega_2) = \int \left|A(|\omega_1|, \omega_2, \omega_3)\right|^2 \mathrm{d}\omega_1 \mathrm{d}\omega_2. \tag{2.116}$$

It immediately follows, that the experimentally observed phase of the cross-peak oscillations is sensitive to a position, at which the temporal dynamics of the spectrum is probed. Experimentally observed phase relations of the beatings detected at separate points in the vicinity of the same cross-peak of the photosynthetic LH2 complex[167] is the result of the measurement away from the peak center and are not related to the energy transfer pathways and their efficiency. This also explains the opposite-phase beatings reported by Collini et al.,[162] while the results of Turner et al.[168] are ambiguous.

To reveal the oscillatory contributions in the ED system we have grouped all contributions into either oscillatory or static as shown in Fig. 2.13a. As a function of t_2, the ED system has only 4 oscillatory and 8 static contributions which give four peaks in both rephasing and nonrephasing spectra. The net result is that the diagonal peaks in the $\mathbf{k}_\mathrm{I}$ and cross-peaks in the $\mathbf{k}_\mathrm{II}$ signals are non-oscillatory in the ED (refer to Appendix A for analytical expressions of oscillation amplitudes for all peaks). The rephasing coherence map of the electronic dimer (Fig. 2.13b) proves the assignment of oscillatory peak positions.

It might look that consideration of the simple quantum beats in spectra of electronic dimer using coherence maps is somewhat too complicated or redundant, but here we just wanted to introduce the principle of such analysis, which will prove to be very useful for more sophisticated systems.

2.3.3 Influence of static disorder on coherences

As it was highlighted in the Introduction, coherently established exciton states are sensitive to the static and dynamic disorder, induced by the environment. Distribution of the energies and mutual orientations of the molecules, that do not change during the investigated time intervals, are often referred to as the diagonal and the off-diagonal static disorder, respectively. Dynamic disorder arises from the time-dependent changes of system's electronic and nuclear parameters.

Both static and dynamic disorder participates in a disruption of the phase relationships (dephasing) of the coherent excitons and influences the extent of exciton delocalization. In large molecular crystals and aggregates,[152,169] the exciton delocalization amounts for a significant influence to excitation transfer and photochemical properties. For example, substantial exciton delocalization was shown to be crucial for the robust, efficient and untrapped excitation transfer through a network of coupled molecules in photosynthetic complexes;[170,171] the enhancement of the quantum transport[32] can be ensured by the environmental noise, driving the system to optimal regime with respect to the exciton localization.

Static disorder significantly reduces the lifetime of the electronic beats. However, recently Dong and Fleming[172] have theoretically demonstrated the opposite effect, that in the presence of substantial static disorder, the lifetime of electronic coherences can increase, resulting in the long-lived integrated two-color photon echo signals. For the proposed mechanism, overlap of inhomogeneously broadened spectral lineshapes is necessary allowing for a part of systems in the disordered ensemble to possess full exciton delocalization and, thus, give a strong long-lived signal.

In this section, we extend the two-color PE study of Dong and Fleming[172] for electronic two-dimensional spectroscopy, which can be related to the PE signal through the projection–slice theorem.[59] We analyze the competition between static and dynamic disorder, both responsible for the decay of the observed quantum beats, and demonstrate that the lifetime and the amplitude of such electronic coherences might be significantly enhanced. We also show, that at this regime the observed beats in the 2D spectra will signify the double value of the resonant coupling, but not the excitonic splitting. We suggest explanations for the out-

comes of a few relevant experiments and discuss, why the electronic or vibrational coherences were or were not observed.

Let us consider the molecular dimer in the theoretical frame of Frenkel excitonic model. If the diagonal or off-diagonal static disorder is neglected, the excitonic splitting Δ_e is fixed and depends on the gap between the site energies of each molecule $\delta_0 \equiv \bar{\epsilon}_2 - \bar{\epsilon}_1$, and the resonant coupling constant J as

$$\Delta_e = \Delta_e^0 \equiv \sqrt{\delta_0^2 + 4J^2}. \tag{2.117}$$

In an ensemble of molecules with the uncorrelated static energy disorder, we assume that the individual distributions of the site energies of both molecules are Gaussian with the same standard deviation σ_D, i. e.,

$$P(\varepsilon_i) = \left(2\pi\sigma_D^2\right)^{-\frac{1}{2}} e^{-\frac{(\epsilon_i - \bar{\epsilon}_i)^2}{2\sigma_D^2}}. \tag{2.118}$$

Here ϵ_i is the energy of the i-th ($i = 1, 2$) molecule, $\bar{\epsilon}_i$ – its mean value. The statistical distribution of the excitonic energy gap Δ_e can then be derived[172] and yields:

$$P(\Delta_e) = \frac{e^{-\frac{\left(\delta_0 + \sqrt{\Delta_e^2 - 4J^2}\right)^2}{2\sigma_D^2}} + e^{-\frac{\left(\delta_0 - \sqrt{\Delta_e^2 - 4J^2}\right)^2}{2\sigma_D^2}}}{\Delta_e^{-1}\sqrt{2\pi}\sigma_D\sqrt{\Delta_e^2 - 4J^2}}. \tag{2.119}$$

This distribution function is shown in Fig. 2.14 for chosen parameters ($J = 150\,\mathrm{cm}^{-1}$, $\delta_0 = 400\,\mathrm{cm}^{-1}$) and at a few different values of the static disorder: $\sigma_D = 40\,\mathrm{cm}^{-1}$, $80\,\mathrm{cm}^{-1}$ and $160\,\mathrm{cm}^{-1}$.

The distribution has a singularity at $\Delta_e = 2J$, which becomes significant at larger values of the static disorder (see the blue line in Fig. 2.14). Such a distribution has two well-expressed parts: a narrow peak at $\Delta_e = 2J$ and a wide distribution, centered at Δ_e^0. These two contributions represent two sub-ensembles of the pool of dimers in the sample and have very different coherent properties. The narrow part of distribution at $\Delta_e = 2J$ represents a sub-ensemble of homo-dimers, for which the site energy gap δ_0 is zero. In homo-dimers, excitons are completely delocalized over the two sites. This means, that their energy correlation functions are identical and decoherence rate is significantly lower than of systems with the large site energy gap.[29,172] The remaining broad part of distribution represents a sub-ensemble of hetero-dimers. Wide distribution of their site energies will result in a negligible contribution to the total spectral signal due to dephasing, caused by the averaging over the coherent oscillatory signals of different frequencies of excitonic splittings, represented by the distribution. From Fig. 2.14 it is evident, that increasing the disorder results in a relative enhancement

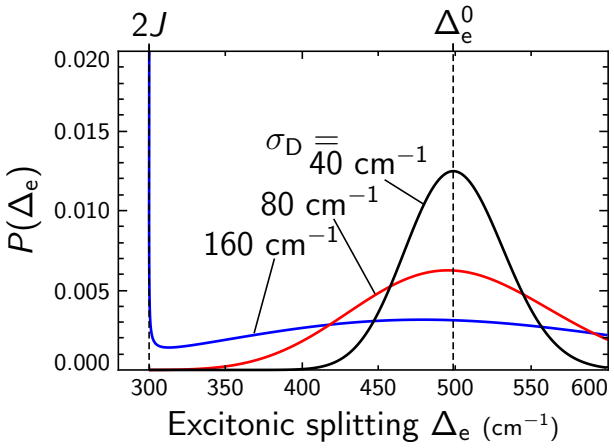

Fig. 2.14. Excitonic splitting energy distribution $P(\Delta_e)$ for different values of static disorder σ_D.

of the total signal, stemming from the sub-ensemble of the homo-dimers.

For simulations of the 2D spectra, we used the third-order system response function formalism, described above. The dynamic disorder was accounted for by treating the dynamics of the bath as the overdamped Brownian oscillator and using the Drude–Lorentz spectral density (Eq. (2.76)). The reorganization energy λ and relaxation rate γ were both set to 50 cm^{-1}. Secular Redfield theory was used to account for the excited state lifetime and population transfer at 77 K temperature. As the excitation transfer rates are not directly related to the discussed effect, the limitations of the secular Redfield theory[173] are not crucial. Static energy disorder was simulated by averaging over 1000 realizations of spectrum calculations using randomly Gaussian-distributed (Eq. (2.118)) site energies.

The 2D spectra, simulated using the same values of static disorder as for Fig. 2.14 and the waiting time t_2 traces of the lower cross-peaks are shown in Fig. 2.15a-c. In all these cases the spectral oscillations (beats) show significant changes with the disorder: the lifetime of coherent beatings when $\sigma_D = 80\,\text{cm}^{-1}$ (Fig. 2.15b) is significantly shorter than for $\sigma_D = 40\,\text{cm}^{-1}$ (Fig. 2.15a), however, increasing the static disorder to $\sigma_D = 160\,\text{cm}^{-1}$ obviously results in much longer coherence lifetime (Fig. 2.15c).

The lifetime of electronic coherent beats are determined by the excitonic gap distribution in Eq. (2.119). In order to characterize the beats at different system's parameters, we performed the Fourier transform over the waiting time t_2 dynamics of each point in spectrum, calculated by taking into account only the coherent contributions (coherent double-sided Feynman diagrams[69]). The Fourier amplitude $\mathcal{A}_{\text{norm}}$, integrated over all excitation/detection frequencies, for the fixed coherence frequency ω_2 (definition in Eq. 2.116) is shown in Fig. (2.16) for the three parameter sets used as in the example above. The width, center frequency and height of these Lorentzian peaks in the dependency will represent the lifetime, the observed frequency and the intensity of the beats, respectively.

In order to study the whole parameter space, we chose to fix the resonance

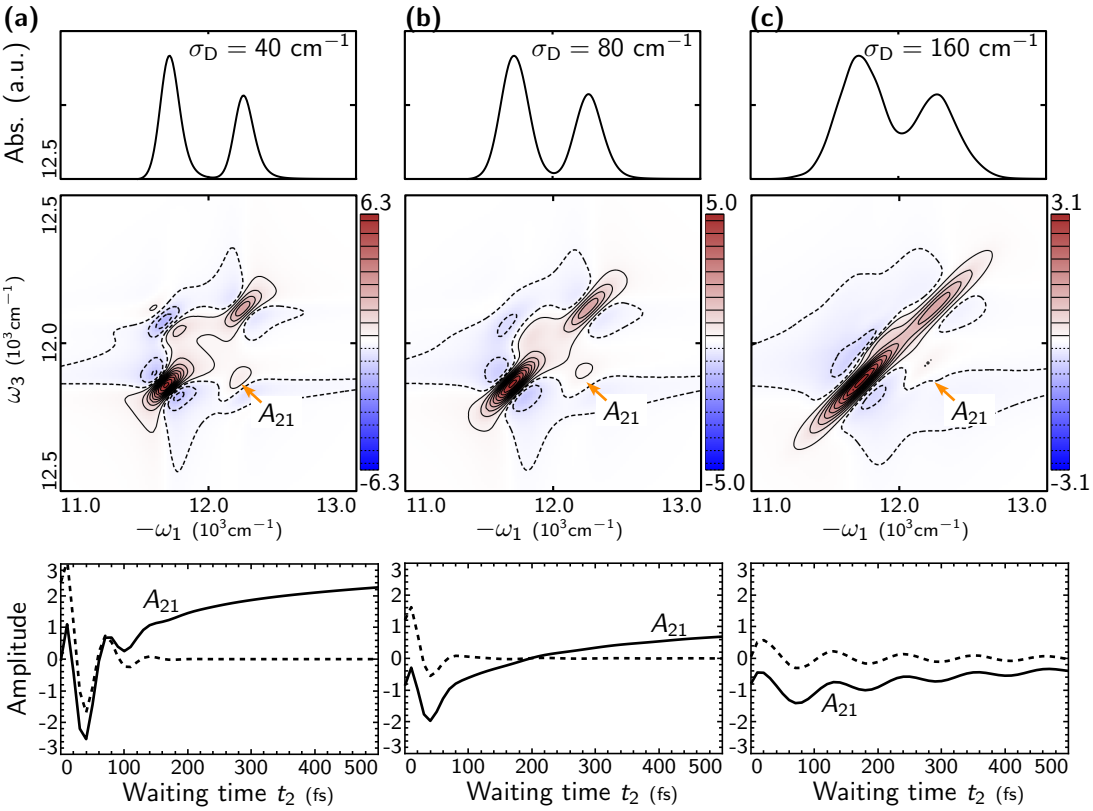

Fig. 2.15. Absorption and 2D spectra at delay time $t_2 = 0$ fs and the lower cross-peak "A_{21}" time dependencies (black solid lines; coherent contributions are shown by dashed lines) in the case of static disorder σ_D equal to 40 cm^{-1}**(a)**, 80 cm^{-1} **(b)** and 160 cm^{-1} **(c)**.

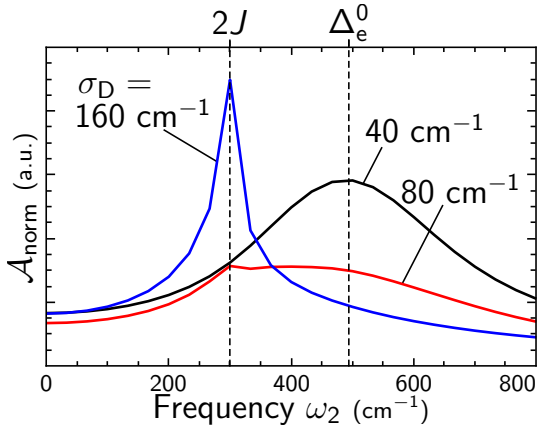

Fig. 2.16. Averaged Fourier amplitude, extracted from the 2D spectra in cases of static disorder $\sigma_D = 40$ cm^{-1}, 80 cm^{-1} and 160 cm^{-1}.

coupling constant at $J = -150$ cm^{-1} and perform the Fourier analysis of the phase space with respect to the site energy gap δ_0 and the standard deviation of the molecular energy distribution, σ_D. The resulting coherence intensity, frequency and lifetime dependencies are shown in Fig. 2.17a-c.

As it can be seen in Fig. 2.17a, the amplitude of the quantum beats decrease both with the disorder and the site energy gap. However, for high values of δ_0, the coherence amplitude has its minimum at $\sigma_D \neq 0$ (see black line in Fig. 2.17a).

A remarkable result is shown in the coherence frequency dependence on the

site energy difference and static disorder in Fig. 2.17b. It follows, that in the case of large disorder ($\sigma_D \gtrsim 100\,cm^{-1}$), the observed oscillation frequency is $2J$ instead of the excitonic gap Δ_e^0 and does not depend on δ_0.

The lifetime dependence (Fig. 2.17c) shows, that the longest coherence lifetime of ~ 1.4 ps is achieved for just slightly disordered homo-dimers ($\sigma_D \to 0$, $\delta_0 \to 0$). Changing the disorder and the energy gap parameters gives a complicated pattern of the coherence lifetime dependence (note the solid line marking the longest lifetime in Fig. 2.17c). First of all, for the large disorder, the lifetime of beats ($0.8 - 1.0$ ps) is virtually independent on site the energy gap δ_0. The shortest lifetime of coherent beats is for those systems, which are slightly disordered, but the monomer site energy difference is large. Interestingly, the area in the phase space which signifies short (< 300fs) lifetime overlaps with the area of systems, which give oscillations with frequency $> 2J$ in Fig. 2.17b.

Thus, the properties of coherent beats, illustrated by the phase space analysis in Fig. 2.17, gives a clear picture of interplay between the static and dynamic disorder in molecular systems. The longest coherence lifetimes and highest intensities will be for those dimers, where the effect of static disorder is negligible. As discussed above, such a regime is achieved in two cases: when the dimer is composed of identical molecules of similar energies ($\delta_0 \lesssim 50\,cm^{-1}$) and the distribution of the site energies is narrow, or, on the contrary, when the disorder value is high, resulting in signal, dominated by the contribution of the homo-dimeric sub-ensemble.

We have defined the spectral dephasing as the effect of decay of quantum beats in spectrum, caused by the averaging over the ensemble, and decoherence as the disruption of coherent exciton, caused by the quantum entanglement of the system and the thermal bath. Thus, the concurrence of dynamic and static disorder translates into interplay of decoherence and spectral dephasing, respectively. The situation, when the static energy disorder is effectively excluded and long-lived quantum beats are observed, can be referred to as the "decoherence-limited" regime of quantum coherences.

We propose, that the regime of decoherence-limited quantum beats ($\sigma_D = 500\,cm^{-1}$) was fulfilled for the biscyanine homo-dimer, studied by the 2D electronic spectroscopy by Halpin et al.[41] However, the proposed electronic coherence of $2J \approx 1600\,cm^{-1}$ could not be extracted due to its overlap with strong vibrational mode of $1400\,cm^{-1}$.

Following the same logic, quantum beats in the 2D spectra of synthetic dimers, recently reported by Hayes et al.,[40] were influenced by both dynamic and static disorder, since the frequencies of observed coherences (lifetimes of $60 - 90$ fs) almost perfectly matched the site energy differences, not the double values of the

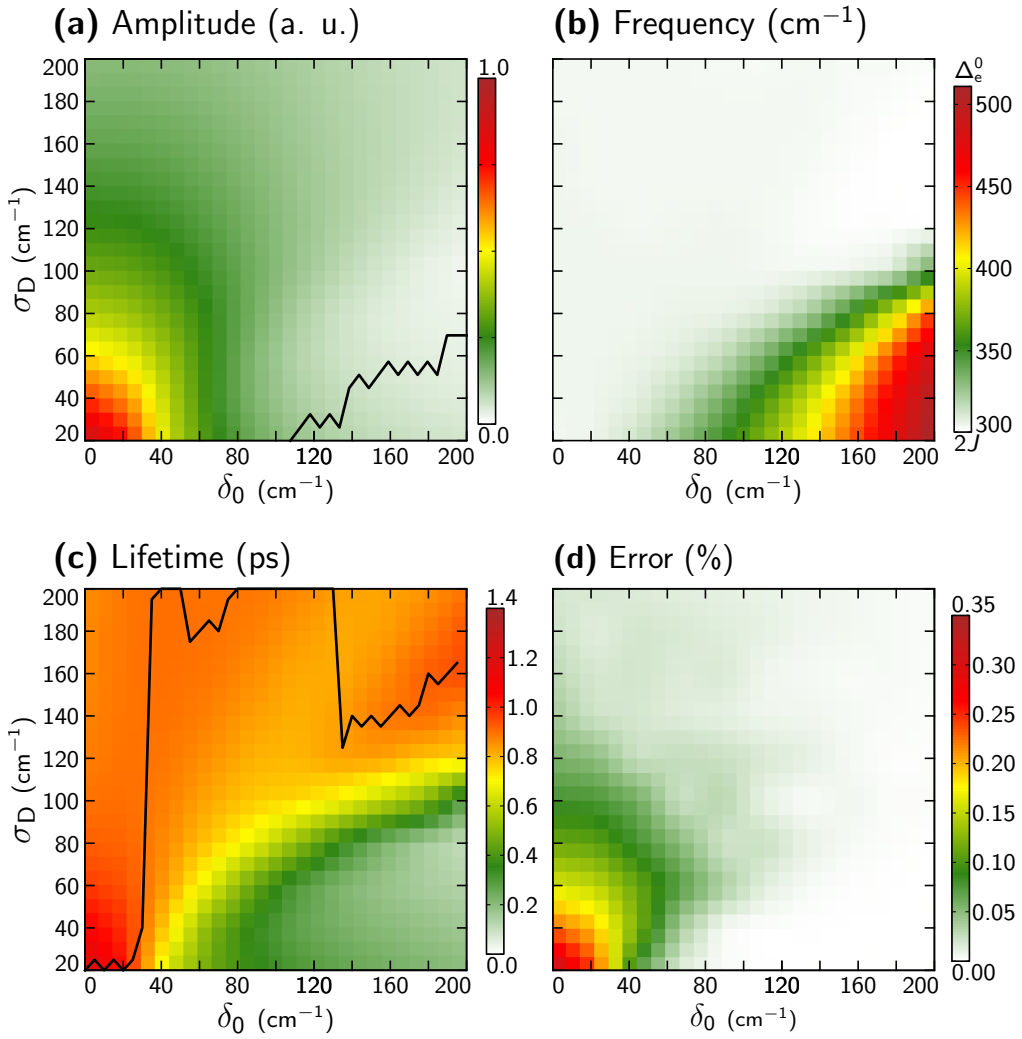

Fig. 2.17. Dependencies of **(a)** normalized amplitude, **(b)** frequency and **(c)** lifetime of coherences on site energy difference δ_0 and static disorder σ_D. Results are obtained from simulations with δ_0 and σ_D steps of 10 cm^{-1} and then interpolated. The error—mean square deviation of the Lorentzian fit—is shown in **(d)** as ratio to the amplitude maximum. Solid black lines in (a) and (c) trace minimal amplitude and maximal lifetime, respectively.

resonant coupling constants.

Another system that can be discussed in the perspective of the considered effect is the bacteriochlorophyll–bacteriopheophytin dimer of the bacterial reaction center. The resonant coupling constant and the amount of static disorder were suggested to be[174] $J = 202\,\mathrm{cm}^{-1}$ and $\sigma_D = 55\,\mathrm{cm}^{-1}$ and the site energy gap[175] $\delta_0 = 650\,\mathrm{cm}^{-1}$. With such parameters, our scheme proposes quantum beats that are formed by both static and dynamic disorder with a similar extent at the same time giving supposedly weak beats at frequencies, different than the excitonic energy gap of $\Delta_e^0 = 665\,\mathrm{cm}^{-1}$. Therefore it is natural, that no such beatings has ever been extracted, only the long-lived coherences of vibrational or mixed origin.[39,176] For the same reason electronic coherences of 305 cm^{-1} and 610 cm^{-1}

witnessing quantum superpositions between known energy states we not observed for the water soluble chlorophyll-binding protein.[42]

In the special pair of the photosystem II reaction center, strong electronic–vibrational mixing with vibrational mode of $250\,\mathrm{cm}^{-1}$ results in overlap in the frequency domain with the decoherence-limited quantum beats of electronic nature of $2J \approx 240\,\mathrm{cm}^{-1}$,[30,31] which were not extracted experimentally, as well.

The considered effect has many implications and complications regarding the experimental observation of coherent beats. Firstly, the frequencies of the detected beats do not necessarily match the frequencies of the corresponding excitonic energy gaps, which can be estimated, for example, as differences between resolved peaks in the absorption spectrum. Secondly, these beats in 2D spectrum at initial waiting times might still be overwhelmed by the short-lived quantum beats of frequencies, corresponding to the excitonic energy gaps, making the observed oscillation frequency waiting time-dependent. The time-averaged short-time Fourier transform[45] might be an useful approach for analysis of such dependencies.

In conclusion, exciton delocalization is the decisive phenomenon, controlling the amplitude and lifetimes of coherences, affected both by dephasing and decoherence. If a complete exciton delocalization is not ensured by the system's parameters and static disorder is negligible, electronic quantum coherences will be too weak or short-lived to be captured. However, a certain amount of static disorder can drive the system to the decoherence-limited regime, where the long-lived electronic quantum coherences will be observed in time-resolved coherent spectroscopy.

Chapter 3

Molecular vibronic excitons

Electronic excitations in molecular aggregates are often denoted as excitonic polarons. These are the localized Frenkel excitons, which comprise vibronically (electronically and vibrationally) excited molecule and vibrationally (but not electronically) excited surrounding molecules. Vibrationally excited molecule has its geometry distorted along some symmetric vibrational coordinates. As it was picturesquely illustrated by Spano[177] for the linear J-aggregates, such a Frenkel exciton can be imagined as a bowling ball on a mattress: the ball and a particular spring beneath it represents vibronic excitation of a molecule, while the neighboring compressed springs are vibrationally excited (although vibrationally excited molecules are elongated, not squeezed). Propagation of such vibronic exciton is complicated and often results in nontrivial spectral signatures. Although the theory of molecular vibronic coupling was extensively developed to capture properties of linear spectroscopic signals of molecular complexes, knowledge about nonlinear spectra (especially 2D ES) is rather limited. Therefore, our goal here is to investigate the properties of 2D spectra, given by the vibronic excitons in molecular complexes.

In this chapter, we will account for the electronic–vibrational coupling in molecular aggregates and by extending the response function formalism for the vibronic excitons. The presented results are based on our reported studies.[34,38,46,47,178,179] Following the presentation logic of the previous chapter, we will start with the description of a single molecule: in Sec. 3.1 we will introduce the displaced oscillator (DO) model and will carry out numerical simulations of a single molecule, coupled to one discrete vibrational mode, using two different approaches.[46,47] In Sec. 3.2 we will derive the response function for a general vibrational aggregate (VA).[34] In Sec. 3.3 we will analyze the properties of the model and the resulting spectra by assuming the most simple system—two vibronically coupled molecules, i. e., a vibrational dimer (VD).[38,179] Four different parameter sets will be used to highlight the possible spectroscopic outcomes and the effects of static energy

disorder will be discussed.

3.1 Harmonic vibrational model of a single molecule

Electronic excitations in molecules are typically approximated as the Franck–Condon transitions: it is considered that the (slow) nuclear degrees of freedom remain frozen during the electronic transition and the fixed molecular nuclear configuration adjusted to the ground electronic state emerges in non-equilibrium conditions with respect to the new electronic state. As the electronic potential energy surface is assumed to be parabolic depending on the nuclear displacement in the vicinity of the equilibrium, a displaced (harmonic) oscillator model can be used in the description of the electronic transition (Fig. 3.1). In one dimension the ground state Hamiltonian is

$$\widehat{h}_m = \frac{1}{2}\left(\widehat{p}_m^2 + \omega_m^2 \widehat{q}_m^2\right). \tag{3.1}$$

Here we have added the index m only for the later convenience, since in Sec.3.2 we will describe the coupled harmonic oscillators and will use index m to enumerate them. ω_m, $\widehat{q}_m$ and $\widehat{p}_m$ is the frequency, coordinate operator and momentum operator of the oscillator. The Hamiltonian can be quantized using bosonic creation/annihilation operators as in eqs. (2.39)–(2.40), yielding

$$\widehat{h}_m = \hbar\omega_m \left[\widehat{a}_m^\dagger \widehat{a}_m + \frac{1}{2}\right]. \tag{3.2}$$

The excited state is described by the same Hamiltonian, just shifted by the energy gap $\varepsilon = \hbar\omega_{\mathrm{eg}}$ and displaced by the coordinate displacement d:

$$\widehat{H} = \widehat{h}_m |\mathrm{g}\rangle\langle\mathrm{g}| + \left[\varepsilon + \widehat{D}^\dagger \widehat{h}_m \widehat{D}\right] |\mathrm{e}\rangle\langle\mathrm{e}|. \tag{3.3}$$

Here, the excited state Hamiltonian of a single molecule was constructed by transforming the ground state Hamiltonian $\widehat{h}_m$ with the coordinate displacement operator $\widehat{D}^\dagger = \exp\left(-\frac{\mathrm{i}}{\hbar} d\widehat{p}\right)$.[8]

Quantum mechanical problem of these harmonic potentials has exact solutions. They constitute an infinite set of wavefunctions $|\psi_m\rangle$ with quantum number $m = 0 \ldots \infty$ and the corresponding energies $E_m = \hbar\omega_0(m + 1/2)$ with respect to the bottom of the corresponding potential surface. For convenience, here we have introduced vibrational frequency $\omega_0 \equiv \omega_m$. Transitions between the sub-states of the electronic ground state and the ones of the electronic excited state determine the vibrational progression in the absorption spectrum. The intensity of each transition is represented by the transition dipole moment $\boldsymbol{\mu}_{mn}$, which is directly

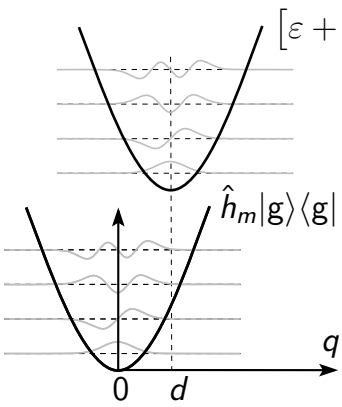

Fig. 3.1. Energy level structure of the displaced oscillator.

related to the overlap integral of the wavefunction $|\psi_m\rangle$ in the ground state and $\widehat{D}^\dagger|\psi_n\rangle$ in the excited state. It is the Franck–Condon wavefunction overlap integral:

$$\begin{aligned} F_{mn} &= \langle\psi_m| \exp\left(-\frac{d}{\sqrt{2}}\left(\widehat{a}^\dagger - \widehat{a}\right)\right)|\psi_n\rangle \\ &= \mathrm{e}^{-\frac{1}{2}s}(-1)^{m-n} s^{\frac{m-n}{2}} \sqrt{m!n!} \sum_{i=0}^{n} \frac{(-s)^i}{i!\,(n-i)!\,(m-n+i)!}, \end{aligned} \tag{3.4}$$

where the Huang–Rhys factor is

$$s = \frac{1}{2}d^2. \tag{3.5}$$

With these assumptions, the absorption spectrum of a single *isolated* molecule can be given by

$$\kappa_{\mathrm{abs}}^{\mathrm{FC}}(\omega) \propto \omega \sum_{m,n=0}^{\infty} \mathrm{e}^{-\beta m\omega_0} |F_{mn}|^2 \mathrm{Re} \int_0^\infty \mathrm{d}t \mathrm{e}^{\mathrm{i}(\omega-\omega_{\mathrm{eg}})t - \mathrm{i}\omega_0(n-m)t - \gamma t}, \tag{3.6}$$

where the phenomenological line-broadening parameter (pure dephasing rate) is γ. Here we could derive the expressions for the 2D spectrum of a single two-level system similarly as we have done in Sec. 2.1.2 with a phenomenological bath, but instead let us formulate the problem for a molecule coupled to a more realistic phonon bath. With the developed theory, we will be able to easily step back to the description of the phenomenological bath, anyway.

To describe the optical properties of a single *not isolated* molecule (i. e. coupled to the phonon bath) we would require to utilize the response function and spectral density formalism introduced before. Here, a very handy property is that the quantum correlation functions of the polarization operator representing the

spectroscopic observables are exactly given in terms of the second-order cumulant expansion with respect to the vibrational modes. Therefore, it is exact for our molecule and we can calculate the shapes of electronic transition bands and the bath-induced time dependence of the spectrum by using the formalism of the lineshape functions. The latter directly comes from the perturbative second-order cumulant expansion of the system density operator propagation, which allows to describe various types of vibrational baths and include these effects explicitly.[69] The absorption coefficient is then given by Eq. (2.20), that is

$$\kappa_{\mathrm{abs}}^{\mathcal{C}}(\omega) \propto \omega \mathrm{Re} \int_0^\infty \mathrm{d}t \mathrm{e}^{\mathrm{i}(\omega-\omega_0)t-g(t)}. \tag{3.7}$$

Here the choice of the lineshape function $g(t)$ reflects the properties of the bath and vibrations. We will restrict ourselves to the lineshape functions corresponding to different damping regimes represented by the spectral density functions in eqs. (2.71), (2.73), (2.76) or (2.78).

In the case when a molecule is coupled to a single undamped or damped high-frequency vibrational mode and a continuum of low-frequency overdamped modes, the spectral density consists of two parts:

$$\mathcal{C}''(\omega) = \mathcal{C}''_{\mathrm{o}}(\omega) + \mathcal{C}''_{\mathrm{vib}}(\omega). \tag{3.8}$$

Here the $\mathcal{C}''_{\mathrm{o}}(\omega)$ mode corresponds to the *semi-classical* $\mathcal{C}''_{\mathrm{o-sc}}(\omega)$ or *quantum overdamped* $\mathcal{C}''_{\mathrm{o-q}}(\omega)$ bath. The second term, $\mathcal{C}''_{\mathrm{vib}}(\omega)$, represents spectral density of molecular vibrations (*undamped* $\mathcal{C}''_{\mathrm{u}}(\omega)$ or *damped* $\mathcal{C}''_{\mathrm{d}}(\omega)$). The total lineshape function then contains two parts as well. Then, for a single two-level system the complete expressions for the rephasing contributions of 2D spectrum is given by Eq. (2.34).

As it was shown, for a general multi-level system the response function is a sum of many contributions, which can be grouped into ESA, SE and GSB terms. Additionally, the pathways responsible for the population transfer are present.[145] Here, we have only two contributions, since the excited state absorption contribution producing negative peaks in the 2D spectrum is not available due to the absence of the doubly-excited state.

3.1.1 Undamped vs. damped harmonic bath

It was shown by us,[47] that the absorption lineshapes of the two-level system, obtained by using solely the *quantum* or *semi-classical* overdamped bath models (i. e., $\mathcal{C}''(\omega) \equiv \mathcal{C}''_{\mathrm{o-q}}(\omega)$ or $\mathcal{C}''(\omega) \equiv \mathcal{C}''_{\mathrm{o-sc}}(\omega)$), differ negligibly despite of a

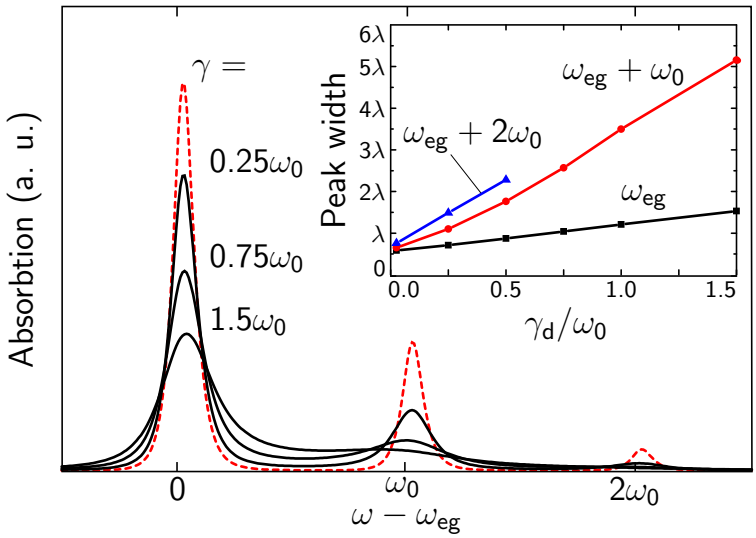

Fig. 3.2. Absorption spectrum of the displaced harmonic oscillator ($s = 0.3$) for different damping strengths $\gamma/\omega_0 = 0.25 - 1.5$ of the damped bath (black solid lines) and for the undamped bath (red dashed line). **Inset:** the widths of three main peaks at different damping strengths; the third peak becomes unresolvable for $\gamma > 0.5\omega_0$.

substantial difference of the shapes of the corresponding spectral density functions (Fig. 2.7b). The peak shape in the absorption spectrum is mainly determined by the imaginary part of the corresponding lineshape function (Fig. 2.7d).

Let us discuss the properties of the undamped and damped harmonic baths by assuming the composite spectral density given by Eq. (3.8) and setting the Huang–Rhys factor of the vibrational mode to $s = 0.3$. In the absorption spectrum, such a system demonstrates three well-resolved peaks of vibrational progression at frequencies $\omega = \omega_{eg}$, $\omega_{eg} + \omega_0$ and $\omega_{eg} + 2\omega_0$ (Fig. 3.2).

The case when the composite spectral density is $\mathcal{C}''_{o-sc}(\omega) + \mathcal{C}''_{u}(\omega)$ corresponds to the overdamped semi-classical bath with undamped vibrations is a commonly used approach, discussed in detail in the literature.[47, 180, 181] The produced vibrational progression in the absorption spectrum is drawn as the red dashed line in Fig. 3.2.

The effects caused by damping of vibrations are significant. The peaks in the progression broaden gradually when the damping strength γ is increased. However, the broadening is not uniform – peaks that are at higher energies are broadened more. This is evident in evaluation of the peak width dependence on the damping strength (inset of Fig. 3.2), obtained by fitting the spectra with multiple Lorentzian functions. As a result, the total spectral lineshape becomes asymmetric: the higher-energy shoulder of the vibrational progression is reduced due to additional broadening. Such broadening indicates a more sophisticated lifetime-induced decay of vibrational states as the model includes the relaxation

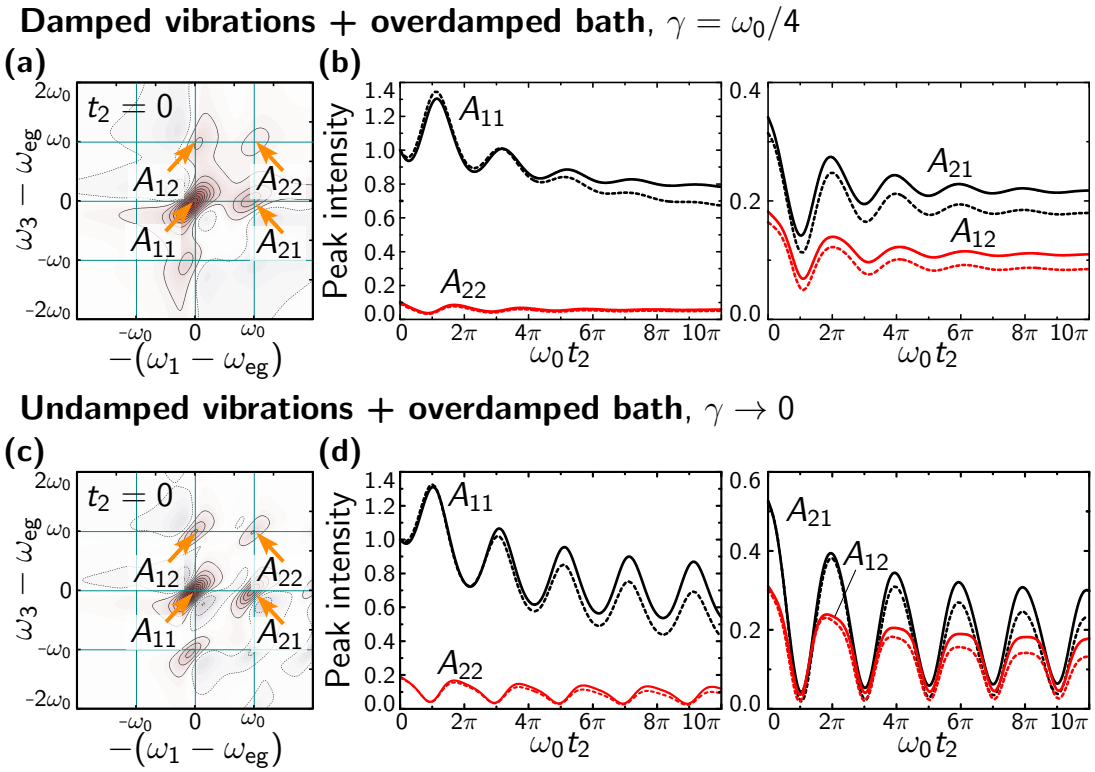

Fig. 3.3. 2D rephasing spectra at $t_2 = 0$ of a single harmonic oscillator with damped **(a)** and undamped **(c)** vibrations and coupled to a semi-classical bath. Intensities of the peaks, indicated as "A_{11}", "A_{21}", etc. are depicted as functions of the waiting time t_2 in the case of damped vibrations **(b)** and undamped vibrations **(d)** coupled to with semi-classical (solid lines) and quantum (dashed lines) overdamped bath. Peak intensity values are normalized to the maximum of the rephasing spectrum at $t_2 = 0$ in both cases.

phenomenon exactly.[34]

The peak lineshapes in the 2D spectrum, obtained by using the damped case, show slightly larger broadenings compared to those of the undamped vibrations (Fig. 3.3). The non-uniform broadening, as follows from the absorption simulations, shows up in the 2D spectrum, as well. For the vibrational bath we separately study two cases: the damped vibrations ($\gamma = \omega_0/4$, Fig. 3.3a-b) and the undamped vibrations ($\gamma \to 0$, Fig. 3.3c-d). In both cases the lineshape function representing the semi-classical overdamped bath is added to the vibrational part. Other parameters are such that the reorganization energy in all cases was the same ($\lambda = 2s\omega_0$).

3.1.2 Vibrations-induced quantum beats in 2D ES

The vibrational wavepacket (coherence) beats show up as temporal oscillations in the 2D spectrum, just like for the ED system. Decay of the coherences in the case of the damped vibrations results in the decay of cross-peaks (Fig. 3.3b).

Considering the phases of oscillations corresponding to different peaks, it is clearly observed that the model of the vibrational bath does not change the phase relationships of peak oscillations. However, the oscillation phase is not the same for all peaks, even if the dynamics are probed at the very centers of the spectral resonances. For example, the phase of the lower diagonal peak "A_{11}" oscillations is opposite to all the other peaks (Fig. 3.3b,d). In the nonrephasing signal both cross-peaks would oscillate with the same phase, while both diagonal peaks – with the opposite phase.[47]

In order to unravel the oscillatory properties (phases) of the 2D spectra we thus need to construct the entire 2D signal from the first principles and recover the source of oscillations in the spectrum, since in the lineshape function approach, the information about phases of oscillations is not explicitly available.

We disassemble the whole 2D spectrum as a sum of all relevant contributions. Assuming that the dephasing is identical for all states, different contributions to the same peak can be summed, as they will have the same shapes. We can then simplify the 2D plot by writing the signal as a sum of all contributions $\overline{\sum}$, which have static (from populations) and oscillatory (from coherences) parts in terms, represented by Eq. (2.111):

$$\begin{aligned} W(\omega_3, t_2, \omega_1) = {} & \mathrm{e}^{-\gamma_2 t_2} \overline{\sum}_{m,n} L_{mn}(\omega_1, \omega_3) \\ & \times \Big[A^{\mathrm{p}}_{mn} + A^{\mathrm{c}}_{mn} \cos(\omega_0 t_2 + \phi_{mn}(\omega_1, \omega_3)) \\ & + A^{\mathrm{cc}}_{mn} \cos(2\omega_0 t_2 + \phi^{(2)}_{mn}(\omega_1, \omega_3)) + \ldots \Big]. \end{aligned} \tag{3.9}$$

Here A^{p}_{mn}, A^{c}_{mn}, A^{cc}_{mn}, etc. are the orientationally averaged prefactors (amplitudes) of different diagrams, contributing to the "A_{mn}" peak. We will restrict ourselves to the analysis of vibrational coherences for the system and consider excitation evolutions that include transitions only between the first two lowest energy levels of the excited and ground state. The only possible coherences in the 2D spectrum are then due to the harmonic oscillator frequency ω_0 and the expansion of different harmonics of coherent beatings in Eq. (3.9) can be truncated down to 2 terms:

$$\begin{aligned} W(\omega_3, t_2, \omega_1) = {} & \mathrm{e}^{-\gamma_2 t_2} \overline{\sum}_{m,n} L_{mn}(\omega_1, \omega_3) \\ & \times \Big[A^{\mathrm{p}}_{mn} + A^{\mathrm{c}}_{mn} \cos(\omega_0 t_2 + \phi_{mn}(\omega_1, \omega_3)) \Big]. \end{aligned} \tag{3.10}$$

As it follows from Eq. (2.113), the phase factor $\phi_{mn}(\omega_1, \omega_3)$ is zero at the peak center. Then, the relative A_{ij} peak oscillation phase is solely determined by the coefficient A^{c}_{mn}.

In order to get the full picture of oscillations in the 2D spectrum of the displaced

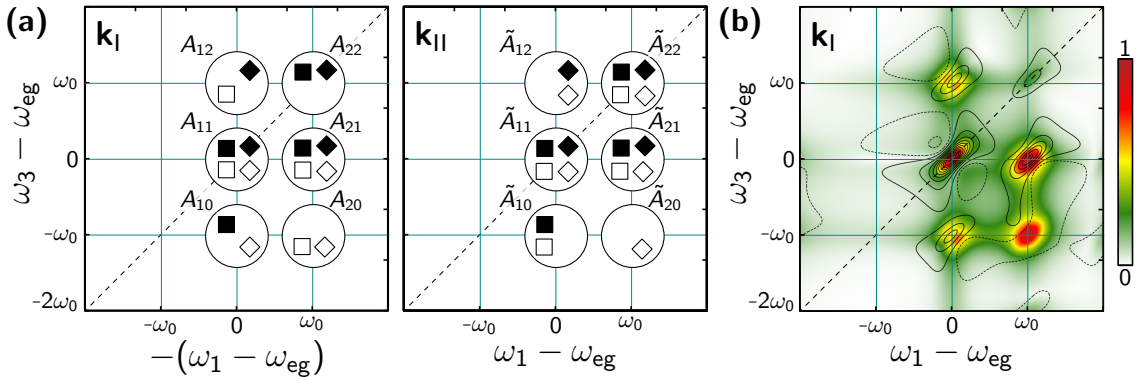

Fig. 3.4. (a) Scheme of contributions to the 2D spectrum of the $\boldsymbol{k}_\mathrm{I}$ and $\boldsymbol{k}_\mathrm{II}$ signals for the displaced oscillator ($\diamond$ – GSB, $\square$ – SE). Full symbols denote non-oscillating contributions in t_2, open symbols – oscillatory in the form of $\pm\cos(\omega_0 t_2)$. **(b)** The coherence map ($\mathbf{k}_\mathrm{I}$ signal) at frequency $\omega_2 = \omega_0$.

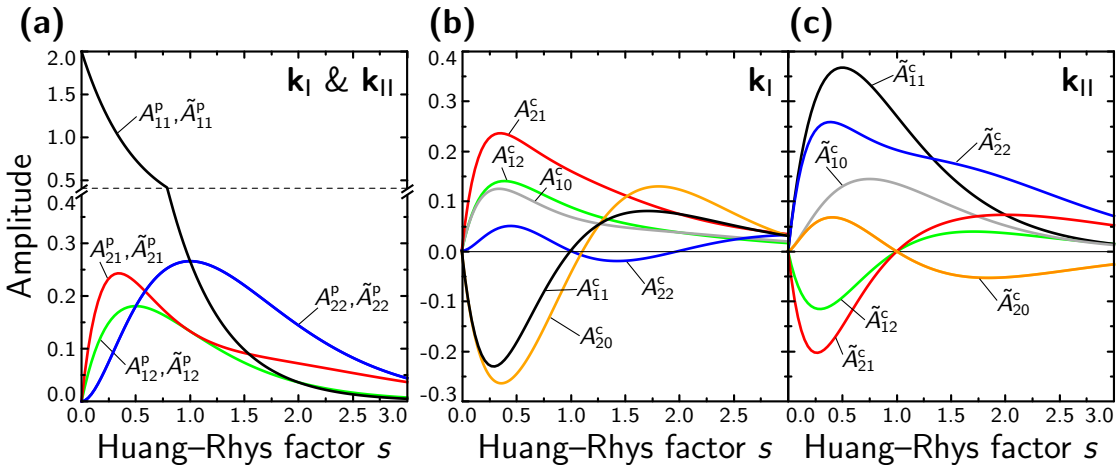

Fig. 3.5. The amplitudes of oscillatory peaks of 2D spectra of the DO model for $\mathbf{k}_\mathrm{I}$ and $\mathbf{k}_\mathrm{II}$ signals. Note that the negative amplitude denotes a phase shift of π of the oscillations. Refer to Appendix B for the analytic expressions of these dependencies.

harmonic oscillator, we have to go through all the double-sided Feynman diagrams, that give coherent contributions of frequency $\omega_2 = \omega_0$ during the waiting time t_2, and assign them to the corresponding peaks in the spectrum. Such a picture is given in Fig. 3.4a for the $\mathbf{k}_\mathrm{I}$ and $\mathbf{k}_\mathrm{II}$ signals. If compared to an analogous scheme for the ED system in Fig. 2.13, it is evident, that the DO system has many more oscillatory contributions in the 2D spectrum. We can show, that the coefficients A^c_{mn} can be expressed via the products of transition dipole moments of various diagrams and, evidently, depend on the Huang–Rhys factor.[46] The analytic expressions of A^c_{mn} and A^p_{mn} for the DO system are derived in Appendix B and their dependencies on the Huang–Rhys factor s are plotted in Fig. 3.5a-c. For the $\mathbf{k}_\mathrm{I}$ signal, the amplitudes A^c_{11} and A^c_{22} maintain the opposite sign when $s < 2$ and are both positive when $2 < s < 3$ (note that $A^\mathrm{c}_{22} = 0$ when only two

vibrational levels are considered). The oscillation amplitudes A^{c}_{11} and A^{c}_{22} change sign at $s = 1$, and both A^{c}_{12} and A^{c}_{21} are always positive. Quantum beatings with t_2 for both diagonal peaks in the $\boldsymbol{k}_{II}$ signal will be in-phase for the whole range of the HR factor. The same pattern holds for the A_{12} and A_{21} cross-peaks, which will oscillate in-phase, but will be of the opposite phase compared to the diagonal peaks in the region of $s < 1$. Note that the sign of the amplitudes changes with the Huang–Rhys factor, since the overlap integral between vibrational wavefunctions can be both positive and negative. The amplitudes of the static contributions are positive in the whole range of parameters and are identical for both $\mathbf{k}_{I}$ and $\mathbf{k}_{II}$ signals.

Contrary to the studied case, the transition dipole properties of the ED result in the picture where all the static amplitudes of the ED are positive and $A^{p}_{11} = \widetilde{A}^{p}_{11}$, $A^{p}_{22} = \widetilde{A}^{p}_{22}$, $A^{p}_{12} = A^{p}_{21} = \widetilde{A}^{p}_{21} = \widetilde{A}^{p}_{12}$ (see Appendix A for analytical expressions of the coefficients). The oscillatory amplitudes are equal: $A^{c}_{12} = A^{c}_{21} = \widetilde{A}^{c}_{11} = \widetilde{A}^{c}_{22}$. The spectral beats with t_2 can thus only have the same phases in the $\mathbf{k}_{I}$ or $\mathbf{k}_{II}$ spectrum, when measured at peak centers. As these relationships do not depend on coupling J and the transition dipole orientations, all ED systems should behave similarly. This property can also be proven to hold for hetero-dimers.

We thus find a very different behavior of oscillatory peaks of the DO and ED systems. The above analysis applies for the central positions of the peaks, which may be difficult to determine if the broadening is large. The phase ϕ varies from $-\pi/2$ to $+\pi/2$ (Eq. (2.111) and Fig. 2.12c) when probing in the vicinity of the peak. However, $\phi = 0$ along the diagonal line for $\mathbf{k}_{I}$ and along the anti-diagonal line for $\mathbf{k}_{II}$. These lines can thus be used as guidelines for reading phase relations of distinct peaks in the 2D spectrum. For instance, the two diagonal peaks can be calibrated by reading their amplitudes at the diagonal line, or the two opposite cross-peaks can be compared by drawing anti-diagonal lines.

The up-to-date experiments are capable of creating broad-band pulses. Thus, the overtones in DO can be excited and beats of $k\omega_0$ frequencies (k is integer) observed. This may become important in the case of large HR factors. Such frequencies are absent in the spectrum of ED. In the case of the finite pulses the pulse overlap region may affect the phase of the oscillatory components in the 2D spectrum. This effect should be considered when the pulse bandwidth is comparable to the system absorption spectrum.

Thus, the analysis presented in this section provides a clear physical picture of electronic and vibrational coherence beatings in the 2D spectra. Based on our simulations, the following conclusions can be drawn:

1. Dynamics of the diagonal peaks and cross-peaks as well as relative phases

between them in the rephasing signal can be classified for vibrational and excitonic systems as follows. (i) Static diagonal peaks and oscillatory off-diagonal peaks signify pure electronic coherences, not involved in energy transport. (ii) Oscillatory diagonal peaks in accord with off-diagonal peaks (0 or π phase relationships) signify vibrational origins.

2. The oscillation phase is 0 for electronic coherences and 0 or π for vibrational coherences. These outcomes hold if the signal is probed at the very center of the spectral resonance. The observed phase of the beatings varies as the signal value is recorded away from the center of an oscillating peak.

3. Consideration of high-frequency *damped* molecular vibrations instead of *undamped* is a more realistic description since it includes dephasing of vibronic motion in a solvent. This correction induces non-uniform peak broadening, changes the position of peaks within the vibrational progression in the absorption, and results in the decay of coherences in the 2D spectrum. The significance of the effect depends on the width of the spectral density function in the vicinity of the resonance. Therefore, having the coherence decay rate and the peak broadening quantitatively evaluated from the experiment, one would be able to estimate the damping parameters of vibrations.

4. The suggested model of the *overdamped quantum* bath is represented by the spectral density, which is directly obtained from the quantum-mechanical correlation function of bath coordinates without invoking the classical correlation function as in the *overdamped semi-classical* bath model. The spectral density of the overdamped quantum bath decays as ω^{-3} at large frequencies, which is preferable to ω^{-1} used in the overdamped semi-classical model. In two-dimensional photon echo signals, it results in increased homogeneous broadening of peaks. Dynamics of quantum beats are not affected by this spectral density; however, the peak intensities and the ratio of rephasing and nonrephasing signals does change.

5. Damping of vibrations causes the decay of beatings; its influence on the peak shape and correlation/anticorrelation of the diagonal peak width and intensity is reported to be insignificant compared to the description of undamped vibrations. Further increase of the damping strength results in instantaneous disappearance of the vibrational coherences and this limit corresponds to purely overdamped vibrational motion.

3.2 Vibrational aggregate model

In the previous chapter, we have introduced two different approaches for simulating the optical response of a molecule with vibrations. In Sec. 3.1.1 the bath was described by the spectral density function, which represented auto-correlations of the electronic site energy fluctuations due to the environment. This model is usually sufficient to obtain proper spectral lineshapes in simulations of uncoupled systems; vibrational modes can be introduced by adding a δ-shaped or finite-bandwidth peaks to the bath spectral density function. In Sec. 3.1.2 the vibrational content was included explicitly into the system Hamiltonian. For a single molecule these two approaches give identical results. However, the first method has two deficiencies when considering coupled molecules. Firstly, it neglects the effects caused by the quantum-mechanical mixing of the vibronic levels of different molecules. Secondly, it does not include vibrational population relaxation as the vibrations are assumed to be in the thermal equilibrium at fixed temperature. These effects could be important if the coupling to vibrations is strong or the vibronic splitting is comparable to the intermolecular excitonic coupling.

Thus, let us develop a general description applicable for molecular aggregates with an arbitrary number of chromophores. We start with the displaced oscillator model of a molecule, introduced in the previous section. The Hamiltonian of an aggregate of realistic molecules then involves three components: electronic states, vibrational structure for each electronic state and the Coulomb coupling between all electronic and vibronic levels. The first two are described by extending the Hamiltonian of a single molecule into the space of a set of molecules and invoking the Heitler–London approximation, which assumes that the aggregate states are constructed from the direct products of the molecular single excitations.[5] Such a Hamiltonian is known as the the Holstein-type electronic–vibrational Hamiltonian.[9,182,183] We consider only manifolds of singly and doubly-excited states. The Coulomb coupling between the m-th and n-th molecule is denoted by the resonance electronic coupling constant J_{mn} and the corresponding term is as follows:

$$\widehat{H}_{\text{Coulomb}} = \sum_{m \neq n} J_{mn} \widehat{B}_m^\dagger \widehat{B}_n. \tag{3.11}$$

We neglect electrostatic interactions between vibrations in the ground state. Within this model, the Hamiltonian for vibrational aggregate (VA) is given by

$$\begin{aligned} \widehat{H}_{\text{VA}} = &\sum_m \left[\epsilon_m + \delta\epsilon_m + \lambda_m - \omega_m \sqrt{s_m} \left(\widehat{a}_m^\dagger + \widehat{a}_m \right) \right] \widehat{B}_m^\dagger \widehat{B}_m \\ &+ \sum_m \omega_m \left(\widehat{a}_m^\dagger \widehat{a}_m + \frac{1}{2} \right) + \sum_{m \neq n} J_{mn} \widehat{B}_m^\dagger \widehat{B}_n. \end{aligned} \tag{3.12}$$

Here ϵ_m is the energy, ω_m is the vibrational frequency, d_m is the displacement in the excited state of the m-th molecule. $\delta\epsilon_m$ is the random excitation energy offset, which will be used later (in Sec. 3.3.3) to incorporate the static disorder of monomeric site energies. For now, we will keep it equal to zero. The reorganization energy is

$$\lambda_m = \frac{\omega_m^2 d_m^2}{2} = \omega_m s_m, \tag{3.13}$$

where s_m is the Huang–Rhys factor of the m-th molecule. Similarly to the electronic aggregate, we get bands corresponding to electronic states, but now the ground state $|\mathrm{g}\rangle$ of the aggregate is not a single quantum level, but a band of vibrational states. Thus, there are states with all chromophores in their electronic ground states, while vibrational excitations are arbitrary:

$$|\mathrm{g}_{(i_1 i_2 \ldots i_N)}\rangle \equiv |\prod_m \mathrm{g}_{i_m}^m\rangle = \left[\prod_m \frac{\left(\widehat{a}_m^\dagger\right)^{i_m}}{\sqrt{i_m!}}\right]|0\rangle. \tag{3.14}$$

Here i_m is a quantum number of a vibrational excitation of the m-th molecule and $|\mathrm{g}_{i_m}^m\rangle$ denotes the electronic ground state of the m-th molecule being in the i_m-th vibrational level.

The singly-excited states are obtained by promoting one of the molecules into its electronic excited state, while the other molecules are in their electronic ground states (vibrational states are arbitrary). We thus get the set of states

$$|\mathrm{e}_{n,(i_1 i_2 \ldots i_N)}\rangle \equiv |\mathrm{e}_{i_n}^n \prod_{\substack{m \\ m\neq n}} \mathrm{g}_{i_m}^m\rangle = \widehat{B}_n^\dagger \left[\prod_m \frac{\left(\widehat{a}_m^\dagger\right)^{i_m}}{\sqrt{i_m!}}\right]|0\rangle. \tag{3.15}$$

The doubly-excited states are obtained similarly,

$$|\mathrm{f}_{kl,(i_1 i_2 \ldots i_N)}\rangle \equiv |\mathrm{e}_{i_k}^k \mathrm{e}_{i_l}^l \prod_{\substack{m \\ m\neq k,l}} \mathrm{g}_{i_m}^m\rangle = \widehat{B}_k^\dagger \widehat{B}_l^\dagger \left[\prod_m \frac{\left(\widehat{a}_m^\dagger\right)^{i_m}}{\sqrt{i_m!}}\right]|0\rangle. \tag{3.16}$$

State ordering $k < l$ is satisfied here.

The proper set of molecular, or site, basis states for the Hamiltonian of the vibrational aggregate is crucial for an accurate treatment of the dynamics of the vibronic excitons. The simplest choice is the so-called one-particle states,[3] sometimes also referred to as coherent exciton scattering approximation.[184] It assumes only states, that account for one vibronically excited molecule leaving all other in their vibrationally unexcited electronic ground states. The two-particle approximation (TPA) of the vibronic states includes the fact that the unexcited molecule can be in an arbitrary vibrational ground state. Thus, the two-particle basis set for the

vibrational aggregate consists of NN_{v}^2 states (here N_{v} accounts for vibrational levels in each ground and excited state potentials and N is the number of molecules in VA). In the case of the one-particle approximation, the basis set size is NN_{v}, which is a great simplification, allowing to significantly reduce the computational cost.[185] Therefore, the one-particle description is a common choice in calculations of spectroscopic signals of vibronically-coupled systems.[23,26,186] Qualitative comparison between various such approximations was discussed by considering linear response in the molecular aggregates by Spano[185] and a model dimer by Schultze et al.[187] The detailed analysis, whether this approximation is proper for the nonlinear response of small molecules, was performed by Bašinskaitė et al.[179] It was shown that for a vibrational dimer, one-particle approximation is too crude to represent the coherent signatures of vibrational and mixed states. Therefore, here we use the complete basis in the model and consider all possible combinations (multi-particle states) of electronic and vibrational excitations.

We simplify the index notation by introducing the N-component vector $\mathbf{i} = (i_1 i_3 ... i_N)$. The basis states can then be written as $|\mathrm{g}_{\mathbf{i}}\rangle$, $|\mathrm{e}_{n,\mathbf{i}}\rangle$ and $|\mathrm{f}_{kl,\mathbf{i}}\rangle$. In the given setup, electronic and vibrational subsystems are coupled only through the term $\left(\widehat{a}_m^\dagger + \widehat{a}_m\right)\widehat{B}_m^\dagger \widehat{B}_m$ in the Hamiltonian (Eq. (3.12)). It thus induces the shifts of electronic energies by creation or annihilation of a vibrational quantum. Otherwise, electronic and vibrational subsystems are independent. The basis set is chosen accordingly. The other basis set is possible by using the shifted vibrational coordinates in the electronic excited states.[179,186,188] However, our approach gives a convenient form for various matrix elements and allows us to easily incorporate the environment as shown below.

The Hamiltonian of the ground state manifold in this basis is diagonal, yielding its matrix elements

$$H_{\mathbf{i},\mathbf{j}}^{(\mathrm{gg})} = \left[\sum_m \omega_m \left(i_m + \frac{1}{2}\right)\right]\delta_{\mathbf{ij}}, \tag{3.17}$$

where $\delta_{\mathbf{ij}} \equiv \prod_m \delta_{i_m j_m}$. Similarly, the Hamiltonian of the singly-excited states is given by

$$\begin{aligned} H_{\mathbf{i},\mathbf{j}}^{(\mathrm{e}_n\mathrm{e}_k)} = {} & \delta_{nk}\left[\epsilon_n + \lambda_n + \sum_m \omega_m \left(i_m + \frac{1}{2}\right)\right]\delta_{\mathbf{ij}} \\ & - \delta_{nk}\omega_n\sqrt{s_n}\langle i_n, j_n\rangle \prod_{\substack{m \\ m\neq n}} \delta_{i_m j_m} + (1-\delta_{nk})J_{nk}\delta_{\mathbf{ij}}, \end{aligned} \tag{3.18}$$

where we have defined the vibrational wavefunction overlap integral as

$$\langle i_n, j_n\rangle \equiv \langle i_n|(\widehat{a}_n^\dagger + \widehat{a}_n)|j_n\rangle = \sqrt{i_n}\delta_{i_n,j_n+1} + \sqrt{j_n}\delta_{i_n,j_n-1}. \tag{3.19}$$

For the doubly-excited states we have

$$
\begin{aligned}
H_{\mathbf{i},\mathbf{j}}^{(\mathsf{f}_{kl}\mathsf{f}_{k'l'})} &= \delta_{kk'}\delta_{ll'}\left[\epsilon_k + \epsilon_l + \lambda_k + \lambda_l + \sum_m \omega_m\left(i_m + \frac{1}{2}\right)\right]\delta_{\mathbf{ij}} \\
&- \delta_{kk'}\delta_{ll'}\omega_k\sqrt{s_k}\langle i_k, j_k\rangle \prod_{\substack{m \\ m\neq k}} \delta_{i_m j_m} + \delta_{kk'}\delta_{ll'}\omega_l\sqrt{s_l}\langle i_l, j_l\rangle \prod_{\substack{m \\ m\neq l}} \delta_{i_m j_m} \\
&+ \left[\delta_{kk'}(1-\delta_{ll'})J_{ll'} + \delta_{ll'}(1-\delta_{kk'})J_{kk'}\right]\delta_{\mathbf{ij}}.
\end{aligned}
\tag{3.20}
$$

The exciton energies (in the eigenstate basis) ε_{e} and ε_{f} are obtained by numerically diagonalizing the matrices defined above. The bands of singly- and doubly-excited states are, however, much more complicated than those of the electronic aggregate due to the coupling between the singly-excited vibronic subbands. In the eigenstate basis all these substates become mixed. The unitary transformation to the eigenstate basis is

$$
|\mathsf{e}_p\rangle = \sum_n \sum_{\mathbf{i}} \psi_{p,\mathbf{i}}^n |\mathsf{e}_{n,\mathbf{i}}\rangle, \tag{3.21}
$$

$$
|\mathsf{f}_r\rangle = \sum_{\substack{kl \\ k<l}} \sum_{\mathbf{i}} \Psi_{r,\mathbf{i}}^{kl} |\mathsf{f}_{kl,\mathbf{i}}\rangle. \tag{3.22}
$$

Note that for high vibronic numbers i, j the Franck–Condon parameter becomes small and these states do not contribute to the spectra. In general, this results in NN_{v}^N singly-excited states and $N(N-1)N_{\mathsf{v}}^N/2$ doubly-excited states, enumerated by indices p and r in the previous expressions, respectively.

For electronic excitations we consider the dipole operator defined by Eq. (2.42):

$$
\widehat{\boldsymbol{\mu}} = \sum_m^N \boldsymbol{\mu}_m \left(\widehat{B}_m^\dagger + \widehat{B}_m\right). \tag{3.23}
$$

The dipole moments representing transitions from the ground state to the singly-excited states and from the singly-excited state to the doubly-excited states are given by

$$
\boldsymbol{\mu}_{\mathsf{g}_{\mathbf{i}}\mathsf{e}_p} = \langle \mathsf{g}_{\mathbf{i}}|\widehat{\boldsymbol{\mu}}|\mathsf{e}_p\rangle = \sum_m^N \boldsymbol{\mu}_m \psi_{p,\mathbf{i}}^m \tag{3.24}
$$

and

$$
\boldsymbol{\mu}_{\mathsf{e}_p\mathsf{f}_r} = \langle \mathsf{e}_p|\widehat{\boldsymbol{\mu}}|\mathsf{f}_r\rangle = \sum_{m,n}^N \sum_{\mathbf{i}} \boldsymbol{\mu}_k \psi_{p,\mathbf{i}}^n \Psi_{r,\mathbf{i}}^{(mn)}. \tag{3.25}
$$

The transition amplitudes thus have the mixed electronic–vibrational nature encoded in the eigenvectors $\psi_{p,\mathbf{i}}^n$ and $\Psi_{r,\mathbf{i}}^{(mn)}$.

Note, that in the Hamiltonian used, no transformation of canonical variables into symmetric and antisymmetric components is performed that would allow us to decouple the Schrödinger equations of the excited and ground states. Therefore, the presented model contains states which are not separated into diabatic or adiabatic ones.

3.2.1 Coupling to the bath

We next include the relaxation using the microscopic dephasing theory, based on the model of linear coupling to the harmonic overdamped bath, described in Sec. 2.2 for a general multi-level system. The system–bath interaction is given in the bilinear form

$$\widehat{H}_{\mathrm{SB}} = \sum_{m\alpha} z_{m\alpha}\widehat{x}_{\alpha}\widehat{q}_{m} + \sum_{m\alpha}\sqrt{2w_{\alpha}}d_{mm,\alpha}\widehat{x}_{\alpha}\widehat{B}_{m}^{\dagger}\widehat{B}_{m}. \tag{3.26}$$

We add the bath and the system–bath interaction Hamiltonians to complete the vibrational aggregate Hamiltonian in Eq. (3.12). From the SB interaction Hamiltonian it immediately follows, that coupling z (the first term in Eq. (3.26)) induces the vibronic off-diagonal couplings and causes intramolecular vibrational population relaxation. Resonance intermolecular interaction J will extend the relaxation into the electronic energy transfer between different molecules. The second term in Eq. (3.26) describes the coupling of the electronic excitation to the bath coordinates via coupling constant $d_{mm,\alpha}$ and results in diagonal fluctuations. Energy fluctuations are treated as identical for each chromophore and, yet, uncorrelated with respect to each other. The non-zero fluctuating matrix elements in the site basis (eqs. (3.14)–(3.16)) are then very simple:

$$\left(\widehat{H}_{\mathrm{SB}}\right)_{\mathbf{i},\mathbf{j}}^{(\mathrm{gg})} = \langle \mathrm{g}_{\mathbf{i}}|\widehat{H}_{\mathrm{SB}}|\mathrm{g}_{\mathbf{j}}\rangle = \mathcal{H}(\mathbf{i},\mathbf{j}), \tag{3.27a}$$

$$\left(\widehat{H}_{\mathrm{SB}}\right)_{\mathbf{i},\mathbf{j}}^{(\mathrm{e}_k\mathrm{e}_l)} = \langle \mathrm{e}_{k,\mathbf{i}}|\widehat{H}_{\mathrm{SB}}|\mathrm{e}_{l,\mathbf{j}}\rangle = \delta_{kl}\left[\mathcal{H}(\mathbf{i},\mathbf{j}) + \mathcal{K}_k(\mathbf{i},\mathbf{j})\right], \tag{3.27b}$$

$$\left(\widehat{H}_{\mathrm{SB}}\right)_{\mathbf{i},\mathbf{j}}^{(\mathrm{f}_{kl}\mathrm{f}_{k'l'})} = \langle \mathrm{f}_{kl,\mathbf{i}}|\widehat{H}_{\mathrm{SB}}|\mathrm{f}_{k'l',\mathbf{j}}\rangle = \delta_{kk'}\delta_{ll'}\left[\mathcal{H}(\mathbf{i},\mathbf{j}) + \mathcal{K}_k(\mathbf{i},\mathbf{j}) + \mathcal{K}_l(\mathbf{i},\mathbf{j})\right]. \tag{3.27c}$$

Here, we defined the auxiliary operators of the bath–space fluctuations

$$\mathcal{H}(\mathbf{i},\mathbf{j}) = \sum_{m\alpha}\sqrt{\frac{z_{m\alpha}^2}{2\omega_m}}\langle i_m, j_m\rangle\widehat{x}_{\alpha}\prod_{\substack{s\\ s\neq m}}^{N}\delta_{i_s j_s} \tag{3.28}$$

and

$$\mathcal{K}_k(\mathbf{i},\mathbf{j}) = \sum_{\alpha}\sqrt{2w_{\alpha}}d_{kk,\alpha}\widehat{x}_{\alpha}\delta_{\mathbf{ij}}. \tag{3.29}$$

Notice that interband fluctuations are absent, so the interband relaxation (electronic relaxation to the ground state) is not included. Transformation to the eigenstate basis yields the characteristics of the eigenstate fluctuations. In the ground state manifold we have eigenstates equivalent to the site basis since the corresponding Hamiltonian is diagonal (Eq. (3.17)). For the manifold of the singly-excited states we get

$$\left(\widehat{H}_{\mathrm{SB}}\right)^{(\mathrm{ee})}_{p_1 p_2} = \sum_{m}^{N} \sum_{\mathbf{i},\mathbf{j}} \psi^{m*}_{p_1,\mathbf{i}} \psi^{m}_{p_2,\mathbf{j}} \left[\mathcal{H}(\mathbf{i},\mathbf{j}) + \mathcal{K}_k(\mathbf{i},\mathbf{j})\right], \tag{3.30}$$

and for the manifold of the doubly-excited states

$$\left(\widehat{H}_{\mathrm{SB}}\right)^{(\mathrm{ff})}_{r_1 r_2} = \sum_{\substack{m,n \\ m>n}}^{N} \sum_{\mathbf{i},\mathbf{j}} \Psi^{(mn)*}_{r_1,\mathbf{i}} \Psi^{(mn)}_{r_2,\mathbf{j}} \left[\mathcal{H}(\mathbf{i},\mathbf{j}) + \mathcal{K}_k(\mathbf{i},\mathbf{j}) + \mathcal{K}_l(\mathbf{i},\mathbf{j})\right]. \tag{3.31}$$

The quantities of interest, which describe the relaxation properties, are the correlation functions of fluctuating Hamiltonian elements. Firstly, we assume that fluctuations of different chromophores are independent. Therefore, we can sort out and assign the bath coordinates to the specific molecules. Since the bath oscillators are independent, correlation functions of the fluctuating operators in the Heisenberg representation with respect to the thermal equilibrium are uncorrelated, i. e.,

$$\langle \widehat{x}_\alpha(t)\widehat{x}_\beta(0)\rangle = \delta_{\alpha\beta}\langle \widehat{x}_\alpha(t)\widehat{x}_\alpha(0)\rangle. \tag{3.32}$$

Secondly, we assume that the energy fluctuations of different molecules are uncorrelated, but the molecules have statistically the same surroundings. The fluctuation correlation function can be introduced, representing vibrational off-diagonal fluctuations:

$$C_0(t) = \sum_{m\alpha} \frac{z^2_{m\alpha}}{2\omega_m} \langle \widehat{x}_\alpha(t)\widehat{x}_\alpha(0)\rangle. \tag{3.33}$$

For the infinite number of bath oscillators they can be conveniently expressed using the spectral density $\mathcal{C}''(\omega)$:[69]

$$C_0(t) = \frac{1}{\pi} \int_{-\infty}^{+\infty} \frac{1}{1 - \mathrm{e}^{-\beta\omega}} \mathrm{e}^{-\mathrm{i}\omega t} \mathcal{C}''(\omega) \mathrm{d}\omega. \tag{3.34}$$

Using these functions we get the eigenstate fluctuation correlation functions $C_{ab,cd}(t) = \langle \left(\widehat{H}_{\mathrm{SB}}(t)\right)_{ab} \left(\widehat{H}_{\mathrm{SB}}\right)_{cd} \rangle = C_0(t) h_{ab,cd}$ for different manifolds, where $h_{ab,cd}$ is the so-called lineshape broadening coefficient. For the electronic ground state manifold where a single eigenstate is equivalent to the original basis state

$|\mathrm{g}_{\mathbf{i}}\rangle$, it yields

$$C^{(\mathrm{gg})}_{\mathbf{ij},\boldsymbol{kl}}(t) = C_0(t)\sum_{m}^{N}\langle i_m, j_m\rangle\langle k_m, l_m\rangle \prod_{\substack{s\\ s\neq m}}^{N}\delta_{i_s j_s}\delta_{k_s l_s}. \tag{3.35}$$

We use the shorthand vector notations $\mathbf{i}_s^- = (i_1, i_2, ..., i_{s-1}, i_s - 1, i_{s+1}, ..., i_N)$ and $\mathbf{i}_s^+ = (i_1, i_2, ..., i_{s-1}, i_s + 1, i_{s+1}, ..., i_N)$, which allow us to explicitly write:

$$\begin{aligned} C^{(\mathrm{gg})}_{\mathbf{ij},\boldsymbol{kl}}(t) = C_0(t)\sum_{s}^{N}\Big\{&\sqrt{i_s j_s}\,\delta_{\mathbf{ij}_s^+}\delta_{\mathbf{kl}_s^+} + \sqrt{(i_s+1)j_s}\,\delta_{\mathbf{i}_s^+\mathbf{j}}\delta_{\mathbf{kl}_s^+} \\ &+ \sqrt{i_s(k_s+1)}\,\delta_{\mathbf{ij}_s^+}\delta_{\mathbf{k}_s^+\mathbf{l}} + \sqrt{(i_s+1)(k_s+1)}\,\delta_{\mathbf{i}_s^+\mathbf{j}}\delta_{\mathbf{k}_s^+\mathbf{l}}\Big\}. \end{aligned} \tag{3.36}$$

Similarly, one can obtain the correlation functions involving the singly- and doubly-excited states: $C^{(\mathrm{ee})}_{p_1p_2,p_3p_4}(t)$, $C^{(\mathrm{ef})}_{p_1p_2,r_1r_2}(t)$ and $C^{(\mathrm{ff})}_{r_1r_2,r_3r_4}(t)$ (see Appendix C for the corresponding expressions).

3.2.2 Excitation transfer

As the bath induces off-diagonal fluctuations in all three bands of states, one has to consider the population relaxation and excitation transfer inside the excited and ground state manifolds (the populations of the doubly-excited states are never created so the transport is not relevant there). In this model, the bath is considered as the intermolecular modes which should be Markovian while intramolecular vibrational coordinates are considered explicitly. Hence, the Redfield theory applies for the Markovian bath. Within the secular Redfield theory,[8] both types of propagators satisfy the Pauli master equation (Eq. (2.80)).

Using the secular Redfield relaxation theory, one can obtain simple expressions for the excited state population transfer rates:

$$K_{\mathrm{e}_{p_2}\mathrm{e}_{p_1}} = h_{\mathrm{e}_{p_2}\mathrm{e}_{p_1},\mathrm{e}_{p_1}\mathrm{e}_{p_2}}\mathcal{C}''\left(\omega_{\mathrm{e}_{p_1}\mathrm{e}_{p_2}}\right)\left[\coth\left(\frac{\beta\omega_{\mathrm{e}_{p_1}\mathrm{e}_{p_2}}}{2}\right)+1\right]. \tag{3.37}$$

See Appendix C for $h_{\mathrm{e}_{p_2}\mathrm{e}_{p_1},\mathrm{e}_{p_1}\mathrm{e}_{p_2}}$. For the ground state vibrational relaxation, one has only two subsets of nonzero terms:

$$K_{\mathrm{g}_{\mathbf{i}_s^-}\mathrm{g}_{\mathbf{i}}} = i_s\mathcal{C}''(\omega_s)\left[\coth\left(\frac{\beta\omega_s}{2}\right)+1\right] \tag{3.38}$$

and

$$K_{\mathrm{g}_{\mathbf{i}_s^+}\mathrm{g}_{\mathbf{i}}} = (i_s+1)\,\mathcal{C}''(-\omega_s)\left[\coth\left(-\frac{\beta\omega_s}{2}\right)+1\right]. \tag{3.39}$$

With these expressions now it is possible to obtain the Green's functions $G_{\mathrm{e}_{p_2}\mathrm{e}_{p_1}}(t)$

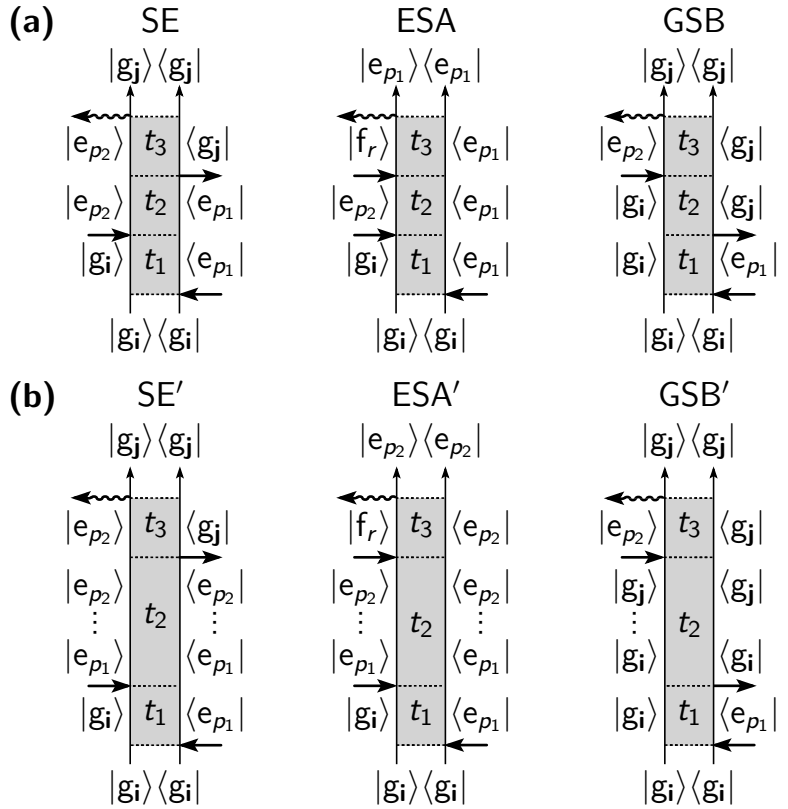

Fig. 3.6. System response function of the rephasing signal of the vibrational aggregate is represented by coherent **(a)** and population transfer **(b)** double-sided Feynman diagrams.

and $G_{g_j g_i}(t)$ for the description of relaxation, and develop the general theory describing the spectroscopic properties of vibronic aggregates.

In Section 2.2.4, the system response function of an electronic-only aggregate was obtained as a sum of response functions, visualized by using the double-sided Feynman diagrams, representing ESA, SE and GSB contributions. In these diagrams (Fig. 2.8), ground- or excited-state populations or coherences evolve during delay time t_2. Additionally, the population transfer pathways ESA′ and SE′ were added up since population state can be transferred during t_2 in the excited state. In the case of vibrational aggregate, this formalism has to be extended to take into account the multi-level electronic ground state. Therefore, additional diagrams with coherences and population transfer in the ground-state manifold have to be included (Fig. 3.6). The following derivation of the response function for the 2D ES is presented in Appendix D.

3.3 Vibrational dimer

To discuss the outcomes of the developed system response function theory for the vibrational aggregate, we consider a vibrational dimer as the simplest molecular

complex exhibiting the vibronic phenomena, as well as the electronic–vibrational interference. Using the notation introduced in eqs. (3.14)–(3.16), we denote the electronic ground state as the state where both molecules are in their ground states with arbitrary vibrational excitations, $|\mathrm{g}_{(ij)}\rangle$. Here indices i and j indicate vibrational excitation of the first and the second molecule, respectively. $|\mathrm{e}_{1,(ij)}\rangle$ denotes the state of the first molecule being in the vibronic excited state maintaining the i-th vibration quantum and the second molecule being in the j-th vibrational ground state; analogously, $|\mathrm{e}_{2,(ij)}\rangle$ corresponds to the state where the second molecule is vibronically excited. Doubly-excited states $|\mathrm{f}_{(ij)}\rangle \equiv \left|\mathrm{f}_{11,(ij)}\right\rangle$ are constructed in a similar way. In terms of these definitions the vibronic set of eigenstates for the singly- and doubly-excited states (state vectors $|\mathrm{e}_p\rangle$ and $|\mathrm{f}_r\rangle$, correspondingly) can be obtained by using the relevant transformations defined by eqs. (3.21) and (3.22):

$$|\mathrm{e}_p\rangle = \sum_{ij} \left(\psi^{(1)}_{p,(ij)} |\mathrm{e}_{1,(ij)}\rangle + \psi^{(2)}_{p,(ij)} |\mathrm{e}_{2,(ij)}\rangle \right), \tag{3.40}$$

$$|\mathrm{f}_r\rangle = \sum_{ij} \Psi_{r,(ij)} |\mathrm{f}_{(ij)}\rangle. \tag{3.41}$$

The corresponding transformation coefficients $\psi^{(n)}_{p,(ij)}$ and $\Psi_{r,(ij)}$ are acquired from the diagonalization of the singly-excited and doubly-excited blocks of the Hamiltonian. The transition dipole moments can then be calculated using eqs. (3.24) and (3.25).

For the demonstrational purposes, the vibrational frequencies, site energies and Huang–Rhys factors of the constituent molecules are taken to be the same and are denoted by $\omega_0 \equiv \omega_1 = \omega_2$, $\epsilon \equiv \epsilon_1 = \epsilon_2 = 12000\,\mathrm{cm}^{-1}$ and $s = s_1 = s_2$, respectively. Also, we analyze the models in the extreme cases of weak and strong system–bath coupling (with Huang–Rhys factor equal to $s = 0.05$ and $s = 0.5$). The Huang–Rhys factor at around $s = 0.05$ is typical for many photosynthetic pigment–protein (P–P) complexes, while in dye molecules, large organic oligomers (for example, J-aggregates) or films it can reach $s = 0.3$–1.0 or more.[189–191]

Four distinct parameter sets are used and we denote the corresponding models as **D1**-**D4**. The motivation of our choice is reflected in Fig. 3.7, where the range of recently experimentally and theoretically investigated systems is represented as points on a schematic two-dimensional phase space with the axes indicating vibrational frequency and electronic resonance interaction constant. The points (systems) can be classified by considering the possible time-resolved experiment with ultra-short laser pulses of typical bandwidth of $\sim 1000 - 2000\ \mathrm{cm}^{-1}$. In the upper–left corner of the figure we then have the weakly-coupled systems with high-frequency vibrations. In this case the experiment would resolve a few peaks of the

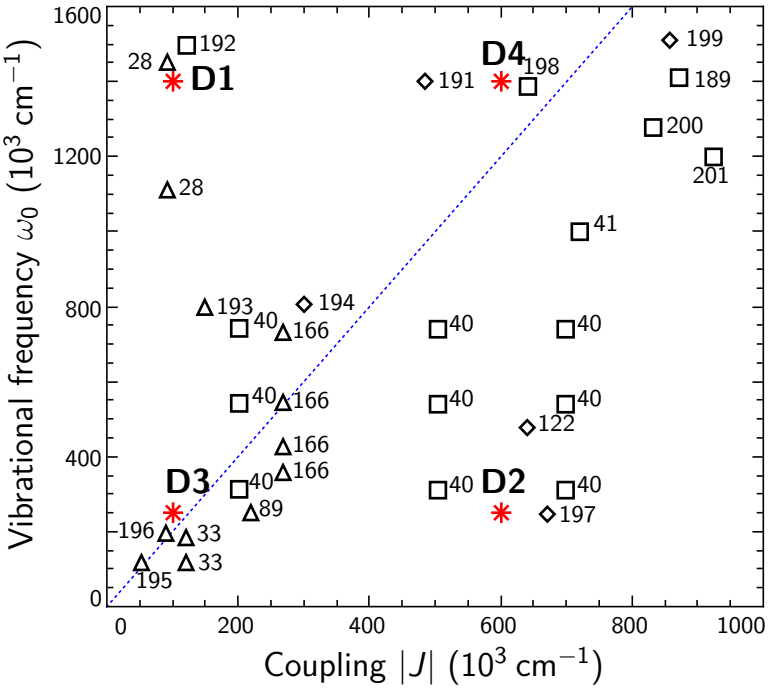

Fig. 3.7. Recently experimentally and theoretically investigated molecular systems (□ – dimeric dyes, △ – weakly-coupled P–P complexes, ◇ – J-aggregates and films), characterized by different electronic resonance coupling constants J and vibrational frequencies ω_0. Dashed line indicates the region of possible electronic–vibrational resonance ($\omega_0 = 2J$). The numbers next to symbols are the references to the corresponding studies. Parameters of model dimer systems **D1**–**D4** considered in Section 3.3 are indicated by asterisks.

vibrational progression at most and the splittings due to electronic coupling would be overlapping. The mixed case, where electronic resonance interactions and vibronic progression would be resolvable along with strong quantum–mechanical mixing of both types of transitions, is present in the upper–right part of the scheme. The laser spectrum would cover only a few peaks in this case. On the lower–left corner we have the mixed systems again, but the laser pulse spectrum could cover all peaks. And, finally, on the lower–right corner we have the case where the full vibrational progression could be observed in the experiment and the electronic splitting should be well-separated.

Thus, the two from our selected parameter sets are considerably away from the electronic–vibrational resonance (**D1** and **D2**) and another two corresponding to mixed conditions (**D3** and **D4**). As one can observe, these models represent four typical molecular systems: weakly-coupled P–P complex with high- and low-frequency vibrations (**D1** and **D3**), the J-aggregate (**D2**) and molecular dye (**D4**). By studying features and peak patterns of the 2D spectra of these systems we will be able to determine separation or mixing of excitonic and vibrational coherences as well as to correlate these properties with coherence lifetimes. Therefore, the theory and the conclusions drawn from the results of these model systems is going

to be general in terms of its application to different molecular aggregates.

In the **D1** model the resonant coupling constant is taken to be $J = 100$ cm^{-1} and the vibrational frequency is chosen to be $\omega_0 = 1400$ cm^{-1}. Such parameters are typical for the photosynthetic P–P complexes, for example, the photosynthetic antenna of cryptophyte protein phycoerythrin 545 (the Huang–Rhys factor is 0.1).[28] We denote this model as the weakly-coupled P–P complex with high-frequency vibration.

In the **D2** model resonant coupling of $J = 600\,\text{cm}^{-1}$ and vibrational frequency $\omega_0 = 250\,\text{cm}^{-1}$ is used. These numbers are typical parameters of, e. g., J-aggregates, coupled to low-frequency intramolecular vibrations. For example, in 2D electronic spectra of PVA/C8O3 tubular J-aggregates, oscillations associated to the 160 cm^{-1} vibration is observed and the strongest coupling between the molecules is in a range of 640–1110 cm^{-1} as it was shown by Milota et al.[122] In the same study, the experimental coherence maps were obtained. In J-aggregates the coupling to vibrations for individual chromophores is known to decrease due to exciton delocalization.[185] It means that, if the aggregate is reduced to a dimer, the Huang–Rhys factor of the monomer should be multiplied by factor of $N/2$ where N is a number of chromophores in the aggregate in the case of complete state delocalization. Therefore, a very strong coupling to vibrations should be considered. In our case, **D2** model with $s = 0.5$ represents the features of a typical J-aggregate.

Parameters of the **D3** model ($J = 100\,\text{cm}^{-1}$, $\omega_0 = 250\,\text{cm}^{-1}$) are, as in the **D1** model, typical for the P–P complexes. However, strong coupling to discrete low-frequency vibrations is considered in the **D3**. For example, in the measurements of two-color photon echo of the light-harvesting complex phycocyanin-645 from cryptophyte marine algae, long-lived oscillations possibly associated to the $194\,\text{cm}^{-1}$ vibrational mode were observed.[196] Similar parameters were also considered to be relevant for the FMO photosynthetic light-harvesting complex.[23,29] Therefore, we assume that the **D3** model effectively represents the weakly-coupled P–P complex coupled to a low-frequency vibrational mode.

Presence of strong resonance electronic interaction between molecules and strong coupling with high-frequency vibrations is typical for many dimeric dyes. Hence, in the **D4** model, the main parameters are set to $J = 600\,\text{cm}^{-1}$ and $\omega_0 = 1400\,\text{cm}^{-1}$ to be similar to ones of perylene bisimide dye with the Huang–Rhys factor of 0.6.[202]

The bath, whose degrees of freedom are not treated explicitly, is represented by the Drude–Lorentz spectral density (Eq. (2.76)) which characterizes the low-frequency fluctuations. In order to get the similar homogeneous broadening in all cases of Huang–Rhys factors, the value of the reorganization energy $\lambda_s = 25\,\text{cm}^{-1}$

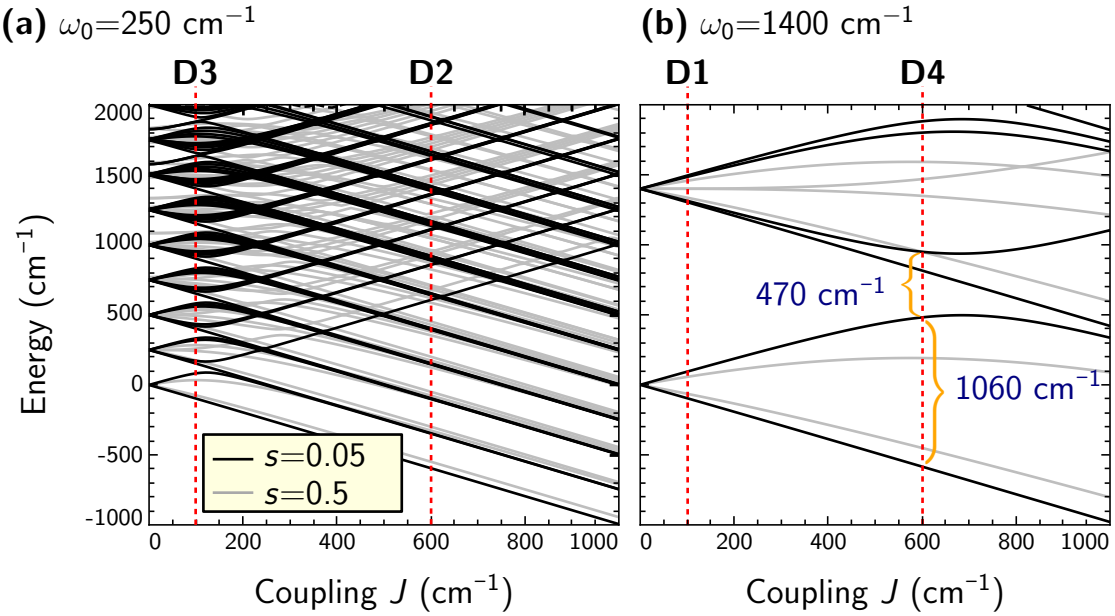

Fig. 3.8. Dependencies of the singly excited state energies on the electronic resonance interaction (J coupling) in the case of the vibrational frequency $\omega_0 = 250\,\mathrm{cm}^{-1}$ **(a)** and $1400\,\mathrm{cm}^{-1}$ **(b)**. The Huang–Rhys factor is $s = 0.05$ (black lines) and $s = 0.5$ (gray lines). Resonant coupling constants corresponding to models **D1–D4** are indicated by the red dashed vertical lines.

is kept constant throughout all simulations. The solvent relaxation rate is set to $\gamma = 50\ \mathrm{cm}^{-1}$. To enhance the effects of damped vibrations we set the site energy fluctuations off in simulations ($d_{mm,\alpha} = 0$). The damping then originates from the z part only (Eq. (3.26)). The molecular transition dipole vectors are taken to have unitary lengths and their orientations are spread by an angle $2\pi/5$. Temperature is set to 150 K ($\beta^{-1} \approx 104\,\mathrm{cm}^{-1}$).

Let us consider the manifold of singly-excited states of all **D1–D4** models. It consists of superpositions of electronic singly-excited states and vibrational excitations of the constituent molecules. The energy dependence on the resonant coupling constant reveals a complex composition of the states within the singly-excited state manifold (Fig. 3.8). For uncoupled molecules ($J = 0$) the ladder-type pattern of vibrational energy states is present as the energies are equally separated by ω_0. Increasing coupling produces the excitonic splitting which can be seen as the red shift of the lowest energy state and appearance of two ladder-type progressions. However, the intermolecular interaction induces repulsion of the energy levels, which is mostly evident where the ladders experience crossing, i. e., in the vicinity of the so-called avoided crossing regions.[179,186,203] We denote the corresponding parameters for which the crossings occur as the electronic–vibrational resonances. The complete mixing of the electronic and vibronic substates is obtained for these resonances. The energy level repulsion effect is more pronounced

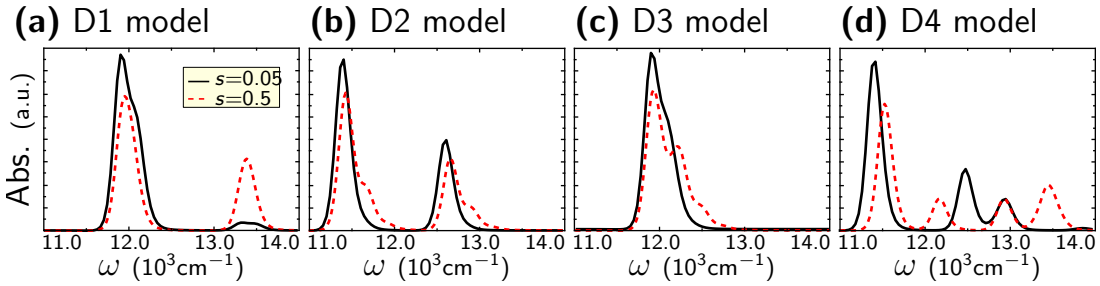

Fig. 3.9. Absorption spectra of dimers **D1**-**D4** in case of Huang–Rhys factors $s = 0.05$ (black solid line) and $s = 0.5$ (red dashed line).

in the case of $s = 0.5$ (see the gray lines in Fig. 3.8).

In models **D1** and **D2** the vibrational frequency ω_0 and resonant coupling constant J differs significantly and we are reasonably away from the resonances as can be seen in Fig. 3.8 (the corresponding resonant coupling values are indicated by vertical lines). Therefore, these models can be considered as rather pure systems. On the contrary, parameters of the **D3** and **D4** models assure that the system is very close to the electronic–vibrational resonances and the spectroscopic signals will be more complex due to mixing.[179]

Properties of the model dimers are reflected in the linear absorption spectra (Fig. 3.9). The **D1** system has intermolecular coupling of the same order as the absorption linewidth. Hence, both electronic transitions (and excitonic splitting) become hidden inside the single peak at $\sim$ 12000 cm^{-1} when the Huang–Rhys factor is $s = 0.05$. Another peak at $\sim$ 13500 cm^{-1} comes from the one-quantum level of the vibrational progression and becomes stronger for $s = 0.5$ (red dashed line).

The **D2** model is completely opposite to the **D1**. The excitonic splitting is large and two absorption peaks approximately at 11500 cm^{-1} and 12700 cm^{-1} show the excitonic system character. As the vibrational frequency is small, we find the vibrational progression on both excitonic lines dependent on the Huang–Rhys factor. The **D1** and **D2** systems, more or less, behave "additively" where the excitonic contributions and the vibrational progressions add up in the absorption.

Models **D3** and **D4** are very different from **D1** and **D2**. In the **D3**, both parameters, the resonance interaction and the vibrational frequency, are small and the absorption spectrum shows a single broad line at $\sim$ 12000 cm^{-1}. While excitonic and vibrational contributions are mixed, as shown in Fig. 3.8a, surprisingly, the absorption spectrum is relatively simple with a single electronic peak shaped by the vibrational progression. However the shape is strongly dependent on the Huang–Rhys factor: for $s = 0.05$, one can resolve two excitonic bands (black solid line), while for $s = 0.5$, the excitonic spectrum disappears and instead the vibrational progression is observed. Hence, the spectrum is more "electronic" for

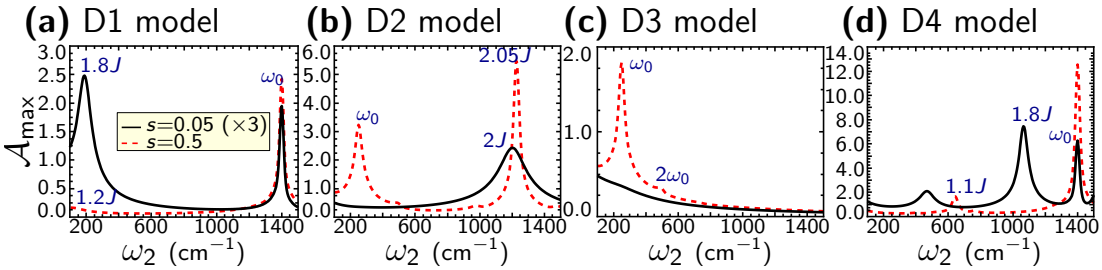

Fig. 3.10. Maximum of the coherence map characterizing oscillations in the 2D spectra of the model dimers D1–D4 (**a–d** panels, respectively) in case of Huang–Rhys factors $s = 0.05$ (black solid lines) and $s = 0.5$ (red dashed lines). The frequency values of the peaks are indicated in the graph.

small s and more "vibronic" for large s.

The fine features of mixed system are expected to be better observed in the model **D4**, which has large energy splittings between levels compared to the **D3**. Indeed, the **D4** model shows non-trivial spectrum even for small value of the Huang–Rhys factor. There is a single lower-excitonic peak at 11500 cm^{-1}, but the higher-excitonic peak is split into two ($\sim$ 12500 cm^{-1} and $\sim$ 13000 cm^{-1}). The large Huang–Rhys factor makes the spectrum even more complicated where we find four peaks and they all are due to superpositions of vibrational and electronic nature. Similar electronic–vibrational mixing and nontrivial spectral properties were obtained for perylene bisimides by Seibt et al.[204] The transition frequencies and intensities are redistributed due to sensitivity of the energy–level spectrum at the avoided crossing region. Hence both **D3** and **D4** systems reflect the mixed *vibronic* features of the vibrational dimer.

The 2D spectra reveal a set of peaks and all of them contain oscillatory contributions in the waiting time, which can be visualized by using the coherence maps, introduced in Sec. 2.3.2.

The amplitudes $\mathcal{A}(\omega_2) \equiv \mathcal{A}_{\mathrm{max}}(\omega_2)$ (Eq. (2.115)) of oscillations for the **D1–D4** models are depicted in Fig. 3.10 and the coherence maps of several dominant frequencies are presented in Fig. 3.11. We next discuss the models separately.

D1 model. Weakly-coupled P–P complex with high-frequency vibration. Two dominant frequencies of 190 cm^{-1} and 1400 cm^{-1} representing oscillations in spectra of the **D1** system are resolved when $s = 0.05$ (Fig. 3.10a). We consider coherence maps at these two frequencies. The former corresponds to the excitonic energy splitting, but the frequency is smaller than $2J$ (190 $\mathrm{cm}^{-1} \approx 1.8J$) due to slight energy level repulsion, present even away from the electronic–vibrational resonance (Fig. 3.8a). The map for $\omega_2 = 190\,\mathrm{cm}^{-1}$ is typical for electronic coherence, as the oscillating features corresponding to the excited state absorption

and ground state bleaching contributions are positioned symmetrically with respect to the diagonal line and the oscillations are in-phase (Fig. 3.11a). Since the distance between the positions is smaller than the homogeneous linewidth, the most intensive oscillations are present on the diagonal due to the constructive interference. The coherence map at $\omega_2 = 1400\,\mathrm{cm}^{-1}$ is a typical reflection of the vibrational coherence, since the oscillations are present both on the diagonal line and on the cross-peaks, characterized by complex phase dependence.[38] The phase of oscillations is shifted by π at the center of the lower diagonal peak compared to the centers of the other peaks, what is also typical for beatings of vibrational coherences.[46] Two more off-diagonal oscillating features at around $\omega_3 = 10500\,\mathrm{cm}^{-1}$ are out of the frequency range in presented coherence maps, hence they would be off-resonant.

Increasing the Huang–Rhys factor to $s = 0.5$ causes stronger mixing in the system. The shape of the coherence map at $\omega_2 = \omega_0$ does not change notably, however, its amplitude increases by factor of ~ 3. The coherence map at $\omega_2 = 120\,\mathrm{cm}^{-1} \approx 1.2J$ closely resembles the map at $\omega_2 = 190\,\mathrm{cm}^{-1}$ when $s = 0.05$. Additional contributions of the excited state absorption appear above the diagonal. Features in this map are not very smooth since the lifetime of oscillations is much shorter (note that symbol sizes in Fig. 3.10a, representing the amplitudes of contributions in the schemes for $s = 0.05$ and $s = 0.5$ are, however, similar).

D2 model. J-aggregate. The strongest frequencies for model **D2** are 250 cm^{-1} and 1250 cm^{-1} (Fig. 3.10b). The coherence map of the **D2** system at $\omega_2 = \omega_0 = 250\,\mathrm{cm}^{-1}$ clearly shows the large contribution from the ground state and excited state vibrations on the diagonal and less significant excited state absorption features in the cross-peaks (Fig. 3.11b). The oscillations are more intensive below the diagonal, which is consistent with the maps of the above-mentioned PVA/C8O3 J-aggregate.[122] Regarding the relative intensities of oscillations associated with electronic ($\omega_2 \approx 2J$) and vibrational ($\omega_2 \approx \omega_0$) coherence, one finds that the relative intensity of electronic coherences has a tendency to decrease when increasing the Huang–Rhys factor. Thus, for $s \gg 1$, maps would be completely dominated by the vibrational coherences. The maps at $\omega_2 = 1200\,\mathrm{cm}^{-1}$ and $\omega_2 = 1230\,\mathrm{cm}^{-1}$ in Fig. 3.11b are typical for electronic coherences as the oscillations are diagonal-symmetric. Note that the energy splitting is much larger than the homogeneous linewidth and the two peaks in the maps are distinguished, c. f. to the corresponding coherence maps in the **D1** model.

D3 model. Weakly-coupled P–P complex with low-frequency vibration. Assignment of oscillations in the **D3** model with strongest peaks shown

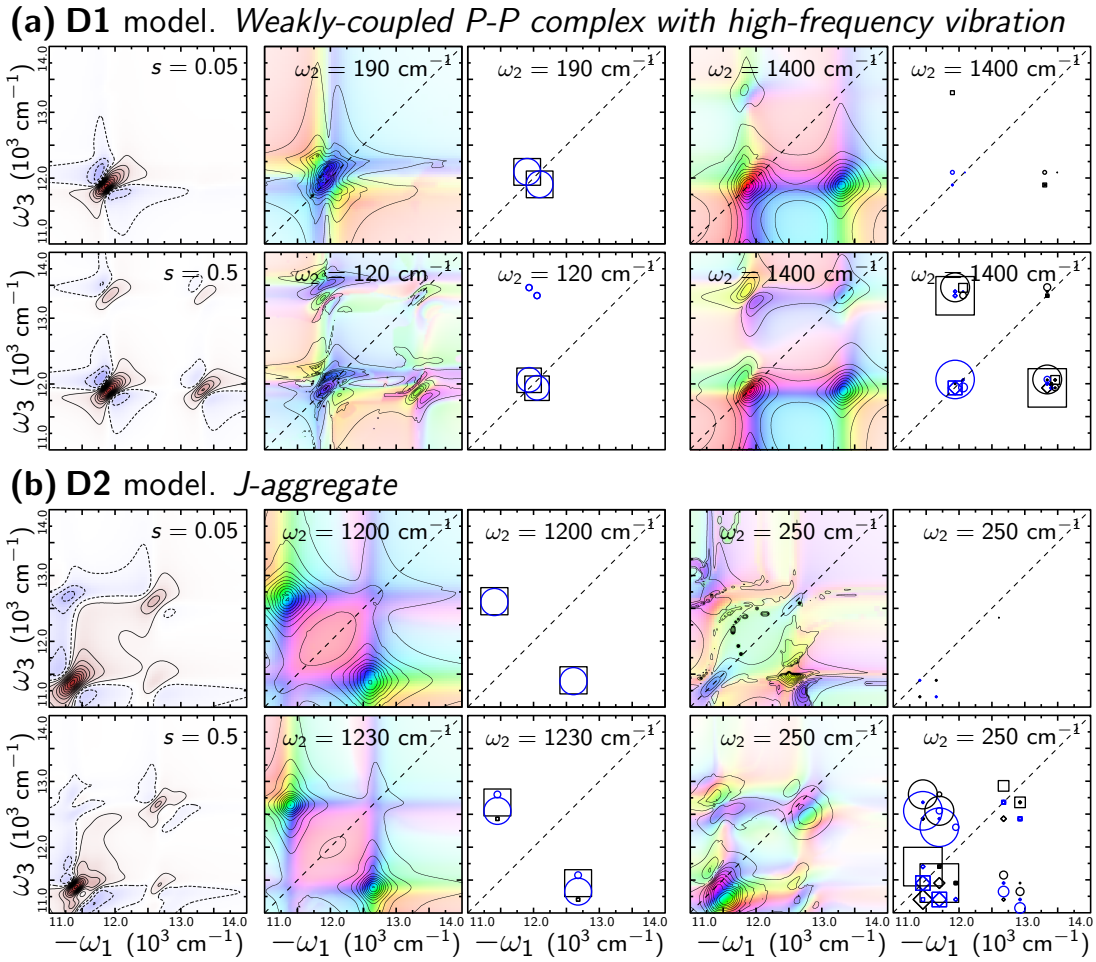

Fig. 3.11. (a) Oscillations in 2D spectra of a weakly-coupled P–P complex with high-frequency vibration (**D1** model) and **(b)** J-aggregate (**D2** model) in case of weak and strong coupling to vibrations ($s = 0.05$ and $s = 0.5$, respectively). 2D rephasing spectra at $t_2 = 0$ and two most significant coherence maps are represented in rows of every model. Schemes of the oscillations-providing contributions (○ – excited state absorption, □ – stimulated emission and ◇ – ground state bleaching) are presented next to the maps. The size of the symbols are proportional to the amplitude of the corresponding contribution. **Continued on page 107...**

in Fig. 3.10c is complicated since the parameters are close to the electronic–vibrational resonance (Fig. 3.8a). It might appear that there is only a continuum of low-frequency oscillations in the spectra for $s = 0.05$ since the maximum amplitude dependence on the frequency does not contain any peaks. However, there are short-lived oscillations at $\omega_2 = 180\,\mathrm{cm}^{-1}$ and $\omega_2 = 250\,\mathrm{cm}^{-1}$, but their coherence maps are not distinguishable due to their small amplitudes (Fig. 3.11c). Increasing the Huang–Rhys factor to $s = 0.5$ enhances the $\omega_2 = \omega_0$ oscillation which, as it can be seen in the scheme next to the map in Fig. 3.11c, is a mixture of many different contributions.

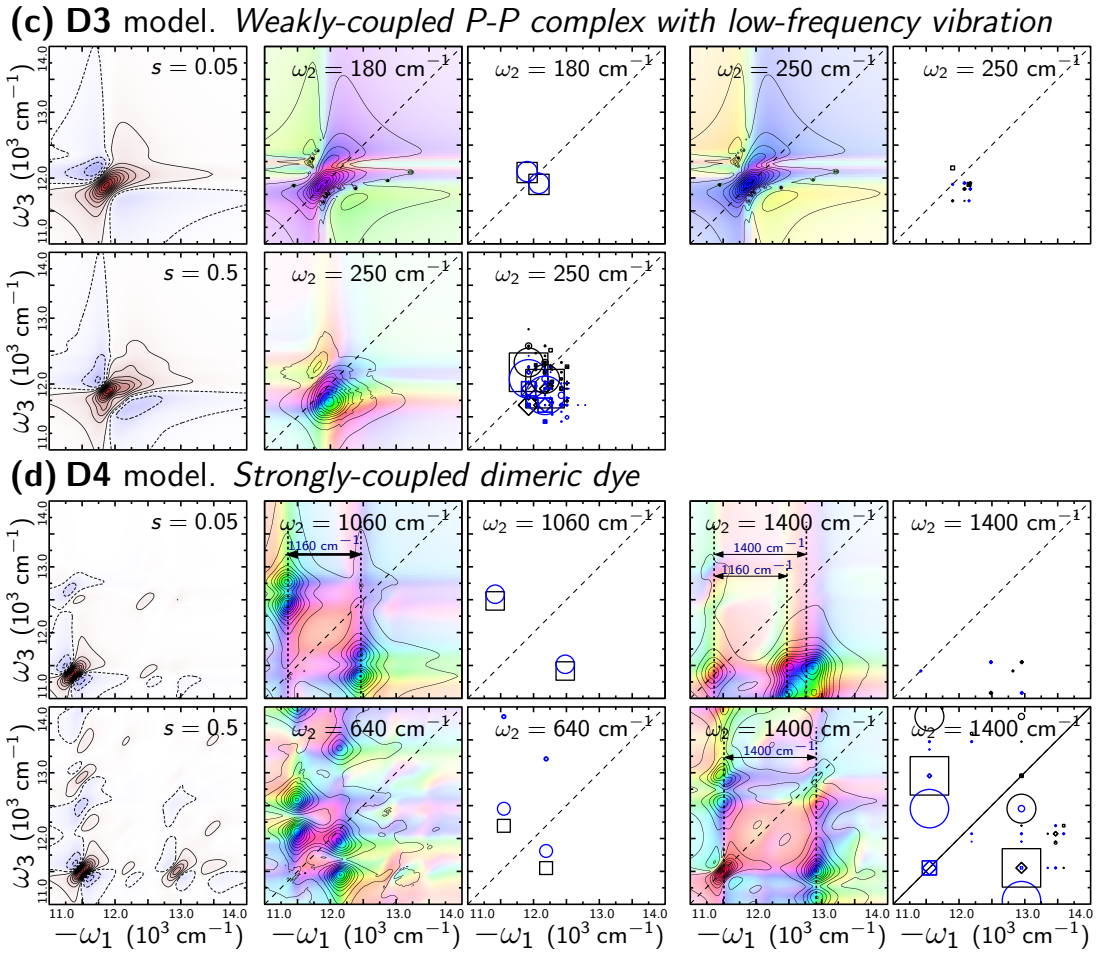

Fig. 3.11. (continued) **(c)** Oscillations of a weakly-coupled P–P complex with low-frequency vibration (**D3** model) and **(d)** a strongly-coupled dimeric dye (**D4** model).

D4 model. Strongly-coupled dimeric dye. In the 2D spectra of the **D4** model for $s = 0.05$, there are 3 clearly separable long-lived oscillations of frequencies $\omega_2 = 0.8J \approx 470\,\mathrm{cm}^{-1}$, $\omega_2 = 1.8J \approx 1060\,\mathrm{cm}^{-1}$ and $\omega_2 = \omega_0$ (Fig. 3.10d). The later two correspond to the excitonic energy splitting and vibrational coherence, respectively, while the $470\,\mathrm{cm}^{-1}$ oscillation signifies beatings between the lower and upper states in the avoided crossing region (the corresponding energy level gaps are indicated in Fig. 3.8b). For $s = 0.5$ the level repulsion effect is even more pronounced, as the gap between the lowest energy states decreases from $1.8J$ to $1.1J$ and the gap of the avoided crossing region increases from $0.8J$ to $1.3J$.

The coherence maps allow us to separate electronic and vibrational coherences in this particular mixed case. When $s = 0.05$ (Fig. 3.11d) the coherence map for $\omega_2 = 1060\,\mathrm{cm}^{-1}$ is typical for electronic coherence. There is an additional signature of the vibronic system, i. e., the oscillatory contribution of the excited state absorption appearing above the stimulated emission. It indicates that the

doubly-excited state manifold is effectively shifted up due to vibronic coupling and, therefore, the peaks are elongated along ω_3 axis in the coherence maps. The $\omega_2 = 1400\,\mathrm{cm}^{-1}$ map is exceptionally created by the ground state vibrations, however, the distances between some oscillating features in the coherence maps are found to be equal to $1060\,\mathrm{cm}^{-1}$ (see the labels with arrows in Fig. 3.11d).

The $\omega_2 = 1400\,\mathrm{cm}^{-1}$ oscillation becomes mixed if $s = 0.5$. As it can be seen in the corresponding scheme of oscillations, contributions from all types of diagrams appear and heavily congest the coherence map. The lowest diagonal peak becomes oscillating due to the stimulated emission and ground state bleaching contributions. The map for the $\omega_2 = 640\,\mathrm{cm}^{-1}$ oscillation is similar to one for $\omega_2 = 1060\,\mathrm{cm}^{-1}$ presented above. Stronger coupling to vibrations induces appearance of additional oscillations in the excited state manifold, seen as two peaks above the diagonal.

Since we consider aggregates of identical molecules, we use the homodimer systems which are symmetric with respect to Hamiltonian parameters (identical energies, couplings and vibrational frequencies). It is well established that for asymmetric heterodimers the chromophore energy difference leads to more quantum mechanical mixing and, thus, vibronic effects are more significant if the resonant coupling and the Huang–Rhys factors are low.[22,205] However, restricting ourselves to the analysis of the homodimer systems allows us to decrease the number of arbitrary parameters and makes the whole discussion more clear without losing significant relevance for physics of realistic systems.

3.3.1 Nature of coherences

There have been many attempts to unambiguously distinguish between vibrational and electronic coherences visible as oscillations in the 2D spectra. However, the question of how to do that is proper only if mixing in the system is low. As we find, two conditions for low mixing can be distinguished:

1. The coupling between vibrational and electronic subsystem has to be weak (small Huang–Rhys factor).

2. The system must not be in a vicinity of electronic–vibrational resonance, represented by the avoided crossing region in the energy spectrum.

These conditions are best to be fulfilled for high-frequency intramolecular vibrations in weakly-coupled P–P complexes and low-frequency vibrations in strongly-coupled aggregates, the **D1** and **D2** models, respectively.

The information about the transition composition can be evaluated from coherent oscillations in some more mixed cases. In the **D4** model, which stands as

an equivalent of the strongly-coupled dimeric dye, the mixture of coherences for $\omega_2 = 1060\,\mathrm{cm}^{-1}$ and $\omega_2 = 1400\,\mathrm{cm}^{-1}$ can be disentangled ($s = 0.05$, Fig. 3.11b). Firstly, the coherence map at $\omega_2 = 1060\,\mathrm{cm}^{-1}$ contains diagonal-symmetric peaks, which would suggest, that this particular coherence is rather electronic. Secondly, there are features in the map at $\omega_2 = 1400\,\mathrm{cm}^{-1}$ separated by $1400\,\mathrm{cm}^{-1}$ and $1060\,\mathrm{cm}^{-1}$ as well as the peak on the diagonal exhibiting high-frequency oscillations. The later fact as well as the obviously stronger oscillations below the diagonal shows that the origin of the $1400\,\mathrm{cm}^{-1}$ oscillation is rather vibrational. The similar analysis can be applied to $s = 0.5$ case, where the evidence of vibrational content is the diagonal oscillating peak in the $\omega_2 = 1400\,\mathrm{cm}^{-1}$ map.

One cannot discriminate between coherences of dominating electronic or vibrational character in weakly-interacting photosynthetic complexes, coupled to low-frequency vibrations. This is clearly demonstrated by the **D3** model in both cases of weak and strong coupling to vibrations (first and second rows in Fig. 3.11a, respectively). The coherences in the system are highly mixed and no typical patterns, which were present in the coherence maps of the other systems, are found here. The coherence map in case of strong coupling to vibrations is composed of many contributions, evolving in the ground and excited states (the second row in Fig. 3.11a), thus, indicating complete state character mixing. Hence, the *electronic* or *vibrational transitions* are proper concepts, while *electronic/vibronic* or *how-much-vibronic* for coherences in this particular system is a vague concept and should be avoided. Instead one should treat such coherences as simply *mixed* or *entangled*, which is a completely proper concept in quantum mechanics.

3.3.2 Lifetime of coherences in aggregates

The fact that some coherences are less visible in the coherence maps is to high degree related to their lifetimes. Obviously, oscillations which decay fast will be poorly captured by the Fourier transform or even will not be present in the maps at all. Let us now concentrate on the maximum of the Fourier amplitude dependence on frequency, $\mathcal{A}_{\max}(\omega_2)$, in case of $s = 0.05$, presented by the solid lines in Fig. 3.10. The widths of the peaks are given by the lifetime of the corresponding oscillations.

The lifetime of the vibrational ground state coherence depends only on the overlap of vibrational frequency and the bath spectral density. It can be deduced from eqs. (3.38) and (3.39). For example, the lifetime of $|\mathrm{g}_{(00)}\rangle\langle\mathrm{g}_{(01)}|$ coherence $\tau_{01} = 2(\gamma_{\mathrm{g}_{(00)}} + \gamma_{\mathrm{g}_{(01)}})^{-1}$ is $\sim$ 3 ps for $\omega_0 = 1400\,\mathrm{cm}^{-1}$ and the width of the corresponding peak in the $\mathcal{A}_{\max}(\omega_2)$ dependence is $\sim 40\,\mathrm{cm}^{-1}$ (Fig. 3.10a and d). The lifetime of $\omega_0 = 250\,\mathrm{cm}^{-1}$ coherence is $\sim$ 500 fs, thus, the corresponding

peak in $\mathcal{A}_{\max}(\omega_2)$ is very broad and, therefore, hardly distinguishable (Fig. 3.10b and c). This effect essentially depends on the spectral density function (including the shape and the amplitude) and its value at the corresponding vibrational frequency. The Drude–Lorentz spectral density decays as ω^{-1} at high frequencies and using some other faster decaying spectral density instead, for example, quantum overdamped[47] or log-normal,[206] is likely to influence the lifetimes coherences at higher frequency.

The lifetimes of coherences in the excited state manifold are not that trivial. On one hand, transfer rates relating electronic states of purely electronic aggregates depend on the absolute value of the bath spectral density at the corresponding frequency. Additionally, they depend on the extent of delocalization of the particular states. On the other hand, transfer rates between vibronic states of a single molecule are the same as of the ground state vibrational states. In our case, these two pictures are merged and the lifetimes of mixed coherences cannot be expressed in simple terms.

It has been shown, that the lifetimes of the excited state vibrational coherences increase significantly, if the electronic level splitting is close to vibrational frequencies even if the Huang–Rhys factor is small ($s < 0.1$).[22,29,33] This is evident in the $\mathcal{A}_{\max}(\omega_2)$ dependencies, as well: the lifetime of the $\omega_2 = 1.8J$ oscillation in the **D1** model is smaller than the corresponding lifetime of the frequency oscillation in the **D4** model by factor of ~ 1.8 while the lifetimes of the $\omega_2 = \omega_0$ coherences are identical. If compared, $\omega_2 = 2J$ oscillations in the **D2** model decay at least 3 times faster than the $\omega_2 = 1.8J$ oscillations in the **D4** model. This phenomenon is easy to understand since in the resonance conditions the oscillatory amplitude should be transferred from vibrational to electronic coherences due to coupling; as vibrational coherences have long lifetime, they support the electronic coherence.

If the Huang–Rhys factors are large ($s \gtrsim 0.5$), low-frequency vibrational coherences in the ground state decay faster than in the case of weak coupling to vibrations discussed above (see dashed lines in Fig. 3.10). This is due to the lower value of the reorganization energy, which is $\lambda = 50\,\mathrm{cm}^{-1}$ for $s = 0.5$ (c. f. $\lambda = 500\,\mathrm{cm}^{-1}$ for $s = 0.05$). Stronger interaction with vibrations induces more mixing in the system. Therefore, we can see long-lived coherences of $\omega_2 = 2.05J$ in the **D2** model. We can thus conclude that *the electronic coherences effectively borrow some lifetime from the vibrational coherences* due to the quantum mechanical mixing. The mixing and borrowing of the dipole strength in excitonic systems is a well-known phenomenon, however the lifetime borrowing has been poorly discussed so far.

The vibrational dimer model is convenient for simulation purposes of typical systems in a wide range of parameters to reflect pigment–protein complexes, J-

aggregates or dimeric molecular dyes. From analysis presented in this chapter, we can conclude, that

1. Regarding the question of distinguishing the electronic or vibrational coherences, the separation is fully defined and proper only if the excitonic and vibrational mixing is small. We have shown that such separation is indeed possible for systems, where the resonant coupling and vibrational frequency is off-resonant, i. e., the system is away from the so-called electronic–vibrational resonance.

2. Lifetime of excitonic coherences is determined by the coupling to discrete modes of intramolecular vibrations. The resonance conditions lead to coherence lifetime borrowing from the vibrational subsystem. The vibrational modes, on their own, are coupled to the continuum of low-frequency bath fluctuations, represented by the spectral density. Thus, the overlap of the spectral density function and frequencies of intramolecular vibrations as well as the form of the spectral density function directly influences the lifetime of electronic coherences.

3.3.3 Influence of static energy disorder on coherences

We have already shown, that the coherent oscillations of electronic and vibrational character are mixed due to intermolecular interactions, especially when the condition of electronic–vibrational resonance is satisfied. Out of the resonance condition, electronic and vibrational coherences exhibit very distinct oscillation patterns. Here we will show, that the coherences have crucially different behavior with respect to the energetic disorder, when the resonance condition is not fulfilled.

Once again, let us consider the vibrational dimer with the Huang–Rhys factors equal for both monomers, $s \equiv s_1 = s_2 = 0.05$. We set vibrational frequency $\omega_0 = 600\,\mathrm{cm}^{-1}$ as the reference parameter and choose the resonant coupling strength $J = -\omega_0/2 = -300\,\mathrm{cm}^{-1}$. We also choose that electronic site energies are separated by the same value as vibrational frequency, $\epsilon_2 - \epsilon_1 = \hbar\omega_0$. Such parameters gives the energy splitting between the states of the most significant transitions of the vibrational dimer $\hbar\omega_{\mathrm{MD}} \approx 867\,\mathrm{cm}^{-1}$, which is approximately equal to the splitting of the vibration-less electronic dimer $\hbar\omega_{\mathrm{ED}} = \sqrt{(\epsilon_2 - \epsilon_1)^2 + 4J^2} \approx 849\,\mathrm{cm}^{-1}$.

The parameter set used in our calculations describes a very general vibrational system. Indeed, the chosen absolute values of parameters are typical for many molecular aggregates of interest, including the photosynthetic pigment–protein complexes. Similar parameters have already been used by investigating the vibronic transition dipole moment borrowing and coherence enhancement effects in

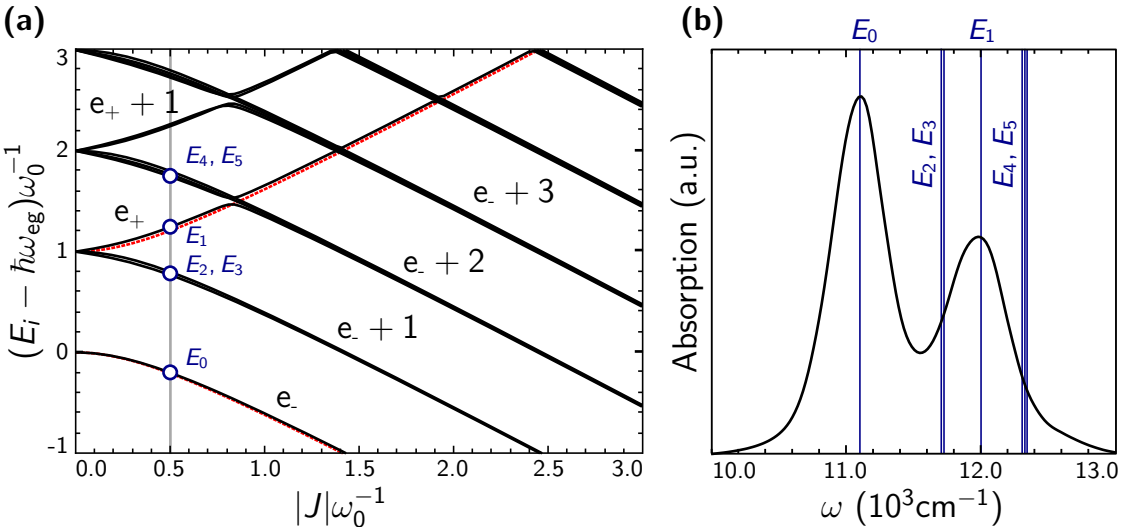

Fig. 3.12. **(a)** Dependence of the energies of the singly-excited states of the vibrational dimer on the resonance interaction (black solid lines). The energies of a purely electronic dimer $E_{e_\pm}$ are represented by the red dashed lines. **(b)** The absorption spectrum of the vibrational dimer with coupling $|J| = 0.5\omega_0$. It corresponds to the energy states indicated by the vertical gray line in **(a)**. Positions of the transitions contributing to the absorption spectrum are indicated by vertical lines.

vibrational dimer systems.[22,23,34,186]

We consider 2D signals of the vibrational dimer, which are calculated using the theory described above. For the sake of simplicity, we assume the pure dephasing as the only mechanism responsible for the homogeneous lineshape formation, also suggesting the same dephasing rates for all coherences and not taking the population transfer into consideration. The static disorder of site energies $\delta\epsilon_m$ in Eq. (3.12) is considered to be responsible for the inhomogeneous broadening that is taken into account by averaging over ensemble (1000 realizations of independent simulations) with the Gaussian distribution with standard deviation σ_D of excitation energies for every molecule.

The dependence of the singly-excited state energies on the resonance interaction is shown in Fig. 3.12a, where our case ($|J|\,\omega_0^{-1} = 0.5$) is indicated by the gray vertical line. A clear separation of electronic excited states (denoted as e_- and e_+, respectively, in Fig. 3.12a) and vibronic states (denoted as $e_\pm + m$, where m – the number of vibrational quanta) is observed.

We assume that the strengths of the transition dipole moments of the monomers are equal and constitute the inter-dipole angle $\frac{2\pi}{5}$. The dephasing rate determining the homogeneous linewidth is set to $\gamma = \omega_0/6$ and central absorption frequency is $\omega_{eg} = 11500\,\mathrm{cm}^{-1}$. One should notice that the model and analysis presented here does not contain any constraints regarding the pigment–pigment coupling strengths and our choice to consider a strongly-coupled vibrational dimer over a

Table 3.1. Mixed character of the lowest singly-excited states ($p = 0 \ldots 5$) of the vibrational dimer. $\omega_p \equiv \hbar^{-1}(E_p - E_0)$ corresponds to the energy gap between the sates that defines the beating frequency, $\mu_{g_{(00)}e_p}$ is the transition dipole moment. χ_p describes the state character, φ_p denotes the angle of the corresponding transition dipole vector with respect to the electronic transition dipole of the first monomer. The square values of the basis transformation coefficients $\psi^{(1)}_{p,(ij)}$ and $\psi^{(2)}_{p,(ij)}$ are also presented, with the most significant values in bold.

p	ω_p (cm^{-1})	$\mu_{g_{(00)}e_p}$	χ_p	φ_p (deg)	States in site basis					
					$\lvert e_{1,(00)}\rangle$	$\lvert e_{2,(00)}\rangle$	$\lvert e_{1,(10)}\rangle$	$\lvert e_{2,(01)}\rangle$	$\lvert e_{1,(01)}\rangle$	$\lvert e_{2,(10)}\rangle$
0	0	1.08	0.96	19.0	**0.82**	**0.14**	0.03	0.00	0.00	0.00
1	867	0.84	0.90	-81.8	**0.15**	**0.76**	0.02	0.01	0.05	0.01
2	581	0.26	0.06	69.3	0.00	0.06	**0.37**	0.09	**0.37**	0.06
3	600	0.17	0.02	19.0	0.02	0.00	**0.38**	0.07	**0.41**	0.07
4	1467	0.13	0.02	-81.3	0.00	0.02	0.09	**0.36**	0.06	**0.36**
5	1480	0.11	0.01	69.8	0.00	0.01	0.08	**0.33**	0.08	**0.36**

weakly-coupled complex have no critical reason.

The electronic interaction with the high-frequency vibrational mode is almost indistinguishable in the absorption spectrum for small Huang–Rhys factor as the only evidence of vibrational content is a sole weak shoulder in the absorption spectrum at $\sim 12600\,\mathrm{cm}^{-1}$ (Fig. 3.12b). For the larger Huang–Rhys factor the stronger vibrational progression would clearly appear in the spectrum, as it was shown previously.

The transformation coefficients $\psi^{(n)}_{p,(ij)}$ and $\Psi_{r,(ij)}$ in eqs. (3.40) and (3.41) provide us with the information about the eigenstate composition which allows the estimation of the amount of mixing between vibrational and electronic states. Transition amplitudes $\mu_{g_{(ij)}e_p}$ between the ground state manifold of the vibrational states and the manifold corresponding to the singly-excited states signify possible interaction configurations. The "vibronic content" in a specific electronic transition can be quantified by the transformation coefficients combined as

$$\chi_p \equiv \left(\psi^{(1)}_{p,(00)}\right)^2 + \left(\psi^{(2)}_{p,(00)}\right)^2. \tag{3.42}$$

The maximum value of this quantity ($\chi_p = 1$) indicates the pure electronic character of the transition, while $\chi_p = 0$ reflects that the corresponding state is vibronic. In a similar manner, the character of coherence of two arbitrary states was defined by Chenu et al.[23] Transitions originating from the zero-vibrational state, i. e. $|g_{(00)}\rangle$ are described in Table 3.1. The two strongest transitions correspond to mostly electronic transitions with $\chi \geq 0.9$, while the other transitions are of dominant vibrational character ($\chi < 0.1$).

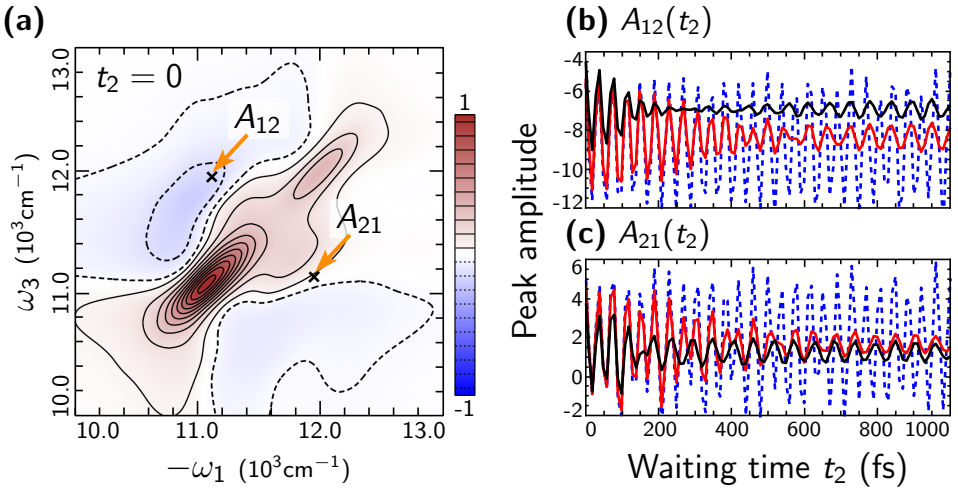

Fig. 3.13. **(a)** Rephasing 2D spectrum of the vibrational dimer at the waiting time $t_2 = 0$, with Gaussian disorder $\sigma_D = 200$ cm^{-1}. Time dependences of the amplitudes of the upper **(b)** and lower **(c)** cross-peaks. Blue dashed lines – no disorder, red solid – $\sigma_D = 20\,$cm^{-1}, black solid – $\sigma_D = 50\,$cm^{-1}.

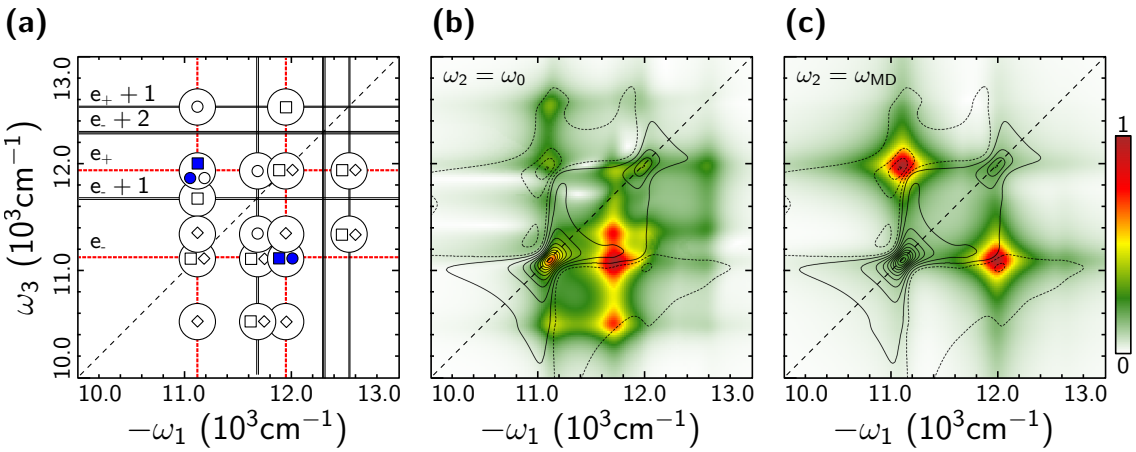

Fig. 3.14. **(a)** Arrangement of the most significant (90% of the total amplitude) oscillatory contributions (◇ – GSB, □ – SE, ○ – ESA) in the 2D spectrum of the vibrational dimer. The oscillations are at vibrational frequency ω_0 (open symbols) or electronic frequency ω_{MD} (full symbols). The oscillation maps at frequencies $\omega_2 = \omega_0$ **(b)** and $\omega_2 = \omega_{MD}$ **(c)** when $\sigma_D = 0$. The color scales of the maps are normalized individually.

The real part of the rephasing 2D spectrum contains three positive features: two diagonal peaks and a clearly distinguishable cross-peak below the diagonal reflecting the coherent resonance coupling between the molecules (Fig. 3.13a). The higher cross-peak is less visible due to the overlap with the excited state absorption contribution. As usual, apparently simple structure of the spectrum disguises the complicated pattern of various overlapping stationary and oscillatory contributions. The multitude of the oscillatory contributions is illustrated in Fig. 3.14a by a scheme, analogous to ones of the electronic dimer (Fig. 2.13a) or the displaced oscillator (Fig. 3.4a).

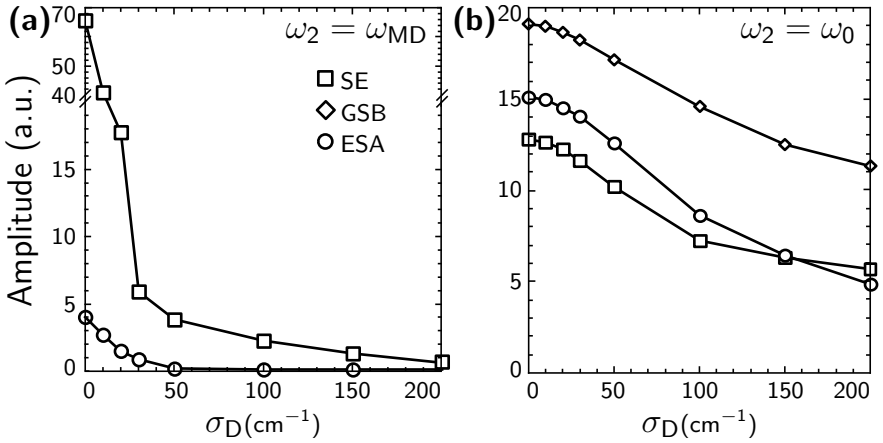

Fig. 3.15. Maximal amplitude of the oscillations dependence on disorder for GSB (diamonds), SE (squares) and ESA (circles) contributions at different beating frequencies: **(a)** $\omega_2 = \omega_{MD}$ and **(b)** $\omega_2 = \omega_0$, corresponding to electronic and vibrational character coherences, respectively.

Coherence maps of the 2D spectra at frequencies corresponding to $\omega_2 = \omega_0$ and $\omega_2 = \omega_{MD}$ are presented in figures 3.14b-c in case of no disorder. The oscillation map at $\omega_2 = \omega_{MD} = \hbar^{-1}(E_1 - E_0)$ involves two states with the most pronounced electronic character ($p = 0$ and $p = 1$ in Table 3.1) and is the same as the purely electronic coherence map of an excitonic dimer, show in Fig. 2.13b and in Ref.,[46] i. e., oscillations appear only in the cross-peaks. As we find in the disordered system ($\sigma_D = 200\,cm^{-1}$) the oscillating patterns are completely dominated by the vibrational frequency ω_0, while the oscillations with the electronic gap frequency ω_{MD} are at least 20 times weaker and, thus, their contribution is negligible.[38]

Visibility of different-character oscillations in the ensemble measurement strongly depends on system inhomogeneity. This can be clearly seen in Fig. 3.13b-c, where the time traces of the A_{12} and A_{21} cross-peaks for different values of the Gaussian disorder ($\sigma_D = 0$, 20 and $50\,cm^{-1}$) are presented. The initial intensive oscillations with the ω_{MD} frequency decay rapidly when the disorder is increased and the only dynamics observed at longer delay times correspond to the vibrational ω_0 beats. The value of the amplitude maximum of the oscillation map can be used to evaluate the strength of the corresponding oscillation.

As it is shown in Fig. 3.15, the amplitude of electronic oscillations decays sharply with the disorder (Fig. 3.15a), while the dependence of the amplitude of vibrational coherences is much more flat (Fig. 3.15b). When the disorder is absent, signatures of electronic coherences mostly reflecting the SE contribution are at least 5 times stronger than those of vibrational character, while for $\sigma_D > 200\,cm^{-1}$ the amplitude of electronic coherences is negligible. Separation of coherences of electronic and vibrational character signify that besides the vibrational beats the electronic beats could be in principle observed and distinguished for the weakly

disordered systems. However, the electronic beats rapidly decay in time in a Gaussian fashion (for uncorrelated Gaussian disorder) as σ_{D}^{-1}. Whereas vibrational beats will prevail for longer times.

We show the separation of beats of electronic and vibrational character for arbitrary system parameters, the resonant condition of the mixed character coherences (for example, when excitonic energy gap is equal to the vibrational frequency) is just a special case of our model. In FMO, where such resonant conditions are met, the electronic coherences at initial times could be of the similar amplitude as those of the vibronic origin, but due to disorder of approximately 25 cm^{-1}; electronic beats will decay in a short time ($\sim$ 200 fs) while vibrational beats would persist over the long time. For highly disordered and uncorrelated systems electronic coherences are not likely to be significant at all unless the decoherence-limited regime for electronic quantum beats, introduced in Sec. 2.3.3, is active and the observed coherent dynamics are due to the ground and the excited state vibrations.

Results presented here are related to the assumption that the vibrational frequencies are not affected by inhomogeneities, which induce the disorder of electronic transition energy. This is often the case as vibrational resonances are less sensitive to the electrostatic configuration of the environment than the delocalized electronic wavefunctions. From the analysis of coherent dynamics of vibrational dimer, experiencing static disorder, it follows that the effect of inhomogeneous disorder on the coherences depends on the character of the involved states. We can conclude, that

1. The amplitude of the electronic character beatings, caused by the coherences in the excited states, is dramatically reduced by the disorder and consequently electronic coherences are quickly dephased.

2. Vibrational character beatings stem from the ground and excited state contributions and depend weakly on the disorder, assuring their long-time survival.

It is also important to consider transition dipole moment orientations φ_p listed in Table 3.1. From that, additional conclusions arise regarding the orientations of the transitions to the "mixed" states – they are different for each state and are also different from the transition dipole moments of monomers. This implies that coherences involving arbitrary states (of electronic or vibrational character) could survive the measurements with polarization schemes, briefly described in Section 2.2.1, devised to suppress all but electronic coherence signals.[39, 149, 207] On the other hand, these polarization schemes can then be used to distinguish between the coherences of purely vibrational (localized on one molecule) and mixed origin.

Chapter 4

Vibronic excitons in a porphyrin nanoring

In this chapter, we applied the theory of vibronic and Frenkel excitons and spectral analysis tools, developed in this thesis, for studying the exciton dynamics of the synthetic molecular nanoring, consisting of six zinc-porphyrin molecules and an inner template (Fig. 4.1), and compared the results with the experimental data*. By using the Frenkel exciton model (Sec. 2.2), we were able to decide on the origin of different electronic states and how it is influenced by the ring deformations. Vibrational dimer model (Sec. 3.3) was used to simulate the quantum beats of vibrational, electronic and mixed origin. The coherence maps, introduced in Sec. 2.3.2, aided in analysis of the experimental spectra and its comparison with the results of the simulations. Here we show, that the effects of the lifetime borrowing (introduced in Sec. 3.3.2) and static energy disorder (discussed in Sec. 2.3.3 and Sec. 3.3.3) are significant for the coherent beatings in the spectrum. By putting all the results of simulations and spectral analysis together, we are able to explain the whole complexity of the nanoring absorption and the two-dimensional spectrum by the non-trivially combined effects of cyclic symmetry, small geometrical deformations, energetic disorder and vibronic coupling.

We have chosen to study this system not only because it requires us to utilize all our developed theoretical tools and, thus, is a perfect illustration for this thesis. There are many factors, which make the six-porphyrin nanoring with an inner template really exceptional:

- The full π-conjugation of the porphyrin ring is ensured. Such nanorings constitute a separate class of small oligomers with remarkably rigid and well-

*2D ES experiments, the results of which are included in this thesis, were performed in Lund University by Jan Alster, Donatas Zigmantas, Ramūnas Augulis and Eglė Bašinskaitė. Details on materials and methods used in the experiment can be found elsewhere.[48]

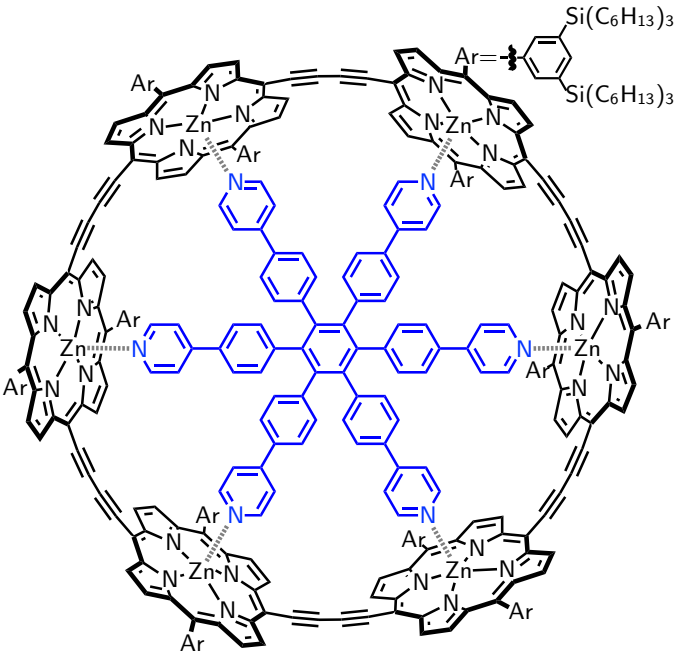

Fig. 4.1. Chemical structure of the nanoring, consisting of six zinc(II) porphyrin molecules forming a belt (the outer macrocycle) around an inner hexapyridyl template. Porphyrins at meso-positions and are interconnected by acetylenes. Chemical structure of the aryl group of 3,5-di(tri-hexylsilane)benzene is shown in the upper right corner.

defined structures. Also, it is a masterpiece of chemical synthesis.[208, 209] The fine structure of the peaks in its absorption spectrum at 77K (Fig. 4.2) suggests that the quantum beatings in 2D ES might be clearly resolvable for this system.

- Symmetric ring-shaped molecular oligomers are abundant in nature. The ring-like arrangement of pigment molecules is a characteristic feature of some photosynthetic light-harvesting complexes, such as the widely studied LH1 and LH2 complexes from the purple bacteria.[210, 211] However, properties of large biomolecular compounds are mostly determined by the surrounding protein environment, which makes their spectra obscured by the spectral overlaps and, therefore, somewhat inconvenient for an unambiguous interpretation of the spectroscopic signals. Obviously, more knowledge about the specificity of the excitation origin and its evolution in these complexes would be gained from the analysis of structurally similar synthetic ring-shaped molecular complexes in solution, maintaining sharp resonances in the absorption spectrum. Therefore, in this context the porphyrin nanoring stands as a very unique model system for better understanding of the fundamentals of exciton dynamics in the ring-shaped molecular systems. So far, different types of light-harvesting complexes from the purple bacteria, not maintaining the full π-conjugation, were the only ring-shaped molecular systems studied using the 2D ES.[64, 167, 212]

- The role of electronic–vibrational mixing in molecular systems is now of a particular interest, since it was recently shown that diabatic coupling to coherent vibrational modes might enhance the rate of EET[28, 29, 193] and of the charge

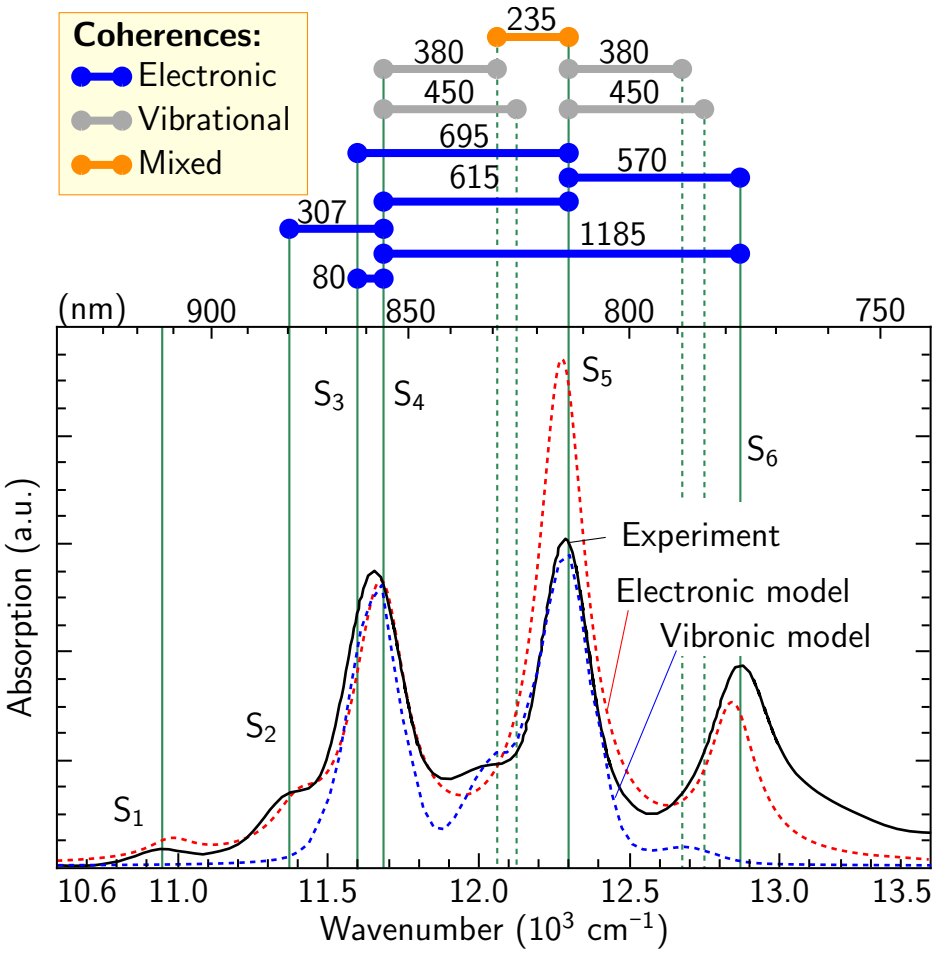

Fig. 4.2. Measured (black solid line) and simulated (red and blue dashed lines) absorption spectrum. Energies of the electronic transitions to states $S_1 - S_6$ are indicated by solid vertical lines; vibrational transitions are indicated by vertical dashed lines. Frequencies of resolved coherent beatings are shown as colored segments, connecting the states involved in the corresponding quantum superpositions.

transfer.[30,31] However, this implies existence of both electronic and vibrational coherences in the same system at the same time, what has never been unambiguously observed experimentally. The porphyrin nanoring system is a solid candidate for this quest.

- The complex optical spectrum of the nanoring with sharp bands in the visible region and the giant Stokes shift indicates its potential to be utilized as the building block for organic optoelectronics.[208,213]

Previous quantum chemistry calculations using the time-dependent density functional theory estimated the lowest-energy $S_0 - S_1$ transition of the nanoring to be around 10566 cm^{-1}. The sequence of almost equally-spaced strong peaks (for the nanoring studied here found at 11655 cm^{-1}, 12295 cm^{-1} and 12862 cm^{-1}) were discussed to stem from the Franck–Condon progression of the vibrational

$\sim 605\,\mathrm{cm}^{-1}$ mode.[214] Indeed, the linear absorption spectrum resembles slightly anharmonic vibrational progression with a large Huang–Rhys factor. Moreover, at the first sight, these peaks should not witness electronic transitions as the absorption spectrum is not typical for a perfectly symmetric ring-shaped molecular complex: assuming the head-to-tail or sandwich-type dipole orientations between the monomers, only one doubly degenerate excitonic transition is optically allowed in similar aggregates.[212] However, it is known that the inner hexapyridyl template is too small for the outer macrocycle causing its deformation.[214] Hence, such breaking of the ring symmetry could influence the electronic spectra and redistribute the strength of the excitonic transitions.

Two separate 2D ES measurements of the fully conjugated porphyrin hexamer nanoring were performed using laser pulses, the spectrum of which was centered either at 800 nm or at 880 nm, thus covering different parts of the absorption spectrum (refer to the upper panels in Fig. 4.3a-b for the corresponding laser spectra).

The 2D spectrum obtained using laser pulses at 880 nm covers the lowest electronic transition (Fig. 4.3a). It is dominated by a strong diagonal peak at $\sim 11655\,\mathrm{cm}^{-1}$. Other features on the diagonal, related to the absorption peaks at $10941\,\mathrm{cm}^{-1}$ (S_1) and $11373\,\mathrm{cm}^{-1}$ (S_2), are much weaker. However, the peaks above the diagonal ("A_{12}", "A_{13}" and "A_{23}") connecting the three diagonal peaks can be clearly resolved in Fig. 4.3a. Excited state absorption shows up as strong negative features below the diagonal overlapping with positive peaks.

Laser pulses with the spectrum centered at 800 nm were used to investigate the spectral range of the other three most prominent transitions. The corresponding 2D spectrum is shown in Fig. 4.3b. The spectrum is very rich in features and at least 17 peaks can be clearly resolved. Interestingly, a peak on the diagonal at around 11655 cm^{-1} consists of two previously not resolved[214,215] contributions separated by $\sim 80\,\mathrm{cm}^{-1}$. It could be estimated from the position of the off-diagonal peaks, indicated as A_{34} and A_{43} in Fig. 4.3c that the energies corresponding to these states are around 11600 cm^{-1} (S_3) and 11680 cm^{-1} (S_4).

To determine the energy dynamics via the manifold of the excited states, the 2D ES data were taken as a function of the waiting time t_2. Feature-rich oscillatory evolution has been observed throughout the whole (ω_1, ω_3) 2D area as a function of t_2. Decaying dynamics was extracted using three-exponential-decay fitting with one variable time constant of 156–250 fs and remaining lifetimes of 235 ps and $\gg$1 ns. The shortest time scale is related to the downward energy relaxation in the exciton manifold. This process is observed as the decay of the peaks on the diagonal of the spectrum and simultaneous increase of the peaks away from the diagonal if no other competing channel exists.[62,216] The longer time scales

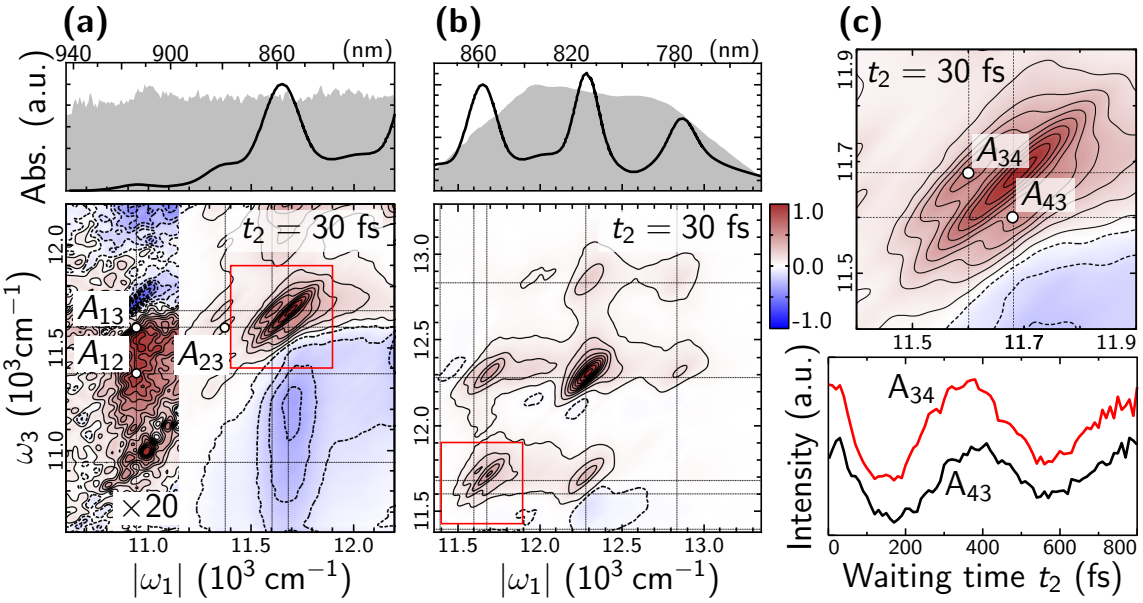

Fig. 4.3. The absorptive two-dimensional spectra obtained using laser pulses centered at 880 nm **(a)** and at 800 nm **(b)**, respectively. In the upper panels, laser pulse and nanoring absorption spectra are shown. In **(a)** the signal value is multiplied by a factor of 20 for the plot range where $\omega_1 < 11157\,\mathrm{cm}^{-1}$. **(c)** Zoomed in region of a degenerate peak in the 800 nm measurement (shown by red squares in **(a)** and **(b)**) and oscillatory dynamics of the "A_{34}" and "A_{43}" peaks. Spectra are drawn using linear color scale, normalized to the maximum of each spectrum. Dashed vertical and horizontal lines indicate the energies of states $S_1 - S_6$.

represent the relaxation from the lowest state of the exciton manifold to the ground or the other (for example, triplet) state.

Coherent beatings in the 2D spectra were analyzed using the coherence maps, constructed using both real and imaginary parts of spectrum. Notice that the evolution of Hermitian conjugate coherences $|a\rangle\langle b|$ and $|b\rangle\langle a|$ then appears at positive and negative ω_2 frequencies, respectively.[217]

Experimental coherence maps at a few selected ω_2 frequencies are shown in Fig. 4.4 and Fig. 4.5. Judging by their pattern, three types of peak configurations can be distinguished. (i) The maps at $\omega_2 = \pm 80$, ± 307, ± 570, ± 615, and $\pm 1150\,\mathrm{cm}^{-1}$ (Fig. 4.4 and Fig. 4.5a) are *diagonally symmetric*, i. e. positive and negative ω_2 features are mirror images of each other with respect to the diagonal as specifically showed in Fig. 4.4 for $\omega_2 = \pm 80\,\mathrm{cm}^{-1}$. (ii) Oscillation maps at $\omega_2 = +380\,\mathrm{cm}^{-1}$ and $-380\,\mathrm{cm}^{-1}$, shown in Fig. 4.5b, are highly *diagonally asymmetric* with the features below the diagonal in the $\omega_2 = -380\,\mathrm{cm}^{-1}$ map significantly stronger than in the $\omega_2 = +380\,\mathrm{cm}^{-1}$ map. (iii) Features in the $\omega_2 = -235\,\mathrm{cm}^{-1}$ and $\omega_2 = +235\,\mathrm{cm}^{-1}$ maps (Fig. 4.5c) are *diagonally asymmetric*, but their amplitudes are of the similar magnitude for positive and negative frequency maps.

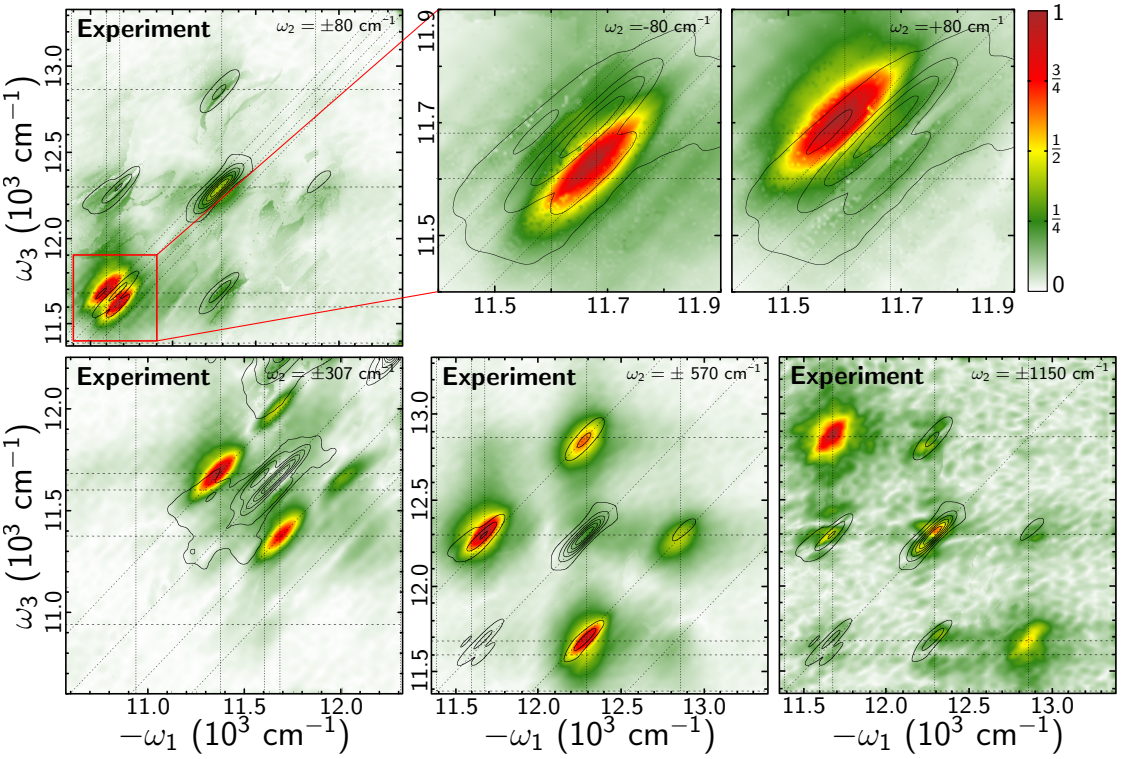

Fig. 4.4. Experimental coherence maps of *electronic* coherences at $\omega_2 = \pm 80$, ± 307, ± 570, and $\pm 1150\,\mathrm{cm}^{-1}$; Intensity of oscillations at each point of a map is indicated by the color scale; background contours show 2D rephasing spectrum at waiting time 30 fs. Each experimental and simulated map for particular frequency is independently normalized to the maximal amplitude of either positive or negative frequency map. Dashed lines parallel to the diagonal are separated by the value of ω_2. Dashed vertical and horizontal lines indicate the energies of transitions to electronic states S_1 through S_6.

We have shown in the previous chapters, that electronic, vibrational, and mixed coherences are manifested by their characteristic patterns and symmetries in the coherence maps. The symmetry of the experimental maps at $\omega_2 = \pm 80$, ± 307, ± 570, $\pm 615\,\mathrm{cm}^{-1}$, and $\pm 1150\,\mathrm{cm}^{-1}$ indicate that the underlying coherences are of the electronic origin. Dephasing times of these coherences are shorter than 300 fs (Table 4.1), oscillations are present only in the off-diagonal regions in the rephasing 2D spectrum, and the peaks at positive and negative ω_2 frequencies are of the same amplitude.

The electronic coherence with $\omega_2 = +80\,\mathrm{cm}^{-1}$ (and $\omega_2 = -80\,\mathrm{cm}^{-1}$) can be assigned to the coherent superposition $|S_4\rangle\langle S_3|$ (and $|S_3\rangle\langle S_4|$) of the closely-positioned electronic states in the vicinity of $11655\,\mathrm{cm}^{-1}$. The electronic coherence at $\omega_2 = \pm 307\,\mathrm{cm}^{-1}$ shows up only in the measurement using laser pulses at 880 nm, signifying electronic quantum beats between states $|S_2\rangle$ and $|S_4\rangle$, that could not be excited by laser pulses at 800 nm.

Beatings with the ± 570, ± 615, $\pm 695\,\mathrm{cm}^{-1}$ and $\pm 1150\,\mathrm{cm}^{-1}$ frequencies rep-

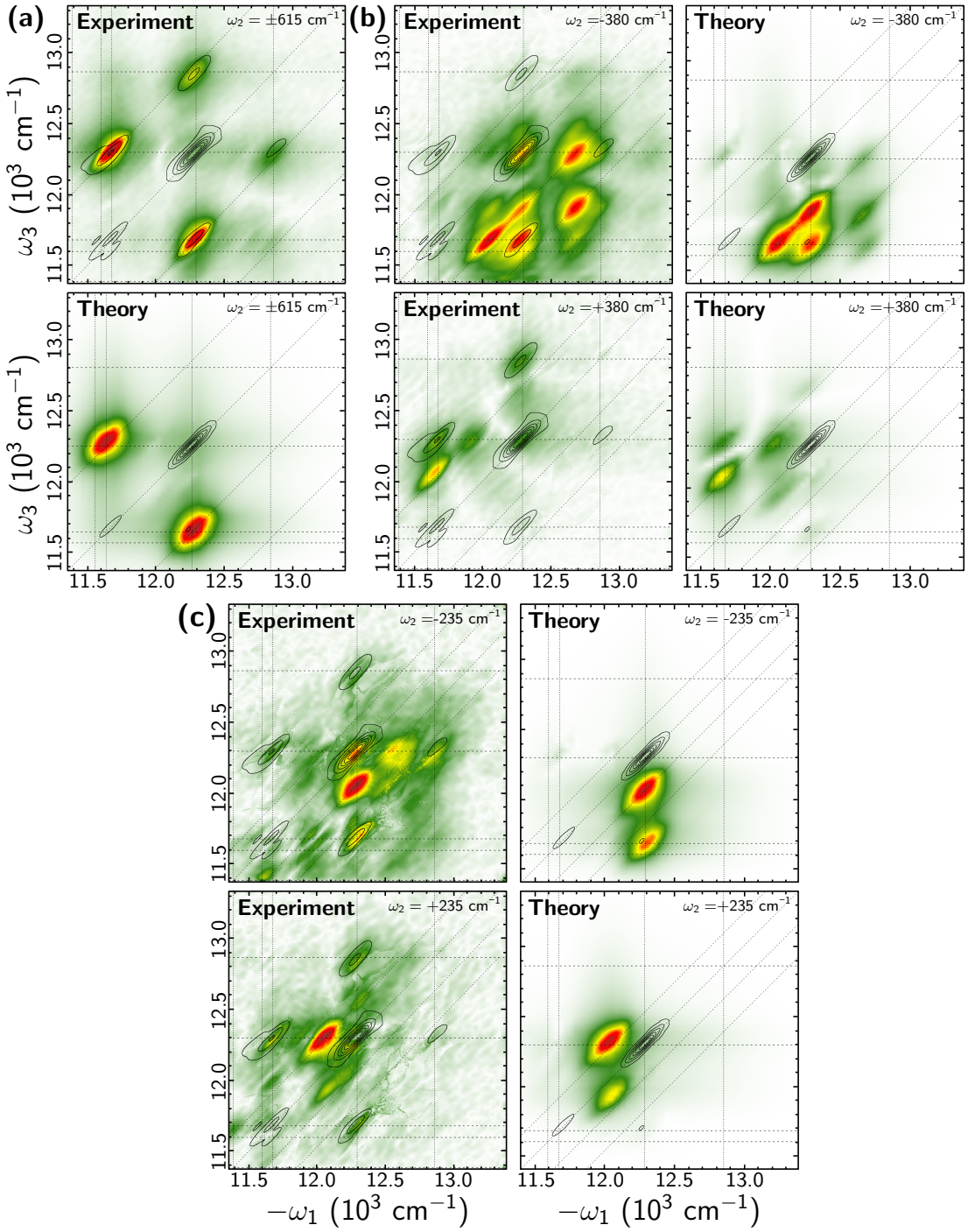

Fig. 4.5. (a) Experimental and simulated oscillation maps for *electronic* coherence at $\omega_2 = \pm 615\,\mathrm{cm}^{-1}$; **(b)** *vibrational* coherence at $\omega_2 = \pm 380\,\mathrm{cm}^{-1}$; **(c)** *mixed* coherence at $\omega_2 = \pm 235\,\mathrm{cm}^{-1}$. Presentation is analogous to Fig. 4.4.

resent quantum coherences $|S_5\rangle\langle S_6|$, $|S_4\rangle\langle S_5|$, $|S_3\rangle\langle S_5|$ and $|S_4\rangle\langle S_6|$ (and their Hermitian conjugates). Thus, our findings imply that states $|S_1\rangle$ through $|S_6\rangle$ are of electronic origin in contrast to the previous assignment[214,215] (it should be noted that the previously suggested vibrational progression does not follow a displaced harmonic oscillator model).

We assign beatings with the $\omega_2 = \pm 380\,\mathrm{cm}^{-1}$ frequency to the vibrational

Table 4.1. Classification of the observed coherences (<700 cm^{-1}). Average of four separate measurements are considered and the extracted dephasing times and standard deviations σ_τ are pointed out. The dephasing times of a few coherences could not be extracted with a reliable experimental error due to the limited resolution. Dephasing times were obtained by fitting complex oscillatory signals in the time domain.[48]

ω_2 (cm^{-1})	Dephasing time (fs)	σ_τ (fs)	Origin of coherence
±80	$\gtrsim$ 500	–	Electronic $\|S_3\rangle\langle S_4\|$
±180	–	–	Vibrational
±235	360	160	Mixed $\|S_4^*\rangle\langle S_5\|$
±307	280	130	Electronic $\|S_2\rangle\langle S_4\|$
±380	> 600	–	Vibrational
±450	–	–	Vibrational
±570	80	20	Electronic $\|S_5\rangle\langle S_6\|$
±615	200	30	Electronic $\|S_4\rangle\langle S_5\|$
±695	190	40	Electronic $\|S_3\rangle\langle S_5\|$

coherence. This follows from the oscillation maps (Fig. 4.5b), which have the pattern of oscillating peaks typical for the vibrational coherence:[46] the $\omega_2 = -380\,cm^{-1}$ map contains many features below the diagonal, while the $\omega_2 = +380\,cm^{-1}$ map is similar to the electronic coherence maps presented in Fig. 4.4 and Fig. 4.5a. In contrast to the electronic coherences, the amplitude of the $\omega_2 = -380\,cm^{-1}$ map is significantly stronger that that of $\omega_2 = +380\,cm^{-1}$. Detailed analysis of the map implies that the vibrational ground state coherences $|g\rangle\langle g^*|$ ($|g^*\rangle$ denotes some vibrationally hot ground state) appear exclusively at $\omega_2 < 0$. Their strong amplitudes are therefore related to the long lifetimes of the ground state vibrations compared with the ones at electronic excited states and mapped onto $\omega_2 = +380\,cm^{-1}$. Similar maps at $\omega_2 = 180\,cm^{-1}$, $450\,cm^{-1}$, and $835\,cm^{-1}$ (not shown) imply their vibrational origin as well. Assignment of coherent beatings at $380\,cm^{-1}$ frequency to intramolecular vibrations of a porphyrin molecule was also recently confirmed by Camargo et al.[127]

However, beatings at $\omega_2 = \pm 235\,cm^{-1}$ point out to the mixed coherence, signifying the superposition state of the $|S_5\rangle$ electronic state and vibronically hot state $|S_4^*\rangle$ ($380\,cm^{-1}$ vibrational mode). The corresponding oscillation map is not typical of neither vibrational nor electronic coherences (see Fig. 4.5c) and the beating frequency $235\,cm^{-1}$ is equal to the difference between the corresponding states.

To support the assignment of the excited states and the natures of the corresponding quantum coherences, two different theoretical models were considered: the *electronic-only* model of six excitonically coupled porphyrin molecules and the *vibrational dimer* model. The electronic-only model is used to capture the con-

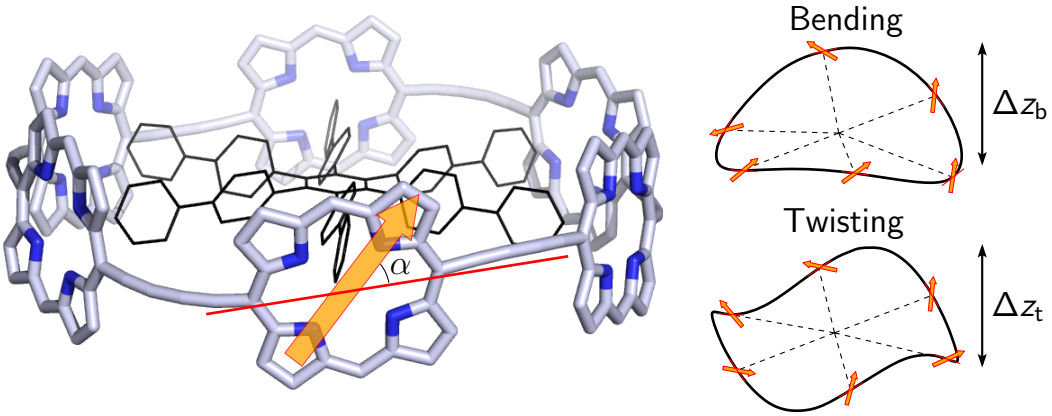

Fig. 4.6. Possible deformations of bending and twisting of the nanoring. Tangential of the nanoring backbone is shown by a red line and angle between the transition dipole moment (arrow) is indicated by α.

nection between the cyclic symmetry of the system and its optical response. The vibrational model supports assignment of the vibrational, electronic, and mixed features.

4.1 Electronic model

It is well known that energies and dipole moments of electronic transitions in the *Q* band region of a single zinc porphyrin molecule depend significantly on many factors and especially on the moieties substituted in the opposite meso-positions of the molecule. Asymmetry and triple carbon–carbon bonds in the bridges between porphyrins induce the red-shift and enhancement of the Q_y transition.[218] The presence of aryl side groups in our compounds ensures such type of symmetry breaking, making the oscillator strength of the Q_y transition much larger than that of the Q_x. Therefore, only one transition dipole (Q_y) per porphyrin rotated by an angle α with respect to the tangent of the nanoring backbone was considered.

In the electronic-only model of porphyrin nanoring Frenkel excitonic Hamiltonian (Eq. (2.86)) was considered. The resonant coupling constants J_{mn} between the *m*-th and *n*-th chromophores were calculated using the dipole–dipole approximation (Eq. (2.87)).

Two types of deformations—twisting and bending of the ring backbone—were taken into consideration (see Fig. 4.6). The vector function of the ring backbone was defined through polar coordinate φ:

$$\mathbf{f}(\varphi) = \mathbf{n}_x \cos\varphi + \mathbf{n}_y \sin\varphi + \mathbf{n}_z \left(\Delta z_b \sin 2\varphi + \Delta z_t \sin 3\varphi\right), \qquad (4.1)$$

where the parameters Δz_b and Δz_t control the extent of both types of deformations. The dipole vectors of each porphyrin were expressed through derivative

Table 4.2. Transition dipole vectors for the Q_y transitions of each porphyrin molecule.

m	μ_x	μ_y	μ_z
1	0.000	0.499	0.866
2	-0.656	0.318	0.687
3	-0.616	-0.296	0.732
4	0.000	-0.553	0.833
5	0.616	-0.296	0.732
6	0.656	0.318	0.687

of the backbone function at points $\varphi_m = \frac{2\pi}{6}(m-1)$, where index $m = 1 \dots 6$ enumerates the chromophores:

$$\boldsymbol{\mu}_m = \frac{\widehat{R}_m \mathbf{f}'(\varphi)}{\left|\widehat{R}_m \mathbf{f}'(\varphi)\right|}. \tag{4.2}$$

Here $\widehat{R}_m$ is the rotation operator, representing rotation of the transition dipole vector by angle α with respect to its middle point and keeping the angle with the ring radius vector constant. Refer to Table 4.2 for the obtained vectors.

Due to the full π-conjugation of the nanoring, the interaction between any two porphyrins cannot be described by the dipole–dipole approximation (see the discussion about more sophisticated methods in Sec. 2.2.4). Therefore, appropriate scaling factors of the coupling constants calculated in the dipole–dipole approximation for the nearest, next-nearest, and next-next-nearest neighbors were obtained by fitting the electronic-only model to the experimental absorption spectrum using the unconstrained nonlinear optimization algorithm. Free parameters used in fitting were: amplitude of porphyrin nanoring twisting Δz_{t}, amplitude of bending of the backbone Δz_{b}, transition dipole rotation α, nearest, next-nearest and next-next-nearest neighbor dimensionless coupling scaling constants ι_{12}, ι_{13} and ι_{14}, respectively. The obtained values were $\Delta z_{\mathrm{z}} = 0.076$, $\Delta z_{\mathrm{b}} = 0.011$, $\alpha = 49^\circ$, $\iota_{12} = -2011$, $\iota_{13} = -6958$ and $\iota_{14} = -1457$ (see Table 4.3 for the Hamiltonian).

The simulated absorption spectrum of this model is presented in Fig. 4.2 by the red dashed line. The agreement with the experimental absorption spectrum is quite good except of the intensity of the S_5 transition. The absence of vibronic coupling in the electronic-only model may be responsible for this discrepancy. Particularly, the electronic model provides the basis of the observed electronic coherences described above. However, additional vibrational/vibronic ingredients are necessary to explain the remaining coherences.

Table 4.3. Hamiltonian matrix used in the electronic-only simulations of the porphyrin nanoring. All values are given in wavenumbers (cm^{-1})

m	1	2	3	4	5	6
1	11775	389.9	-339.7	-81.2	-339.7	389.9
2	389.9	11775	103.2	-154.7	-2.3	353.6
3	-339.7	103.2	11775	407.0	166.6	-2.3
4	-81.2	-154.7	407.0	11775	407.0	-154.7
5	-339.7	-2.3	166.6	407.0	11775	103.2
6	389.9	353.6	-2.3	-154.7	103.2	11775

4.2 Vibrational model

For qualitative simulations of the vibronic coupling in the porphyrin nanoring we used the theoretical approach developed for a vibrational dimer,[34,179] extended by including two vibrational modes. We assume that two electronic states with the highest oscillator strengths, S_4 and S_5, are coupled to two vibrational modes of $380\,cm^{-1}$ and $450\,cm^{-1}$ with the Huang–Rhys factors of 0.03 and 0.01, respectively. This allows to significantly improve the description of the absorption spectrum in the range of S_4 and S_5 peaks (Fig. 4.2).

Diagonal uncorrelated disorder of monomers' site energies $\varepsilon_1 = 11940\,cm^{-1}$ and $\varepsilon_2 = 12000\,cm^{-1}$ with standard deviation of $100\,cm^{-1}$ was simulated by averaging over 500 realizations of the 2D spectra, calculated at waiting times up to 2 ps at 10 fs intervals. For coherence maps, Fourier transform of time dependence of each point was performed after subtraction of a three-exponential fit of the signal and multiplication with the Gaussian window, resulting in suppression of the signal at waiting time 2 ps by a factor of 10.

Simulated coherence maps, corresponding to electronic, vibrational and mixed coherences are shown in Fig. 4.4b-d. Although we included only two electronic states in the vibrational model, calculated and experimental maps of the vibrational coherences at $\pm 380\,cm^{-1}$, the electronic coherences at $\pm 615\,cm^{-1}$, and the mixed coherences at $\pm 235\,cm^{-1}$ are in a very good agreement with the experimental ones, confirming our assignments.

Summary of the results

In this thesis, we have addressed the questions regarding exciton dynamics in molecular systems. We have started with the basic perturbative description of the third-order polarization in material and signal detection, i. e. the third-order system response function formalism, and demonstrated the typical spectral signatures of a few simple model systems in a textbook style.[159] Starting with the description of the Frenkel excitons, we have virtually separated two phenomena of dephasing (arising from the static energetic disorder) and decoherence (from the quantum state's entanglement with the environment), both destructively influencing the phase relationship of the established coherent exciton. We have demonstrated, that the interplay between these two mechanisms can lead to drastically different outcomes regarding the observed quantum beatings in the 2D spectrum: in some cases coherence is destroyed almost instantaneously, while sometimes it can survive for picoseconds. Such behavior is determined by the parameters of the system, the system–bath coupling and the amount of the environment-related static energy disorder.

We have expanded the Frenkel exciton formalism to account for the explicit intramolecular and intermolecular vibrations and its signatures in the two-dimensional electronic spectrum, using the Holstein-type vibronic exciton Hamiltonian.[179] In order to conveniently and systematically assess the huge amount of information, provided by the oscillations of multiple experimental or simulated 2D spectra, we have introduced the so-called coherence maps, constructed from a set of the time-resolved 2D spectra.[38,178] Consideration of such maps immediately gave a very distinct picture of coherent evolution of electronic, vibrational and quantum-mechanically mixed molecular eigenstates. We have shown, how these signatures can be classified in order to unravel the origin of the quantum beatings.[34,46,47]

By the analysis of vibronic exciton dynamics in the porphyrin nanoring we resolved electronic, vibrational and mixed coherences, supported by theoretical simulations. That is, we have found an experimental evidence of coherences of different physical origins existing in the same system at the same time.[48] This was a missing piece in a general discussion of electronic–vibrational interference in molecular systems.

We have also shown, how analysis of coherent beatings in 2D ES can aid in disentangling the energy level structure of the excited states and their cooperativity. This turns out to manifest even in the absorption spectrum, where we identify electronic transitions, the intensity and positions of which are non-trivially defined by vibronic coupling (together with small ring deformations). In the analysis of the coherence maps, the whole "zoo" of vibronic excitons gets raised and they inter-operate to maintain long coherence lifetimes and coherent excitation evolution. Such coherent quantum properties of a supermolecular system are reported for the first time, but should be general for molecular aggregates.

We have reported a similar study of quantum beats in the experimental data of the fucoxanthin–chlorophyll protein.[49] In contrast to the porphyrin nanoring, no beatings of electronic origin were obtained, most probably due to fast dephasing. However, analysis of the coherence dynamics allowed us to identify chlorophyll *a* and fucoxanthin intramolecular vibrations dominating over the first few picoseconds of the 2D spectrum. The results, presented in this thesis, has been already applied in analysis of quantum beatings in the photosynthetic reaction center and subsequently aided in proposing the effect, how electronic–vibrational interference can speed-up the charge transfer in the earliest stages of the oxygenic photosynthesis.[30]

Bibliography

[1] E. W. Knapp, Lineshapes of molecular aggregates. Exchange narrowing and intersite correlation, Chem. Phys. **85**, 73–82 (1984).

[2] V. A. Malyshev, F. Domínguez-Adame, Motional narrowing effect in one-dimensional Frenkel chains with configurational disorder, Chem. Phys. Lett. **313**, 255–260 (1999).

[3] M. R. Philpott, Theory of the coupling of electronic and vibrational excitations in molecular crystals and helical polymers, J. Chem. Phys. **55**, 2039 (1971).

[4] J. Frenkel, On the transformation of light into heat in solids. II, Phys. Rev. **37**, 1276–1294 (1931).

[5] A. Davydov, *A Theory of Molecular Excitions* (Mc.Graw–Hill, New York, 1962).

[6] L. Valkunas, D. Abramavicius, T. Mančal, *Molecular Excitation Dynamics and Relaxation* (Wiley-VCH, Weinheim, 2013).

[7] M. Pope, C. E. Swenberg, *Electron Processes in Organic Crystals* (Oxford University Press, New York, 1999).

[8] V. May, O. Kühn, *Charge and Energy Transfer Dynamics in Molecular Systems* (Wiley-VCH, Weinheim, 2011).

[9] R. L. Fulton, M. Gouterman, Vibronic coupling. II. Spectra of dimers, J. Chem. Phys. **41**, 2280–2286 (1964).

[10] J. N. Murrell, J. A. Pople, The intensities of the symmetry-forbidden electronic bands of benzene, Proc. Phys. Soc. A **69**, 245 (1956).

[11] I. B. Bersuker, *The Jahn–Teller Effect* (Cambridge University Press, 2006).

[12] M. H. Vos, F. Rappaport, J.-C. Lambry, J. Breton, J.-L. Martin, Visualization of coherent nuclear motion in a membrane protein by femtosecond spectroscopy, Nature **363**, 320–325 (1993).

[13] M. Chachisvilis, O. Kühn, T. Pullerits, V. Sundström, Excitons in photosynthetic purple bacteria: Wavelike motion or incoherent hopping?, J. Phys. Chem. B **101**, 7275–7283 (1997).

[14] S. Savikhin, D. R. Buck, W. S. Struve, Oscillating anisotropies in a bacteriochlorophyll protein: Evidence for quantum beating between exciton levels, Chem. Phys. **223**, 303–312 (1997).

[15] G. Engel, T. Calhoun, E. Read, T. Ahn, T. Mančal, Y.-C. Cheng, R. Blankenship, G. Fleming, Evidence for wavelike energy transfer through quantum coherence in photosynthetic systems, Nature **446**, 782–786 (2007).

[16] A. Nemeth, F. Milota, T. Mančal, V. Lukeš, J. Hauer, H. Kauffmann, J. Sperling, Vibrational wave packet induced oscillations in two-dimensional electronic spectra. I. Experiments, J. Chem. Phys. **132**, 184514 (2010).

[17] H.-P. Breuer, F. Petruccione, *The Theory of Open Quantum Systems* (Oxford University Press, New York, 2002).

[18] M. Schlosshauer, *Decoherence and the Quantum-to-Classical Transition*, The frontiers collection (Springer, Berlin Heidelberg, Berlin, 2007).

[19] G. Panitchayangkoon, D. Hayes, K. A. Fransted, J. Caram, E. Harel, J. Wen, R. Blankenship, G. Engel, Long-lived quantum coherence in photosynthetic complexes at physiological temperature, Proc. Natl. Acad. Sci. USA **107**, 12766–12770 (2010).

[20] R. E. Blankenship, *Molecular Mechanisms of Photosynthesis* (John Wiley & Sons, 2013).

[21] N. Christensson, F. Milota, J. Hauer, J. Sperling, O. Bixner, A. Nemeth, H. Kauffmann, High frequency vibrational modulations in two-dimensional electronic spectra and their resemblance to electronic coherence signatures, J. Phys. Chem. B **115**, 5383–5391 (2011).

[22] V. Tiwari, W. K. Peters, D. M. Jonas, Electronic resonance with anticorrelated pigment vibrations drives photosynthetic energy transfer outside the adiabatic framework, Proc. Natl. Acad. Sci. USA **110**, 1203–1208 (2013).

[23] A. Chenu, N. Christensson, H. F. Kauffmann, T. Mančal, Enhancement of vibronic and ground-state vibrational coherences in 2D spectra of photosynthetic complexes, Sci. Rep. **3**, 2029 (2013).

[24] R. Tempelaar, T. L. C. Jansen, J. Knoester, Vibrational beatings conceal evidence of electronic coherence in the FMO light-harvesting complex, J. Phys. Chem. B **118**, 12865–12872 (2014).

[25] J. Schulze, O. Kühn, Explicit correlated exciton-vibrational dynamics of the FMO complex, J. Phys. Chem. B **119**, 6211–6216 (2015).

[26] J. M. Womick, S. A. Miller, A. M. Moran, Probing the dynamics of intraband electronic coherences in cylindrical molecular aggregates, J. Phys. Chem. A **113**, 6587–6598 (2009).

[27] G. Panitchayangkoon, D. Voronine, D. Abramavicius, J. Caram, N. Lewis, S. Mukamel, G. Engel, Direct evidence of quantum transport in photosynthetic light-harvesting complexes, Proc. Natl. Acad. Sci. USA **108**, 20908–20912 (2011).

[28] A. Kolli, E. O'Reilly, G. Scholes, A. Olaya-Castro, The fundamental role of quantized vibrations in coherent light harvesting by cryptophyte algae, J. Chem. Phys. **137**, 174109 (2012).

[29] A. W. Chin, J. Prior, R. Rosenbach, F. Caycedo-Soler, S. F. Huelga, M. B. Plenio, The role of non-equilibrium vibrational structures in electronic coherence and recoherence in pigment–protein complexes, Nature Phys. **9**, 113–118 (2013).

[30] F. D. Fuller, J. Pan, A. Gelzinis, V. Butkus, S. S. Senlik, D. E. Wilcox, C. F. Yocum, L. Valkunas, D. Abramavicius, J. P. Ogilvie, Vibronic coherence in oxygenic photosynthesis, Nature Chem. **6**, 706–711 (2014).

[31] E. Romero, R. Augulis, V. I. Novoderezhkin, M. Ferretti, J. Thieme, D. Zigmantas, R. van Grondelle, Quantum coherence in photosynthesis for efficient solar-energy conversion, Nature Phys. **10**, 676–682 (2014).

[32] P. Rebentrost, M. Mohseni, I. Kassal, S. Lloyd, A. Aspuru-Guzik, Environment-assisted quantum transport, New J. Phys. **11**, 033003 (2009).

[33] N. Christensson, H. Kauffmann, T. Pullerits, T. Mančal, Origin of long-lived coherences in light-harvesting complexes, J. Phys. Chem. B **116**, 7449–7454 (2012).

[34] V. Butkus, L. Valkunas, D. Abramavicius, Vibronic phenomena and exciton–vibrational interference in two-dimensional spectra of molecular aggregates, J. Chem. Phys. **140**, 034306 (2014).

[35] M. Schröter, S. Ivanov, J. Schulze, S. Polyutov, Y. Yan, T. Pullerits, O. Kühn, Exciton–vibrational coupling in the dynamics and spectroscopy of Frenkel excitons in molecular aggregates, Phys. Rep. **567**, 1–78 (2015).

[36] M. Klessinger, J. Michl, *Excited States and Photochemistry of Organic Molecules* (Wiley-VCH, New York, 1995).

[37] D. R. Yarkony, Conical intersections: The new conventional wisdom, J. Phys. Chem. A **105**, 6277–6293 (2001).

[38] V. Butkus, D. Zigmantas, D. Abramavicius, L. Valkunas, Distinctive character of electronic and vibrational coherences in disordered molecular aggregates, Chem. Phys. Lett. **587**, 93–98 (2013).

[39] S. Westenhoff, D. Paleček, P. Edlund, P. Smith, D. Zigmantas, Coherent picosecond exciton dynamics in a photosynthetic reaction center, J. Am. Chem. Soc. **134**, 16484–16487 (2012).

[40] D. Hayes, G. B. Griffin, G. S. Engel, Engineering coherence among excited states in synthetic heterodimer systems, Science **340**, 1431–1434 (2013).

[41] A. Halpin, P. J. M. Johnson, R. Tempelaar, R. S. Murphy, J. Knoester, T. L. C. Jansen, R. J. D. Miller, Two-dimensional spectroscopy of a molecular dimer unveils the effects of vibronic coupling on exciton coherences, Nature Chem. **6**, 196–201 (2014).

[42] J. Alster, H. Lokstein, J. Dostál, A. Uchida, D. Zigmantas, 2D spectroscopy study of water-soluble chlorophyll-binding protein from *Lepidium virginicum*, J. Phys. Chem. B **118**, 3524–3531 (2014).

[43] Y.-C. Cheng, G. R. Fleming, Coherence quantum beats in two-dimensional electronic spectroscopy, J. Phys. Chem. A **112**, 4254–4260 (2008).

[44] V. Perlík, C. Lincoln, F. Šanda, J. Hauer, Distinguishing electronic and vibronic coherence in 2D spectra by their temperature dependence, J. Phys. Chem. Lett. **5**, 404–407 (2014).

[45] C. Kreisbeck, T. Kramer, A. Aspuru-Guzik, Disentangling electronic and vibronic coherences in two-dimensional echo spectra, J. Phys. Chem. B **117**, 9380–9385 (2013).

[46] V. Butkus, D. Zigmantas, L. Valkunas, D. Abramavicius, Vibrational vs. electronic coherences in 2D spectrum of molecular systems, Chem. Phys. Lett. **545**, 40–43 (2012).

[47] V. Butkus, L. Valkunas, D. Abramavicius, Molecular vibrations-induced quantum beats in two-dimensional electronic spectroscopy, J. Chem. Phys. **137**, 044513 (2012).

[48] V. Butkus, J. Alster, E. Bašinskaitė, R. Augulis, P. Neuhaus, H. L. Anderson, L. Valkunas, D. Abramavicius, Z. D., Diversity of coherences in electronic spectra of supermolecular nanoring, arXiv preprint 1503.00870 (2015).

[49] V. Butkus, A. Gelzinis, R. Augulis, A. Gall, C. Büchel, B. Robert, D. Zigmantas, L. Valkunas, D. Abramavicius, Coherence and population dynamics of chlorophyll excitations in FCP complex: Two-dimensional spectroscopy study, J. Chem. Phys. **21**, 212414 (2015).

[50] R. R. Ernst, Nuclear magnetic resonance Fourier transform spectroscopy (Nobel lecture), Angew. Chem. Int. Ed. Engl. **31**, 805–823 (1992).

[51] R. R. Ernst, G. Bodenhausen, A. Wokaun, et al., *Principles of Nuclear Magnetic Resonance in One and Two Dimensions*, volume 14 (Clarendon Press Oxford, 1987).

[52] The nobel prize in chemistry 1991, `http://www.nobelprize.org/nobel_prizes/chemistry/laureates/1991/`, accessed: 2015-06-10.

[53] W. Zhuang, T. Hayashi, S. Mukamel, Coherent multidimensional vibrational spectroscopy of biomolecules: Concepts, simulations, and challenges, Angew. Chem. Int. Ed. **48**, 3750–3781 (2009).

[54] M. Khalil, N. Demirdöven, A. Tokmakoff, Coherent 2D IR spectroscopy: molecular structure and dynamics in solution, J. Phys. Chem. **107**, 5258–5279 (2003).

[55] P. Hamm, M. Zanni, *Concepts and Methods of 2D Infrared Spectroscopy* (Cambridge University Press, 2011).

[56] S. Mukamel, D. Abramavicius, L. Yang, W. Zhuang, I. V. Schweigert, D. V. Voronine, Coherent multidimensional optical probes for electron correlations and exciton dynamics: From NMR to X-rays, Acc. Chem. Res. **42**, 553–562 (2009).

[57] W. S. Warren, Optical analogs of NMR phase coherent multiple pulse spectroscopy, J. Chem. Phys. **75**, 5956 (1981).

[58] S. Mukamel, Multidimensional femtosecond correlation spectroscopies of electronic and vibrational excitations, Annu. Rev. Phys. Chem. **51**, 691–729 (2000).

[59] D. M. Jonas, Two-dimensional femtosecond spectroscopy, Annu. Rev. Phys. Chem. **54**, 425–63 (2003).

[60] M. Cho, Coherent two-dimensional optical spectroscopy, Chem. Rev. **108**, 1331–1418 (2008).

[61] P. Tian, D. Keusters, Y. Suzaki, W. S. Warren, Femtosecond phase-coherent two-dimensional spectroscopy, Science **300**, 1553–1555 (2003).

[62] T. Brixner, J. Stenger, H. M. Vaswani, M. Cho, R. E. Blankenship, G. R. Fleming, Two-dimensional spectroscopy of electronic couplings in photosynthesis, Nature **434**, 625–628 (2005).

[63] B. Brüggemann, P. Kjellberg, T. Pullerits, Non-perturbative calculation of 2D spectra in heterogeneous systems: Exciton relaxation in the FMO complex, Chem. Phys. Lett. **444**, 192–196 (2007).

[64] D. Zigmantas, E. L. Read, T. Mančal, T. Brixner, A. T. Gardiner, R. J. Cogdell, G. R. Fleming, Two-dimensional electronic spectroscopy of the B800-B820 light-harvesting complex, Proc. Natl. Acad. Sci. USA **103**, 12672–12677 (2006).

[65] F. Milota, J. Sperling, A. Nemeth, H. Kauffmann, Two-dimensional electronic photon echoes of a double band J-aggregate: Quantum oscillatory motion versus exciton relaxation, Chem. Phys. **357**, 45–53 (2009).

[66] D. Abramavicius, D. V. Voronine, S. Mukamel, Unravelling coherent dynamics and energy dissipation in photosynthetic complexes by 2D spectroscopy, Biophys. J. **94**, 3613–3619 (2008).

[67] A. V. Pisliakov, T. Mančal, G. R. Fleming, Two-dimensional optical three-pulse photon echo spectroscopy. II. Signatures of coherent electronic motion and exciton population transfer in dimer two-dimensional spectra, J. Chem. Phys. **124**, 234505 (2006).

[68] D. Abramavicius, V. Butkus, J. Bujokas, L. Valkunas, Manipulation of two-dimensional spectra of excitonically coupled molecules by narrow-bandwidth laser pulses, Chem. Phys. **372**, 22–32 (2010).

[69] S. Mukamel, *Principles of Nonlinear Optical Spectroscopy* (Oxford University Press, New York, 1995).

[70] D. Abramavicius, B. Palmieri, D. Voronine, F. Šanda, S. Mukamel, Coherent multidimensional optical spectroscopy of excitons in molecular aggregates; Quasiparticle versus supermolecule perspectives, Chem. Rev. **109**, 2350–2408 (2009).

[71] F. D. Fuller, J. P. Ogilvie, Experimental implementations of two-dimensional Fourier transform electronic spectroscopy, Annu. Rev. Phys. Chem. **66**, 667–690 (2015).

[72] T. Brixner, T. Mančal, I. V. Stiopkin, G. R. Fleming, Phase-stabilized two-dimensional electronic spectroscopy, J. Chem. Phys. **121**, 4221–4236 (2004).

[73] M. Cho, H. M. Vaswani, T. Brixner, J. Stenger, G. R. Fleming, Exciton analysis in 2D electronic spectroscopy, J. Phys. Chem. B **109**, 10542–10556 (2005).

[74] S. I. E. Vulto, M. A. de Baat, S. Neerken, F. R. Nowak, H. van Amerongen, J. Amesz, T. J. Aartsma, Excited state dynamics in FMO antenna complexes from photosynthetic green sulfur bacteria: A kinetic model, J. Phys. Chem. B **103**, 8153–8161 (1999).

[75] T. D. Ladd, F. Jelezko, R. Laflamme, Y. Nakamura, C. Monroe, J. L. O'Brien, Quantum computers, Nature **464**, 45–53 (2010).

[76] G. D. Scholes, Quantum-coherent electronic energy transfer: Did nature think of it first?, J. Phys. Chem. Lett. **1**, 2–8 (2010).

[77] J. Strümpfer, M. Sener, K. Schulten, How quantum coherence assists photosynthetic light-harvesting, J. Phys. Chem. Lett. **3**, 536–542 (2012).

[78] N. Lambert, Y.-N. Chen, Y.-C. Cheng, C.-M. Li, G.-Y. Chen, F. Nori, Quantum biology, Nature Phys. **9**, 10–18 (2012).

[79] M. Mohseni, Y. Omar, G. S. Engel, M. B. Plenio, *Quantum Effects in Biology* (Cambridge University Press, 2014).

[80] T. Förster, Zwischenmolekulare Energiewanderung und Fluoreszenz, Ann. Physik **6**, 55 (1948).

[81] A. G. Redfield, On the theory of relaxation processes, IBM J. Res. Dev. **1**, 19–31 (1957).

[82] D. Abramavicius, S. Mukamel, Quantum oscillatory exciton migration in photosynthetic reaction centers, J. Chem. Phys. **133**, 064510 (2010).

[83] D. Abramavicius, S. Mukamel, Exciton dynamics in chromophore aggregates with correlated environment fluctuations, J. Chem. Phys. **134**, 174504 (2011).

[84] C. Olbrich, J. Strümpfer, K. Schulten, U. Kleinekathöfer, Quest for spatially correlated fluctuations in the FMO light-harvesting complex, J. Phys. Chem. B **115**, 758–764 (2011).

[85] I. Kassal, J. Yuen-Zhou, S. Rahimi-Keshari, Does coherence enhance transport in photosynthesis?, The Journal of Physical Chemistry Letters **4**, 362–367 (2013).

[86] S. Lloyd, M. Mohseni, Symmetry-enhanced supertransfer of delocalized quantum states, New J. Phys. **12**, 075020 (2010).

[87] G. S. Schlau-Cohen, T. R. Calhoun, N. S. Ginsberg, E. L. Read, M. Ballottari, R. Bassi, R. van Grondelle, G. R. Fleming, Pathways of energy flow in LHCII from two-dimensional electronic spectroscopy, J. Phys. Chem. B **113**, 15352–15363 (2009).

[88] A. Gelzinis, L. Valkunas, F. D. Fuller, J. P. Ogilvie, S. Mukamel, D. Abramavicius, Tight-binding model of the photosystem II reaction center: Application to two-dimensional electronic spectroscopy, New J. Phys. **15**, 075013 (2013).

[89] H. Lee, Y.-C. Cheng, G. Fleming, Coherence dynamics in photosynthesis: Protein protection of excitonic coherence, Science **316**, 1462–1465 (2007).

[90] J. Dostál, T. Mančal, R. Augulis, F. Vácha, J. Pšenčik, D. Zigmantas, Two-dimensional electronic spectroscopy reveals ultrafast energy diffusion in chlorosomes, J. Am. Chem. Soc. **134**, 11611–11617 (2012).

[91] J. M. Anna, E. E. Ostroumov, K. Maghlaoui, J. Barber, G. D. Scholes, Two-dimensional electronic spectroscopy reveals ultrafast downhill energy transfer in photosystem I trimers of the cyanobacterium *Thermosynechococcus elongatus*, J. Phys. Chem. Lett. **3**, 3677–3684 (2012).

[92] J. Dostál, J. Pšenčík, D. Zigmantas, Tracking energy flow through the intact photosynthetic apparatus, in *11th Nordic Femtochemistry Conference* (Vilnius, Lithuania, 2014), 31.

[93] S. T. Cundiff, S. Mukamel, Optical multidimensional coherent spectroscopy, Physics Today **66**, 44–49 (2013).

[94] E. Papagiannakis, I. H. M. van Stokkum, H.Fey, C. Büchel, R. van Grondelle, Spectroscopic characterization of the excitation energy transfer in the fucoxanthin-chlorophyll protein of diatoms, Photosynth. Res. **86**, 241–50 (2005).

[95] C. Wilhelm, C. Büchel, J. Fisahn, R. Goss, T. Jakob, J. LaRoche, J. Lavaud, M. Lohr, U. Riebesell, K. Stehfest, K. Valentin, P. G. Kroth, The regulation of carbon and nutrient assimilation in diatoms is significantly different from green algae, Protist **157**, 91–124 (2006).

[96] L. Premvardhan, B. Robert, A. Beer, C. Büchel, Pigment organization in fucoxanthin chlorophyll a/c_2 proteins (FCP) based on resonance Raman spectroscopy and sequence analysis, Biochim. Biophys. Acta **1797**, 1647–1656 (2010).

[97] N. Gildenhoff, J. Herz, K. Gundermann, C. Büchel, J. Wachtveitl, The excitation energy transfer in the trimeric fucoxanthin–chlorophyll protein from *Cyclotella meneghiniana* analyzed by polarized transient absorption spectroscopy, Chem. Phys. **373**, 104–109 (2010).

[98] P. G. Falkowski, R. T. Barber, V. Smetacek, Biogeochemical controls and feedbacks on ocean primary production, Science **281**, 200–206 (1998).

[99] C. B. Field, M. J. Behrenfeld, J. T. Randerson, P. Falkowski, Primary production of the biosphere: Integrating terrestrial and oceanic components, Science **281**, 237–240 (1998).

[100] D. G. Mann, The species concept in diatoms, Phycologia **38**, 437–495 (1999).

[101] E. Songaila, R. Augulis, A. Gelzinis, V. Butkus, A. Gall, C. Büchel, B. Robert, D. Zigmantas, D. Abramavicius, L. Valkunas, Ultrafast energy transfer from chlorophyll c_2 to chlorophyll *a* in fucoxanthin–chlorophyll protein complex, J. Phys. Chem. Lett. **4**, 3590–3595 (2013).

[102] A. Gelzinis, V. Butkus, E. Songaila, R. Augulis, A. Gall, C. Büchel, B. Robert, D. Abramavicius, D. Zigmantas, L. Valkunas, Mapping energy transfer channels in fucoxanthin–chlorophyll protein complex, Biochim. Biophys. Acta **1847**, 241–247 (2015).

[103] J. A. Myers, K. L. Lewis, P. F. Tekavec, J. P. Ogilvie, Two-color two-dimensional Fourier transform electronic spectroscopy with a pulse-shaper, Opt. Express **16**, 17420–17428 (2008).

[104] M. Kullmann, S. Ruetzel, J. Buback, P. Nuernberger, T. Brixner, Reaction dynamics of a molecular switch unveiled by coherent two-dimensional electronic spectroscopy, J. Am. Chem. Soc. **133**, 13074–13080 (2011).

[105] N. Krebs, I. Pugliesi, J. Hauer, E. Riedle, Two-dimensional Fourier transform spectroscopy in the ultraviolet with sub-20 fs pump pulses and 250–720 nm supercontinuum probe, New J. Phys. **15**, 085016 (2013).

[106] F. D. Fuller, J. P. Ogilvie, Continuum probe two-dimensional electronic spectroscopy of the photosystem II reaction center, EPJ Web of Conferences **41**, 08018 (2013).

[107] T. A. A. Oliver, N. H. C. Lewis, G. R. Fleming, Correlating the motion of electrons and nuclei with two-dimensional electronic-vibrational spectroscopy, Proc. Nat. Acad. Sci. USA **111**, 10061–10066 (2014).

[108] A. Hagfeldt, M. Grätzel, Molecular photovoltaics, Acc. Chem. Res. **33**, 269–277 (2000).

[109] A. J. Heeger, Semiconducting polymers: The third generation, Chem. Soc. Rev. **39**, 2354–2371 (2010).

[110] Y. Song, C. Hellmann, N. Stingelin, G. D. Scholes, The separation of vibrational coherence from ground- and excited-electronic states in P3HT film, J. Chem. Phys. **142**, 212410 (2015).

[111] P. Parkinson, C. Müller, N. Stingelin, M. B. Johnston, L. M. Herz, Role of ultrafast torsional relaxation in the emission from polythiophene aggregates, J. Phys. Chem. Lett. **1**, 2788–2792 (2010).

[112] R. Kersting, U. Lemmer, R. F. Mahrt, K. Leo, H. Kurz, H. Bässler, E. O. Göbel, Femtosecond energy relaxation in π-conjugated polymers, Phys. Rev. Lett. **70**, 3820–3823 (199).

[113] A. Ruseckas, P. Wood, I. D. W. Samuel, G. R. Webster, W. J. Mitchell, P. L. Burn, V. Sundström, Ultrafast depolarization of the fluorescence in a conjugated polymer, Phys. Rev. B **72**, 115214 (2005).

[114] F. Milota, P. Baum, J. Sperling, E. Riedle, K. Matuszna, H. Kauffmann, 2D optical spectroscopy of a conjugated polymer with tuneable visible 15 fs-pulses from a 200 kHz NOPA, in P. Corkum, D. Jonas, R. Miller, A. Weiner (eds.), *Ultrafast Phenomena XV* (Springer Berlin Heidelberg, 2007), volume 88 of *Springer Series in Chemical Physics*, 359–361.

[115] E. Collini, G. D. Scholes, Coherent intrachain energy migration in a conjugated polymer at room temperature, Science **323**, 369–373 (2009).

[116] Y. Song, S. N. Clafton, R. D. Pensack, T. W. Kee, G. D. Scholes, Vibrational coherence probes the mechanism of ultrafast electron transfer in polymer–fullerene blends, Nat. Commun. **5**, 4933 (2014).

[117] H. Yamagata, F. C. Spano, Strong photophysical similarities between conjugated polymers and J-aggregates, J. Phys. Chem. Lett **5**, 622–632 (2014).

[118] E. E. Jelley, Spectral absorption and fluorescence of dyes in the molecular state, Nature **138**, 1009 (1936).

[119] G. Scheibe, Über die Veränderlichkeit der Absorptionsspektren in Lösungen und die Nebenvalenzen alsihre Ursache, Angew. Chem. **49**, 563 (1936).

[120] F. Würthner, T. E. Kaiser, C. R. Saha-Möller, J-aggregates: From serendipitous discovery to supramolecular engineering of functional dye materials, Angew. Chem. Int. Ed. **50**, 3376–3410 (2011).

[121] F. Milota, J. Sperling, A. Nemeth, H. F. Kauffmann, Two-dimensional electronic photon echoes of a double band J-aggregate: Quantum oscillatory motion versus exciton relaxation, Chem. Phys. **357**, 45–53 (2009).

[122] F. Milota, V. Prokhorenko, T. Mančal, H. von Berlepsch, O. Bixner, H. Kauffmann, J. Hauer, Vibronic and vibrational coherences in two-dimensional electronic spectra of supramolecular J-aggregates, J. Phys. Chem. A **117**, 6007–6014 (2013).

[123] J. Lim, D. Paleček, F. Caycedo-Soler, C. N. Lincoln, J. Prior, H. von Berlepsch, S. F. Huelga, M. B. Plenio, D. Zigmantas, J. Hauer, Vibronic origin of long-lived coherence in an artificial molecular light harvester, Nat. Comm. **6** (2015).

[124] I. Stiopkin, T. Brixner, M. Yang, G. R. Fleming, Heterogeneous exciton dynamics revealed by two-dimensional optical spectroscopy, J. Phys. Chem. B **110**, 20032–20037 (2006).

[125] A. G. Dijkstra, T. la Cour Jansen, J. Knoester, Localization and coherent dynamics of excitons in the two-dimensional optical spectrum of molecular J-aggregates, J. Chem. Phys. **128**, 164511 (2008).

[126] R. Moca, S. R. Meech, I. A. Heisler, Two-dimensional electronic spectroscopy of chlorophyll a: Solvent dependent spectral evolution, J. Phys. Chem. B **119**, 8623–8630 (2015).

[127] F. V. A. Camargo, H. L. Anderson, S. R. Meech, I. A. Heisler, Full characterization of vibrational coherence in a porphyrin chromophore by two-dimensional electronic spectroscopy, J. Phys. Chem. A, **119**, 95–101 (2014).

[128] G. Nardin, T. M. Autry, G. Moody, R. Singh, H. Li, S. T. Cundiff, Multi-dimensional coherent optical spectroscopy of semiconductor nanostructures: Collinear and non-collinear approaches, J. Appl. Phys. **117**, 112804 (2015).

[129] S. T. Cundiff, T. Zhang, A. D. Bristow, D. Karaiskaj, X. Dai, Optical two-dimensional Fourier transform spectroscopy of semiconductor quantum wells, Acc. Chem. Res. **42**, 1423–1432 (2009).

[130] B. P. Fingerhut, M. Richter, J.-W. Luo, A. Zunger, S. Mukamel, 2D optical photon echo spectroscopy of a self-assembled quantum dot, Ann. Phys. (Berlin) **525**, 31–42 (2012).

[131] K. J. Karki, J. R. Widom, J. Seibt, I. Moody, M. C. Lonergan, T. Pullerits, A. H. Marcus, Coherent two-dimensional photocurrent spectroscopy in a PbS quantum dot photocell, Nat. Commun. **5** (2014).

[132] J. Seibt, T. Hansen, T. Pullerits, 3D spectroscopy of vibrational coherences in quantum dots: Theory, J. Phys. Chem. B **117**, 11124–11133 (2013).

[133] J. Seibt, T. Pullerits, Beating signals in 2D spectroscopy: Electronic or nuclear coherences? Application to a quantum dot model system, J. Phys. Chem. C **117**, 18728–18737 (2013).

[134] V. M. Huxter, T. A. A. Oliver, D. Budker, G. R. Fleming, Vibrational and electronic dynamics of nitrogen-vacancy centres in diamond revealed by two-dimensional ultrafast spectroscopy, Nature Phys. **9**(11), 744–749 (2013).

[135] L. Childress, R. Walsworth, M. Lukin, Atom-like crystal defects: From quantum computers to biological sensors, Phys. Today **67**, 38 (2014).

[136] R. W. Boyd, *Nonlinear Optics* (Academic Press, 2003), 2nd edition.

[137] M. Cho, *Two-Dimensional Optical Spectroscopy* (CRC Press, Boca Raton, 2009).

[138] S. Rahav, S. Mukamel, Multidimensional optical spectroscopy of a single molecule in a current-carrying state, J. Chem. Phys. **133**, 244106 (2010).

[139] H.-S. Tan, Theory and phase-cycling scheme selection principles of collinear phase coherent multi-dimensional optical spectroscopy, J. Chem. Phys. **129**, 124501 (2008).

[140] D. Brinks, F. D. Stefani, F. Kulzer, R. Hildner, T. H. Taminiau, Y. Avlasevich, K. Mullen, N. F. van Hulst, Visualizing and controlling vibrational wave packets of single molecules, Nature **465**, 905–908 (2010).

[141] M. Aeschlimann, T. Brixner, A. Fischer, C. Kramer, P. Melchior, W. Pfeiffer, C. Schneider, C. Strüber, P. Tuchscherer, D. V. Voronine, Coherent two-dimensional nanoscopy, Science **333**, 1723–1726 (2011).

[142] F. D. Fuller, D. E. Wilcox, J. P. Ogilvie, Pulse shaping based two-dimensional electronic spectroscopy in a background free geometry, Opt. Express **22**, 1018–1027 (2014).

[143] R. Kubo, Generalized cumulant expansion method, J. Phys. Soc **17**, 1100 (1962).

[144] R. Kubo, A stochastic theory of line shape, Adv. Chem. Phys. **15**, 101–127 (1969).

[145] D. Abramavicius, L. Valkunas, S. Mukamel, Transport and correlated fluctuations in the nonlinear optical response of excitons, Europhys. Lett. **80**, 17005 (2007).

[146] M. Cho, G. R. Fleming, The integrated photon echo and solvation dynamics. II. Peak shifts and 2D photon echo of a coupled chromophore, J. Chem. Phys. **123**, 114506 (2005).

[147] D. L. Andrews, T. Thirunamachandran, On three-dimensional rotational averages, J. Chem. Phys. **67**, 5026–5033 (1977).

[148] D. V. Voronine, D. Abramavicius, S. Mukamel, Coherent control of cross-peaks in chirality-induced two-dimensional optical signals of excitons, J. Chem. Phys. **125**, 4504 (2006).

[149] G. S. Schlau-Cohen, A. Ishizaki, T. R. Calhoun, N. S. Ginsberg, M. Ballottari, R. Bassi, G. R. Fleming, Elucidation of the timescales and origins of quantum electronic coherence in LHCII, Nature Chem. **4**, 389–395 (2012).

[150] D. Voronine, D. Abramavicius, S. Mukamel, Coherent control of pump-probe signals of helical structures by adaptive pulse polarizations, J. Chem. Phys. **124**, 034104 (2006).

[151] M. Yang, G. R. Fleming, Influence of phonons on exciton transfer dynamics: comparison of the Redfield, Förster, and modified Redfield equations, Chem. Phys. **275**, 355 – 372 (2002).

[152] H. van Amerongen, L. Valkunas, R. van Grondelle, *Photosynthetic Excitons* (World Scientific, Singapore, 2000).

[153] D. Abramavicius, B. Palmieri, S. Mukamel, Extracting single and two-exciton couplings in photosynthetic complexes by coherent two-dimensional electronic spectra, Chem. Phys. **357**, 79–84 (2009).

[154] R. M. Pearlstein, *Chlorophylls* (CRC Press: Boca Raton, FL, 1991), chapter Theoretical interpretation of antenna spectra, 1047–1078.

[155] B. P. Krueger, G. D. Scholes, G. R. Fleming, Calculation of couplings and energy-transfer pathways between the pigments of LH2 by the ab initio transition density cube method, J. Phys. Chem. B **102**, 5378–5386 (1998).

[156] M. E. Madjet, A. Abdurahman, T. Renger, Intermolecular coulomb couplings from ab initio electrostatic potentials: Application to optical transitions of strongly coupled pigments in photosynthetic antennae and reaction centers, J. Phys. Chem. B **110**, 17268–17281 (2006).

[157] O. Rancova, J. Sulskus, D. Abramavicius, Insight into the structure of photosynthetic LH2 aggregate from spectroscopy simulations, J. Phys. Chem. B **116**, 7803–7814 (2012).

[158] D. Abramavicius, L. Valkunas, S. Mukamel, Transport and correlated fluctuations in the nonlinear optical response of excitons, Europhys. Lett. **80**, 17005 (2007).

[159] V. Butkus, D. Abramavicius, A. Gelzinis, L. Valkunas, Two-dimensional optical spectroscopy of molecular aggregates, Lith. J. Phys. **50**, 267–303 (2010).

[160] P. Kjellberg, B. Brüggemann, T. Pullerits, Two-dimensional electronic spectroscopy of an excitonically coupled dimer, Phys. Rev. B **74**, 024303 (2006).

[161] V. Balevičius Jr., A. Gelzinis, D. Abramavicius, T. Mančal, L. Valkunas, Excitation dynamics and relaxation in a molecular heterodimer, Chem. Phys. **404**, 94–102 (2012).

[162] E. Collini, C. Wong, K. Wilk, P. Curmi, P. Brumer, G. Scholes, Coherently wired light-harvesting in photosynthetic marine algae at ambient temperature, Nature **463**, 644–647 (2010).

[163] N. Christensson, K. Žídek, N. Magdaong, A. LaFountain, H. Frank, D. Zigmantas, Origin of the bathochromic shift of astaxanthin in lobster protein: 2D electronic spectroscopy investigation of β-crustacyanin, J. Phys. Chem. B **117**, 11209–11219 (2013).

[164] T. Calhoun, N. Ginsberg, G. Schlau-Cohen, Y.-C. Cheng, M. Ballottari, R. Bassi, G. Fleming, Quantum coherence enabled determination of the energy landscape in light-harvesting complex II, J. Phys. Chem. B **113**, 16291–16295 (2009).

[165] D. B. Turner, Y. Hassan, G. D. Scholes, Exciton superposition states in cdse nanocrystals measured using broadband two-dimensional electronic spectroscopy, Nano Lett. **12**, 880–886 (2012).

[166] M. Ferretti, V. I. Novoderezhkin, E. Romero, R. Augulis, A. Pandit, D. Zigmantas, R. van Grondelle, The nature of coherences in the B820 bacteriochlorophyll dimer revealed by two-dimensional electronic spectroscopy, Phys. Chem. Chem. Phys. **16**, 9930–9939 (2014).

[167] E. Harel, G. S. Engel, Quantum coherence spectroscopy reveals complex dynamics in bacterial light-harvesting complex 2 (LH2), Proc. Natl. Acad. Sci. USA **109**, 706–711 (2012).

[168] D. B. Turner, K. E. Wilk, P. M. G. Curmi, G. D. Scholes, Comparison of electronic and vibrational coherence measured by two-dimensional electronic spectroscopy, J. Phys. Chem. Lett. **2**, 1904–1911 (2011).

[169] W. Barford, D. Trembath, Exciton localization in polymers with static disorder, Phys. Rev. B **80**, 165418 (2009).

[170] M. Mohseni, P. Rebentrost, S. Lloyd, A. Aspuru-Guzik, Environment-assisted quantum walks in photosynthetic energy transfer, J. Chem. Phys. **129**, 174106 (2008).

[171] A. Ishizaki, G. R. Fleming, Theoretical examination of quantum coherence in a photosynthetic system at physiological temperature, Proc. Natl. Acad. Sci. USA **106**, 17255–17260 (2009).

[172] H. Dong, G. R. Fleming, Inhomogeneous broadening induced long-lived integrated two-color coherence photon echo signal, J. Phys. Chem. B **118**, 8956–8961 (2014).

[173] A. Ishizaki, G. R. Fleming, On the adequacy of the Redfield equation and related approaches to the study of quantum dynamics in electronic energy transfer, J. Chem. Phys. **130**, 234110 (2009).

[174] X. J. Jordanides, G. D. Scholes, W. A. Shapley, J. R. Reimers, G. R. Fleming, Electronic couplings and energy transfer dynamics in the oxidized primary electron donor of the bacterial reaction center, J. Phys. Chem. B **108**, 1753–1765 (2004).

[175] X. J. Jordanides, G. D. Scholes, G. R. Fleming, The mechanism of energy transfer in the bacterial photosynthetic reaction center, J. Phys. Chem. B **105**, 1652–1669 (2001).

[176] I. S. Ryu, H. Dong, G. R. Fleming, Role of electronic-vibrational mixing in enhancing vibrational coherences in the ground electronic states of photosynthetic bacterial reaction center, J. Phys. Chem. B **118**, 1381–1388 (2014).

[177] F. C. Spano, *J-aggregates* (World Scientific, 2012), chapter Vibronic coupling in *J*-aggregates, 49–75, 2nd edition.

[178] V. Butkus, D. Zigmantas, L. Valkunas, D. Abramavicius, Phase relationships of spectral oscillations in 2D molecular spectroscopy, EPJ Web of Conferences **41**, 05021 (2013).

[179] E. Bašinskaitė, V. Butkus, D. Abramavicius, L. Valkunas, Vibronic models for nonlinear spectroscopy simulations, Photosynth. Res. **121**, 95–106 (2014).

[180] T. Mančal, A. Nemeth, F. Milota, V. Lukeš, H. Kauffmann, J. Sperling, Vibrational wave packet induced oscillations in two-dimensional electronic spectra. II. Theory, J. Chem. Phys. **132**, 184515 (2010).

[181] D. Egorova, Detection of electronic and vibrational coherences in molecular systems by 2D electronic photon echo spectroscopy, Chem. Phys. **347**, 166–176 (2008).

[182] T. Holstein, Studies of polaron motion: Part I. The molecular-crystal model, Ann. Phys. **8**, 325–342 (1959).

[183] T. Renger, V. May, O. Kühn, Ultrafast excitation energy transfer dynamics in photosynthetic pigment–protein complexes, Phys. Rep. **343**, 137–254 (2001).

[184] A. Eisfeld, J. S. Briggs, The J-band of organic dyes: Lineshape and coherence length, Chem. Phys. **281**, 61–70 (2002).

[185] F. C. Spano, The spectral signatures of Frenkel polarons in H- and J-aggregates, Acc. Chem. Res. **43**, 429–439 (2010).

[186] S. Polyutov, O. Kühn, T. Pullerits, Exciton-vibrational coupling in molecular aggregates: Electronic versus vibronic dimer, Chem. Phys. **394**, 21–28 (2012).

[187] A. Schulze, M. Torbjörnsson, O. Kühn, T. Pullerits, Exciton coupling induces vibronic hyperchromism in light-harvesting complexes, New J. Phys. **16**, 045010 (2014).

[188] A. Eisfeld, L. Braun, W. Strunz, J. Briggs, J. Beck, V. Engel, Vibronic energies and spectra of molecular dimers, J. Chem. Phys. **122**, 134103 (2005).

[189] J. Seibt, V. Dehm, F. Würthner, V. Engel, Circular dichroism spectroscopy of small molecular aggregates: Dynamical features and size effects, J. Chem. Phys. **128**, 204303 (2008).

[190] O. Bixner, V. Lukeš, T. Mančal, J. Hauer, F. Milota, M. Fischer, I. Pugliesi, M. Bradler, W. Schmid, E. Riedle, Ultrafast photo-induced charge transfer unveiled by two-dimensional electronic spectroscopy, J. Chem. Phys. **136**, 204503 (2012).

[191] F. C. Spano, J. Clark, C. Silva, R. H. Friend, Determining exciton coherence from the photoluminescence spectral line shape in poly(3-hexylthiophene) thin films, J. Chem. Phys. **130**, 074904 (2009).

[192] A. Moran, J. Maddox, J. Hong, J. Kim, R. Nome, G. Bazan, S. Mukamel, N. Scherer, Optical coherence and theoretical study of the excitation dynamics of a highly symmetric cyclophane-linked oligophenylenevinylene dimer, J. Chem. Phys. **124**, 194904 (2006).

[193] J. Womick, A. Moran, Vibronic enhancement of exciton sizes and energy transport in photosynthetic complexes, J. Phys. Chem. B **115**, 1347–1356 (2011).

[194] Q. Liu, J. Ye, Y. Zhao, Multimode vibronic spectra of the Holstein molecular crystal model, Phys. Chem. Chem. Phys. **12**, 6045–6053 (2010).

[195] J. Adolphs, T. Renger, How proteins trigger excitation energy transfer in the FMO complex of green sulfur bacteria, Biophys. J. **91**, 2778–2797 (2006).

[196] G. Richards, K. Wilk, P. Curmi, H. Quiney, J. Davis, Coherent vibronic coupling in light-harvesting complexes from photosynthetic marine algae, J. Phys. Chem. Lett. **3**, 272–277 (2012).

[197] T. Kobayashi, *J – aggregates* (World Scientific: Singapore, 1996).

[198] B. Kopainsky, J. Hallermeier, W. Kaiser, The first step of aggregation of PIC: The dimerization, Chem. Phys. Lett. **83**, 498–502 (1981).

[199] H. Fidder, Absorption and emission studies on pure and mixed J-aggregates of pseudoisocyanine, Chem. Phys. **341**, 158–168 (2007).

[200] W. West, S. Pearce, The dimeric state of cyanine dyes, J. Phys. Chem. **69**, 1894–1903 (1965).

[201] I. Baraldi, M. Caselli, F. Momicchioli, G. Ponterini, D. Vanossi, Dimerization of green sensitizing cyanines in solution. A spectroscopic and theoretical study of the bonding nature, Chem. Phys. **275**, 149–165 (2002).

[202] J. Seibt, P. Marquetand, V. Engel, Z. Chen, V. Dehm, F. Würthner, On the geometry dependence of molecular dimer spectra with an application to aggregates of perylene bisimide, Chem. Phys. **328**, 354–362 (2006).

[203] M. Schröter, T. Pullerits, O. Kühn, Unraveling the quantum state mixing of excitonic and vibronic excitations in the dynamics of molecular aggregates, Ann. Phys. (Berlin) (2015).

[204] J. Seibt, K. Renziehausen, D. V. Voronine, V. Engel, Probing the geometry dependence of molecular dimers with two-dimensional-vibronic spectroscopy, J. Chem. Phys. **130**, 134318 (2009).

[205] M. F. Gelin, L. Z. Sharp, D. Egorova, W. Domcke, Bath-induced correlations and relaxation of vibronic dimers, J. Chem. Phys. **136**, 034507 (2012).

[206] A. Kell, X. Feng, M. Reppert, R. J. Jankowiak, On the shape of the phonon spectral density in photosynthetic complexes, J. Phys. Chem. B **117**, 7317–7323 (2013).

[207] M. T. Zanni, N.-H. Ge, Y. S. Kim, R. M. Hochstrasser, Two-dimensional IR spectroscopy can be designed to eliminate the diagonal peaks and expose only the crosspeaks needed for structure determination, Proc. Natl. Acad. Sci. USA **98**, 11265–11270 (2001).

[208] M. C. O'Sullivan, J. K. Sprafke, D. V. Kondratuk, C. Rinfray, T. D. W. Claridge, A. Saywell, M. O. Blunt, J. N. O'Shea, P. H. Beton, M. Malfois, H. L. Anderson, Vernier templating and synthesis of a 12-porphyrin nanoring, Nature **469**, 72–75 (2011).

[209] A. V. Aggarwal, A. Thiessen, A. Idelson, D. Kalle, D. Würsch, T. Stangl, F. Steiner, S.-S. Jester, Vogelsang, S. Höger, J. M. Lupton, Fluctuating exciton localization in giant π-conjugated spoked-wheel macrocycles, Nature Chem. **5**, 964–970 (2013).

[210] J. Strümpfer, K. Schulten, Light harvesting complex II B850 excitation dynamics, J. Chem. Phys. **131**, 225101 (2009).

[211] S. Niwa, L.-J. Yu, K. Takeda, Y. Hirano, T. Kawakami, Z.-Y. Wang-Otomo, K. Miki, Structure of the LH1–RC complex from *Thermochromatium tepidum* at 3.0Å, Nature **508**, 228–232 (2014).

[212] E. L. Read, G. S. Schlau-Cohen, G. S. Engel, T. Georgiou, M. Z. Papiz, G. R. Fleming, Pigment organization and energy level structure in light-harvesting complex 4: Insights from two-dimensional electronic spectroscopy, J. Phys. Chem. B **113**, 6495–6504 (2009).

[213] X. Guo, M. Baumgarten, K. Müllen, Designing π-conjugated polymers for organic electronics, Prog. Polym. Sci. **38**, 1832–1908 (2013).

[214] J. K. Sprafke, D. V. Kondratuk, M. Wykes, A. L. Thompson, M. Hoffmann, R. Drevinskas, W.-H. Chen, C. K. Yong, J. Kärnbratt, J. E. Bullock, M. Malfois, M. R. Wasielewski, B. Albinsson, L. M. Herz, D. Zigmantas, D. Beljonne, H. L. Anderson, Belt-shaped π-systems: Relating geometry to electronic structure in a six-porphyrin nanoring, J. Am. Chem. Soc. **133**, 17262–17273 (2011).

[215] M. Hoffmann, J. Karnbratt, M.-H. Chang, L. M. Herz, B. Albinsson, H. L. Anderson, Enhanced π conjugation around a porphyrin[6] nanoring, Angew. Chem. Int. Ed. **47**, 4993–4996 (2008).

[216] J. Dostál, F. Vácha, J. Pšenčík, D. Zigmantas, 2D electronic spectroscopy reveals excitonic structure in the baseplate of a chlorosome, J. Phys. Chem. Lett. **5**, 1743–1747 (2014).

[217] H. Li, A. D. Bristow, M. E. Siemens, G. Moody, S. T. Cundiff, Unraveling quantum pathways using optical 3D Fourier-transform spectroscopy, Nat. Commun. **4**, 1390 (2013).

[218] K. S. Kim, S. B. Noh, T. Katsuda, S. Ito, A. Osuka, D. Kim, Charge transfer induced enhancement of near-IR two-photon absorption of 5,15-bis(azulenylethynyl) zinc(II) porphyrins, Chem. Commun. **24**, 2479–2481 (2007).

Appendix A

Amplitudes of peaks in 2D spectrum of electronic dimer

Asuming the *XXXX* experimental direction (all four electric fields are polarized along the same axis) and the spatial configuration of dipole moments in a two-chromophore system described in Sec. 2.3, analytical expressions of intensities of each pathway, contributing to the rephasing and nonrephasing spectrum can be obtained

The orientationally-averaged products (Eq. (2.55)) of transition dipole moments can be written for the full set of double-sided Feynman diagrams (the ESA, SE and GSB contributions), shown in Fig. 2.8. Here we adopt notation $\mathcal{A}^{\mathsf{X}}_{cd}$ denoting the $\mathsf{X} \in \{\mathsf{ESA}, \mathsf{SE}\}$ contribution, maintaining coherence or population $|c\rangle\langle d|$ during the waiting time t_2, or $\mathsf{X} = \mathsf{GSB}$ contribution, maintaining population in the ground state during t_2 and coherences $|\mathsf{g}\rangle\langle \mathsf{e}_c|$ and $|\mathsf{e}_d\rangle\langle \mathsf{g}|$ during time intervals t_1 and t_3, respectively.

$$\mathcal{A}^{\mathsf{ESA}}_{\mathsf{e}_1\mathsf{e}_2} = \mathcal{A}^{\mathsf{ESA}}_{\mathsf{e}_2\mathsf{e}_1} = \langle \boldsymbol{\mu}_{g\mathsf{e}_2}\boldsymbol{\mu}_{g\mathsf{e}_1}\boldsymbol{\mu}_{\mathsf{e}_2\mathsf{f}}\boldsymbol{\mu}_{\mathsf{e}_1\mathsf{f}}\rangle = -\frac{1}{15}\sin^2\phi, \tag{A.1}$$

$$\mathcal{A}^{\mathsf{ESA}}_{\mathsf{e}_1\mathsf{e}_1} = \mathcal{A}^{\mathsf{SE}}_{\mathsf{e}_1\mathsf{e}_1} = \langle \boldsymbol{\mu}^2_{g\mathsf{e}_1}\boldsymbol{\mu}^2_{\mathsf{e}_1\mathsf{f}}\rangle = \frac{1}{5}\left(1+\cos\phi\right)^2, \tag{A.2}$$

$$\mathcal{A}^{\mathsf{ESA}}_{\mathsf{e}_2\mathsf{e}_2} = \langle \boldsymbol{\mu}^2_{g\mathsf{e}_2}\boldsymbol{\mu}^2_{\mathsf{e}_2\mathsf{f}}\rangle = \frac{1}{5}\left(1-\cos\phi\right)^2, \tag{A.3}$$

$$\mathcal{A}^{\mathsf{SE}}_{\mathsf{e}_1\mathsf{e}_2} = \mathcal{A}^{\mathsf{SE}}_{\mathsf{e}_2\mathsf{e}_1} = \langle \boldsymbol{\mu}^2_{g\mathsf{e}_2}\boldsymbol{\mu}^2_{g\mathsf{e}_1}\rangle = \frac{1}{15}\sin^2\phi, \tag{A.4}$$

$$\mathcal{A}^{\mathsf{SE}}_{\mathsf{e}_1\mathsf{e}_1} = \langle \boldsymbol{\mu}^2_{g\mathsf{e}_1}\boldsymbol{\mu}^2_{\mathsf{e}_1\mathsf{f}}\rangle = \frac{1}{5}\left(1+\cos\phi\right)^2, \tag{A.5}$$

$$\mathcal{A}^{\mathsf{SE}}_{\mathsf{e}_2\mathsf{e}_2} = \langle \boldsymbol{\mu}^2_{g\mathsf{e}_2}\boldsymbol{\mu}^2_{\mathsf{e}_2\mathsf{f}}\rangle = \frac{1}{5}\left(1-\cos\phi\right)^2, \tag{A.6}$$

$$\mathcal{A}^{\mathsf{GSB}}_{\mathsf{e}_1\mathsf{e}_2} = \mathcal{A}^{\mathsf{GSB}}_{\mathsf{e}_2\mathsf{e}_1} = \langle \boldsymbol{\mu}^2_{g\mathsf{e}_2}\boldsymbol{\mu}^2_{g\mathsf{e}_1}\rangle = \frac{1}{15}\sin^2\phi, \tag{A.7}$$

$$\mathcal{A}^{\mathrm{GSB}}_{\mathrm{e_1e_1}} = \langle \boldsymbol{\mu}^2_{g\mathrm{e}_1} \boldsymbol{\mu}^2_{\mathrm{e}_1\mathrm{f}} \rangle = \frac{1}{5}\left(1+\cos\phi\right)^2, \tag{A.8}$$

$$\mathcal{A}^{\mathrm{GSB}}_{\mathrm{e_2e_2}} = \langle \boldsymbol{\mu}^2_{g\mathrm{e}_2} \boldsymbol{\mu}^2_{\mathrm{e}_2\mathrm{f}} \rangle = \frac{1}{5}\left(1-\cos\phi\right)^2. \tag{A.9}$$

Here we adopt notation A^{p}_{nm} and A^{c}_{nm} for intensities of a peak, emerging at $\omega_1 = \varepsilon_{\mathrm{e}_n}$, $\omega_3 = \varepsilon_{\mathrm{e}_m}$ and maintaining a population (non-oscillating contribution, superscript "p") or a coherence (oscillating contribution, superscipt "c") during waiting time t_2, respectively. The amplitudes in the nonrephasing spectrum are indicated with tilde ("$\sim$") symbols:

$$A^{\mathrm{p}}_{11} = \tilde{A}{}^{\mathrm{p}}_{11} = \mathcal{A}^{\mathrm{SE}}_{\mathrm{e_1e_1}} + \mathcal{A}^{\mathrm{GSB}}_{\mathrm{e_1e_1}} = \frac{2}{5}\left(1+\cos\phi\right)^2, \tag{A.10}$$

$$A^{\mathrm{p}}_{22} = \tilde{A}{}^{\mathrm{p}}_{22} = \mathcal{A}^{\mathrm{SE}}_{\mathrm{e_2e_2}} + \mathcal{A}^{\mathrm{GSB}}_{\mathrm{e_2e_2}} = \frac{2}{5}\left(1-\cos\phi\right)^2, \tag{A.11}$$

$$A^{\mathrm{p}}_{21} = \tilde{A}{}^{\mathrm{p}}_{21} = -\mathcal{A}^{\mathrm{ESA}}_{\mathrm{e_2e_2}} + \mathcal{A}^{\mathrm{GSB}}_{\mathrm{e_2e_1}} = -\frac{1}{5}\left(1-\cos\phi\right)^2 + \frac{1}{15}\sin^2\phi, \tag{A.12}$$

$$A^{\mathrm{p}}_{12} = \tilde{A}{}^{\mathrm{p}}_{12} = -\mathcal{A}^{\mathrm{ESA}}_{\mathrm{e_1e_1}} + \mathcal{A}^{\mathrm{GSB}}_{\mathrm{e_1e_2}} = -\frac{1}{5}\left(1+\cos\phi\right)^2 + \frac{1}{15}\sin^2\phi. \tag{A.13}$$

$$A^{\mathrm{c}}_{11} = A^{\mathrm{c}}_{22} = \tilde{A}{}^{\mathrm{c}}_{12} = \tilde{A}{}^{\mathrm{c}}_{21} = 0, \tag{A.14}$$

$$A^{\mathrm{c}}_{21} = \tilde{A}{}^{\mathrm{c}}_{22} = -\mathcal{A}^{\mathrm{ESA}}_{\mathrm{e_2e_1}} + \mathcal{A}^{\mathrm{SE}}_{\mathrm{e_2e_1}} = \frac{2}{15}\sin^2\phi, \tag{A.15}$$

$$A^{\mathrm{c}}_{12} = \tilde{A}{}^{\mathrm{c}}_{11} = -\mathcal{A}^{\mathrm{ESA}}_{\mathrm{e_1e_2}} + \mathcal{A}^{\mathrm{SE}}_{\mathrm{e_1e_2}} = \frac{2}{15}\sin^2\phi. \tag{A.16}$$

Appendix B

Amplitudes of peaks in 2D spectrum of displaced oscillator

The Franck–Condon factor for transition from one ground state level to some excited state level of the displaced oscillator is given by Eq. (3.4). By assuming all the relevant Feynman diagrams to the 2D spectrum (Fig. B.1), we can get the analytical expressions for all peaks, positioned at $\omega_1 = \varepsilon + m\omega_0$ and $\omega_3 = \varepsilon + n\omega_0$, where $m = 0, 1, ...$ and $n = 0, \pm 1, ...$. The third parameter $k = 0, 1, ...$ describes various contributions is the oscillation frequency during the waiting time t_2, $\omega_2 = k\omega_0$. Thus, the amplitude in the rephasing signal will be:

$$A(m,n,k) = F_{0m}\Big(F_{km}F_{0,n+k}F_{k,n+k} + F_{0,m+k}F_{m+k-n,m}F_{m+k-n,m+k} + F_{0,m-k}F_{m-k-n,m}F_{m-k-n,m-k}\Big) \tag{B.1}$$

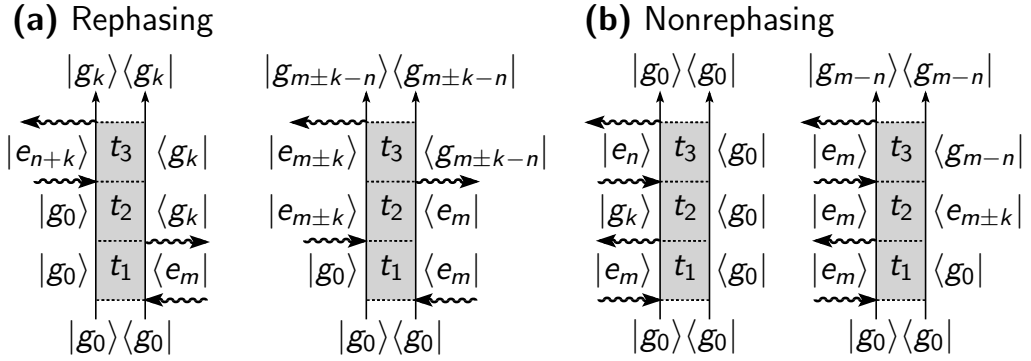

Fig. B.1. Diagrams for peaks positioned at $\omega_1 = \varepsilon + m\omega_0$, $\omega_3 = \varepsilon + n\omega_0$ and oscillating with frequency $\omega_2 = k\omega_0$ and corresponding FC factors for each interaction. Note that all indices cannot be negative. The corresponding diagram is zero otherwise.

and the amplitude of the nonrephasing signal:

$$\widetilde{A}(m,n,k) = F_{0m}\Big(F_{km}F_{kn}F_{0,n} + F_{0,m+k}F_{m-n,m+k}F_{m-n,m} + F_{0,m-k}F_{m-n,m-k}F_{m-n,m}\Big). \tag{B.2}$$

These amplitudes are related to those, given in Fig. 3.4, as $A^{\mathrm{p}}_{mn} \equiv A(m-1,n-1,0)$ and $\widetilde{A}^{\mathrm{c}}_{mn} \equiv \widetilde{A}(m-1,n-1,0)$. The amplitudes of the four most prominent peaks are then:

$$A^{\mathrm{p}}_{11} = \widetilde{A}^{\mathrm{p}}_{11} = 2\mathrm{e}^{-2s}, \tag{B.3}$$

$$A^{\mathrm{p}}_{22} = \widetilde{A}^{\mathrm{p}}_{22} = 2s^2\mathrm{e}^{-2s}, \tag{B.4}$$

$$A^{\mathrm{p}}_{21} = \widetilde{A}^{\mathrm{p}}_{21} = s\left(s^2-2s+2\right)\mathrm{e}^{-2s}, \tag{B.5}$$

$$A^{\mathrm{p}}_{21} = \widetilde{A}^{\mathrm{p}}_{21} = s\mathrm{e}^{-2s}. \tag{B.6}$$

Amplitudes of the oscillatory contributions in the rephasing spectrum:

$$A^{\mathrm{c}}_{11} = 2s\,(s-1)\,\mathrm{e}^{-2s}, \tag{B.7}$$

$$A^{\mathrm{c}}_{22} = \frac{s^2}{\sqrt{2}}\,(1-s)\,(2-s)\,\mathrm{e}^{-2s}, \tag{B.8}$$

$$A^{\mathrm{c}}_{21} = \frac{s}{4\sqrt{2}}\left(8\sqrt{2}-\left(8\sqrt{2}+4\right)s+\left(4\sqrt{2}+10\right)s^2-6s^3+s^4\right)\mathrm{e}^{-2s}, \tag{B.9}$$

$$A^{\mathrm{c}}_{12} = \frac{s}{2\sqrt{2}}\left(s^2-2s+2\sqrt{2}\right)\mathrm{e}^{-2s}, \tag{B.10}$$

$$A^{\mathrm{c}}_{10} = \frac{1}{2}s(s^2-2s+2)\mathrm{e}^{-2s}, \tag{B.11}$$

$$A^{\mathrm{c}}_{20} = s\left(2s-2+\frac{6}{\sqrt{2}}s^3(s-3)\right)\mathrm{e}^{-2s}. \tag{B.12}$$

In the nonrephasing spectrum:

$$\widetilde{A}^{\mathrm{c}}_{11} = 2s\mathrm{e}^{-2s}, \tag{B.13}$$

$$\widetilde{A}^{\mathrm{c}}_{22} = s\left(\frac{3}{2}s^2-2s+2\right)\mathrm{e}^{-2s}, \tag{B.14}$$

$$\widetilde{A}^{\mathrm{c}}_{21} = s(s-1)(\frac{1}{2}s^2-s+2)\mathrm{e}^{-2s}, \tag{B.15}$$

$$\widetilde{A}^{\mathrm{c}}_{12} = s\,(s-1)\,\mathrm{e}^{-2s}, \tag{B.16}$$

$$\widetilde{A}^{\mathrm{c}}_{10} = s^{3/2}\mathrm{e}^{-2s}, \tag{B.17}$$

$$\widetilde{A}^{\mathrm{c}}_{20} = s^{3/2}(1-s)\mathrm{e}^{-2s}. \tag{B.18}$$

Appendix C

Correlation functions of vibrational aggregate

In this appendix, expressions of correlation functions characterizing fluctuations in manifolds of singly- and doubly-excited states are derived, using the system–bath coupling Hamiltonian definitions given by eqs. (3.30) and (3.31).

Singly-excited eigenstates are obtained by the unitary transformation, and we get similar symmetry properties as for correlation function in the ground-state manifold (Eq. (3.35)). We assume, that correlations due to electronic and vibrational diagonal fluctuations are just scaled by some arbitrary constants κ_{e} and κ_{v}, respectively,

$$C_0(t) = \sum_{m\alpha} \frac{z_{m\alpha}^2}{2\omega_m} \langle \widehat{x}_\alpha(t) \widehat{x}_\alpha(0) \rangle, \tag{C.1}$$

$$\kappa_{\mathrm{e}} C_0(t) = 2 \sum_{\alpha} w_\alpha d_\alpha^2 \langle \widehat{x}_\alpha(t) \widehat{x}_\alpha(0) \rangle, \tag{C.2}$$

$$\kappa_{\mathrm{v}} C_0(t) = \sum_{m\alpha} z_{m\alpha} d_\alpha \sqrt{\frac{w_\alpha}{\omega_m}} \langle \widehat{x}_\alpha(t) \widehat{x}_\alpha(0) \rangle. \tag{C.3}$$

Since coupling to the surroundings is identical for each molecule, $d_{mm,\alpha}$ was set to d_α here. The correlation function for the eigenstates can be written as

$$\begin{aligned} C^{(\mathrm{ee})}_{p_1 p_2, p_3 p_4}(t) = C_0(t) \sum_{m,n}^{N} \sum_{\mathbf{i},\mathbf{j}} \sum_{\boldsymbol{k},\boldsymbol{l}} \sum_{a}^{N} \psi^{m*}_{p_1,\mathbf{i}} \psi^{m}_{p_2,\mathbf{j}} \psi^{n*}_{p_3,\boldsymbol{k}} \psi^{n}_{p_4,\boldsymbol{l}} \\ \times \Big\{ \langle i_a, j_a \rangle \langle k_a, l_a \rangle \prod_{\substack{s \\ s \neq a}} \delta_{i_s j_s} \delta_{k_s l_s} + \kappa_{\mathrm{v}} \langle i_a, j_a \rangle \prod_{\substack{s \\ s \neq a}} \delta_{i_s j_s} \delta_{\mathbf{kl}} \\ + \kappa_{\mathrm{v}} \langle k_a, l_a \rangle \prod_{\substack{s \\ s \neq a}} \delta_{k_s l_s} \delta_{\mathbf{ij}} + \kappa_{\mathrm{e}} \delta_{\mathbf{ij}} \delta_{\mathbf{kl}} \Big\}. \end{aligned} \tag{C.4}$$

Here the first sum is over different chromophores, the second and third sum is

over the vibrational levels of the whole aggregate and finally the sum over a is over the different vibrational modes (which is identical to the number of sites since each site has one vibrational coordinate). We then get the following result:

$$\begin{aligned} C^{(\mathrm{ee})}_{p_1p_2,p_3p_4}(t) = C_0(t)\sum_{\mathbf{i},\mathbf{k}}\sum_{s}^{N}\Big\{&\sqrt{i_s k_s}\,\xi^{p_1p_2}_{\mathbf{i}_s^-}\xi^{p_3p_4}_{\mathbf{k}_s^-} + \sqrt{(i_s+1)k_s}\,\xi^{p_1p_2}_{\mathbf{i}_s^+}\xi^{p_3p_4}_{\mathbf{k}_s^-} \\ &+ \sqrt{i_s(k_s+1)}\,\xi^{p_1p_2}_{\mathbf{i}_s^-}\xi^{p_3p_4}_{\mathbf{k}_s^+} + \sqrt{(i_s+1)(k_s+1)}\,\xi^{p_1p_2}_{\mathbf{i}_s^+}\xi^{p_3p_4}_{\mathbf{k}_s^+} \\ &+ \kappa_{\mathrm{e}}\xi^{p_1p_2}_{\mathbf{i}}\xi^{p_3p_4}_{\mathbf{k}} + \kappa_{\mathrm{v}}\xi^{p_3p_4}_{\mathbf{k}}\left[\sqrt{i_s}\,\xi^{p_1p_2}_{\mathbf{i}_s^-} + \sqrt{i_s+1}\,\xi^{p_1p_2}_{\mathbf{i}_s^+}\right] \\ &+ \kappa_{\mathrm{v}}\xi^{p_1p_2}_{\mathbf{i}}\left[\sqrt{k_s}\,\xi^{p_3p_4}_{\mathbf{k}_s^-} + \sqrt{k_s+1}\,\xi^{p_3p_4}_{\mathbf{k}_s^+}\right]\Big\} \end{aligned} \tag{C.5}$$

Here

$$\xi^{p_ap_b}_{\mathbf{i}_s^\pm} = \sum_{n}^{N}\psi^{n*}_{p_a,\mathbf{i}}\psi^{n}_{p_b,\mathbf{i}_s^\pm} \tag{C.6}$$

and

$$\xi^{p_ap_b}_{\mathbf{i}} = \sum_{n}^{N}\psi^{n*}_{p_a,\mathbf{i}}\psi^{n}_{p_b,\mathbf{i}}. \tag{C.7}$$

For the functions involving the double excitations we can write similarly:

$$\begin{aligned} C^{(\mathrm{ef})}_{p_1p_2,r_1r_2}(t) = C_0(t)\sum_{s}^{N}\Big\{&\sqrt{i_s k_s}\,\xi^{p_1p_2}_{\mathbf{i}_s^-}\Xi^{r_1r_2}_{\mathbf{k}_s^-} + \sqrt{(i_s+1)k_s}\,\xi^{p_1p_2}_{\mathbf{i}_s^+}\Xi^{r_1r_2}_{\mathbf{k}_s^-} \\ &+ \sqrt{i_s(k_s+1)}\,\xi^{p_1p_2}_{\mathbf{i}_s^-}\Xi^{r_1r_2}_{\mathbf{k}_s^+} + \sqrt{(i_s+1)(k_s+1)}\,\xi^{p_1p_2}_{\mathbf{i}_s^+}\Xi^{r_1r_2}_{\mathbf{k}_s^+} \\ &+ 2\kappa_{\mathrm{e}}\xi^{p_1p_2}_{\mathbf{i}}\Xi^{r_1r_2}_{\mathbf{k}} + 2\kappa_{\mathrm{v}}\Xi^{r_1r_2}_{\mathbf{k}}\left[\sqrt{i_s}\,\xi^{p_1p_2}_{\mathbf{i}_s^-} + \sqrt{i_s+1}\,\xi^{p_1p_2}_{\mathbf{i}_s^+}\right] \\ &+ \kappa_{\mathrm{v}}\xi^{p_1p_2}_{\mathbf{i}}\left[\sqrt{k_s}\,\Xi^{r_1r_2}_{\mathbf{k}_s^-} + \sqrt{k_s+1}\,\Xi^{r_1r_2}_{\mathbf{k}_s^+}\right]\Big\} \end{aligned} \tag{C.8}$$

and

$$\begin{aligned} C^{(\mathrm{ff})}_{r_1r_2,r_3r_4}(t) = C_0(t)\sum_{s}^{N}\Big\{&\sqrt{i_s k_s}\,\Xi^{r_1r_2}_{\mathbf{i}_s^-}\Xi^{r_3r_4}_{\mathbf{k}_s^-} + \sqrt{(i_s+1)k_s}\,\Xi^{r_1r_2}_{\mathbf{i}_s^+}\Xi^{r_3r_4}_{\mathbf{k}_s^-} \\ &+ \sqrt{i_s(k_s+1)}\,\Xi^{r_1r_2}_{\mathbf{i}_s^-}\Xi^{r_3r_4}_{\mathbf{k}_s^+} + \sqrt{(i_s+1)(k_s+1)}\,\Xi^{r_1r_2}_{\mathbf{i}_s^+}\Xi^{r_3r_4}_{\mathbf{k}_s^+} \\ &+ 4\kappa_{\mathrm{e}}\Xi^{r_1r_2}_{\mathbf{i}}\Xi^{r_3r_4}_{\mathbf{k}} + 2\kappa_{\mathrm{v}}\Xi^{r_1r_2}_{\mathbf{i}}\left[\sqrt{k_s}\,\Xi^{r_3r_4}_{\mathbf{k}_s^-} + \sqrt{k_s+1}\,\Xi^{r_3r_4}_{\mathbf{i}_s^+}\right] \\ &+ 2\kappa_{\mathrm{v}}\Xi^{r_3r_4}_{\mathbf{i}}\left[\sqrt{i_s}\,\Xi^{r_1r_2}_{\mathbf{i}_s^-} + \sqrt{i_s+1}\,\Xi^{r_1r_2}_{\mathbf{i}_s^+}\right]\Big\} \end{aligned} \tag{C.9}$$

where

$$\Xi^{r_1r_2}_{\mathbf{i}_s^\pm} = \sum_{\substack{m,n\\ m>n}}^{N}\Psi^{(mn)*}_{r_1,\mathbf{i}}\Psi^{(mn)}_{r_2,\mathbf{i}_s^\pm} \tag{C.10}$$

and

$$\Xi_{\mathbf{i}}^{r_1 r_2} = \sum_{\substack{m,n \\ m>n}}^{N} \psi_{r_1,\mathbf{i}}^{(mn)*} \psi_{r_2,\mathbf{i}}^{(mn)}. \tag{C.11}$$

The lineshape broadening coefficients $h_{\mathsf{e}_{p_1}\mathsf{e}_{p_2},\mathsf{e}_{p_3}\mathsf{e}_{p_4}}$, $h_{\mathsf{e}_{p_1}\mathsf{e}_{p_2},\mathsf{f}_{r_1}\mathsf{f}_{r_2}}$ and $h_{\mathsf{f}_{r_1}\mathsf{f}_{r_2},\mathsf{f}_{r_3}\mathsf{f}_{r_4}}$, according to the definition in Sec. 3.2.1, are then just the time-independent parts (sums) on the right hand-sides of eqs. (C.5),(C.8) and (C.9), respectively. They are used in calculations of transfer rates within the singly-excited state manifold (Eq. (3.2.1)) and lineshape functions for the response functions (see Appendix D). Values of $\kappa_{\mathsf{e}} = \kappa_{\mathsf{v}} = 0$ were used in calculations.

Appendix D

Response functions of vibrational aggregate

We consider the photon echo signals of the 2D electronic spectroscopy in the impulsive limit. The expressions of the system response function here are presented by following the notation used in Fig. 3.6. The expressions for the response involve the spectral lineshape functions $g_{ab}(t) \equiv h_{aa,bb}g_0(t)$. These are given by the linear integral transformation of the bath correlation functions, $g_0(t) = \int_0^t \mathrm{d}t' \int_0^{t'} \mathrm{d}t'' \langle C_0(t'')C_0(0)\rangle$.[69,70] The response functions of the photon echo (rephasing) signal when transport is ignored are then

$$S_{\mathrm{GSB}}(t_1,t_2,t_3) = \mathrm{i}^3\theta(t_1)\theta(t_2)\theta(t_3)\sum_{\mathbf{ij}}\sum_{p_1p_2} p_{\mathrm{g_i}}(\delta_{\mathbf{i},\mathbf{j}}G_{\mathrm{g_ig_i}}(t_2)+\zeta_{\mathbf{i},\mathbf{j}}) \tag{D.1}$$
$$\times \left\langle \boldsymbol{\mu}_{\mathrm{g_ie}_{p_1}}\boldsymbol{\mu}_{\mathrm{e}_{p_1}\mathrm{g_j}}\boldsymbol{\mu}_{\mathrm{g_je}_{p_2}}\boldsymbol{\mu}_{\mathrm{e}_{p_2}\mathrm{g_i}}\right\rangle \mathrm{e}^{\mathrm{i}\xi_{\mathrm{e}_{p_1}\mathrm{g_i}}t_1-\mathrm{i}\xi_{\mathrm{g_ig_j}}t_2-\mathrm{i}\xi_{\mathrm{e}_{p_2}\mathrm{g_j}}t_3}$$
$$\times \mathrm{e}^{\phi_{\mathrm{e}_{p_1}\mathrm{g_j}\mathrm{e}_{p_2}\mathrm{g_i}}(0,t_1,t_1+t_2+t_3,t_1+t_2)},$$

$$S_{\mathrm{SE}}(t_1,t_2,t_3) = \mathrm{i}^3\theta(t_1)\theta(t_2)\theta(t_3)\sum_{\mathbf{ij}}\sum_{p_1p_2} p_{\mathrm{g_i}}(\delta_{p_1p_2}G_{\mathrm{e}_{p_1}\mathrm{e}_{p_2}}(t_2)+\zeta_{p_1p_2}) \tag{D.2}$$
$$\times \left\langle \boldsymbol{\mu}_{\mathrm{g_ie}_{p_1}}\boldsymbol{\mu}_{\mathrm{g_ie}_{p_2}}\boldsymbol{\mu}_{\mathrm{e}_{p_2}\mathrm{g_j}}\boldsymbol{\mu}_{\mathrm{e}_{p_2}\mathrm{g_j}}\right\rangle \mathrm{e}^{\mathrm{i}\xi_{\mathrm{e}_{p_1}\mathrm{g_i}}t_1-\mathrm{i}\xi_{\mathrm{e}_{p_2}\mathrm{e}_{p_1}}t_2-\mathrm{i}\xi_{\mathrm{e}_{p_1}\mathrm{g_j}}t_3}$$
$$\times \mathrm{e}^{\phi_{\mathrm{e}_{p_1}\mathrm{g_j}\mathrm{e}_{p_2}\mathrm{g_i}}(0,t_1+t_2,t_1+t_2+t_3,t_1)}$$

and

$$S_{\mathrm{ESA}}(t_1,t_2,t_3) = -\mathrm{i}^3\theta(t_1)\theta(t_2)\theta(t_3)\sum_{\mathbf{i}}\sum_{p_1p_2}\sum_{r} p_{\mathrm{g_i}}(\delta_{p_1p_2}G_{\mathrm{e}_{p_1}\mathrm{e}_{p_1}}(t_2)+\zeta_{p_1p_2}) \tag{D.3}$$
$$\times \left\langle \boldsymbol{\mu}_{\mathrm{g_ie}_{p_1}}\boldsymbol{\mu}_{\mathrm{g_ie}_{p_2}}\boldsymbol{\mu}_{\mathrm{e}_{p_2}\mathrm{f}_r}\boldsymbol{\mu}_{\mathrm{f}_r\mathrm{e}_{p_1}}\right\rangle \mathrm{e}^{\mathrm{i}\xi_{\mathrm{e}_{p_1}\mathrm{g_i}}t_1-\mathrm{i}\xi_{\mathrm{e}_{p_2}\mathrm{e}_{p_1}}t_2-\mathrm{i}\xi_{\mathrm{f}_r\mathrm{e}_{p_1}}t_3}$$
$$\times \mathrm{e}^{\phi_{\mathrm{e}_{p_1}\mathrm{f}_r\mathrm{e}_{p_2}\mathrm{g_i}}(0,t_1+t_2+t_3,t_1+t_2,t_1)}.$$

Here, the complex variable $\xi_{ab} = \omega_{ab} - \mathrm{i}\frac{1}{2}(\gamma_a + \gamma_b)$ is used to take into account the state dephasing due to finite lifetime, $\gamma_a = \frac{1}{2}\sum_{a' \neq a} k_{aa'}$. $p_{\mathrm{g_i}}$ is the Boltzmann probability for the system to be in the **i**-th vibrational state prior the excitation. Angular brackets $\langle ... \rangle$ denote orientationally averaged transition dipole moment products; the random orientation of the whole complex with respect to the incident field is assumed. The auxiliary function is

$$\begin{aligned}\phi_{\mathrm{e}_{p_1} c \mathrm{e}_{p_2} \mathrm{g_i}}(\tau_4, \tau_3, \tau_2, \tau_1) &= -g_{\mathrm{e}_{p_1}\mathrm{e}_{p_1}}(\tau_{43}) - g_{cc}(\tau_{32}) - g_{\mathrm{e}_{p2}\mathrm{e}_{p2}}(\tau_{21}) \\ &+ g_{\mathrm{e}_{p_1} c}(\tau_{32}) + g_{\mathrm{e}_{p_1} c}(\tau_{43}) - g_{\mathrm{e}_{p_1} c}(\tau_{42}) - g_{\mathrm{e}_{p_1}\mathrm{e}_{p_2}}(\tau_{32}) + g_{\mathrm{e}_{p_1}\mathrm{e}_{p_2}}(\tau_{31}) + g_{\mathrm{e}_{p_1}\mathrm{e}_{p_2}}(\tau_{42}) \\ &- g_{\mathrm{e}_{p_1}\mathrm{e}_{p_2}}(\tau_{41}) + g_{c\mathrm{e}_{p_2}}(\tau_{21}) + g_{c\mathrm{e}_{p_2}}(\tau_{32}) - g_{c\mathrm{e}_{p_2}}(\tau_{31}) \\ &- g_{c\mathrm{g_i}}(\tau_{21}) + g_{c\mathrm{g_i}}(\tau_{24}) + g_{c\mathrm{g_i}}(\tau_{31}) - g_{c\mathrm{g_i}}(\tau_{34}),\end{aligned} \tag{D.4}$$

where c stands for either doubly-excited state f_r, or ground state $\mathrm{g_j}$. Response function components with transport are

$$\begin{aligned}S_{\mathrm{GSB}'}(t_1, t_2, t_3) &= \mathrm{i}^3\theta(t_1)\theta(t_2)\theta(t_3)\sum_{\mathbf{ij}}\sum_{p_1 p_2} p_{\mathrm{g_i}}\zeta_{\mathbf{ij}}\, G_{\mathrm{g_j g_i}}(t_2) \\ &\times \left\langle \boldsymbol{\mu}_{\mathrm{g_i}}\boldsymbol{\mu}_{\mathrm{e}_{p_1}\mathrm{g_i}}\boldsymbol{\mu}_{\mathrm{g_j e}_{p_2}}\boldsymbol{\mu}_{\mathrm{e}_{p_2}\mathrm{g}_j}\right\rangle \mathrm{e}^{\mathrm{i}\xi_{\mathrm{e}_{p_1}\mathrm{g_i}}t_1 - \mathrm{i}\xi_{\mathrm{e}_{p_2}\mathrm{g_j}}t_3 + \varphi^*_{\mathrm{e}_{p_2}\mathrm{g_j}\mathrm{e}_{p_2}\mathrm{e}_{p_1}}(\mathbf{t})},\end{aligned} \tag{D.5}$$

$$\begin{aligned}S_{\mathrm{SE}'}(t_1, t_2, t_3) &= \mathrm{i}^3\theta(t_1)\theta(t_2)\theta(t_3)\sum_{\mathbf{ij}}\sum_{p_1 p_2} p_{\mathrm{g_i}}\zeta_{p_1 p_2}\, G_{\mathrm{e}_{p_2}\mathrm{e}_{p_1}}(t_2) \\ &\times \left\langle \boldsymbol{\mu}_{\mathrm{g_i e}_{p_1}}\boldsymbol{\mu}_{\mathrm{g_i e}_{p_1}}\boldsymbol{\mu}_{\mathrm{e}_{p_2}\mathrm{g_j}}\boldsymbol{\mu}_{\mathrm{e}_{p_2}\mathrm{g_j}}\right\rangle \mathrm{e}^{\mathrm{i}\xi_{\mathrm{e}_{p_1}\mathrm{g_i}}t_1 - \mathrm{i}\xi_{\mathrm{e}_{p_2}\mathrm{g_j}}t_3 + \varphi^*_{\mathrm{e}_{p_2}\mathrm{g_j}\mathrm{e}_{p_2}\mathrm{e}_{p_1}}(\mathbf{t})},\end{aligned} \tag{D.6}$$

and

$$\begin{aligned}S_{\mathrm{ESA}'}(t_1, t_2, t_3) &= -i^3\theta(t_1)\theta(t_2)\theta(t_3)\sum_{\mathbf{i}}\sum_{p_1 p_2}\sum_{r} p_{\mathrm{g_i}}\zeta_{p_1 p_2}\, G_{\mathrm{e}_{p_2}\mathrm{e}_{p_1}}(t_2) \\ &\times \left\langle \boldsymbol{\mu}_{\mathrm{g_i e}_{p_1}}\boldsymbol{\mu}_{\mathrm{g_i e}_{p_1}}\boldsymbol{\mu}_{\mathrm{e}_{p_2}\mathrm{f}_r}\boldsymbol{\mu}_{\mathrm{f}_r\mathrm{e}_{p_2}}\right\rangle \mathrm{e}^{\mathrm{i}\xi_{\mathrm{e}_{p_1}\mathrm{g_i}}t_1 - \mathrm{i}\xi_{\mathrm{f}_r\mathrm{e}_{p_2}}t_3 + \varphi^*_{\mathrm{f}_r\mathrm{e}_{p_2}\mathrm{e}_{p_2}\mathrm{e}_{p_1}}(\mathbf{t})}.\end{aligned} \tag{D.7}$$

Here

$$\begin{aligned}\varphi_{c\mathrm{b}\mathrm{e}_{p_2}\mathrm{e}_{p_1}}(t_1, t_2, t_3) &= -g_{\mathrm{e}_{p_1}\mathrm{e}_{p_1}}(t_1) - g_{bb}(t_3) - g^*_{cc}(t_3) \\ &- g_{b\mathrm{e}_{p_1}}(t_1 + t_2 + t_3) + g_{b\mathrm{e}_{p_1}}(t_1 + t_2) + g_{b\mathrm{e}_{p_1}}(t_2 + t_3) \\ &- g_{b\mathrm{e}_{p_1}}(t_2) + g_{c\mathrm{e}_{p_1}}(t_1 + t_2 + t_3) - g_{c\mathrm{e}_{p_1}}(t_1 + t_2) \\ &- g_{c\mathrm{e}_{p_1}}(t_2 + t_3) + g_{c\mathrm{e}_{p_1}}(t_2) + g_{cb}(t_3) + g^*_{bc}(t_3) \\ &+ 2\mathrm{i}\mathrm{Im}[g_{c\mathrm{e}_{p_2}}(t_2 + t_3) - g_{c\mathrm{e}_{p_2}}(t_2) - g_{c\mathrm{e}_{p_2}}(t_3) \\ &+ g_{b\mathrm{e}_{p_2}}(t_2) - g_{b\mathrm{e}_{p_2}}(t_2 + t_3) + g_{b\mathrm{e}_{p_2}}(t_3).\end{aligned} \tag{D.8}$$

Index

Acknowledgments

During the years of my PhD studies, I met many amazing people, outstanding scientists, the best specialists in their fields, and even had a privilege of working with some of them or at least having a glass of beer. I would like to thank them all.

Most of all, I would like to thank professors Leonas Valkūnas and Darius Abramavičius. I greatly appreciate their supervision, exceptional enthusiasm, overwhelming support and infinite patience.

I would like to express my gratitude to Tomáš Mančal, Donatas Zigmantas and Graham R. Fleming for their hospitality during my stays in their labs as a visiting student and our fruitful collaboration. Many thanks for all fellow students and researchers in Vilnius University, Center for Physical Sciences and Technology, Charles University in Prague, Lund University, and University of California, Berkeley for a creative and friendly atmosphere.

Also, many thanks go to some of the reviewers and referees of my publications for not rejecting them. I acknowledge the support from the Research Council of Lithuania, Vilnius University Mobility Fund of Doctoral Studies, and European Social Fund.

Outside academia, I cannot thank Adolfas Stanevičius, my teacher of physics, enough. Without his encouragement and patience, physics would have never made me its student.

And lastly, I would like to thank to my family and friends for their support and love, and give my special thanks to Dr. Eglė Gabrytė.

Vytautas Butkus
Vilnius, 2015